

14 November 2008 | \$10

Science



AAAS



COVER

A montage showing three views of a 5-millimeter-long juvenile medaka, with the nervous system imaged with a digital scanned laser light sheet fluorescence microscope. This technique has been used to reconstruct embryogenesis in zebrafish. See [page 1065](#).

Image: Philipp Keller, Lazaro Centanin, Annette Schmidt/EMBL

DEPARTMENTS

- 1019 [Science Online](#)
- 1021 [This Week in Science](#)
- 1026 [Editors' Choice](#)
- 1028 [Contact Science](#)
- 1031 [Random Samples](#)
- 1033 [Newsmakers](#)
- 1120 [New Products](#)
- 1121 [Science Careers](#)

EDITORIAL

- 1025 [A Call to Serve](#)
by William A. Wulf and Anita K. Jones

NEWS OF THE WEEK

- Obama Victory Raises Hopes for New Policies, Bigger Budgets
New Congress Looks Familiar 1034
- European Union Floats Tighter Animal-Research Rules 1037
- SCIENCESCOPE** 1037
- Vatican Science Conference Offers an Ambiguous Message 1038
- Statin Therapy Reduces Disease in Healthy Volunteers—But How, Exactly? 1039

NEWS FOCUS

- The Birth of Childhood 1040
>> Report p. 1089; Science Podcast
- Minnesota Ecologist Pushes Prairie Biofuels 1044
- A Bunch of Trouble 1046



1040

LETTERS

- European Union and NIH Collaborate 1048
E. A. Zerhouni and J. Potočník
- Skeptical of Assisted Colonization
I. Davidson and C. Simkanin
- Assisted Colonization Won't Help Rare Species
D. Huang
- Where Species Go, Legal Protections Must Follow
G. Chapron and G. Samelius
- Response *O. Hoegh-Guldberg et al.*

CORRECTIONS AND CLARIFICATIONS 1050

BOOKS ET AL.

- Trace Fossil Analysis 1051
A. Seilacher, reviewed by S. Jensen
- In Sputnik's Shadow The President's Science Advisory Committee and Cold War America 1052
Z. Wang, reviewed by G. A. Good
- Sant Ocean Hall *reviewed by L. D. Jenkins* 1053

POLICY FORUM

- Certificates of Confidentiality and Compelled Disclosure of Data 1054
L. M. Beskow, L. Dame, E. J. Costello

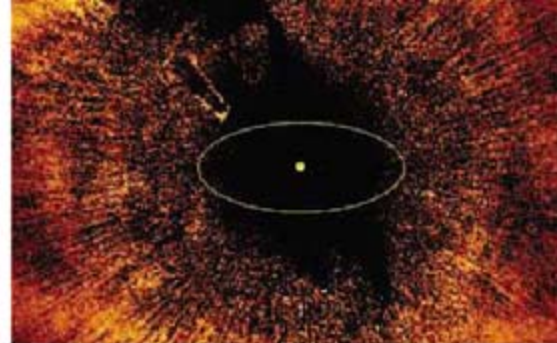
PERSPECTIVES

- A Sideways Glance at Chemical Reactivity 1056
D. A. Blank >> Report p. 1073
- A Biolinguistic Agenda 1057
M. D. Hauser and T. Bever
- RT Slides Home... 1059
S. G. Sarafianos and E. Arnold >> Report p. 1092
- Understanding Glacier Flow in Changing Times 1061
R. B. Alley, M. Fahnestock, I. Joughin
- A Protein Pupylation Paradigm 1062
S. Mukherjee and K. Orth >> Report p. 1104



1053

[CONTENTS continued >>](#)



SCIENCE EXPRESS

www.sciencexpress.org

ASTRONOMY

Optical Images of an Exosolar Planet 25 Light-Years from Earth

P. Kalas et al.

Images from the Hubble Space Telescope reveal a Jupiter-sized planet, perhaps with a surrounding dust disk, orbiting about 115 astronomical units from a nearby main sequence star.

[10.1126/science.1166609](https://doi.org/10.1126/science.1166609)

ASTRONOMY

Direct Imaging of Multiple Planets Orbiting the Star HR 8799

C. Marois et al.

Infrared images from the Keck and Gemini telescopes reveal three giant planets orbiting counterclockwise around a young star, in a scaled-up version of our solar system.

>> *Science Podcast*

[10.1126/science.1166585](https://doi.org/10.1126/science.1166585)

PERSPECTIVE: Exoplanets—Seeing Is Believing

M. S. Marley

[10.1126/science.1167569](https://doi.org/10.1126/science.1167569)

MEDICINE

Genomic Loss of microRNA-101 Leads to Overexpression of Histone Methyltransferase EZH2 in Cancer

S. Varambally et al.

In some human prostate cancers, a genomic deletion eliminates a key regulatory microRNA, which results in disruption of gene silencing mechanisms.

[10.1126/science.1165395](https://doi.org/10.1126/science.1165395)

CELL BIOLOGY

A Role for the ESCRT System in Cell Division in Archaea

R. Y. Samson, T. Obita, S. M. Freund, R. L. Williams, S. D. Bell

A class of proteins required for membrane trafficking and cytokinesis in eukaryotes is also unexpectedly required in some Archaea for cell division.

[10.1126/science.1165322](https://doi.org/10.1126/science.1165322)

TECHNICAL COMMENT ABSTRACTS

PLANETARY SCIENCE

Comment on "Ancient Asteroids Enriched in Refractory Inclusions" 1050

D. C. Hezel and S. S. Russell

[full text at www.sciencemag.org/cgi/content/full/322/5904/1050a](http://www.sciencemag.org/cgi/content/full/322/5904/1050a)

Response to Comment on "Ancient Asteroids Enriched in Refractory Inclusions"

J. M. Sunshine et al.

[full text at www.sciencemag.org/cgi/content/full/322/5904/1050b](http://www.sciencemag.org/cgi/content/full/322/5904/1050b)

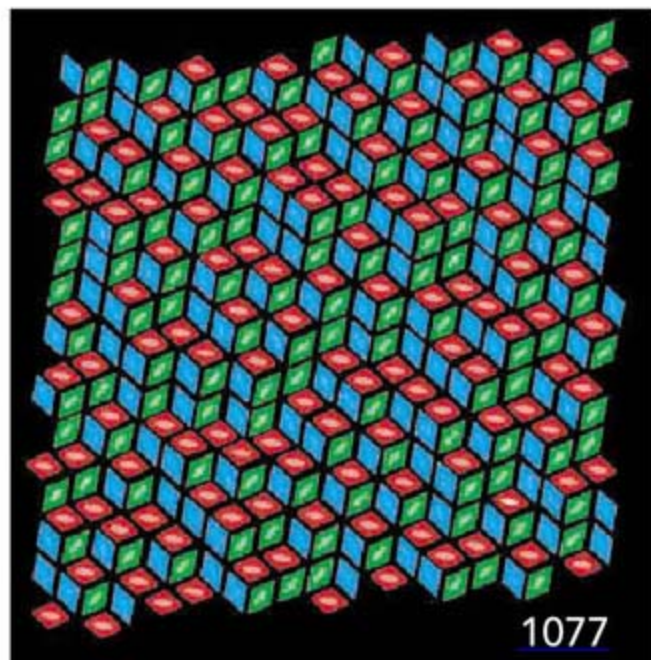
BREVIA

ECOLOGY

Physiographic Control on the Development of *Spartina* Marshes 1064

G. Fragoso and T. Spencer

Erosion of sediment is harmful to the growth of marsh grass, possibly explaining salt marsh die-back, a phenomenon thought to be a result of sea-level changes.



RESEARCH ARTICLE

DEVELOPMENTAL BIOLOGY

Reconstruction of Zebrafish Early Embryonic Development by Scanned Light Sheet Microscopy 1065

P. J. Keller, A. D. Schmidt, J. Wittbrodt, E. H. K. Stelzer

Digitized tracking of each cell during the first 24 hours of zebrafish development reveals how the body axis and germ layer are formed and provides a community resource.

REPORTS

MATERIALS SCIENCE

Kinetics of Individual Nucleation Events Observed in Nanoscale Vapor-Liquid-Solid Growth 1070

B. J. Kim et al.

Transmission electron microscopy reveals the kinetics of nucleation and growth of silicon particles from liquid gold-silicon droplets, the first step in growing nanowires.

CHEMISTRY

Spectroscopic Tracking of Structural Evolution in Ultrafast Stilbene Photoisomerization 1073

S. Takeuchi et al.

Raman spectroscopy offers a global view of how all the atoms move during the photoinduced picosecond isomerization of stilbene.

>> *Perspective p. 1056*

CHEMISTRY

Random Tiling and Topological Defects in a Two-Dimensional Molecular Network 1077

M. O. Blunt et al.

An organic molecule absorbed on graphite forms networks that represent an intermediate state between crystalline ordering and amorphous packing.

[CONTENTS continued >>](#)

REPORTS CONTINUED...

CHEMISTRY

Observing the Creation of Electronic Feshbach Resonances in Soft X-ray-Induced O₂ Dissociation 1081

A. S. Sandhu et al.

Attosecond spectroscopy reveals that a second electron cannot be ionized from an oxygen molecule until the nuclei, which repel each other, have moved about 30 angstroms apart.

ATMOSPHERIC SCIENCE

Photosynthetic Control of Atmospheric Carbonyl Sulfide During the Growing Season 1085

J. E. Campbell et al.

The atmospheric concentration of carbonyl sulfide, a trace gas consumed by land plants along with carbon dioxide, can be used to estimate the amount of photosynthesis occurring on land.

ANTHROPOLOGY

A Female *Homo erectus* Pelvis from Gona, Ethiopia 1089

S. W. Simpson et al.

A nearly complete pelvis of an adult female *Homo erectus* reveals that its morphology had evolved in response to increasing fetal brain size, not environmental factors. >> *News story p. 1040*

BIOCHEMISTRY

Slide into Action: Dynamic Shuttling of HIV Reverse Transcriptase on Nucleic Acid Substrates 1092

S. Liu et al.

As it converts viral single-stranded RNA to double-stranded DNA, HIV reverse transcriptase shuttles between the ends of the nucleic acid, flipping its orientation. >> *Perspective p. 1059*

IMMUNOLOGY

***Batf3* Deficiency Reveals a Critical Role for CD8 α^+ Dendritic Cells in Cytotoxic T Cell Immunity** 1097

K. Hildner et al.

In mice, an identifiable subset of antigen-presenting cells is necessary for a normal immune cell response to viral infection and for efficient rejection of tumor cells.

IMMUNOLOGY

Del-1, an Endogenous Leukocyte-Endothelial Adhesion Inhibitor, Limits Inflammatory Cell Recruitment 1101

E. Y. Choi et al.

An endogenous inhibitor of immune cell adhesion dampens recruitment of immune cells to sites of inflammation.

CELL BIOLOGY

Ubiquitin-Like Protein Involved in the Proteasome Pathway of *Mycobacterium tuberculosis* 1104

M. J. Pearce et al.

A prokaryotic version of ubiquitin, a eukaryotic tag for protein degradation, is linked to lysines in prokaryotic proteins destined for destruction, a process called pupylation.

>> *Perspective p. 1062*

MICROBIOLOGY

Genome of an Endosymbiont Coupling N₂ Fixation to Cellulolysis Within Protist Cells in Termite Gut 1108

Y. Hongoh et al.

In the termite gut, an endosymbiotic bacterium fixes atmospheric nitrogen within the cells of its cellulose-digesting host protist, allowing the insect to thrive on wood.

MICROBIOLOGY

Globally Distributed Uncultivated Oceanic N₂-Fixing Cyanobacteria Lack Oxygenic Photosystem II 1110

J. P. Zehr et al.

An abundant marine cyanobacteria group fixes nitrogen but lacks the genes for carbon fixation and oxygen production, forcing a reevaluation of nitrogen and carbon cycling.

>> *Science Podcast*

PLANT SCIENCE

***Arabidopsis* Stomatal Initiation Is Controlled by MAPK-Mediated Regulation of the bHLH SPEECHLESS** 1113

G. R. Lampard, C. A. MacAlister, D. C. Bergmann

Positive and negative developmental signals that determine the locations of gas-exchanging leaf pores converge on a specific domain within a transcription factor.

PLANT SCIENCE

Regulatory Genes Control a Key Morphological and Ecological Trait Transferred Between Species 1116

M. Kim et al.

A key trait—asymmetric flowers with large petals—moves between flower species when a cluster of regulatory genes is transferred from a hybrid to a recipient parent.



1108



SCIENCE (ISSN 0036-8075) is published weekly on Friday, except the last week in December, by the American Association for the Advancement of Science, 1200 New York Avenue, NW, Washington, DC 20005. Periodicals Mail postage (publication No. 484460) paid at Washington, DC, and additional mailing offices. Copyright © 2008 by the American Association for the Advancement of Science. The title SCIENCE is a registered trademark of the AAAS. Domestic individual membership and subscription (51 issues): \$144 (\$74 allocated to subscription). Domestic institutional subscription (51 issues): \$770; Foreign postage extra: Mexico, Caribbean (surface mail) \$55; other countries (air assist delivery) \$85. First class, airmail, student, and emeritus rates on request. Canadian rates with GST available upon request, GST #1254 88122. Publications Mail Agreement Number 1069624. SCIENCE is printed on 30 percent post-consumer recycled paper. Printed in the U.S.A.

Change of address: Allow 4 weeks, giving old and new addresses and 8-digit account number. Postmaster: Send change of address to AAAS, P.O. Box 96178, Washington, DC 20090-6178. Single-copy sales: \$10.00 current issue, \$15.00 back issue prepaid includes surface postage; bulk rates on request. Authorization to photocopy material for internal or personal use under circumstances not falling within the fair use provisions of the Copyright Act is granted by AAAS to libraries and other users registered with the Copyright Clearance Center (CCC) Transactional Reporting Service, provided that \$20.00 per article is paid directly to CCC, 222 Rosewood Drive, Danvers, MA 01923. Science is indexed in the Reader's Guide to Periodical Literature and in several specialized indexes.



Printed on
30% post-consumer
recycled paper.

CONTENTS continued >>



Keratin in claws.

SCIENCE NOW

www.sciencenow.org

HIGHLIGHTS FROM OUR DAILY NEWS COVERAGE

So That's Why Chickens Have Combs

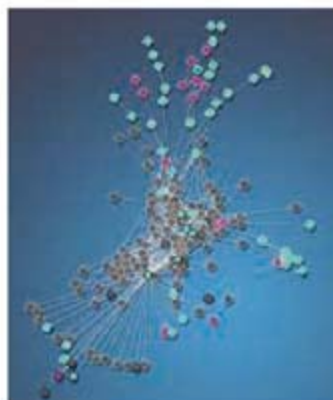
Birds and reptiles make hair proteins, just like mammals do.

Earth's Strange Tango With the Sun

Mysterious magnetic portals link our planet to its star.

Bird Brains Split Lookout Duty

A migrating bird rests half of its brain while the other half remains alert.



A Wnt pathway interaction.

SCIENCE SIGNALING

www.sciencesignaling.org

THE SIGNAL TRANSDUCTION KNOWLEDGE ENVIRONMENT

RESEARCH ARTICLE: Cripto Localizes Nodal at the Limiting Membrane of Early Endosomes

M.-H. Blanchet, J. A. Le Good, V. Oorschot, S. Baflast, G. Minchiotti, J. Klumperman, D. B. Constam

Cripto facilitates ALK4 signaling by attenuating intraendosomal sorting of internalized Nodal.

RESEARCH ARTICLE: New Regulators of Wnt/ β -Catenin Signaling Revealed by Integrative Molecular Screening

M. B. Major, B. S. Roberts, J. D. Berndt, S. Marine, J. Anastas, N. Chung, M. Ferrer, X. Yi, C. L. Stoick-Cooper, P. D. von Haller, L. Kategaya, A. Chien, S. Angers, M. MacCoss, M. A. Cleary, W. T. Arthur, R. T. Moon

Integration of protein-protein interaction networks and human genome-wide RNAi screens produces mechanistic insight into Wnt/ β -catenin signaling.

PODCAST

M. B. Major, R. T. Moon, A. M. VanHook

Ben Major and Randall Moon discuss their screen for cell type-specific modifiers of Wnt signaling.

E-LETTER: Calcium-Sensing Receptor Function in the Skeleton—Alternative Interpretations

L. D. Quarles and M. Pi

E-LETTER: Response to Quarles and Pi

W. Chang, C. Tu, T.-H. Chen, D. Bikle, D. Shoback

A letters exchange debates an alternative interpretation of the observations recently presented by Chang *et al.* (*Sci. Signal.* **1** (35), ra1).



Conflict of interest: A big career gamble.

SCIENCE CAREERS

www.sciencecareers.org/career_development

FREE CAREER RESOURCES FOR SCIENTISTS

Conflicts of Interest and Physician-Scientists

J. B. Finkelstein

Clinician-researchers need to take threats from conflicts of interest seriously.

A Career Niche at the Interface of Academe and Industry

E. Pain

Spanish biologist David Ràfols used his technology and industry experience to create his open-innovation company.

Learning to Let Go While Trusting Your Data

S. Webb

New investigators must take responsibility for the integrity of their lab's data, even as direct control over that data declines.

From the Archives: Do You Really Want Your Name on That Paper?

K. Cottingham et al.

Science Careers looks at the ethics of authorship, responsibility, and keeping careful records in the lab.

SCIENCE PODCAST

www.sciencemag.org/multimedia/podcast

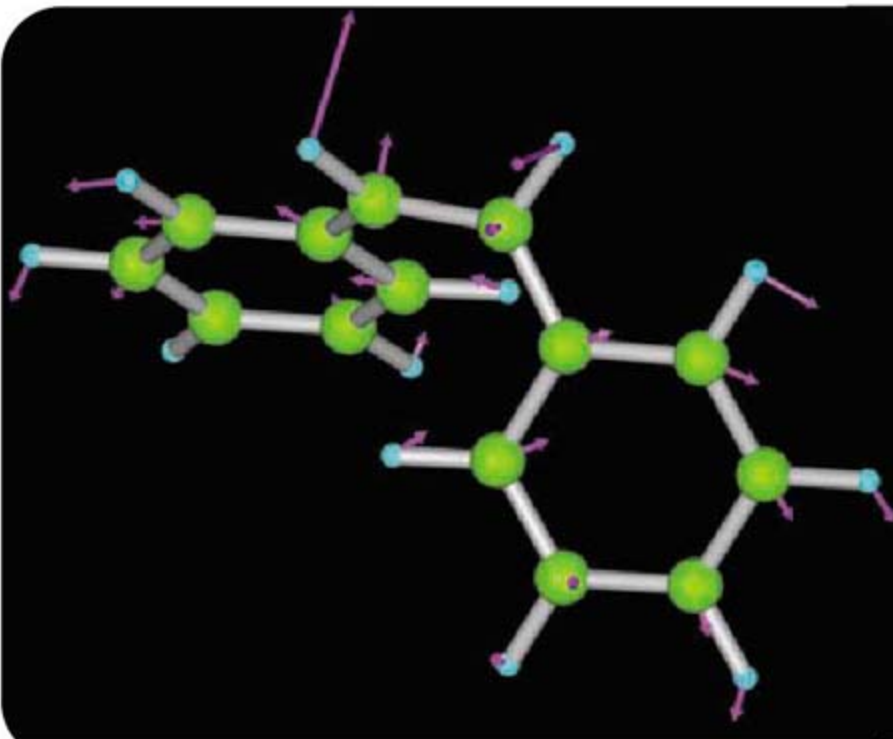
FREE WEEKLY SHOW

Download the 14 November

Science Podcast to hear about pictures of a nearby multi-planet system, marine cyanobacteria that lack genes for oxygen-evolving photosynthesis, the evolution of childhood, and more.



Separate individual or institutional subscriptions to these products may be required for full-text access.

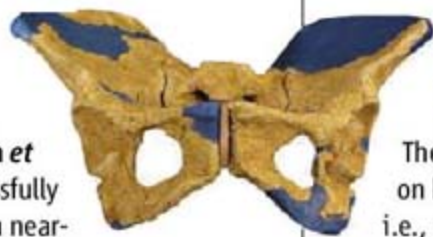


<< How Stilbene Twists

Over the last decade, ultrafast vibrational spectroscopy has offered detailed glimpses into how molecules rearrange upon excitation. However, the available information tends to be confined to the small segment of the molecule that is most actively changing. Takeuchi *et al.* (p. 1073; see the Perspective by Blank) used a coherent Raman technique to track vibrations more globally across the framework of stilbene during its photoinduced *cis-to-trans* isomerization about the central C=C double bond. Tracking the steady frequency shift of a skeletal vibration and then modeling the process theoretically produced a thorough picture of the order in which different portions of the molecule move, starting with a lengthening of the double bond and extending to the twisting of pendant H atoms out of plane.

Homo erectus Hips

Human pelvic morphology is central to the understanding of obstetrics, sexual dimorphism, and neonatal brain size and patterns of brain growth, as well as the evolution of body form and its relation to locomotor refinements and adaptation to tropical environments. However, sufficiently preserved pelvic bones are very rare in the fossil record, and only few such hominid fossils are known from the entire Plio-Pleistocene record of Africa. Simpson *et al.* (p. 1089) have successfully recovered, and restored a near-complete adult female *Homo erectus* pelvis from Gona, Afar, Ethiopia, dated to ~0.9 to 1.4 million years ago. The *H. erectus* pelvis was much more australopithecine-like than hitherto thought, and allowed a neonate brain size 25 to 30% larger than earlier estimates, suggesting that *H. erectus* lacked a fully human-like phase of infant dependency. Additionally, *H. erectus* did not have the tall narrow body form of modern humans adapted to tropical, semi-arid environments or hips adapted for long distance running, previously thought to characterize *H. erectus*.



Quantifying Global Photosynthesis

formation of the dication, but, as the nuclei repel one another, the dication becomes accessible at a separation distance of roughly 30 angstroms. At that stage, a transient state (a Feshbach resonance) can be observed, which persists due to spin-orbit coupling before eventually decaying through further ionization or radiative relaxation.

The utility of climate models rests in part on how well the uptake of CO₂ by plants, i.e., photosynthesis, can be represented, because carbon and climate are so inextricably entwined. However, how much photosynthesis actually occurs on a global scale is very difficult to measure, because the available techniques are either indirect, or direct but not amenable to large-scale application. Campbell *et al.* (p. 1085) show using measurements made during the North American growing season that carbonyl sulfide, COS, is a good surrogate for CO₂, and that the quantitative relationship between the two that has been measured in the laboratory also extends to the bulk atmosphere. Thus, the measurement of vertical atmospheric concentration gradients of COS should reflect how much photosynthesis is occurring over continents during the growing season.

Digitizing Development

Current microscopes provide neither the speed nor the low phototoxicity required for recordings of entire embryos over long periods of time, which would be required to reconstruct a com-

plete picture of vertebrate development. Keller *et al.* (p. 1065, published online 9 October; see 10 October news story by Vogel; cover) developed digital scanned laser light sheet fluorescence microscopy that overcomes these limitations and delivers quantitative information for entire zebrafish embryos at subcellular resolution. The data provide a developmental blueprint of a vertebrate species and simultaneously track about 20,000 cells up to a stage in which major organs show function.

Disordering of Surface Tiles

Molecular networks on surfaces could provide a readily interrogated model for understanding the structural basis of glasses, but often the interactions between molecules lead to well-ordered arrays. Blunt *et al.* (p. 1077) used scanning tunneling microscopy to investigate an intermediate case between crystals and glasses in which an organic molecule (*p*-terphenyl-3,5,3',5'-tetracarboxylic acid) absorbed on graphite locally organizes into rhombus tiles. The tiles have a nonperiodic arrangement and are not ordered translationally. Networks formed as junctions of three to six molecules with hexagonal symmetry, and triangular defects could form and move through the network causing reordering of the local arrangement.

Putting the Brakes on Inflammation

Numerous adhesion receptors of the selectin, integrin, or immunoglobulin family promote inflammatory cell recruitment. In contrast, inhibitors of the leukocyte adhesion cascade are

Oxygen Torn Apart

When molecules are photoionized with excess energy, they can relax by ejecting a second electron. However, photoionized oxygen has appeared to relax in this way only after the nuclei spread a substantial distance apart. By pairing recently developed attosecond x-ray pulse generation techniques with precise ion imaging, Sandhu *et al.* (p. 1081) uncover the detailed dynamics underlying this behavior. The initially generated O²⁺ ion quickly drops below the energy threshold for

Continued from page 1021

not well known. Now **Choi *et al.*** (p. 1101) have characterized developmental endothelial locus-1 (Del-1) as an endogenous inhibitor of the leukocyte adhesion cascade. Del-1, which is an endothelially expressed, secreted molecule, is a ligand of the major leukocyte adhesion receptor LFA-1. Soluble Del-1 inhibited neutrophil adhesion under both static and physiologic flow conditions. Endothelial Del-1 deficiency promoted increased leukocyte adhesion, and mice lacking Del-1 displayed significantly higher neutrophil accumulation during lung inflammation, which was reversed in Del-1/LFA-1 double deficient mice. Thus Del-1 interacts with LFA-1 preventing inflammatory cell recruitment.

Ubiquitin's Pup(py)?

Ubiquitin is a universal modifier used by eukaryotes to tag proteins for degradation. Now **Pearce *et al.*** (p. 1104, published online 2 October; see the Perspective by **Mukherjee and Orth**) describe a ubiquitin-like protein system they call Pup in prokaryotes. Pup appears to be required for protein degradation by the *Mycobacterium tuberculosis* (Mtb) proteasome. Because proteasome function is essential for the virulence of Mtb, the Pup conjugation pathway could potentially be targeted for the development of antituberculosis drugs.



From Flower to Flower

Although horizontal gene transfer has been extensively studied in bacteria, its role in the evolution of multicellular plants and animals has been explored little. **M. Kim *et al.*** (p. 1116)

analyze a key morphological and ecological trait transferred naturally between two higher eukaryotic species, flowers of the genus *Senecio*. The transfer involves introgression of a cluster of regulatory genes that control flower morphology. The genes are expressed in the outer regions of the developing flower where they promote the production of asymmetric florets with large petals, yielding a daisy-like head that confers higher levels of outcrossing. Thus, regulatory genes can allow a key morphological and ecological trait to be gained, lost, and regained during evolution, providing a more dynamic view of evolutionary change than the traditional one which considers each lineage as evolving independently.

Sole Food

Termites have a formidable capacity for digesting dead wood. Consequently they have become major pests destroying man-made structures around the world. The biochemical talents required for digesting wood are much sought after by humans for processing biofuels, but because wood is an unbalanced foodstuff and lacks nitrogen, no simple solution is available. Termites owe their success to arrays of symbiotic microorganisms possessing complementary metabolisms. **Hongoh *et al.*** (p. 1108) have sequenced the genome of a dominant bacterial symbiont living within a dominant protozoan that lives in termite guts. The sequence reveals genes that allow the bacterium to fix atmospheric nitrogen, to recycle nitrogen from waste nitrogen products from its protozoan host, and to make amino acids for its own and both its host's and its host's host's use. The energy required for nitrogen fixation is considerable and the bacterium obtains this not only from hydrogen produced during nitrogen fixation but also from the anaerobic fermentation of sugars released from cellulose by the protozoan.

To Be or Not to Be?

The tiny pores, or stomata, that open and close on a leaf's surface allow for the exchange of gases according to the needs of the plant's physiology. The number of stomata formed during development is a result of competing signals that activate or repress pore formation. **Lampard *et al.*** (p. 1113) now show how these competing signals converge so that their inputs result in one question: Will there or won't there be a stoma placed here? The transcription factor SPEECHLESS, which activates stomatal development programs, can be phosphorylated by certain mitogen-activated protein kinases (MAPKs), a group of kinases that, among myriad other functions, repress formation of stomata. All the phosphorylation sites are contained within the 93-amino acid MAPK target domain of SPEECHLESS, which thus integrates positive and negative signals.

CREDIT: KIM ET AL.

We're making a difference...

HudsonAlpha is passionate about translating the promise of genomics into measurable real-world results.

So can you

Applications for postdoctoral fellows and computational biologists are welcome, in the laboratories of Drs. Rick Myers and Devin Absher. Highly-motivated applicants must have a background in genomics, epigenetics, human genetics, population genetics, and/or cancer biology. Experience with microarrays or next-generation sequencing technologies, and ability to generate and analyze large, complex datasets are both preferred.

absher.hudsonalpha.org
myers.hudsonalpha.org

Send resume and cover letter to Dr. Chris Gunter, director of research affairs.
resumes@hudsonalpha.org.



HUDSONALPHA
INSTITUTE FOR BIOTECHNOLOGY
Huntsville, Alabama
hudsonalpha.org



William A. Wulf is a University Professor in the Department of Computer Science at the University of Virginia, Charlottesville, VA; president emeritus of the U.S. National Academy of Engineering; and former Assistant Director of the U.S. National Science Foundation.



Anita K. Jones is a University Professor in the Department of Computer Science at the University of Virginia, Charlottesville, VA; former Director of Defense Research and Engineering at the U.S. Department of Defense; and former vice chair of the U.S. National Science Board.

A Call to Serve

ONCE BARACK OBAMA BECOMES THE 44TH PRESIDENT OF THE UNITED STATES IN JANUARY 2009, he will, sooner or later, appoint individuals to science and technology policy positions within the executive branch of government. It seems as though every science- and engineering-related think tank either has published, or shortly will, a report calling on the new administration to appoint these people quickly and give them the authority and tools to do their job.

But it is not just an administration choice; qualified scientists and engineers need to be willing to take those jobs. The quality of the decisions and actions of an administration directly depends on the quality of those appointees and others who serve. Our premise is that every engineer and every scientist ought to include service to their country in their career plan.

Too often we have heard “I am too busy,” or “my research is my service to the country,” or various disparaging remarks about government bureaucrats and not wanting to be associated with them. There are several reasons why technically literate people should serve. First, they are needed. The world is more technologically sophisticated than it has ever been, and today most public policy issues have technical dimensions. Without sound technical input, some bad public policy will result. Without unrelenting oversight by individuals with technical expertise to ensure sound implementation, foolish actions will be taken.

The U.S. population broadly supports the nation’s research and, frankly, in return the research community owes it to society to ensure that the best possible policy decisions are made. And there is a self-interest factor. This community believes that increased support for research would benefit the nation in the long term, but that case needs to be made from within the government as well as from the outside. The same argument is valid for other nations as well. Lastly, government service can be intellectually interesting. Executive agencies have resources to deal with problems. The challenge is to address them creatively and effectively.

Scientists and engineers think about problems differently. For example, lawyers, who disproportionately populate government positions, are trained to marshal an argument to support a predetermined conclusion (e.g., the client is innocent). In contrast, scientists and engineers are taught to analyze and design so that the outcome is not predetermined but is derived from the constraints of the problem. They collect relevant information, and only solutions that fit the data are acceptable. Scientists and engineers also think in terms of the total problem—for today and for tomorrow. An engineer will design a bridge to be taken down cost-effectively at the end of its life. This culture of thought and analytic tools and decision-making methods needs to have a stronger influence in decisions made about issues that at their root involve science or technology.

So how might one try out such service? One approach is to volunteer to advise some element of the government. Once a person is seen to contribute, they are increasingly called on to advise at higher levels. This can lead to appointment to more senior advisory bodies. Alternatively, an individual can apply to be a program officer in a federal or state government agency. Universities routinely grant leaves of absence for such service. Although one does not begin as the head of an agency, these program officer positions wield considerable resources and can materially address important challenges.

We believe that the scientists and engineers of all countries need to step up. Every one has a contribution to make. Shouting from the sidelines does not work. And if the technical community does not engage, we will get what we deserve.

— William A. Wulf and Anita K. Jones



PHYSICS

Polarization Puzzle

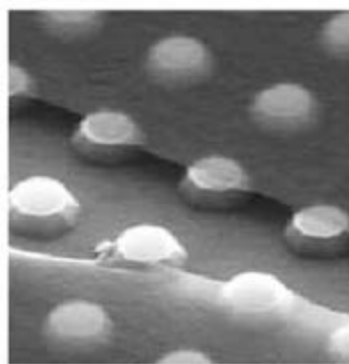
When very high-intensity light strikes a solid surface, it can liberate multiple electrons and ions that then continue to collide rapidly with one another, forming a plasma state. These collisions in turn lead to emission across a broader spectrum of wavelengths, as kinetic and electromagnetic energy steadily interconvert. The chaos of such a process might be expected to distribute the emitted light across completely random orientations. However, Liu *et al.* make the surprising observation that under certain conditions, the plasma produced from a silicon (Si) surface initially emits a continuum of ultraviolet light that is >95% polarized. The optimal conditions involved focusing a pair of ultrashort laser pulses spaced 80 ps apart in time onto a Si(111) crystal face; this dual pulse sequence proved key to maximizing the effect. The degree of polarization was also highly sensitive to the distance between the surface and the laser focus, and scaled inversely with pulse intensity (at least within the range sufficient to induce plasma emission). — JSY

Appl. Phys. Lett. **93**, 161502 (2008).

MATERIALS SCIENCE

Graphene Oxide Resonators

One potential application for graphene (sheets of graphite only one or several layers thick) is as a resonator in nanoelectromechanical systems, in part because of the high ratio of stiffness to mass. However, the formation of large-area films of exfoliated graphene and manipulation of the graphene flakes are experimentally challenging.



An alternative is to use a related material, graphene oxide, in which the graphene film is chemically modified with oxygenated substituents.

Robinson *et al.* rapidly deposited graphene oxide platelets onto glass by spin casting along with rapid solvent evaporation, which formed ultrathin continuous films. These films could then be chemically reduced, and despite being as thin as 4 nm, could be released from the substrate by being dipped into basic solution. They could then



PHYSIOLOGY

Four Wings Are Better Than Two

The hindwings of butterflies and moths are necessary for agility, but not for flight itself. In experiments in which the hindwings of cabbage butterflies and gypsy moths were removed, Jantzen and Eisner found that the forewings were sufficient for these lepidopterans to remain airborne, despite the fact that they constitute only half the total wing area. However, video recordings showed that removal of the hindwing, which is mechanically coupled to the forewing, resulted in substantial deficits in several measures of flight performance, such as linear and turning acceleration. Hence, the hindwing may have evolved as an adaptation for rapid maneuverability in the face of pursuit by predators, chiefly bats and birds. — AMS

Proc. Natl. Acad. Sci. U.S.A. **105**, 16636 (2008).

be suspended onto substrates patterned with circular holes (between about 3 and 7 μm in diameter) in order to form drum resonators. Laser interferometry revealed that these membranes resonate in the radiofrequency range and have quality factors up to 4000, which is comparable to those of diamond oscillators and exceeds typical values for graphene oscillators (10 to 200). This increase relative to graphene reflects the enhanced adhesion of graphene oxide to glass surfaces through surface oxygen groups. — PDS

Nano Lett. **8**, 3441 (2008).

MOLECULAR BIOLOGY

Keeping One's Identity

The phenotype of a cell is in part defined by its pattern of active versus inactive gene expression. During development, progenitor cells divide and differentiate down specific lineages, and daughter cells retain the same activity profile as the cell

from which they were derived. It is necessary to preserve these markers of cell identity through mitosis, when transcription ceases and many chromatin-binding proteins that determine gene activity dissociate from the DNA. Most of the chromatin becomes tightly compacted, but some active regions remain open, due to the binding of specific factors to gene promoters. This enables transcription to resume more easily after cell division and is known as gene bookmarking, being analogous to the way a bookmark allows one to open a book at a specific page; gene-specific bookmarking factors have been identified. TATA-binding protein (TBP) is an essential basal transcription factor, which remains bound to active promoters during mitosis, and Xing *et al.* show that TBP acts as a general bookmarking factor by recruiting the phosphatase PP2A. This enzyme inactivates condensin, which is a large protein complex involved in compacting chromosomes during mitosis. Understanding general mecha-

nisms of bookmarking could be important for controlling cellular behavior during reprogramming, when differentiated cells need to be wiped clean of their previous identity. — HP*

Nat. Cell Biol. **10**, 1318 (2008).

PSYCHOLOGY

Don't Get Even, Stay Mad

Declarations of unintentionality ("I didn't mean to hurt you") often suffice to defuse tense situations and to reduce or eliminate vengeful responses to a harmful act. But does the reining in of aggressive behavior reflect deliberate and effortful control of those impulses, or does the claim of a lack of purpose serve to dissolve one's anger? Using a social evaluation setting, Krieglmeier *et al.* obtain evidence linking the attribution of intention to a conscious overriding of impulsive aggression. They presented students with positive or negative ratings (from an unseen partner) of their ideas for naming a new energy drink; half of the students who had received negative feedback were then told that their partner had mistaken the high-low direction of the rating scale and had in fact intended to assign them positive marks. When assessed specifically for anger using an implicit measure and for behavior by means of the same rating scale, this set of students displayed a lower level of aggression as compared to the students whose negative assessments had been intentional (although they still exhibited a higher level of hostility than the students who had received positive ratings initially). In contrast, learning that the negative ratings had been delivered in error and that the actual intent had been to send positive feedback had no effect on the levels of implicit anger. — GJC

J. Exp. Soc. Psych. **44**, 10.1016/j.jesp.2008.10.003 (2008).

CELL BIOLOGY

Can You Hear Me Now?

It's a bit like talking to your neighbor at a dinner party with a megaphone, but Tovey *et al.* report that the stimulation of calcium release

*Helen Pickersgill is a locum editor in *Science's* editorial department.



through inositol 1,4,5-trisphosphate receptors (IP₃R) results from enormous amounts (1000 times greater than the amount needed to activate protein kinase A) of the second messenger cAMP produced by adenylyl cyclase (AC) molecules that are closely apposed to the IP₃R channel. The authors were led to this unorthodox interpretation by their exploration of the mechanisms by which parathyroid hormone (PTH), which itself does not cause the release of calcium, enhanced the effects of other hormones on the release via IP₃Rs of calcium from internal stores. Only PTH analogs that activated AC potentiated calcium release. High concentrations of cAMP analogs were sufficient to reproduce the effects of PTH and were not additive with the effects of the hormone. The authors propose that AC and IP₃Rs are in such close proximity that activation of the cyclase produces a massive all-or-none response of the channel that is resistant to modulation by agents that alter cytoplasmic concentrations of cAMP; immunoprecipitation experiments confirmed the prediction that IP₃Rs and AC were associated physically. Such signaling complexes would have on-off or switchlike properties and could allow graded responses by recruitment of more activated complexes rather than graded response at an individual complex. To add to the complexity, the IP₃R-associated isoform of AC is inhibited by calcium. Thus, localized concentrations of cAMP and calcium might oscillate as a result of feedback inhibition. — LBR

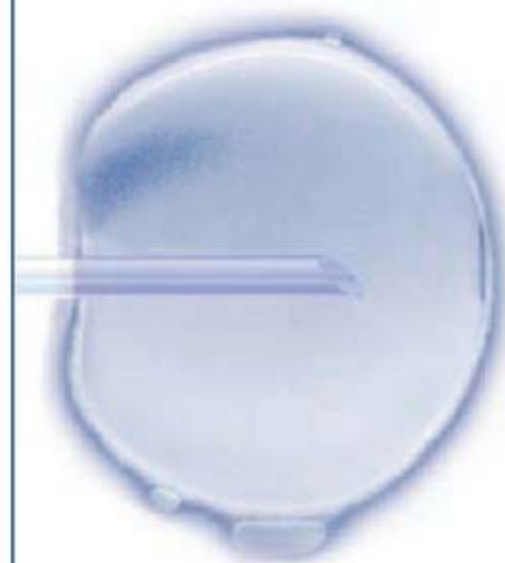
J. Cell Biol. **183**, 297 (2008).

CHEMISTRY

Delivering More Than Charge

A small platinum or carbon wire inserted into a solution environment can yield substantial chemical insight through charge exchange with local compounds. One limitation of such electrode sensing, however, is that only electrons can be shuttled back and forth. Chen *et al.* have engineered a microfluidic apparatus, which they term a chemistode, that can deliver or remove complex molecules from specific sites with a spatial resolution of 15 μm. The system relies on a fluorocarbon carrier fluid that pulls well-separated aqueous droplets through a channel that briefly opens to contact a substrate surface for molecular exchange. Analytes absorbed from the substrate can then be subjected to a wide range of traditional spectrometric probing techniques. The authors demonstrate the device through a measurement of insulin secretion kinetics by murine islet of Langerhans cells. — JSY

Proc. Natl. Acad. Sci. U.S.A. **105**, 16843 (2008).



Inject

some life
into your career.

We've got **Careers**
down to a **Science**.

- Job Search
- Resume/CV Database
- Grant Information
- Careers Forum & Advice
- and more...

Science Careers

From the journal *Science* AAAS

ScienceCareers.org

1200 New York Avenue, NW
Washington, DC 20005

Editorial: 202-326-6550, FAX 202-289-7562

News: 202-326-6581, FAX 202-371-9227

Bateman House, 82-88 Hills Road
Cambridge, UK CB2 1LQ

+44 (0) 1223 326500, FAX +44 (0) 1223 326501

SUBSCRIPTION SERVICES For change of address, missing issues, new orders and renewals, and payment questions: 866-434-AAAS (2227) or 202-326-6417, FAX 202-842-1065. Mailing addresses: AAAS, P.O. Box 96178, Washington, DC 20090-6178 or AAAS Member Services, 1200 New York Avenue, NW, Washington, DC 20005

INSTITUTIONAL SITE LICENSES please call 202-326-6755 for any questions or information

REPRINTS: Author Inquiries 800-635-7181

Commercial Inquiries 803-359-4578

PERMISSIONS 202-326-7074, FAX 202-682-0816

MEMBER BENEFITS AAAS/Barnes&Noble.com bookstore www.aaas.org/bn; AAAS Online Store www.apisource.com/aaas/ code MKB6; AAAS Travels: Betchart Expeditions 800-252-4910; Apple Store www.apple.com/store/aaas; Bank of America MasterCard 1-800-833-6262 priority code FAA3YU; Cold Spring Harbor Laboratory Press Publications www.cshlpress.com/affiliates/aaas.htm; GEICO Auto Insurance www.geico.com/landingpage/go51.htm?logo=17624; Hertz 800-654-2200 CDP#343457; Office Depot https://bsd.officedepot.com/portalLogin.do; Seabury & Smith Life Insurance 800-424-9883; Subaru VIP Program 202-326-6417; VIP Moving Services www.vipmayflower.com/domestic/index.html; Other Benefits: AAAS Member Services 202-326-6417 or www.aaasmember.org.

science_editors@aaas.org (for general editorial queries)

science_letters@aaas.org (for queries about letters)

science_reviews@aaas.org (for returning manuscript reviews)

science_bookrevs@aaas.org (for book review queries)

Published by the American Association for the Advancement of Science (AAAS), *Science* serves its readers as a forum for the presentation and discussion of important issues related to the advancement of science, including the presentation of minority or conflicting points of view, rather than by publishing only material on which a consensus has been reached. Accordingly, all articles published in *Science*—including editorials, news and comment, and book reviews—are signed and reflect the individual views of the authors and not official points of view adopted by AAAS or the institutions with which the authors are affiliated.

AAAS was founded in 1848 and incorporated in 1874. Its mission is to advance science, engineering, and innovation throughout the world for the benefit of all people. The goals of the association are to: enhance communication among scientists, engineers, and the public; promote and defend the integrity of science and its use; strengthen support for the science and technology enterprise; provide a voice for science on societal issues; promote the responsible use of science in public policy; strengthen and diversify the science and technology workforce; foster education in science and technology for everyone; increase public engagement with science and technology; and advance international cooperation in science.

INFORMATION FOR AUTHORS

See pages 634 and 635 of the 1 February 2008 issue or access www.sciencemag.org/about/authors

EDITOR-IN-CHIEF **Bruce Alberts**

EXECUTIVE EDITOR **Monica M. Bradford**

DEPUTY EDITORS

R. Brooks Hanson, Barbara R. Jasny,

Katrina L. Kelner

NEWS EDITOR

Colin Norman

EDITORIAL SUPERVISORY SENIOR EDITOR Phillip D. Szurumi; **SENIOR EDITOR/PERSPECTIVES** Lisa D. Chong; **SENIOR EDITORS** Gilbert J. Chin, Pamela J. Hines, Paula A. Kiberstis (Boston), Marc S. Lavine (Toronto), Beverly A. Purnell, L. Bryan Ray, Guy Riddihough, H. Jesse Smith, Valda Vinson; **ASSOCIATE EDITORS** Kristen L. Mueller, Jake S. Yeston, Laura M. Zahn; **ONLINE EDITOR** Stewart Williams; **ASSOCIATE ONLINE EDITORS** Robert Frederick, Tara S. Marathe; **WEB CONTENT DEVELOPER** Martyn Green; **BOOK REVIEW EDITOR** Sherman J. Suter; **ASSOCIATE LETTERS EDITOR** Jennifer Sills; **EDITORIAL MANAGER** Cara Tate; **SENIOR COPY EDITORS** Jeffrey E. Cook, Cynthia Howe, Harry Jadh, Barbara P. Ordway, Trista Wagoner; **COPY EDITORS** Chris Filiatreau, Lauren Kmeck; **EDITORIAL COORDINATORS** Carolyn Kyle, Beverly Shields; **PUBLICATIONS ASSISTANTS** Ramatoulaye Diop, Joi S. Granger, Jeffrey Hearn, Lisa Johnson, Scott Miller, Jerry Richardson, Jennifer A. Seibert, Brian White, Anita Wynne; **EDITORIAL ASSISTANTS** Carlos L. Durham, Emily Guise, Patricia M. Moore; **EXECUTIVE ASSISTANT** Sylvia S. Kihara; **ADMINISTRATIVE SUPPORT** Maryrose Madrid

NEWS DEPUTY NEWS EDITORS Robert Coontz, Eliot Marshall, Jeffrey Mervis, Leslie Roberts; **CONTRIBUTING EDITORS** Elizabeth Culotta, Polly Shulman; **NEWS WRITERS** Yudhijit Bhattacharjee, Adrian Cho, Jennifer Couzin, David Grimm, Constance Holden, Jocelyn Kaiser, Richard A. Kerr, Eli Kintisch, Andrew Lawler (New England), Greg Miller, Elizabeth Pennisi, Robert F. Service (Pacific NW), Erik Stokstad; **INTERN** Rachel Zerkowitz; **CONTRIBUTING CORRESPONDENTS** Jon Cohen (San Diego, CA), Daniel Ferber, Ann Gibbons, Robert Koenig, Mitch Leslie, Charles C. Mann, Virginia Morell, Evelyn Strauss, Gary Taubes; **COPY EDITORS** Linda B. Felaco, Melvin Gatling, Melissa Raimondi; **ADMINISTRATIVE SUPPORT** Scherraine Mack, Fannie Groom; **BUREAU** New England: 207-549-7755, San Diego, CA: 760-942-3252, FAX 760-942-4979, Pacific Northwest: 503-963-1940

PRODUCTION DIRECTOR James Landry; **SENIOR MANAGER** Wendy K. Shank; **ASSISTANT MANAGER** Rebecca Doshi; **SENIOR SPECIALISTS** Steve Forrester, Chris Redwood; **SPECIALIST** Anthony Rosen; **PREFLIGHT DIRECTOR** David M. Tompkins; **MANAGER** Marcus Spiegler

ART DIRECTOR Yael Kats; **ASSOCIATE ART DIRECTOR** Laura Creveling; **ILLUSTRATORS** Chris Bickel, Katharine Sutcliffe; **SENIOR ART ASSOCIATES** Holly Bishop, Preston Huey, Nayomi Kevityiyagala; **ART ASSOCIATE** Jessica Newfield; **PHOTO EDITOR** Leslie Blizard

SCIENCE INTERNATIONAL

EUROPE (science@science-int.co.uk) **EDITORIAL: INTERNATIONAL MANAGING EDITOR** Andrew M. Sugden; **SENIOR EDITOR/PERSPECTIVES** Julia Fahrenkamp-Uppenbrink; **SENIOR EDITORS** Caroline Ash, Stella M. Hurtley, Ian S. Osborne, Peter Stern; **ASSOCIATE EDITOR** Maria Cruz; **EDITORIAL SUPPORT** Deborah Dennison, Rachel Roberts, Alice Whaley; **ADMINISTRATIVE SUPPORT** John Cannell, Janet Clements; **NEWS: EUROPE NEWS EDITOR** John Travis; **DEPUTY NEWS EDITOR** Daniel Clery; **CONTRIBUTING CORRESPONDENTS** Michael Balter (Paris), John Bohannon (Vienna), Martin Enserink (Amsterdam and Paris), Gretchen Vogel (Berlin); **INTERN** Sara Coelho

ASIA Japan Office: Asca Corporation, Eiko Ishioka, Fusako Tamura, 1-8-13, Hirano-cho, Chuo-ku, Osaka-shi, Osaka, 541-0046 Japan; +81 (0) 6 6202 6272, FAX +81 (0) 6 6202 6271; asca@os.gulf.or.jp; **ASIA NEWS EDITOR** Richard Stone (Beijing: rstone@aaas.org); **CONTRIBUTING CORRESPONDENTS** Dennis Normile (Japan: +81 (0) 3 3391 0630, FAX +81 (0) 3 5936 3531; dnormile@gol.com); Hao Xin (China: +86 (0) 10 6307 4439 or 6307 3676, FAX +86 (0) 10 6307 4358; cindyhao@gmail.com); Pallava Bagla (South Asia: +91 (0) 11 2271 2896; pbagla@vsnl.com)

EXECUTIVE PUBLISHER **Alan I. Leshner**

PUBLISHER **Beth Rosner**

FULFILLMENT SYSTEMS AND OPERATIONS (membership@aaas.org); **DIRECTOR** Wayne Butler; **SENIOR SYSTEMS ANALYST** Jonny Blaker; **CUSTOMER SERVICE SUPERVISOR** Pat Butler; **SPECIALISTS** Latoya Casteel, LaVonda Crawford, Vicki Linton, April Marshall; **DATA ENTRY SUPERVISOR** Cynthia Johnson; **SPECIALISTS** Eintou Bowden, Tarrika Hill, William Jones

BUSINESS OPERATIONS AND ADMINISTRATION DIRECTOR Deborah Rivera-Wienhold; **ASSISTANT DIRECTOR, BUSINESS OPERATIONS** Randy Yi; **MANAGER, BUSINESS ANALYSIS** Michael LoBue; **MANAGER, BUSINESS OPERATIONS** Jessica Tierney; **FINANCIAL ANALYSTS** Priti Pamnani, Celeste Troxler; **RIGHTS AND PERMISSIONS: ADMINISTRATOR** Emilie David; **ASSOCIATE** Elizabeth Sandler; **MARKETING DIRECTOR** John Meyers; **MARKETING MANAGER** Allison Pritchard; **MARKETING ASSOCIATES** Aimee Aponte, Alison Chandler, Mary Ellen Crowley, Marcia Leach, Julianne Wielga, Wendy Wise; **INTERNATIONAL MARKETING MANAGER** Wendy Sturley; **MARKETING EXECUTIVE** Jennifer Reeves; **MARKETING/MEMBER SERVICES EXECUTIVE** Linda Rusk; **DIRECTOR, SITE LICENSING** Tom Ryan; **DIRECTOR, CORPORATE RELATIONS** Eileen Bernadette Moran; **PUBLISHER RELATIONS, RESOURCES SPECIALIST** Kiki Forsythe; **SENIOR PUBLISHER RELATIONS SPECIALIST** Catherine Holland; **PUBLISHER RELATIONS, EAST COAST** Phillip Smith; **PUBLISHER RELATIONS, WEST COAST** Philip Tsolakidis; **FULFILLMENT SUPERVISOR** Iquo Edim; **ELECTRONIC MEDIA: MANAGER** Elizabeth Harman; **PROJECT MANAGER** Trista Snyder; **ASSISTANT MANAGER** Lisa Stanford; **SENIOR PRODUCTION SPECIALISTS** Christopher Coleman, Walter Jones; **PRODUCTION SPECIALISTS** Nichele Johnston, Kimberly Oster

ADVERTISING DIRECTOR, WORLDWIDE AD SALES Bill Moran

PRODUCT (science_advertising@aaas.org); **MIDWEST/WEST COAST/UK CANADA** Rick Bongiovanni: 330-405-7080, FAX 330-405-7081; **EAST COAST/E. CANADA** Laurie Faraday: 508-747-9395, FAX 617-507-8189; **UK/EUROPE/ASIA** Roger Goncalves: TEL/FAX +41 43 234 1358; **JAPAN** Masuyoshi Yoshikawa: +81 (0) 3 3235 5961, FAX +81 (0) 3 3235 5852; **SENIOR TRAFFIC ASSOCIATE** Deandra Simms

COMMERCIAL EDITOR Sean Sanders: 202-326-6430

PROJECT DIRECTOR, OUTREACH Brianna Blaser

CLASSIFIED (advertise@sciencereads.org); **US: RECRUITMENT SALES MANAGER** Ian King: 202-326-6528, FAX 202-289-6742; **INSIDE SALES MANAGER: MIDWEST/CANADA** Daryl Anderson: 202-326-6543; **INSIDE SALES REPRESENTATIVE** Karen Foote: 202-326-6740; **KEY ACCOUNT MANAGER** Joribah Able; **NORTHEAST** Alexis Fleming: 202-326-6578; **SOUTHEAST** Tina Burks: 202-326-6577; **WEST** Nicholas Hintibidze: 202-326-6533; **SALES COORDINATORS** Erika Foad, Rohan Edmonson, Shirley Young; **INTERNATIONAL: SALES MANAGER** Tracy Holmes: +44 (0) 1223 326525, FAX +44 (0) 1223 326532; **SALES** Susanne Kharraz, Dan Pennington, Alex Palmer; **SALES ASSISTANT** Louise Moore; **JAPAN** Masuyoshi Yoshikawa: +81 (0) 3 3235 5961, FAX +81 (0) 3 3235 5852; **ADVERTISING PRODUCTION OPERATIONS MANAGER** Deborah Tompkins; **SENIOR PRODUCTION SPECIALIST/GRAPHIC DESIGNER** Amy Hardcastle; **SENIOR PRODUCTION SPECIALIST** Robert Buck; **SENIOR TRAFFIC ASSOCIATE** Christine Hall; **PUBLICATIONS ASSISTANT** Mary Lagnaoui

AAAS BOARD OF DIRECTORS **RETIRING PRESIDENT, CHAIR** David Baltimore; **PRESIDENT** James J. McCarthy; **PRESIDENT-ELECT** Peter C. Agre; **TREASURER** David E. Shaw; **CHIEF EXECUTIVE OFFICER** Alan I. Leshner; **BOARD** Lynn W. Enquist, Susan M. Fitzpatrick, Alice Gast, Linda P. B. Katehi, Nancy Knowlton, Cherry A. Murray, Thomas D. Pollard, Thomas A. Woolsey



ADVANCING SCIENCE. SERVING SOCIETY

SENIOR EDITORIAL BOARD

John I. Brauman, Chair, Stanford Univ.
Richard Losick, Harvard Univ.
Robert May, Univ. of Oxford
Marcia McNutt, Monterey Bay Aquarium Research Inst.
Linda Partridge, Univ. College London
Vera C. Rubin, Carnegie Institution
Christopher R. Somerville, Univ. of California, Berkeley

BOARD OF REVIEWING EDITORS

Joanna Aizenberg, Harvard Univ.
R. McNeill Alexander, Leeds Univ.
David Altschuler, Broad Institute
Arturo Alvarez-Buylla, Univ. of California, San Francisco
Richard Amasino, Univ. of Wisconsin, Madison
Angelika Amon, MIT
Meinrat O. Andreae, Max Planck Inst., Mainz
Kristi S. Anseth, Univ. of Colorado
John A. Bargh, Yale Univ.
Cornelia I. Bargmann, Rockefeller Univ.
Ben Barnes, Stanford Medical School
Marisa Bartolomei, Univ. of Penn. School of Med.
Ray H. Baughman, Univ. of Texas, Dallas
Stephen J. Benkovic, Penn State Univ.
Michael J. Bevan, Univ. of Washington
Tom Bisseling, Wageningen Univ.
Mina Bissell, Lawrence Berkeley National Lab
Peer Bork, EMBL
Dianna Bowles, Univ. of York
Robert W. Boyd, Univ. of Rochester
Paul M. Brakefield, Leiden Univ.
Dennis Bray, Univ. of Cambridge
Stephen Buratowski, Harvard Medical School
Joseph A. Burns, Cornell Univ.
William P. Butz, Population Reference Bureau
Peter Carmeliet, Univ. of Leuven, VIB
Gerbrand Cedez, MIT
Mildred Cho, Stanford Univ.
David Clapham, Children's Hospital, Boston
David Clary, Oxford University
J. M. Claverie, CNRS, Marseille

Jonathan D. Cohen, Princeton Univ.
Stephen M. Cohen, Temasek Life Sciences Lab, Singapore
Robert H. Crabtree, Yale Univ.
F. Fleming Crim, Univ. of Wisconsin
William Cumberland, Univ. of California, Los Angeles
George Q. Daley, Children's Hospital, Boston
Jeff L. Dangl, Univ. of North Carolina
Stanislas Dehaene, Collège de France
Edward DeLong, MIT
Emmanouil T. Dermitzakis, Wellcome Trust Sanger Inst.
Robert Desimone, MIT
Dennis Discher, Univ. of Pennsylvania
Scott C. Doney, Woods Hole Oceanographic Inst.
Peter J. Donovan, Univ. of California, Irvine
W. Ford Doolittle, Dalhousie Univ.
Jennifer A. Doudna, Univ. of California, Berkeley
Julian Downward, Cancer Research UK
Denis Duboule, Univ. of Geneva/EPFL Lausanne
Christopher Dye, WHO
Richard Ellis, Cal Tech
Gerhard Ertl, Fritz-Haber-Institut, Berlin
Douglas H. Erwin, Smithsonian Institution
Mark Estelle, Indiana Univ.
Barry Everitt, Univ. of Cambridge
Paul G. Falkowski, Rutgers Univ.
Ernst Fehr, Univ. of Zurich
Tom Fenchel, Univ. of Copenhagen
Alain Fischer, INSERM
Scott E. Fraser, Cal Tech
Chris D. Frith, Univ. College London
Wulffram Gerstner, EPFL Lausanne
Charles Godfrey, Univ. of Oxford
Diane Griffin, Johns Hopkins Bloomberg School of Public Health
Christian Haass, Ludwig Maximilians Univ.
Niels Hansen, Technical Univ. of Denmark
Dennis L. Hartmann, Univ. of Washington
Chris Hawkesworth, Univ. of Bristol
Martin Heimann, Max Planck Inst., Jena
James A. Hendler, Rochester Polytechnic Inst.
Ray Hilborn, Univ. of Washington
Ove Hoegh-Guldberg, Univ. of Queensland
Ronald R. Hoy, Cornell Univ.
Olli Ikkala, Helsinki Univ. of Technology
Meyer B. Jackson, Univ. of Wisconsin Med. School

Stephen Jackson, Univ. of Cambridge
Steven Jacobsen, Univ. of California, Los Angeles
Peter Jonas, Universität Freiburg
Barbara B. Kahn, Harvard Medical School
Daniel Kahne, Harvard Univ.
Gerard Karsenty, Columbia Univ. College of P&S
Bernhard Keimer, Max Planck Inst., Stuttgart
Elizabeth A. Kelloff, Univ. of Missouri, St. Louis
Alan B. Krueger, Princeton Univ.
Lee Kump, Penn State Univ.
Mitchell A. Lazar, Univ. of Pennsylvania
Virginia Lee, Univ. of Pennsylvania
Norman L. Letvin, Beth Israel Deaconess Medical Center
Olle Lindvall, Univ. Hospital, Lund
John Lis, Cornell Univ.
Richard Losick, Harvard Univ.
Ke Lu, Chinese Acad. of Sciences
Andrew P. MacKenzie, Univ. of St Andrews
Raul Madariaga, Ecole Normale Supérieure, Paris
Anne Magurran, Univ. of St Andrews
Virginia Miller, Washington Univ.
Yasushi Miyashita, Univ. of Tokyo
Richard Morris, Univ. of Edinburgh
Edward Moser, Norwegian Univ. of Science and Technology
Naoto Nagaosa, Univ. of Tokyo
James Nelson, Stanford Univ. School of Med.
Timothy W. Nilsen, Case Western Reserve Univ.
Roeland Nolte, Univ. of Nijmegen
Helga Nowotny, European Research Advisory Board
Eric N. Olson, Univ. of Texas, SW
Eric O'Shea, Harvard Univ.
Elinor Ostrom, Indiana Univ.
Jonathan T. Overpeck, Univ. of Arizona
John Pendry, Imperial College
Philippe Poulin, CNRS
Mary Power, Univ. of California, Berkeley
Molly Przeworski, Univ. of Chicago
David J. Read, Univ. of Sheffield
Les Real, Emory Univ.
Colin Renfrew, Univ. of Cambridge
Trevor Robbins, Univ. of Cambridge
Barbara A. Romanowicz, Univ. of California, Berkeley
Edward M. Rubin, Lawrence Berkeley National Lab
Jürgen Sandkühler, Medical Univ. of Vienna
David S. Schimel, National Center for Atmospheric Research

David W. Schindler, Univ. of Alberta
Georg Schulz, Albert-Ludwigs-Universität
Paul Schulze-Lefert, Max Planck Inst., Cologne
Christine Seidman, Harvard Medical School
Terrence J. Sejnowski, The Salk Institute
David Sibley, Washington Univ.
Montgomery Slatkin, Univ. of California, Berkeley
George Somero, Stanford Univ.
Joan Steitz, Yale Univ.
Elisbeth Stern, ETH Zürich
Jerome Strauss, Virginia Commonwealth Univ.
Glenn Telling, Univ. of Kentucky
Marc Tessier-Lavigne, Genentech
Jurg Tschopp, Univ. of Lausanne
Michiel van der Klis, Astronomical Inst. of Amsterdam
Derek van der Kooy, Univ. of Toronto
Bert Vogelstein, Johns Hopkins Univ.
Ulrich H. von Andrian, Harvard Medical School
Bruce D. Walker, Harvard Medical School
Christopher A. Walsh, Harvard Medical School
Graham Warren, Yale Univ. School of Med.
Colin Watts, Univ. of Dundee
Detlef Weigel, Max Planck Inst., Tübingen
Jonathan Weissman, Univ. of California, San Francisco
Ellen D. Williams, Univ. of Maryland
Ian A. Wilson, The Scripps Res. Inst.
Jerry Workman, Stowers Inst. for Medical Research
John R. Yates III, The Scripps Res. Inst.
Jan Zaenen, Leiden Univ.
Martin Zatz, NIMH, NIH
Huda Zoghbi, Baylor College of Medicine
Maria Zuber, MIT

BOOK REVIEW BOARD

John Aldrich, Duke Univ.
David Bloom, Harvard Univ.
Angela Creager, Princeton Univ.
Richard Shweder, Univ. of Chicago
Ed Wasserman, DuPont
Lewis Wolpert, Univ. College London

Fish Online

At right are the dried remains of *Haemulon sciurus*, in one of the beautiful high-resolution photos, now online, of 168 fish specimens classified by 18th century Swedish naturalist Carl Linnaeus. The fish are in the collection of the Linnean Society of London (www.linnean.org), which sponsored the project with the help of Japan's Emperor Akihito, an ardent amateur ichthyologist known for his contributions to the taxonomy of gobioid fishes. Linnaeus's *Systema Naturae*, the recognized starting point for biological classification, was published in 1735. Linnean plant and insect databases are already online.



Oil and Mud

Was the continuing eruption of Lusi, the Indonesian mud volcano that began 30 months ago, triggered by a distant earthquake or by the drilling of a nearby gas well? The question has spurred fierce arguments among scientists (*Science*, 13 June, p. 1406).



Opponents squared off in a debate last month at a meeting of the American Association of Petroleum Geologists in Cape Town, South Africa. Geologists Richard Davies of Durham University in the U.K. and Mark Tingay of Curtin University of Technology in Perth, Australia, argued that drillers had tapped into a highly pressurized aquifer that fractured weak rock in the unprotected borehole and that the magnitude-6.3 earthquake occurring 2 days before Lusi's eruption was too small and remote to have any effect. Rocky Sawolo, drilling adviser for the oil company Lapindo Brantas, and geologist Adriano Mazzini of the University of Oslo, Norway, claimed that well pressures were within acceptable limits and that the earthquake reactivated a nearby fault.

At the end, the moderator, geologist John Underhill of the University of Edinburgh, U.K., called for a vote. Of 74 scientists voting, 42 agreed that drilling triggered the eruption. Only three opted for the earthquake scenario, 13 favored both factors, and the rest found the evidence inconclusive.

The issue is more than academic. If Indonesian courts agree with the scientists, Lapindo Brantas could have to pay tens of millions of dollars in compensation to 10,000 families and dozens of business owners who have lost properties to the rising tide of mud.

Saving Michael Caine

It's a criminal conundrum: \$4 million in stolen gold and the crooks who just pulled off the heist teeter in a bus off the edge of a mountaintop. "Hang on, lads, I've got an idea," says actor Michael Caine. Then the 1969 movie *The Italian Job* cuts to the credits.

Now, to celebrate the movie's 40th anniversary, the Royal Chemistry Society (RCS) in London is asking fans to come up with an engineering idea to get Caine and his cronies out of their dilemma. "It's a way of pointing out that science is all around us—

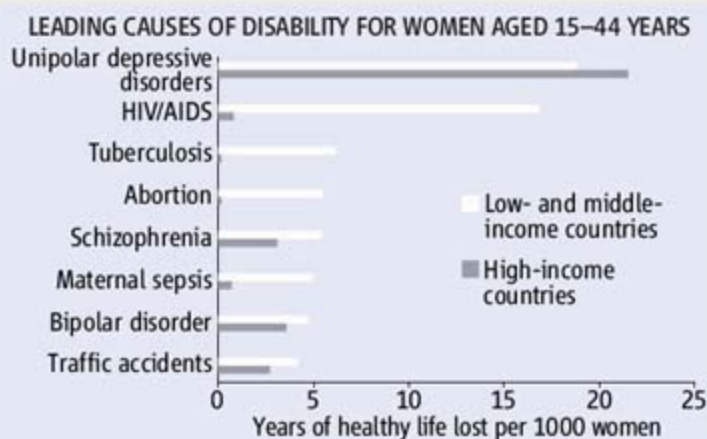
including a bank robbery," says RCS spokesperson Brian Emsley.

Entrants have until 1 January to submit a solution that includes a description of the physics and engineering challenges involved. Drawings and schematics are encouraged; no deus ex machina—such as a convenient helicopter—allowed.

The winner will receive a 3-night visit to Turin, Italy, where the movie's action takes place. Daniel Frey, a mechanical engineer at the Massachusetts Institute of Technology in Cambridge, who is not involved in the competition, says the challenge underscores the ingenuity required in science. "There's more than one way to skin this cat," he says. He says principles such as equilibrium and inertia could help entrants tackle the problem. For example, the bus's toppling might be delayed briefly, allowing time for some intervention, if the balance between the gold and the people were changed.

WORLDWIDE BLIGHT

Depression is the most disabling condition in the world, according to the World Health Organization. In its annual report issued last month, *Global Burden of Disease: 2004 Update*, authors found that unipolar depressive disorders account for more years of disability than any



other condition—for both sexes, but especially females (see chart)—in rich and poor countries alike. Also high on the list are alcohol-use disorders (particularly for males), hearing and vision problems, and migraines. In a ranking of causes of years of healthy life lost, depression is surpassed only by lower respiratory infections and diarrheal diseases.

<< Campaigns

NANOBAMA. Let's hope there's a microscope at the White House, because one of the first gifts Barack Obama will receive once he becomes president is a batch of these miniportraits, about half a millimeter wide and made out of about 150 million carbon nanotubes each. They were created a week before the 4 November election by mechanical engineer John Hart and his colleagues at the University of Michigan, Ann Arbor. Hart says he wasn't making a political statement, although he does support Obama. "I just wanted to draw attention to the importance of research for economic development and to promote public interest in science and technology," he says. For more images, go to www.nanobliss.com.



INSIDE GOVERNMENT

CHANGES AT NIH. Alan Krensky has resigned from his job overseeing a new office coordinating research across the U.S. National Institutes of Health (NIH) as part of a realignment of the director's office.

Krensky was brought in by NIH Director Elias Zerhouni in July 2007 to head its Office of Portfolio Analysis and Strategic Initiatives (OPASI), launched a year earlier (*Science*, 17 August 2007, p. 887). But observers told *Science* that Krensky clashed with institute directors. Krensky denies any tension, saying that he found NIH to be "as collaborative as you get."

Krensky's exit follows Zerhouni's on 31 October and a directive from Congress to fold OPASI into a new division that will also oversee NIH offices of social sciences, women's health, and AIDS. "We all agreed that this was a good time for a change in leadership," says NIH acting Director Raynard Kington. Lana Skirboll, who heads NIH's science policy office, will serve as acting director of the new division. Krensky says that OPASI was "a small, flexible think tank" and adds that the new division "is very different" because of its broader oversight, which makes it more bureaucratic. His "plan right now" is to work full-time in his NIH cancer immunology lab, where he had been spending half a day a week.

MOVERS

PAYING HIS DUES. Two years before Fred Spilhaus became executive director of the American Geophysical Union (AGU) in 1970, the association raised its annual dues to \$20. This month, the 70-year-old Spilhaus announced he will step down from his post in June 2009, and, incredibly enough, the dues haven't budged.

"There were a few things I did that really worked," says Spilhaus, who cites that bargain-

basement price as one reason the association's membership rose from 10,000 to 55,000 during his tenure. "The strategy was to keep the members and make room for everybody around the world." About 30% of its members reside



outside the United States, and most also maintain an allegiance to a specialty society of seismologists, geologists, oceanographers, or meteorologists.

Trained as a physical oceanographer, Spilhaus took over in 1970 when AGU was a committee of the

U.S. National Academy of Sciences with 40 full-time employees. Within 2 years, he helped transform it into an independent society that now publishes 5300 articles per year and supports 178 staffers. Next month, its annual meeting will attract 16,000 attendees to San Francisco, California.

IN THE COURTS

BAYING FOR BLOOD. Biopure, a Massachusetts biotech company that makes a blood substitute called Hemopure, has filed a defamation suit against U.S. National Institutes of Health (NIH) researcher Charles Natanson over a study highlighting the risks from using the product. Hemopure is sold in South Africa and is under development in the United States and Europe.

Biopure charges that it suffered "significant financial harm" as a result of Natanson's article published online 28 April in the *Journal of the American Medical Association (JAMA)* and letters he wrote to health officials in the United Kingdom and South Africa alerting them to the paper. The suit, filed 10 October in U.S. District Court in Washington,

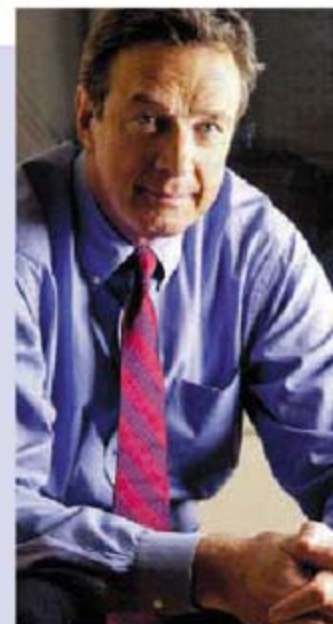
D.C., also notes that the *JAMA* article did not disclose that Natanson had applied for a patent on technology to make artificial blood safer and "seeks to benefit financially from widespread adoptions of the contentions he makes," Biopure wrote in its suit. Natanson revealed the patent in *JAMA* in July.

Natanson's meta-analysis of 16 trials on five blood-substitute products, including Hemopure, concluded that the products increased the risk of death by 30% (*ScienceNOW*, 28 April: sciencenow.sciencemag.org/cgi/content/full/2008/428/1). Natanson declined to comment for this story but noted in April that "we need to move from humans back to animals, until we find a formulation that has less toxicity." On 4 November, Natanson asked the judge to dismiss the case.

Deaths

SHELF LIFE. Science fiction author Michael Crichton, who wrote bestsellers such as *Jurassic Park* and *The Andromeda Strain*, died of cancer 5 November. He was 66.

Crichton entertained millions, and many say his lifetime's work raised the public's interest in science. But Crichton also received his share of criticism from scientists, most notably for a 2004 novel, *State of Fear*, which portrayed global warming as a hoax. Kendrick Frazier, editor of *Skeptical Inquirer*, says the book "probably caused a lot of mischief and misunderstanding about the seriousness of global warming and climate change." But, Frazier says, no one can deny Crichton's skills as a storyteller.





SCIENCE AND THE ELECTION

Obama Victory Raises Hopes for New Policies, Bigger Budgets

Make no mistake: U.S. scientists hope that the election last week of Barack Obama as president and a larger Democratic majority in both houses of Congress will usher in an era of sustained, healthy increases in the federal funding of basic research. But money isn't everything, and in a time of yawning deficits and urgent demands on the federal treasury, those increases may not happen anytime soon.

Propping up a shaky economy will be job #1 for Obama once he takes the oath of office on 20 January 2009. So scientists and science policymakers will be looking to the new president to first make good on campaign promises that don't require big outlays, such as elevating the status of the president's science adviser, lifting a ban on new human embryonic stem (ES) cell lines, and restoring the integrity of federal decision making, including scrapping some environmental regulations based on questionable science.

At the top of the list for many is the early appointment of a science adviser with the additional title of assistant to the president. (The

current adviser, John Marburger, wasn't nominated until June 2001 and ranks a step below assistant on the White House pecking order.) Those actions would be a sign that the president-elect recognizes the importance of science to the country, says Ralph Cicerone, president of the U.S. National Academy of Sciences. "The world still loves and respects U.S. science, and it can be an instrument of good will—and good policies," says Cicerone. "When we wrote to both campaigns this summer, we did not say, 'Put more money into science.' What we said is that they need science to govern effectively."

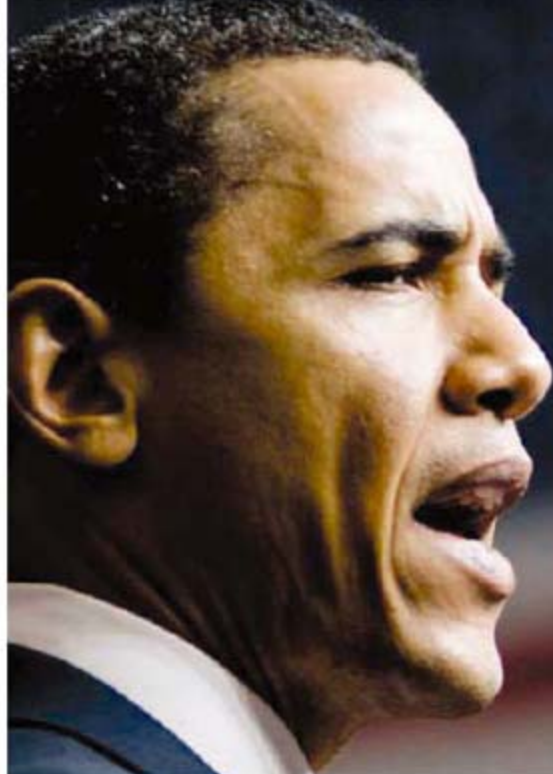
Some want Obama to go further and make the director of the Office of Science and Technology Policy (historically a second job for the science adviser) part of his Cabinet. Neal Lane, who held both posts during President Bill Clinton's second term, doesn't think that's necessary. But he agrees that regular access to the president and his Cabinet secretaries is essential. "The Cabinet table is pretty full already," says Lane, who emphasizes that Obama hasn't solicited his advice. "As long as

you're invited to all the meetings, that's all the status you need."

Stem cell researchers are confident that Obama will act swiftly on his promise to reverse President George W. Bush's policy of restricting federal funding for research on human ES cells to lines derived before 9 August 2001. Science lobbyists are shooting for a two-pronged attack: a speedy executive order, followed by legislation that would allow federally funded researchers to work with any lines derived from embryos that would otherwise be discarded by fertility clinics. Bush vetoed such legislation twice. But Representative Diana DeGette (D-CO) already has a new version ready. Introduced in the waning days of this Congress, it would allow research to be conducted on human ES cells "regardless of the date" they were derived and require the Department of Health and Human Services to issue research guidelines.

R. Alta Charo, a lawyer and bioethicist at the University of Wisconsin Law School in Madison, says Obama could simply tell the U.S. National Institutes of Health (NIH) to go ahead and fund research on newer lines. But Tony Mazzaschi of the Association of American Medical Colleges in Washington, D.C., thinks an executive order would be the best way to clarify a picture complicated by a 2007 presidential directive that urges NIH to

I PROMISE THAT* ...



My Administration will increase funding for basic research ... at a rate that would double budgets over the next decade. ... We are clearly underinvesting in research across the spectrum of scientific and engineering disciplines.

My Administration will make the R&D tax credit permanent.

I will lift the current Administration's ban on federal funding of research on [human] embryonic stem cell lines created after 9 August 2001. ... Embryonic stem cells remain the gold standard.

I will reestablish the National Aeronautics and Space Council, reporting to the president.

I believe that we can continue to modify plants safely with new genetic methods, abetted by stringent tests for environmental and health effects and stronger regulatory oversight.

I will implement a market-based cap-and-trade system to reduce carbon emissions by the amount scientists say is necessary: 80% below 1990 levels by 2050. ... I will require all pollution credits to be auctioned.

I will work actively to ensure that the U.S. ratifies the Law of the Sea Convention.

My Administration will work to guarantee students access to strong science curriculum at all grade levels.

*Answers to ScienceDebate 2008

CREDIT: MICHAEL CZERWONKA/EPA/CORBIS



explore “alternative” ways of generating pluripotent ES-like cells.

Environmental advocates are also hoping that Obama will overturn several rules and regulations put into place over the past 8 years. For example, David Wilcove, an ecologist at Princeton University, and others are pushing to reinstate into the National Forest Management Act of 1976 a regulatory requirement to maintain viable populations of vertebrates; that provision was removed in 2005 to provide greater flexibility, to the benefit of the logging industry.

In the meantime, environmentalists are nervously watching as the Department of the Interior tries to finalize several rules, including one that relaxes the requirement for federal agencies to consult with biologists at the Fish and Wildlife Service about actions that would impact endangered species (*Science*, 22 August, p. 1030). “This rule really is a dramatic weakening of the safety net that protects endangered species,” says Andrew Wetzler of the Natural Resources Defense Council in New York City. In August, a campaign official said Obama opposes the changes. If the department completes its work before Bush leaves office, however, reversing the last-minute rulemaking will take considerable time and effort.

Scientists haven’t forgotten about money, of course—especially Obama’s campaign pledge to double federal spending for basic research over the next decade. University and research lobbyists are hoping the new president’s backing, combined with strong bipartisan support, will help them achieve the ramp-up in funding for the National Science Foundation, the Department of Energy’s Office of Science, and the National Institute of Standards and Technology that’s authorized in the America COMPETES Act of 2007 but that has been an empty promise so far.

Some help could come as early as next week, during a lame-duck session of the outgoing Congress, if Democratic leaders and Republican Bush can agree on a short-term stimulus package. There’s an outside chance that the package could include something to shore up the nation’s research infrastructure in the current 2009 fiscal year, which runs through 30 September. “Funding for the COMPETES Act is still a high priority, whether it gets done in a stimulus package for 2009 or as part of next year’s [2010] budget,” says Robert Berdahl, president of the 62-member

NEW CONGRESS LOOKS FAMILIAR

Democratic science powerbrokers in Congress have retained their seats. But a major reshuffling of Senate committee posts is under way that could affect research and training issues.

In the 435-member House of Representatives, where incomplete returns show Democrats gaining 20 seats, the leadership of the House Science Committee will remain unchanged after victories by representatives Bart Gordon (D-TN), the chair, and Ralph Hall (R-TX), the ranking minority member. The chairs of the 12 House appropriations subcommittees, who together oversee all federal research budgets, were also reelected, as was Representative David Obey (D-WI), the head of the full committee. The House retained its contingent of three Ph.D. physicists. Representatives Vern Ehlers (R-MI) and Rush Holt (D-NJ) won easily, and Representative Bill Foster (D-IL) parlayed a victory in a March special election into a full 2-year term with help from hundreds of physicists at Fermi National Accelerator Laboratory in Batavia, Illinois, where Foster worked until 2006.

In contrast, a more heavily Democratic Senate will see several new faces in leadership positions. Senator Daniel Inouye (D-HI) will succeed the ailing Senator Robert Byrd (D-WV), who turns 91 next week, atop the full appropriations committee. His move frees up the chairmanship of the Commerce, Science, and Transportation Committee, which is expected to go to Senator Jay Rockefeller (D-WV). Senator Joe Lieberman (I-CT) could be ousted as chair of the Homeland Security and Government Affairs panel for his vigorous support of Republican John McCain, who remains in the Senate. In addition, Democratic governors in Illinois and Delaware will name replacements for Obama and Vice President-elect Joe Biden.

—JEFFREY MERVIS

Association of American Universities in New York City. “The point is that none of the goals of the new Administration—on energy, on the economy, on climate change—can be realized without an increased investment in science.”

With a federal deficit that could hit \$1 trillion next year, however, such an investment is a hard sell. “Mr. Obama has promised so many things, but they all cost money,” says Representative Vern Ehlers (R-MI), one of the most insistent voices for research and education in Congress. Still, Ehlers says that adequate funding for the COMPETES Act is his top priority, too.

Obama’s campaign promises included a pledge to give NASA \$2 billion to cover the transition from the space shuttle to a new launcher. A new report from the Government Accountability Office identifies the shuttle transition as one of 13 critical issues facing the next Administration and Congress, and the loss of thousands of high-paying jobs in the electorally important state of Florida is a political challenge as well. But it may not be clear until early spring, when Obama rolls out his 2010 budget request, whether the money would be a one-time boost or spread out over several years, and how it would affect NASA’s regular budget.

Speaking last week to a National Research Council panel reviewing civilian space policy, NASA Administrator Michael Griffin

said the agency requires between \$2 billion and \$3 billion more annually to retire the shuttle, build the new launcher, and keep science programs on track. Griffin, who told the panel that he doesn’t expect to be asked to stay on, said he hopes Obama and the new Congress will, nevertheless, stick with current plans for a new launcher and human missions to the moon. Griffin also hopes that the new president won’t let his budget officials block the program. Characteristically blunt, he also advised the president-elect to rethink his promise to reestablish an Aeronautics and Space Council within the White House, saying that an earlier version under President George H.W. Bush was ineffective because it lacked budgetary authority.

With the election won, the high-profile group of scientists that funneled advice to the Obama campaign has been disbanded. Some of its members, however, hope that his transition team may still be willing to listen to their thoughts on science-related appointments and issues, especially if packaged as proposed vehicles to help revive a badly slumping economy. Otherwise, scientists will have to be content joining the throng that’s rooting for better times come Inauguration Day.

—CONSTANCE HOLDEN, ANDREW LAWLER,
ELI KINTISCH, JEFFREY MERVIS,
AND ERIK STOKSTAD



Scientific lobbying. Primatologist Jane Goodall (*left*) and members of the Dr Hadwen Trust, here addressing the European Parliament, urged E.U. politicians to restrict animal experimentation.

ANIMAL RESEARCH

European Union Floats Tighter Animal-Research Rules

European researchers have responded with a mixture of relief and anxiety to a long-awaited proposal for new regulations on animal research in the European Union (E.U.). Released last week by the European Commission, the executive body of the E.U., the proposal* would ban the use of great apes in medical experiments, but it does not include a complete prohibition on all research on non-human primates, for which many animal-welfare groups had vigorously lobbied. The new proposal would, however, extend E.U. oversight for the first time to experiments involving certain invertebrates.

Scientific organizations say some of the draft regulations threaten to slow research without providing clear benefits to animals. And activists on both sides of the debate have vowed to push for changes before the rules become final, a process that could take more than a year. "We still have concerns," says Simon Festing of the Research Defence Society in London, which represents medical researchers and opposed the push for the full primate ban.

The E.U. adopted its current animal-research regulations in 1986, and officials have been discussing an update since 2001. One of the most contentious issues has been experiments on nonhuman primates. Animal-welfare groups have been lobbying for a ban on the use of monkeys and great apes, and last year the European Parliament passed a nonbinding resolution calling for a gradual phaseout of all experiments on nonhuman

primates. But the commission's proposal calls only for an end to scientific "procedures" on great apes, with exceptions for behavioral studies, research that could prevent the extinction of the species, or in the case of outbreaks of human disease. Because no medical research on great apes has taken place in the E.U. since 2002, many observers see the ban as a token move. The draft does include a proposal to phase out the use of any primates caught in the wild, eventually allowing research only with captive-bred animals, a shift that could raise the cost of primate experiments.

The new directive sets out detailed requirements for ethical and scientific review of research involving animals, stressing the "3Rs" of reducing the number of animals used, refining techniques to lessen pain and discomfort, and replacing animal studies with alternatives. For the first time, the E.U. would require researchers to receive ethics committee approval for research on fetal non-human vertebrates in the final third of their development and on several groups of invertebrates, including lampreys, octopuses, squid, and decapod crustaceans such as crabs and lobsters, that have shown evidence of being able to experience pain and distress.

Wolfgang Stein, a neuroscientist at the University of Ulm in Germany who works with crabs, says he is not yet sure what to make of the proposal. He studies invertebrates in part because the moral questions are easier, he says; the animals don't feel pain the way vertebrates do. "If you cut a leg off, 5 seconds later they don't seem to mind that much. It doesn't mean they don't feel▶

*ec.europa.eu/environment/chemicals/lab_animals/proposal_en.htm

China Looks Ahead

BEIJING—China's scientific community is accustomed to planning in 5-year or even 15-year increments. Now, an elite panel of 100-odd scientists organized by the Chinese Academy of Sciences (CAS) is compiling a report on vital research directions over the next 50 years. "In China, we sometimes don't know where we want to go. People like to be guided," says panelist Gao Fu of CAS's Institute of Microbiology here. Although it's impossible to know which research areas will be hot in 2058, the report, expected to be finalized next month, will flag sure bets for long-term investment such as research on chronic diseases.

—RICHARD STONE

Military Science, Reloaded

The U.S. Department of Defense (DOD) plans to award \$80 million in grants this fiscal year to academic scientists as part of a new \$400 million investment over 5 years in basic research. The 5-year grants will fund work in emerging areas such as countering weapons of mass destruction, network sciences, energy and power management, quantum information sciences, and bio-inspired systems. The Pentagon's \$208 million increase for basic research in 2009 was a lone bright spot among science agencies, which otherwise saw their budgets frozen through at least March 2009. DOD also hopes to fund 40 additional researchers in the Presidential Early Career Award for Scientists and Engineers program, under which DOD currently gives out a few dozen 3- to 5-year grants of \$100,000 per year.

—YUDHIJIT BHATTACHARJEE

This Jaguar's Built for Speed

Oak Ridge National Laboratory's upgraded supercomputer, dubbed Jaguar, has broken the petaflops barrier. Jaguar's ability to perform 1.3 quadrillion calculations per second leaves it second only to the Road Runner at Lawrence Livermore nuclear weapons lab in California, and Jaguar's accessible to the entire scientific community. Oak Ridge astrophysicist Bronson Messer says the petascale machine will allow scientists to track up to 150 isotopes created during a supernova; current terascale computers can follow only 13. "We should be able to go from getting a general picture of supernovas to being able to predict things," he says. Now officials with the Department of Energy and the U.S. National Science Foundation hope to establish petascale machines at Oak Ridge and elsewhere to serve more scientists.

—ELI KINTISCH

discomfort, but it is different” from what a vertebrate experiences, he says. Stein is open to some oversight, but he is wary of having to go through the same sort of review required of vertebrate experiments. “The species we work with is considered food,” he says. “From what I can see, they have a better life in our tanks than in the supermarket.”

Emily McIvor, policy director for the Dr Hadwen Trust in Hitchin, U.K., which lobbies for alternatives to animal research, says the proposal is a step in the right direction, although she says that she would have preferred to see a

complete ban on the use of primates. The commission’s attention to research into alternatives to primate use is “very inadequate,” she says.

Scientific organizations, however, have expressed concern that the new levels of regulation will add bureaucratic headaches for researchers without reducing animal suffering. “We are in favor of good regulations,” says Festing. “But if you’re spending all your time filling out paperwork, that doesn’t help the animals.” Still, he says, the draft is better than some expected based on early rumors that had emerged from Brussels.

The fight is far from over. The commission’s proposal still has to receive approval from the European Parliament and the European Council of Ministers before becoming official E.U. policy. “We have more concerns about the Parliament” adding burdensome amendments, Festing says, noting that a number of European politicians opposed to animal research have refused to meet with scientific organizations. “We have seen little evidence that [members of Parliament] are ensuring that they are informed on the science.”

—GRETCHEN VOGEL

EVOLUTION

Vatican Science Conference Offers an Ambiguous Message

Scientists who gathered at the Vatican last week for a closed-door conference* on evolutionary origins are giving the event mixed reviews. Those who hoped for a clear statement of support for evolution from the Catholic Church went home empty-handed. Others, expecting little, were happy with a détente between science and faith. But a few criticize what they heard from the Vatican’s controversial point man on evolution, Austrian Cardinal Christoph Schönborn. “He believes there are gaps in evolution and [that] God acts in those gaps,” says John Abelson, a molecular biologist at the University of California, Davis, who gave a talk at the meeting. This is a “nearly 19th century” view, Abelson says, amounting to support for the intelligent design movement. Pope Benedict XVI did not clarify his own ambiguous statements on evolution.

The meeting was organized by the Pontifical Academy of Sciences, an international group of scientists who advise the pope. Astrophysicist Stephen Hawking of the University of Cambridge in the U.K., Nobel Prize-winning biochemist Marshall Nirenberg, and others gave lectures on the origins of everything from galaxies in the early universe to cellular life on Earth. It was like many scientific conferences except that the pope showed up to bless the proceedings, and the first talk, titled “The Reflections of Joseph Ratzinger Pope Benedict XVI on Evolution,” was given by Schönborn, a theologian.

Schönborn first came to scientists’ attention 3 years ago when he penned an editorial in *The New York Times* shortly after the new pope’s election that openly supported intelligent design (*Science*, 12 August 2005, p. 996). “Evolution in the sense of common ancestry might be true,” the Vienna archbishop wrote, “but evolution in the neo-Darwinian sense—an unguided, unplanned process of random variation and natural selection—is not.”



Hands on. Pope Benedict with astrophysicist Stephen Hawking, one of several famous scientists who spoke at the Pontifical Academy of Sciences.

Schönborn’s prepared talk at the conference was not the source of controversy. “It was so very abstract,” says Gereon Wolters, a philosopher of science at the University of Konstanz, Germany. “It offered the standard view that evolution is okay” but that “evolutionism”—a term used by religious conservatives for the promotion of atheism through evolutionary biology—“is not.” Some scientists even saw signs of progress in the talk. “I was relieved to hear the cardinal clearly distancing himself from intelligent design,”

says Francis Collins, former director of the U.S. National Human Genome Research Institute in Bethesda, Maryland, “referring to that ‘school’ as having made mistakes.”


The sparks flew when the cardinal fielded questions. “He still expressed reservations about whether evolution can account for all aspects of biology,” says Collins, including whether Darwinian evolution can account for the generation of species.

“It was preposterous,” says Abelson, who says that the meeting took “a step backwards” in the church’s relationship with science. Wolters was disappointed, too: “Schönborn has the same intention as the pope has—to fight evolutionism,” he says, but “he is just repeating this creationist gibberish” used by U.S. proponents of intelligent design. Wolters adds: “Fighting science in this way is a losing game.”

Other scientists at the meeting disagree. The cardinal’s doubts about evolution do not represent a conflict between the church and science, says Werner Arber, a geneticist at the University of Basel, Switzerland, who co-organized the meeting. “Relations continue to be good.” Schönborn gave “a confused lecture,” says Peter Raven, director of the Missouri Botanical Garden in St. Louis and a member of the academy, but “the church’s position on evolution, insofar as it can be said to have one, is unchanged. ... There is a belief in a creator who existed before the big bang and set the universe in motion, which is something that cannot be proved or disproved by science.”

—JOHN BOHANNON

*Scientific Insights into the Evolution of the Universe and of Life, Vatican City, 31 October–4 November 2008.



Arteries at risk. In a massive study, people with high blood levels of c-reactive protein benefited from a cholesterol-lowering drug.

CARDIOVASCULAR HEALTH

Statin Therapy Reduces Disease in Healthy Volunteers—But How, Exactly?

The 17,800-person JUPITER trial, a major test of drug therapy to prevent heart disease, enjoyed a blitz of attention this week. Some experts—including the trial's leaders—celebrated it as a huge success in preventing cardiovascular disease and proving the value of c-reactive protein (CRP), an indicator of inflammation, as a risk marker for heart disease. Proponents hail the trial for carving out a new class of people who could benefit from cholesterol drugs but who now don't get them because their cholesterol levels are normal.

The JUPITER trial comes with a host of caveats, however, muddying the picture of what we know and don't know about inflammation's role in cardiovascular disease. Most important, no one can say why the anti-cholesterol drug it tested, the potent statin Crestor, actually helped the participants, all of whom had elevated CRP levels.

Crestor had two effects in the nearly 9000 people who took it (the rest received a placebo): It lowered CRP by 37%, and it lowered LDL, or "bad," cholesterol by 50%. Heart attacks and strokes in the treated group were roughly half those in the placebo cohort, and mortality was 20% lower. Most argue that the statin helped because it reduced normal LDL cholesterol to even lower levels. The more controversial theory is that the benefit came at least in part from the reduction of CRP levels. JUPITER—funded by Crestor's manufacturer, AstraZeneca—was not designed to answer questions about CRP, but speculation has begun.

Cardiologists have long debated whether CRP should be included in their arsenal of risk indicators, and despite its nuances,

JUPITER is likely to edge them in that direction. Studies over the past decade have found that people with high CRP levels tend to suffer more heart attacks and strokes, but the picture is murky because CRP is nonspecific—high CRP levels are linked to any number of diseases. "It's a marker for not being a healthy individual," says Mark Pepys of University College London. Even so, could CRP levels help pick up people at risk of heart disease who are now flying under the radar?

Yes, the authors of JUPITER say unequivocally. "By focusing on inflammation, we seemed to hit the sweet spot" in identifying and helping at-risk patients who are otherwise missed, says Paul Ridker, a cardiologist at Brigham and Women's Hospital in Boston, who led the trial and holds a patent on a method for testing CRP. JUPITER's results were reported online 9 November in *The New England Journal of Medicine (NEJM)* and presented the same day at the American Heart Association meeting in New Orleans, Louisiana.

Many others are more circumspect. One reason for caution, says Eric Topol, a cardiologist and director of the Scripps Translational Science Institute in San Diego, California, is that JUPITER's actual benefits are "a little hard to tease out." He wonders: "Were they really treating high CRP, or were they treating a potpourri of other risk factors" in people who also had high CRP levels? The study participants had normal cholesterol levels and were described as healthy volunteers, but most were also overweight, 15% were smokers, and 40% had metabolic syndrome. All these qualities are known to boost CRP levels. That raises a related ques-

tion that has nothing to do with CRP, says cardiologist Benjamin Scirica of Brigham and Women's Hospital. Should patients who have normal cholesterol but some common risk factors, such as high blood pressure or obesity, be treated with statins to push their cholesterol to even lower levels? "I think [JUPITER] expands the thinking about risk factors," says Scirica, who, like Topol, was not involved in the trial.

But the fundamental question of whether high CRP levels actually cause disease—and whether JUPITER worked because it lowered CRP—remains unresolved. More and more scientists are rejecting this argument, in part because of a genetics study published on 30 October in *NEJM*. In that work, a Danish group analyzing DNA from more than 50,000 people found that variations in the CRP gene don't cause heart disease—suggesting that although CRP blood levels correlate with disease, the protein is not causing it. Børge Nordestgaard, a genetic epidemiologist and physician at Copenhagen University Hospital who led the genetics study and participated in the JUPITER trial, believes that CRP is a consequence, not a cause, of atherosclerosis. He suggests that cholesterol penetrates the walls of arteries and that white blood cells swoop in to remove it. That creates inflammation and raises CRP. Thus, by this line of thinking, high CRP levels indicate atherosclerosis that might not have shown itself in symptoms.

The genetics study has convinced some that "CRP doesn't appear to be a driving force" in heart disease, says Topol. He and others who endorse this view suspect that the benefits of JUPITER are due to lowering LDL cholesterol. JUPITER recruited only people with relatively healthy LDL levels—on average, about 100. But "we know there's a straight line from LDL cholesterol to cardiovascular risk," no matter what the starting number, says Pepys, who has studied CRP for decades. LDL came down about 50% in JUPITER—a drop that is consistent with the 54% reduction in heart attacks, Pepys says.

Ridker, however, believes that genetics can explain only so much and that the best way to determine whether CRP causes disease is by testing whether a drug that lowers it preserves health. Isis Pharmaceuticals in Carlsbad, California, is developing such a CRP inhibitor. CEO Stanley Crooke says, "The core question is less whether something causes the disease but whether selective reduction of that target reduces that disease." The company has already begun testing its CRP inhibitor for safety in healthy volunteers. —JENNIFER COUZIN



The Birth of Childhood

Unlike other apes, humans depend on their parents for a long period after weaning. But when—and why—did our long childhood evolve?

Mel was just 3.5 years old when his mother died of pneumonia in 1987 in Tanzania. He had still been nursing and had no siblings, so his prospects were grim. He begged weakly for meat, and although adults gave him scraps, only a 12-year-old named Spindle shared his food regularly, protected him, and let him sleep with him at night. When Spindle took off for a month, another adolescent, Pax, came to Mel's rescue, giving him fruit and a place to sleep until Spindle returned. Mel survived to age 10.

Fortunately for Mel, he was an orphan chimpanzee living in the Gombe Stream National Park rather than a small child living in the slums of a big city. With only sporadic care from older children, a 3-year-old human orphan would not have survived.

Mel's story illustrates the uniqueness of one facet of human life: Unlike our close cousins the chimpanzees, we have a prolonged period of development after weaning, when children depend on their parents to feed them, until at least age 6 or 7. Street

children from Kathmandu to Rio de Janeiro do not survive on their own unless they are at least 6. "There's no society where children can feed themselves after weaning," says anthropologist Kristen Hawkes of the University of Utah in Salt Lake City. By contrast, "chimpanzees don't have childhoods. They are independent soon after weaning,"

says anthropologist Barry Bogin of Loughborough University in Leicestershire, U.K.

Humans are also the only animals that stretch out the teenage years, having a final growth spurt and delaying reproduction until about 6 years after puberty.

On average, women's first babies arrive at age 19, with a worldwide peak of first babies at age 22.5. This lengthy period of development—comprised of infancy, juvenile years, and adolescence—is a hallmark of the human condition; researchers have known since the 1930s that we take twice as long as chimpanzees to reach adulthood. Even though we are only a bit bigger than chimpanzees, we mature and reproduce a decade later and live 2 to 3 decades longer, says Bogin.

Online sciencemag.org

S Hear more about childhood's beginning in a podcast with author Ann Gibbons.

Given that we are unique among mammals, researchers have been probing how this pattern of growth evolved. They have long scrutinized the few, fragile skulls and skeletons of ancient children and have now developed an arsenal of tools to better gauge how childhood has changed over the past 3 million years. Researchers are scanning skulls and teeth of every known juvenile with electron microscopes, micro-computed tomography scans, or powerful synchrotron x-rays and applying state-of-the-art methods to create three-dimensional virtual reconstructions of the skulls of infants and the pelvises of mothers. They're analyzing life histories in traditional cultures to help understand the advantages of the human condition. In addition, some new fossils are appearing. On page 1089 of this issue, researchers report the first nearly complete pelvis of a female *Homo erectus*, which offers clues to the prenatal growth of this key human species.

All of this is creating some surprises. One direct human ancestor, whose skeleton looks much like our own, turns out to have grown up much faster than we do. The life histories of our closest evolutionary cousins, the Neandertals, remain controversial, but some researchers suspect that they may have had the longest childhoods of all. The new lines of evidence are helping researchers close in on the time when childhood began to lengthen. "Evidence suggests

CREDITS (LEFT TO RIGHT): SARAH LEEN AND BECKY HALE/NATIONAL GEOGRAPHIC; M. NEWMAN/LP/GETTY IMAGES; PHOTOS.COM; BRIAN M. WOOD



Changing face of childhood. Childhood has more than doubled in length in modern humans as compared to chimpanzees and the Dikika baby australopithecine (*reconstructed in lower left*). Delaying child-birth allows for bigger, stronger mothers who can give birth more frequently, as seen for example in traditional hunter-gatherer societies (*upper right*).

that much of what makes our life history unique took shape during the evolution of the genus *Homo* and not before,” says anthropologist Holly Smith of the University of Michigan, Ann Arbor.

Live fast, die young

Back in 1925, Australian anatomist Raymond Dart announced the discovery of that rarest of rare specimens, the skull of an early hominin child. Dart estimated that the australopithecine he called the Taung baby had been about 6 years old when it died about 2 million years ago, because its first permanent molar had erupted. As modern parents know, the first of the baby teeth fall out and the first permanent molars appear at about age 6. Dart assumed that early hominins—the group made up of humans and our ancestors but not other apes—matured on much the same schedule as we do, an assumption held for 60 years. Growing up slowly was seen as a defining character of the human lineage.

Then in 1984, anatomists Christopher Dean and Timothy Bromage tested a new method to calculate the chronological ages of fossil children in a lab at University College London (UCL). Just as botanists add up tree rings to calculate the age of a tree, they counted microscopic lines on the surface of teeth that are laid down weekly as humans grow. The pair counted the lines on teeth of australopithecine children about as mature as the Taung child and were confounded: These hominin children were only about 3.5 years old rather than 6. They seemed to be closer to the chimpanzee pattern, in which the first permanent molar erupts at about age 3.5. “We concluded that [the australopithecines] were more like living great apes in their pace of development than modern humans,” says Dean.

Their report in *Nature* in 1985 shook the field and focused researchers on the key questions of when and why our ancestors adopted the risky strategy of delaying reproduction. Many other slow-growing, large-bodied animals, such as rhinos, elephants, and chimpanzees, are now threatened with extinction, in part because they delay reproduction so long that their offspring risk dying before they replace themselves. Humans are the latest to begin reproducing, yet we seem

Childhood Stages

	Age at weaning (years)	Age at eruption of first molar (years)	Female age at first breeding (years) (estimated by 3rd molar eruption in fossils)	Average maximum life span (years)
Chimpanzees, <i>Pan troglodytes</i>	4.0	4.0	11.5	45
Lucy, <i>Australopithecus afarensis</i>	4.0?	4.0?	11.5	45
<i>Homo erectus</i>	?	4.5	14.5 (est.)	60? (est.)
Modern humans, <i>Homo sapiens</i>	2.5	6.0	19.3	70

Milestones. Key events show that modern humans live slower and die later than our ancestors did.

immune from those risks, given that there are 6.6 billion of us on the planet. “When did we escape those constraints? When did we extend our childhood?” asks biological anthropologist Steven Leigh of the University of Illinois, Urbana-Champaign.

The Taung baby and the other australopithecine children, including the relatively recent discovery of a stunning fossil of a 3-year-old *Australopithecus afarensis* girl from Dikika, Ethiopia, show that it happened after the australopithecines. So researchers have zeroed in on early *Homo*, which appeared in Africa about 2 million years ago.

Unfortunately, there are only a few jaw

tors to share many key elements of the modern human body plan, with a brain considerably larger than that of earlier hominins. And unlike the petite australopithecines, this Turkana youth was big: He weighed 50 kilograms, stood 163 centimeters tall, and looked like he was 13 years old, based on modern human standards. Yet two independent tooth studies suggested ages from 8 or 9 to 10.5 years old.

Now a fresh look at the skeleton concludes that, despite the boy’s size, he was closer to 8 years old when he died. Dean and Smith make this case in a paper in press in an edited volume, *The First Humans: Origin of the Genus Homo*. The skeleton and tooth microstructure of the boy and new data on other members of his species suggest that he attained more of his adult height and mass earlier than modern human children do. Today, “you won’t find an 8-year-old boy with body weight, height, and skeletal age that are so much older,” says Dean.

He and Smith concluded that the boy did not experience a “long, slow period of growth” after he was weaned but grew up earlier, more like a chimpanzee. They estimate the species’ age at first reproduction at about 14.5, based on the eruption of its third molar, which in both humans and chimpanzees erupts at about the age they first reproduce. This 8-year-old Turkana Boy was probably more independent than a 13-year-old modern human, the researchers say, suggesting that *H. erectus* families were quite different from ours and did not stay together as long.

The new, remarkably complete female pelvis described in this issue, however, suggests that life history changes had begun in *H. erectus*. Researchers led by Sileshi Semaw of the Stone Age Institute at Indiana University, Bloomington, found the pelvis in the badlands of Gona, Ethiopia. They present a chain of inference that leads from pelvis, to brain size, to life history strategy.

They assume that the nearly complete



Big for his age. The 8-year-old Turkana Boy, reconstructed here, grew up faster than modern humans do.

bits of early *Homo* infants and young children to nail down their ages. Most of what we know comes from a single skeleton, a *H. erectus* boy who died about 1.6 million years ago near Lake Turkana, Kenya. *H. erectus* was among the first human ances-

pelvis belongs to *H. erectus*, because other *H. erectus* fossils were found nearby and because it resembles fragmentary pelvises for the species. Lead author Scott Simpson of Case Western Reserve University in Cleveland, Ohio, paints a vivid picture of a short female with wide hips and an “obstetrically capacious” pelvic opening that could have birthed babies with brain sizes of up to 315 milliliters. That’s 30% to 50% of the adult brain size for this species and larger than previously predicted based on a reconstruction of the Turkana Boy’s incomplete pelvis. However, the new estimate does match with newborn brain size predicted by the size of adult brains in *H. erectus*, says Jeremy DeSilva of Worcester State College in Massachusetts, who made such calculations online in September in the *Journal of Human Evolution*.

The wide pelvis suggests *H. erectus* got a head start on its brain development, putting on extra gray matter in utero rather than later in childhood. That’s similar to living people, whose brains grow rapidly before birth, says Simpson. But if *H. erectus*’s fetal growth approached that of modern humans, it built proportionately more of its brain before birth, because its brain never became as massive as our own.

Thus, *H. erectus* grew its brain before birth like a modern human, while during childhood it grew up faster like an ape. With a brain developing early, *H. erectus* toddlers may have spent less time as helpless children than modern humans do, says paleoanthropologist Alan Walker of Pennsylvania State University in State College. This suggests *H. erectus* children were neither chimplike nor humanlike but perhaps somewhere in between: “Early *H. erectus* possessed a life history unlike any species living today,” write Dean and Smith.

“If you look at its morphology, it fits in our genus, *Homo*,” says Smith. “But in terms of life history, they fit with australopithecines.”

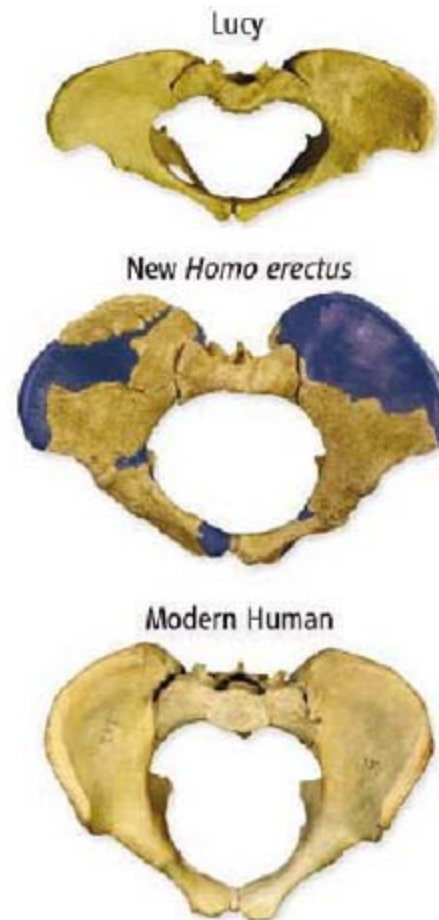
Live slow, die old?

If *H. erectus* was just beginning to slow down its life history, when did humans take the last steps, to our current late-maturing life plan? Three juvenile fossil members of *H. antecessor*, who died 800,000 years ago in Atapuerca, Spain, offer tantalizing clues. An initial study in 1999, based on rough estimates of tooth eruption, found that this species matured like a modern human, says José María Bermúdez de Castro of the Museo Nacional de Ciencias Naturales in Madrid. Detailed studies of tooth microstructure are eagerly awaited to confirm this.

In the meantime, another recent study has shown that childhood was fully extended by the time the first members of our species, *H. sapiens*, appeared in northern Africa about 200,000 years ago. In 2007, researchers examined the daily, internal tooth lines of a *H. sapiens* child who lived 160,000 years ago in Jebel Irhoud, Morocco. They used x-rays from a powerful particle accelerator in Grenoble, France (*Science*, 7 December 2007, p. 1546), to study the teeth without destroying



More siblings?
Hutterite families often had nine children each.



Ancient hipsters. A fossil female pelvis from *Homo erectus* (middle) shows that the species could birth babies with bigger heads than Lucy’s species (top) but smaller than a modern human’s.

them and found that the 8-year-old Jebel Irhoud child had grown as slowly as a modern 8-year-old, according to Harvard University paleoanthropologist Tanya Smith, who co-led the study.

That analysis narrowed the window of time when humans evolved the last extension of our childhood to between 800,000 years ago and 200,000 years ago. To constrain it still further, Tanya Smith and her colleagues recently trained their x-ray vision on our closest relatives: the extinct Neandertals, who shared their last ancestor with us about 500,000 years ago. First, the researchers sliced a molar of a Belgian Neandertal that was at the same stage of dental development as the 8-year-old Jebel Irhoud child and counted its internal growth lines.

They found that it had reached the same dental milestones more rapidly and proposed that Neandertals grew up faster than we do. That suggests that a fully extended childhood evolved only in our species, in the past 200,000 years.

But Tanya Smith’s results conflict with earlier studies by Dean and colleagues who also sliced Neandertal teeth and found that they had formed slowly, like those of modern humans. The case is not closed: Smith and paleontologist Paul Tafforeau of the European Synchrotron Radiation Facility in Grenoble, France, spent weeks last year imaging juvenile Neandertals and early members of *H. sapiens*, and they expect to publish within a year.

Meanwhile, new data with implications for Neandertal growth rates are coming in from other sources. The brain sizes of a Neandertal newborn and two infants show that they were at the upper end of the size range for modern humans, suggesting that their brains grew faster than ours after birth, according to virtual reconstructions by Christoph Zollikofer and anthropologist Marcia Ponce de León of the University of Zurich (*Science*, 12 September, p. 1429).

Those rapidly growing brains don’t necessarily imply a rapid life history, warn



Zollikofer and Ponce de León. They argue that because Neandertals' brains were more massive, they did not complete brain growth earlier than modern humans even though they grew at a faster rate. "They have to get those bigger brains somehow," says Holly Smith. For now, Neandertals' life history remains controversial.

Why wait?

If childhood began to change in *H. erectus* and continued to get longer in our own species and possibly Neandertals, then the next question is why. What advantage did our ancestors gain from delaying reproduction so long? Many researchers agree that childhood allows us to learn from others, in order to improve our survival skills and prepare us to be better parents. Historically, researchers have also argued that humans need a long childhood to allow enough time for our larger brain to mature.

But in fact, a big brain doesn't directly cause the extension of childhood, because the brain is built relatively early. "Everyone speaks about slow human development, but the human brain develops very fast," says Zollikofer. It doubles in size in the first year of life and achieves 95% of its adult size by the age of 5 (although white matter grows at least to age 18). "We get our brains done; then, we sit around for much longer than other species before we reproduce," says Leigh. "It's almost like humans are building the outside, getting the scaffolding of the house up early, and then filling in after that."

However, there's a less direct connection between brains and life history: Big brains are so metabolically expensive that primates must postpone the age of reproduction in order to build them, according to a paper last year in the *Journal of Human Evolution* (*Science*, 15 June 2007, p. 1560). "The high metabolic costs of rapid brain growth require delayed maturation so that mothers can bear the metabolic burdens associated with high brain growth," says Leigh. "Fast brain growth tells us that maturation is late."

That's why Ponce de León and Zollikofer think that the Neandertals' rapid brain growth implies late, rather than early, maturation: Neandertal mothers must have been large and strong—and by implication, rela-

tively old—to support infants with such big, fast-growing brains. Indeed, say the Zurich pair, Neandertals may have had even longer childhoods than we do now. Childhood, like brain size, may have reached its zenith in Neandertals and early *H. sapiens*. As our brains got smaller over the past 50,000 years, we might have begun reproducing slightly earlier than Neandertals.

ers. Indeed, humans start having babies 8 years later than chimpanzees, and both species stop by about age 45 to 50. But once human mothers begin, they more than make up for their delayed start, pushing out babies on average 3.4 years apart in traditional forager societies without birth control, compared with 5.9 years for wild chimpanzees, says Bogin. This rapid-fire reproduction produces more babies for human

hunter-gatherers, who have peak fertility rates of 0.31 babies per given year compared with 0.22 for chimpanzees. And human mothers who start even later than age 19 have more surviving babies. For example, in the 1950s, the Anabaptist Hutterites of North America, who eschewed birth control, had their first babies on average at age 22 and then bore children every 2 years. They produced an amazing nine children per mother, says Bogin, who has studied the group.

Such fecundity, however, requires a village or at least an extended family with fathers and grandmothers around to help provision and care for the young. That's something that other primates cannot provide consistently, if at all, says Hawkes (*Science*, 25 April 1997, p. 535). She proposed that grandmothers' provisioning allows mothers to wean early and have babies more

closely together, a vivid example of the way humans use social connections to overcome biological constraints—and allow mothers to have more babies than they could raise on their own. "Late maturation works well for humans because culture lets us escape the constraints other primates have," says Leigh.

The key is to find out when our ancestors were weaned, says Holly Smith. Younger weaning implies that mothers had enough social support to feed weaned children and space babies more closely. "Weaning tells us when *Homo* species start stacking their young," says Smith. Indeed, Dean and Louise Humphrey of the Natural History Museum in London are testing a method that detects the chemical signature of weaning in human teeth. Humans may be slow starters, but our social safety net has allowed us to stack our babies closely together—and so win the reproductive sweepstakes, leaving chimpanzees, and the extinct Neandertals, far behind.

—ANN GIBBONS



Tooth time. Tanya Smith uses a synchrotron accelerator to x-ray fossil teeth (above); molar eruption helps age other specimens such as Turkana Boy (left).

To explore such questions, recent interdisciplinary studies are teasing out the reproductive advantages of waiting to become parents. Many analyses cite an influential life history model by evolutionary biologist Eric Charnov of the University of New Mexico, Albuquerque. The model shows that it pays to have babies early if parents face a high risk of death. Conversely, mammals that face a lower risk of dying benefit if they wait to reproduce, because older mothers can grow bigger, stronger bodies that grow bigger babies, who are more likely to survive. "The driving force of a prolonged life history schedule is almost certainly a reduction in mortality rates that allows growth and life span to extend and allows for reproduction to extend further into adulthood in a more spread-out manner," says Dean.

Researchers such as Loughborough's Bogin have applied Charnov's model to modern humans, proposing that delaying reproduction creates higher quality human moth-

RENEWABLE ENERGY

Minnesota Ecologist Pushes Prairie Biofuels

David Tilman wants to mix it up by growing native grasses for energy. Many agronomists disagree

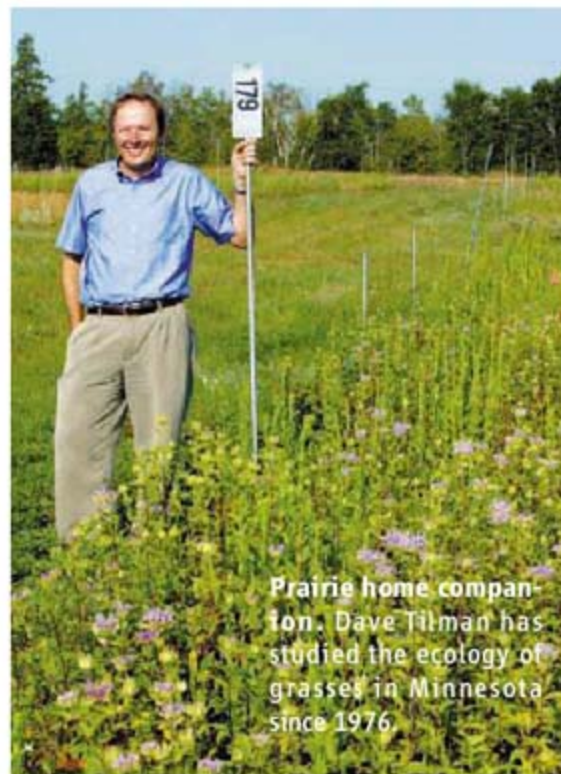
EAST BETHEL, MINNESOTA—Over the past 3 decades, David Tilman has set up thousands of field experiments here, 70 km outside of Minneapolis, probing some of the most fundamental questions about prairie ecosystems. So, the University of Minnesota (UM), Twin Cities, ecologist never imagined he'd undertake the considerably more practical task of developing new climate-friendly crops for biofuels—that is, until 2005, when he realized he'd done it inadvertently, as part of a long-term ecological study at Cedar Creek Ecosystem Science Reserve.

On one 11-m- \times -11-m square plot was a healthy stand of switchgrass, an abundantly growing perennial that the U.S. government is promoting as an alternative to corn as a feedstock for ethanol. Nearby was a plot of switchgrass mixed with 15 native perennial grasses that tend to grow less verdantly each year. Neither plot received irrigation or fertilizer. Yet, when Tilman and colleagues analyzed 12 years' worth of data, the mixed plots delivered more than twice the yearly biomass per hectare—suggesting a potentially much more efficient biofuel source with a much smaller “carbon footprint.” “We expected higher productivity—maybe 50%. But nothing like the 238% we now see,” said Tilman during a recent walk through his 121 hectares of field sites.

To Tilman, the findings suggest that for producing biofuel feedstocks, the mixtures are “more stable than monoculture, more reliable than monoculture, and more productive than monoculture”—and more environmentally friendly. Because different species occupy different ecosystem niches and perform different functions—say,

adding nutrients to the soil or resisting drought—mixtures of prairie grasses can thrive on marginal lands without energy-intensive inputs such as fertilizer and irrigation. In addition, they can boost biodiversity and replenish depleted soils. “This is bigger than just biofuels,” Tilman says.

Tilman's proposal to grow the mixtures as ethanol feedstocks, published in the 8 December 2006 issue of *Science* (p. 1598), won plaudits from top ecologists and inspired the U.S. Congress to include prairie biofuels in a \$100 million national biomass-planting program. The Minnesota legislature kicked in roughly \$3 million for state studies of prairie grasses. But Tilman's idea drew a firestorm of criticism from many agronomists, who said it



Prairie home companion. Dave Tilman has studied the ecology of grasses in Minnesota since 1976.

Plots thickened. Scientists are examining the potential for biofuels of various prairie grass combinations.

overstated the potential climate benefits. They charged that Tilman's methodology exaggerated the productivity of mixed grasses and underestimated the expense and difficulty of scaling up test plots to commercial size. “Most people don't believe [his idea] could be practical,” says agronomist and geneticist Stephen Moose of the University of Illinois, Urbana-Champaign.

The upbeat, fast-talking ecologist concedes that several questions must be answered before his strategy goes prime time. “I'm not one to believe we've found the be-all and end-all of biofuels,” Tilman says. But he thinks it is worth a try. And so do a handful of ecologists and agronomists in seven Midwestern states; like Tilman, they are starting larger trials to test his concept under different conditions.

A mixed bag

Tilman's proposal contrasts sharply with the recent thrust of biofuels research. Today, U.S. farmers produce some 29 billion liters of ethanol a year from corn. But corn-based ethanol is no longer seen as a relatively cheap, environmentally friendly alternative to petroleum-based fuels. Experts say it's too carbon-intensive. Fertilizing, harvesting, and refining corn into fuel takes a lot of energy, and the sugar-conversion process wastes most of the plant's biomass, primarily cellulose. Using prime farmland to grow biofuels not only contributes to rising global food prices but also leads indirectly to cutting down trees for farmland overseas—and that, in turn, releases more carbon.

In search of a substitute for corn ethanol, President George W. Bush launched a \$150 million, two-pronged federal research program in 2006 to identify cellulose feedstocks for biofuels, such as switchgrass, as well as the enzymatic and microbial methods to convert plant cellulose into fuels, an equally daunting challenge. Last year, the U.S. Congress passed a law requiring refiners to produce an estimated 61 billion liters of cellulosic biofuels by 2022.

In terms of potential new feedstocks, the part of the challenge on which Tilman is working, the U.S. departments of Energy and Agriculture have focused so far on switchgrass, waste-plant material from farms, poplar trees, and a tall European perennial grass called *Miscanthus*. Their emphasis has been to grow these crops as monocultures on large plots of prime farmland, using conventional high-input agricul-

CREDITS (TOP TO BOTTOM): UNIVERSITY OF MINNESOTA; TIM RUMMELHOFF

tural techniques. Tilman, by contrast, advocates growing biofuel stocks with minimal or no fertilizer on some of the nation's more than 5 million hectares of marginal soils—farmland with nutrient-depleted soils, worn-out hayfields, or on the edges of streams or highways, “using mixtures of plants which will grow there anyway,” says ecologist Clarence Lehman, a research partner of Tilman's at UM.

The soils on Tilman's experimental plots are about as marginal as they come in the Midwest. They were too sandy for general farming to begin with, and then, in 1993, Tilman and his colleagues scooped off the top 15 centimeters of soil to ensure that each plot had roughly the same depleted levels of nutrients such as nitrogen and phosphorus. They measured the output of hundreds of mixed-species plots, publishing a string of high-profile papers that demonstrate the stability and productivity of biodiverse ecosystems.

Although Tilman didn't realize it at the time, he was also creating an ideal laboratory to test potential feedstock crops for biofuels that could grow on the world's 700 million hectares of degraded land. These days, that lab is abuzz with activity. Since 2006, the researchers have expanded the fieldwork to examine the agricultural and environmental implications of growing prairies for biofuels. They maintain test plots planted in various monocultures of prairie species, six-species mixtures, and 60-species mixtures. As Tilman reported in 2006, the mixed prairie grass plots produced the equivalent of 1500 liters of ethanol per hectare in net energy yield as opposed to 620 liters from switchgrass. (The net energy yield reflects the total amount of fuel produced minus the energy used to produce it, including energy required to make fertilizer and to run farm equipment.)

To gauge productivity, Tilman's team measures aboveground growth from samples cropped close to the ground. Obtaining accurate data requires a platoon of several dozen summer students, who spend hours a day sifting through thousands of kilograms of dried soil, leafs, and twigs to separate bits of each species for weighing. Others obtain underground biomass samples at various depths. “It's not easy,” laughed Andrew Chua, a University of California, San Diego,

undergraduate, who had removed his shirt as he pounded a steel probe through dry soil one afternoon in late August. The elbow grease will pay off in the winter, says Tilman, when full results from this fall's harvest will be available.

A question of benefits

But Tilman has a long way to go to convince mainstream agronomists. His critics say that his experiments inflate biomass yields, suggesting that prairie grass biofuels would be more carbon efficient than they actually are. And critics see big expenses to boot.

To maintain the correct mixture of species, Tilman's team hand-weeds the plots each year. Each autumn, they remove bio-

switchgrass monocultures have a higher net energy yield, he asserts. In work published this year in the *Proceedings of the National Academy of Sciences*, he showed that tests of switchgrass on full-scale plots on 10 Midwestern farms, treated with the standard 60 to 100 kg per hectare of nitrogen fertilizer each year, delivered net energy yields of between 2250 and 3300 liters of ethanol per hectare—more than twice the net benefit Tilman's mixtures provided.

Tilman is quick to point out that Vogel's soils were mostly richer than his, providing an inherent advantage, although he acknowledges that switchgrass could potentially offer net benefits. Large head-to-head experiments using the same soil are now under way to settle the question, with results expected next year.

Vogel's team has grown mixed-species plots in recent years, and Tilman is comparing watered and fertilized plots of switchgrass with his mixtures.

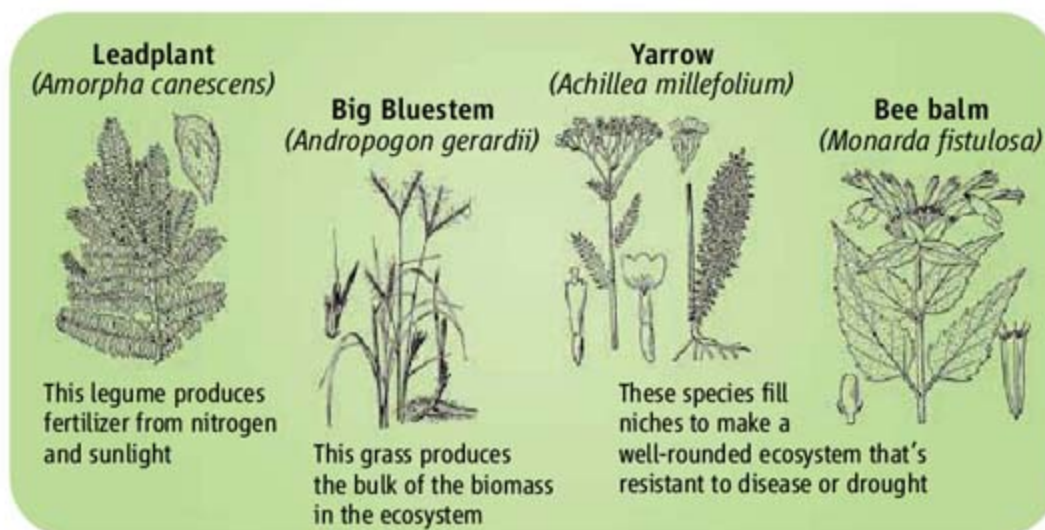
Prairie grass mixtures will be expensive initially for farmers, Tilman acknowledges: The seeds can cost between two and 10 times more per kilogram than switchgrass. But he expects costs to fall as demand increases, and he hopes other environmental advantages will give mixtures a fair shot.

To pin down the biodiversity benefits of managed prairies, the state of Minnesota is supporting research on roughly 800 hectares of marginal lands across six sites to compare the effects of different harvesting techniques on game birds, insects, and other wildlife.

Lehman is studying whether the grasses' root systems might take up excess chemicals that leach in from nearby agricultural fields. The U.S. Geological Survey is funding experiments using chemical tracers on several of Tilman's test plots to measure the uptake of nitrogen, endocrine disrupters, and antibiotics.

Although many agronomists remain skeptical, the overall environmental advantages of prairie grass biofuels have inspired some to test Tilman's approach. When the 2006 paper appeared, “people were saying this ecologist is doing a lot of talking but he doesn't have the data behind it,” says UM agronomist Craig Sheaffer. But now he's setting up large-scale field trials of the mixtures himself.

—ELI KINTISCH



We are family. These four plants are representative of the dozens of species that make up naturally biodiverse prairies.

mass for measurement from small sections of certain plots, which are burned in the spring. But burning may be giving the grasses an artificial advantage, allowing nutrients such as phosphorus and potassium to be incorporated back into the soil, says agronomist Kenneth Cassman of the University of Nebraska, Lincoln (UNL). A farmer seeking to sell biomass to an ethanol refinery, in contrast, would harvest the entire crop each year, removing the nutrients with a resultant decline in overall productivity, he contends. Tilman concedes that his test plots may be benefiting from conserved nutrients, although he notes that the amount of inputs required are nonetheless minimal.

Leading switchgrass proponent Kenneth Vogel of UNL and the U.S. Department of Agriculture takes aim at the most salient finding of Tilman's 2006 work: that mixed grasses were more than twice as productive as switchgrass per hectare without inputs for either. Mixed species may have won out in Tilman's small plots, says Vogel, and watering and fertilizing switchgrass fields may require more energy. But with inputs,



PLANT GENOMICS

A Bunch of Trouble

The banana is endangered and largely ignored by funding agencies, researchers, and breeders. But things might finally be going its way

2001 was supposed to be the year of the banana. That summer, a handful of researchers gathered in a small room at the U.S. National Science Foundation (NSF) in Arlington, Virginia, to form a consortium to sequence the fruit. Scientists had just deciphered the genome of *Arabidopsis*, with the rice genome close behind, and the banana community desperately wanted to be next. A new strain of soil fungus was threatening the commercial banana, and the community was convinced that a genome project could provide the genetic tools needed to save the crop. “The time was ripe,” says Emile Frison, then head of the consortium. He predicted that within 5 years—a time period that would see the launch of major efforts to sequence corn, sorghum, and even green algae—banana buffs would have their genome.

Today, they’re still waiting.

That’s quite an indignity for one of the world’s most popular fruits. Americans consume as many kilograms of bananas as apples and oranges combined, and in many

African countries, bananas make up nearly half of all calories consumed. What’s more, the banana most of us are familiar with—the Cavendish (*Musa acuminata*)—is in danger of disappearing. The soil fungus Frison fretted about in 2001 causes a nasty blight known as Panama disease that has devastated crops in Malaysia, the Philippines, and China. If the disease makes its way to Latin America, it could wipe out the Cavendish in less than 10 years. African bananas, too, have begun to disappear, victims of globalization and unsustainable farming practices.

Yet the banana continues to sit on the shelf while other crops benefit from research dollars and attention. Some blame the United States for failing to support the fruit as it has other major food crops. Others blame the banana community for being too fragmented to unite behind a single project. And still others blame the banana itself, for a bizarre biology that frustrates breeders and researchers alike.

At last, however, banana researchers may

have found a benefactor: A French research agency will announce funding for the long-awaited genome project next week. The community just hopes it’s not too late. “If the Cavendish is wiped out, there’s nothing to replace it,” says Nicolas Roux, Frison’s successor as coordinator of the Global *Musa* Genomics Consortium. “We’re sitting on a time bomb.”

A crop in crisis

Juan Fernando Aguilar Moran has been trying to defuse that bomb for 7 years, not through sequencing but through breeding. As the chief breeder at the Honduran Agricultural Research Foundation (FHIA) in San Pedro Sula, the world’s largest banana and plantain breeding center, Aguilar Moran is hoping to produce a variety that’s hardier than the Cavendish. But the banana’s not making it easy.

Unlike rice, wheat, and corn—the three crops that are eaten in larger quantities than the banana—most bananas are completely sterile. Unusual breeding in the Cavendish’s past, for example, has led to a plant with three sets of chromosomes that has no seeds, no pollen, and no sex life. Farmers must hack off a piece of the plant and coax it into putting down roots, meaning a Cavendish eaten in Iowa today is genetically identical to one consumed in Ireland 30 years ago.

Faced with such a prudish plant, breeders like Aguilar Moran must instead turn to its wild relatives to create new varieties, and they, too, produce few viable seeds. Adding to the hassle, the plants grow at about one-fifth of the pace of rice, wheat, and corn, so experiments take years to complete. That may explain why there are only five breeding programs in the world dedicated to the banana versus hundreds for those other crops. “It’s a lot of work,” says Aguilar Moran.

So why does he persist? Two words: Gros Michel. The Cavendish’s predecessor, “Big Mike,” used to be the developed world’s banana of choice. But an early incarnation of Panama disease known as Race 1 decimated the fruit—and nearly took the banana industry with it—in the mid-1900s. The Cavendish—a lucky, last-minute find originally from China—was resistant, but Aguilar Moran says its days are numbered. The new form of Panama disease that has invaded Asia, known as Race 4, takes no pity on the Cavendish. Because every plant is genetically identical, they’re all equally susceptible to the same diseases. Once Race 4 hits the banana heartland in Latin America, says Aguilar Moran, it’s game over for our favorite fruit.

Another dark shadow is black sigatoka, a fungus that turns banana leaves black and blocks photosynthesis. Over the 50 years the

pathogen has been on the scene, fungicides have become increasingly ineffective against it. "In Central America, we need to spray once a week," says Aguilar Moran.

Black sigatoka is on the march in Africa, too, but it's just one of many threats to that continent's bananas. Frison, now the director general of Bioversity International, a nonprofit that coordinates research into improving the lot of bananas and other crops, says that in Eastern Africa, farmers have been growing bananas on the same plots for 100 years, which has led to a decline in soil fertility. "They can't grow bananas anymore," he says.

Banana biodiversity is also suffering: Due to globalization, African farmers increasingly grow only the varieties they can sell at the market, says Frison. Whereas the average farmer used to cultivate a dozen varieties, now he only grows four or five. Without human-assisted propagation, the rest of the varieties disappear. That means less raw material for breeders like Aguilar Moran.

The forgotten fruit

Of course, diseases and loss of biodiversity plague many of the world's other major food crops. But they have one distinct advantage over the banana:

People care about them. The United States, China, and other countries have spent far more on rice, corn, and wheat than they have on bananas. In 2008, for example, the U.S. Agency for International Development funded

about \$9 million in rice research but just over \$1 million in banana research. "It puzzles us," says Richard Markham, a program director at Bioversity International. Most funding agencies in developed countries don't take the Cavendish seriously, he says, and they don't realize that the vast majority of other bananas are a staple food source for millions. (In Uganda, the word for "banana" and "food" is the same.) "It's hugely neglected and underinvested."

Even the banana industry doesn't seem to care. Banana suppliers Dole Food Co. and Chiquita Brands International have largely stayed out of banana research for the past 20 years, says Markham, although Chiquita has recently begun funding FHIA. Critics say the companies are shortsighted and that they haven't learned the lessons of the Gros Michel disaster. (Representatives for Dole and Chiquita did not return phone calls for this article.)

Regardless, the assumption that these companies are looking out for the banana has kept the public sector away, says Markham.

The lack of attention has dealt a huge blow to efforts to sequence the banana. Frison hoped the 2001 meeting at NSF would mobilize a big investment, but nobody jumped on board. "We only found small and scattered money," he says. Roux took over for Frison in 2003, and over the next 4 years the Global *Musa* Genomics Consortium collected members—37 institutions in all, including the J. Craig Venter Institute and the Max Planck Institute for Chemical Ecology—but not much funding.

Hoping for U.S. support, the consortium approached the U.S. Department of Energy's (DOE's) Joint Genome Institute (JGI) in January 2008. JGI has a program to which research communities can apply to have the DNA of their favorite organism deciphered.

Roux says JGI seemed enthusiastic about the banana. But this summer, the consortium learned that it didn't make the cut. Duckweed and sea grass did.



Consumed. Bananas are a staple food in developing countries, but they are also victims of fungal diseases.

JGI's James Bristow says these species fit better into DOE's mission of investigating species for alternative fuels and bioremediation, though he admits to being disappointed by the reviewers' decision. "It's an important and endangered worldwide food crop," he says. "There's no question that this genome should be sequenced."

Jane Silverthorne, who headed NSF's Plant Genome Research Program from 1999 to 2007, says the bigger problem may be that the banana community is just not as well-organized as other crop communities. "It's small and fragmented" she says. Some banana proponents would rather see money put into subsistence farming than sequencing, Markham points out, "and even within molecular biology, some say we don't need the entire sequence—or that we should wait until the cost of sequencing comes down."

Nonetheless, Markham says it would be a "huge boost" for banana researchers to have

the sequence. The trick is finding someone who will step up to fund it.

Slipping into the future

That someone might just be France. When members of the banana consortium gathered at the JGI workshop in January to present their sequencing plan, they got an unexpected boost from Francis Quétier, then deputy director of French sequencing giant Genoscope. Quétier announced that his institute would do half the work needed to generate a reliable sequence by covering the genome four times over. It had settled on a close relative of the Cavendish with only two sets of chromosomes. "Everyone cheered wildly," says Markham. But there was a catch: The French National Research Agency (ANR) would fund the project only with help from an international partner. When JGI subsequently passed on the banana, "the whole thing looked like it would unravel," Markham says.

Now Quétier, who recently became a program coordinator in genomics at ANR, says

the agency is about to announce that it will fund the project anyway—and that it plans to sequence the entire genome. "We are at the beginning of the story," he says. "I'm very optimistic."

James Dale can't wait. A banana biotechnologist at the Queensland University of Technology in Brisbane, Australia, Dale has been trying to develop a better banana for 12 years through genetic modification. Once the sequence reveals the full range of genes in banana, he says, biotechnologists like him will be a step

closer to using the banana's own genes to, say, boost disease-resistance.

That's not all. With the sequence, basic researchers can do comparative genetics with other crops and figure out how bananas got so strange in the first place. Even traditional breeders like Aguilar Moran will benefit: Molecular markers found in the genome will help them home in on traits of interest and better select varieties for crossing. "A tremendous amount of information will come out of this," says Dale.

Frison is also optimistic. As he did in 2001, he's predicting that the banana genome is within reach—and with it a brighter future for the fruit. "We've reached a turning point," he says. Bristow thinks that Frison might be right this time. "Once you've got a little bit of data, it starts to get interesting," he says. "Nothing rallies a community like some progress."

—DAVID GRIMM



LETTERS

edited by Jennifer Sills

European Union and NIH Collaborate

THE NATIONAL INSTITUTES OF HEALTH (NIH) AND THE EUROPEAN Commission (EC) recently decided to reinforce our mutual interest in scientific collaboration. We believe that greater trans-Atlantic cooperation and smarter competition in science will lead to faster breakthroughs in health research and ultimately to a better quality of life for the citizens of the world.

The NIH has a long tradition of funding collaborations between U.S. and European scientists. To this end, the NIH recently clarified its policies for funding global collaborations (1). And on 3 September 2008, the European Commission published a new call for proposals within the health theme of its Seventh Framework Programme for Research and Development (2). For the first time, the EC has announced that researchers working in U.S. institutions are

eligible not only to participate in EC-supported research projects but also to receive funds from the EC if they are part of a consortium with European Union (EU) investigators.



Partners. Former NIH Director Elias Zerhouni (left) and European Commissioner for Science and Research Janez Potočnik (right) make their new collaboration official.

We live at a time of great scientific opportunity, where global collaborations are essential for facilitating scientific discoveries aimed at improving public health. As science has become more complex, so has the need for both specialization and multidisciplinary approaches to problem-solving. While discovery increasingly depends on a new level of collaboration, it also depends on expertise, which may not reside within one country or even within one continent. A prime example of global collaboration is the tremendously successful Human Genome Project, which reached its goals ahead of time and under budget. Similarly, global collaboration is essential to the conduct of clinical trials and genetic research, where disease prevalence in a given region enables research that could otherwise not be conducted in the confines of a single country.

We hope that our initiative, aimed at opening our research programs, will serve as a launch pad for wider and more intense U.S.-EU cooperation in health as well as in other areas of research. This is a historic step for our institutions today, and we are confident that it will also prove to be a significant step for the future of science.

ELIAS A. ZERHOUNI¹ AND JANEZ POTOČNIK²

¹Former Director, National Institutes of Health, Bethesda, MD 20892, USA. E-mail: zerhoune@mail.nih.gov. ²European Commissioner for Science and Research, Science and Research European Union, European Commission, Brussels B-1049, Belgium. E-mail: janez.potocnik@ec.europa.eu

References

1. Updates and Reminders on NIH Policy Pertaining to Grants to Foreign Institutions, International Organizations and Domestic Grants with Foreign Components (<http://grants.nih.gov/grants/guide/notice-files/NOT-OD-09-010.html>).
2. Seventh Research Framework Programme (<http://cordis.europa.eu/fp7/dc/index.cfm>).

Skeptical of Assisted Colonization

O. HOEGH-GULDBERG *ET AL.* ("ASSISTED COLONIZATION and rapid climate change," Policy Forum, 18 July, p. 345) outlined a decision-tree framework for conservationists to use when considering the fate of species endangered by climate change. Although the likelihood of species extinction may require consideration of drastic action, there are several reasons to be skeptical of the assisted colonization proposal: (i) A number of within-continent or within-geographic region introductions, including intentional ones, have proved calamitous for the recipient ecosystem (1–3). (ii) Other short-distance, regional-scale incursions across

breached biogeographic barriers have also had negative consequences [such as the migration of marine species across the Suez Canal that is known as the Lessepsian migration (4)]. (iii) A potential recipient area would have to be deemed of much lesser conservation value than the (single) species being assisted. Such a decision would be the antithesis of the flagship species approach currently adopted by conservationists. (iv) The resilience of a recipient region, already experiencing climate-induced stress itself, is unlikely to be assisted or enhanced by an introduced species. (v) The extent of knowledge required to provide detailed scientific understanding of the potential consequences of assisted colonization should not be underestimated; there are good reasons for bioinvasion ecologists to avoid

experiments that require introducing potentially invasive propagules to uninfected areas, and regulations require secure retention of non-native propagules for laboratory experiments. (vi) There already exists an approach to assist the persistence of endangered species: collaborative captive breeding programs of zoos and wildlife parks.

Any strategy to combat the negative impacts of a global phenomenon like climate change requires comprehensive frameworks. A species-by-species approach such as assisted colonization may be an overwhelming endeavor and is likely to encounter insurmountable policy conflicts between proponents and recipient regions. Such large-scale, manmade interference with species distributions in the wild does not have a glorious history and may prove a step too far as

CREDIT: MICHAEL SPENCER/NIH



HIV's dynamic
transcriptase

1059



Degradation
parallels

1062

a hedge against extinction.

IAN DAVIDSON¹* AND CHRISTINA SIMKANIN²

¹Aquatic Bioinvasion Research and Policy Institute, Portland State University and Smithsonian Environmental Research Center, Portland, OR 97207, USA. ²Department of Biology, University of Victoria, Victoria, BC V8W 3N5, Canada.

*To whom correspondence should be addressed. E-mail: idavidso@pdx.edu

References

1. S. J. Kupferberg, *Ecology* **78**, 1736 (1997).
2. J. D. Olden *et al.*, *Biol. Invasions* **8**, 1621 (2006).
3. J. M. Mueller, J. J. Hellmann, *Conserv. Biol.* **22**, 562 (2008).
4. B. S. Galil, *Biol. Invasions* **2**, 177 (2000).

Assisted Colonization Won't Help Rare Species

THE POLICY FORUM "ASSISTED COLONIZATION and rapid climate change" (O. Hoegh-Guldberg *et al.*, 18 July, p. 345) spells hope for our attempt to avert the worst of today's climate-induced extinction crisis. Unfortunately, the framework that the authors proposed and the discussions preceding this (1, 2) have oversimplified the process of assisted colonization. Species in need of such an intervention are often uncommon or rare and may be understudied. Introducing them to new locations may help them keep up with climate change, but most of the other threats they have been facing (such as disease and poaching) are not likely to be left behind (3, 4). These may even be exacerbated when species are moved across national boundaries; distinct systems of governance and management can impede conservation efforts (5). As a result, the number of threatened species that qualify for such a measure is likely low.

Indeed, data from the Report "One-third of reef-building corals face elevated extinction risk from climate change and local impacts" (K. E. Carpenter *et al.*, 25 July, p. 560) show precisely that. Of the 231 coral species listed in threatened categories, 186 (81%) are rare or uncommon. Worse still, we have virtually no fundamental knowledge on the biology of 70% of these corals, complicating the decision to translocate them. Moreover, at least 35 of them are harvested for the coral trade (more than 1000 pieces per year). It would be hard to imagine that

assisted colonization will improve their fate. I urge caution in committing species to such movements until we are fairly confident that this will do more good than harm.

DANWEI HUANG

Scripps Institution of Oceanography, University of California, San Diego, La Jolla, CA 92093, USA, and Department of Biological Sciences, National University of Singapore, 117543, Singapore. E-mail: huangdanwei@ucsd.edu

References

1. M. L. Hunter, *Conserv. Biol.* **21**, 1356 (2007).
2. J. S. McLachlan, J. J. Hellmann, M. W. Schwartz, *Conserv. Biol.* **21**, 297 (2007).
3. C. K. Dodd Jr., R. A. Seigel, *Herpetologica* **47**, 336 (1991).
4. T. D. Steury, D. L. Murray, *Biol. Conserv.* **117**, 127 (2004).
5. G. H. Copp *et al.*, *J. Appl. Ichthyol.* **21**, 242 (2005).

Where Species Go, Legal Protections Must Follow

THE POLICY FORUM "ASSISTED COLONIZATION and rapid climate change" (O. Hoegh-Guldberg *et al.*, 18 July, p. 345) proposes moving species outside their historic range to mitigate biodiversity loss induced by climate change. However, this approach will be successful only if legal policies, especially the implementation of the Endangered Species Act (ESA), change as well. Establishing a new population requires both availability of adequate habitat and strong legal protection.

Policy-makers should recognize that areas predicted by bioclimatic models to be the most suitable for a species in the long term should now be considered "essential for conservation" under ESA section 3 and therefore designated as critical habitat. This should occur even if these areas are not currently suitable for the

species. Designation of new populations established by assisted colonization as "experimental" under ESA section 10(j) should be avoided; this provides weaker protection than exists for naturally occurring populations and will ultimately jeopardize the populations most critical to a species' long-term survival (1).

GUILLAUME CHAPRON* AND GUSTAF SAMELIUS

Grimso Wildlife Research Station, Swedish University of Agricultural Sciences, Riddarhyttan 73091, Sweden.

*To whom correspondence should be addressed. E-mail: gchapron@carnivoreconservation.org

Reference

1. J. Kostyack, D. Rohlf, *Environ. Law Report.* **38**, 10203 (2008).

Response

THE LETTERS IN RESPONSE TO OUR POLICY FORUM highlight many of the risks and consequences of making bad decisions, the logical consideration of which is the focus of our decision framework. The robust risk assessment framework we propose includes assisted colonization as one option among the full array of other strategies available to ecosystem managers.

Davidson and Simkanin correctly note that there are serious risks associated with ill-conceived assisted colonization, including the effects on source populations and the impact of translocated organisms at their destinations, which we mentioned in our Policy Forum. It is true that some short-distance translocations will be ill advised for recipient ecosystems and human communities, but the literature indicates that this risk escalates as organisms and ecosystems become more divergent. Evidently, there is no single strategy that will work across the board for all taxa, ecosystems, and regions. This is why we presented a decision framework rather than a prescription. The decision framework allows risks and benefits to be reviewed systematically, prior to any attempt to move species, communities, or ecosystems in response to climate change.

Neither Davidson and Simkanin nor Huang acknowledge that the risks of action must be balanced against the risks of inaction, which have frequently been high. During past periods of major climate shifts (changes of 6° to 10°C), the Earth experienced massive changes to the distribution and abundance of its biological systems. Recent temperature increases in many parts of the world exceed those seen during previous shifts (1). Redistribution in the modern world is also curtailed by human-dominated landscapes, which severely limit the total area of suitable natural habitats and create barriers to disper-

Letters to the Editor

Letters (~300 words) discuss material published in *Science* in the previous 3 months or issues of general interest. They can be submitted through the Web (www.submit2science.org) or by regular mail (1200 New York Ave., NW, Washington, DC 20005, USA). Letters are not acknowledged upon receipt, nor are authors generally consulted before publication. Whether published in full or in part, letters are subject to editing for clarity and space.

sal and migration. Even though the risks of translocation may be prohibitive in most situations, to ignore this option as species, communities, or ecosystems dwindle to extinction is not an option. Our framework systematically examines the advantages and risks of assisted colonization along with the full suite of other conservation options.

We agree with Chapron and Samelius that policy must be developed to recognize the importance of future habitats for organisms in a world that is changing from decade to decade. Equally important is the necessity for developing new policies that provide protection for newly transferred colonies, especially given that these are intended to be long-term as opposed to experimental translocations. Without the rapid evolution of policy in concert with innovative biological solutions, attempts to move species and communities to new locations ahead of climate change will be doomed to failure.

OVE HOEGH-GULDBERG,^{1*}

LESLEY HUGHES,² SUE MCINTYRE,³

DAVID B. LINDENMAYER,⁴ CAMILLE PARMESAN,⁵

HUGH P. POSSINGHAM,⁶ CHRIS D. THOMAS⁷

¹Centre for Marine Studies, Australian Research Council Centre for Excellence in Reef Studies and the Coral Reef Targeted

Research Project, The University of Queensland, St Lucia, QLD 4072, Australia. ²Department of Biological Sciences, Macquarie University, NSW 2109, Australia. ³Australian Commonwealth Scientific and Industrial Research Organisation (CSIRO) Sustainable Ecosystems, Post Office Box 284, Canberra, ACT 2601, Australia. ⁴Fenner School of Environment and Society, The Australian National University, Canberra, ACT 0200, Australia. ⁵Department of Integrative Biology, University of Texas, Austin, TX 78712, USA. ⁶The Ecology Centre, Centre for Applied Environmental Decision Analysis, The University of Queensland, St Lucia, QLD 4072, Australia. ⁷Department of Biology, University of York, Post Office Box 373, York YO10 5YW, UK.

*To whom correspondence should be addressed. E-mail: oveh@uq.edu.au

Reference

- O. Hoegh-Guldberg *et al.*, *Science* **318**, 1737 (2007).

TECHNICAL COMMENT ABSTRACTS

COMMENT ON "Ancient Asteroids Enriched in Refractory Inclusions"

Dominik C. Hezel and Sara S. Russell

Sunshine *et al.* (Reports, 25 April 2008, p. 514) reported that certain asteroids contain 30 ± 10 volume percent calcium- and aluminum-rich inclusions (CAIs). We contend that the amount of CAIs in CV chondrites is two to three times as low as the 10 volume percent assumed by

the authors; thus, we question whether the CAI-rich bodies they studied are indeed older than known asteroids or formed before the injection of ²⁶Al into the solar nebula.

Full text at www.sciencemag.org/cgi/content/full/322/5904/1050a

RESPONSE TO COMMENT ON "Ancient Asteroids Enriched in Refractory Inclusions"

J. M. Sunshine, H. C. Connolly Jr., T. J. McCoy, S. J. Bus, L. M. La Croix

Although the exact abundance of phases in carbonaceous chondrites remains debatable, a potentially lower absolute abundance of calcium- and aluminum-rich inclusions (CAIs) in the Allende meteorite does not change our fundamental conclusion. In a relative comparison, CAI-rich asteroids contain two to three times as many CAIs as the most CAI-rich meteorites. These asteroids are therefore greatly enriched in the earliest solar system materials and remain enticing targets for future exploration.

Full text at www.sciencemag.org/cgi/content/full/322/5904/1050b

CORRECTIONS AND CLARIFICATIONS

News of the Week: "Chinese cave speaks of a fickle sun bringing down ancient dynasties" by R. A. Kerr (7 November, p. 837). The stalagmite sample analyzed was 0.12 meters long, not 1.2 meters long as reported.

FREE
with registration

Science Alerts in Your Inbox

Get daily and weekly E-alerts on the latest breaking news and research!

Science News This Week
Brief summaries of the journal's news content

ScienceNOW Weekly Alert
Weekly headline summary

Science Express Notification
Articles published in advance of print

Science Posting Notification
Alert when weekly issue is posted

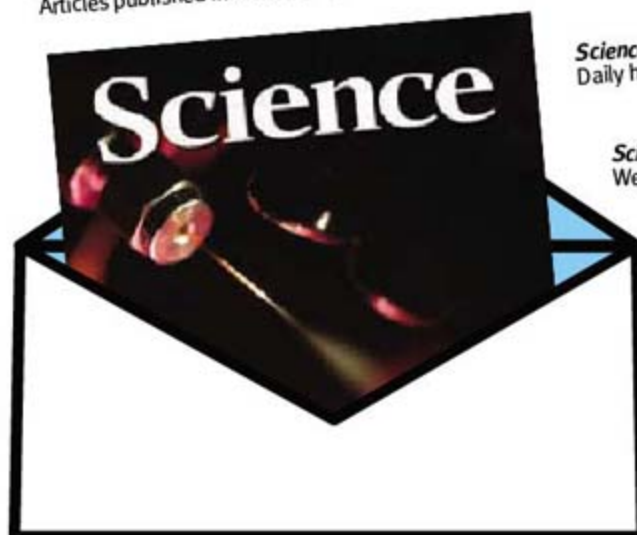
ScienceNOW Daily Alert
Daily headline summary

Science Magazine TOC
Weekly table of contents

Science Signaling TOC
Weekly table of contents

Editors' Choice
Highlights of the recent literature

This Week in Science
Summaries of research content



Get the latest news and research from *Science* as soon as it is published. Sign up for our e-alert services and you can know when the latest issue of *Science* or *Science Express* has been posted, peruse the latest table of contents for *Science* or *Science Signaling*, and read summaries of the journal's research, news content, or Editors' Choice column, all from your e-mail inbox. To start receiving e-mail updates, go to:

sciencemag.org/ema



PALEONTOLOGY

Reading Behavior from the Rocks

Sören Jensen

Adolph Seilacher has made substantial contributions to sedimentology, taphonomy, functional morphology, and more recently to the interpretation of Ediacara-type fossils, but it is with ichnology (the study of trace fossils) that his name is most closely associated. Trace fossils—burrows, tracks, trails, and other evidence of organism-sediment interactions preserved in the rock record—are unique in that they can provide direct evidence of how animals lived millions of years ago, sometimes recording events lasting a few minutes or less. No one has been quite so successful in bringing trace fossils to life as Seilacher, and the long-anticipated *Trace Fossil Analysis*, which grew out of courses he gave at Tübingen University, offers an excellent introduction to his approach.

One of the book's plates includes a Sherlock Holmes-like silhouette. This is a reasonable allusion to Seilacher's ability to recreate a scenario of trace producer and behavior on the basis of evidence that may at first seem unpromising—for example, in deducing the “adventures of an Early Cambrian trilobite” from faint scratches on a bedding plane. Seilacher's ichnological publications span half a century and have played a large role in shaping the field. They are characterized by an economic and precise prose, also found in the book, but more than anything else what sets them apart are his drawings. It is therefore fitting that Seilacher structured *Trace Fossil Analysis* around his sketches and diagrams of distinctive and representative ichnogenera. These are arranged in 75 plates, each accompanied by about one page of text (“in the form of extended captions”). The plates and text are grouped into chapters with titles such as “Burrows of Short Bulldozers,” “Deep-sea Farmers,” and “Cruziana Stratigraphy.” Through his discussions of informative examples, Seilacher addresses such topics as the application of trace fossils in environmental studies, the study of trilobite trace fossils, and the analysis of deep-sea trace fossils.

Readers already acquainted with Seilacher's

publications will find much that is familiar, but the book also contains a number of new illustrations and the text is sprinkled with fresh insights and thoughts. For example, the section examining the evidence for pre-Ediacaran trace fossils includes images and discussion of the 1.7-billion-year-old (1.7-Ga) Sterling biota of western Australia (1). Here Seilacher also mentions a new take on the Chorhat “worm burrows” (circa 1.5 Ga) from India. He now suggests foam menisci as an alternative to his earlier interpretation (2) that these structures were made by wormlike animals even though they are much older than the presumed origin of metazoans.

In a text as wide-ranging as this, there are of course details with which not everyone will agree. One such instance appears in the chapter “Pseudo-Traces,” where Seilacher interprets *Protospiralichnus* from the Early Cambrian of Siberia as a system of concentric microfaults. Having had the opportunity to examine this material in Moscow, I agree with the original interpretation of this structure as a trace fossil resulting from concentrated cir-

cling motion (a type of trace fossil commonly known from Cambrian strata as “*Taphrhelminthopsis*” circularis).

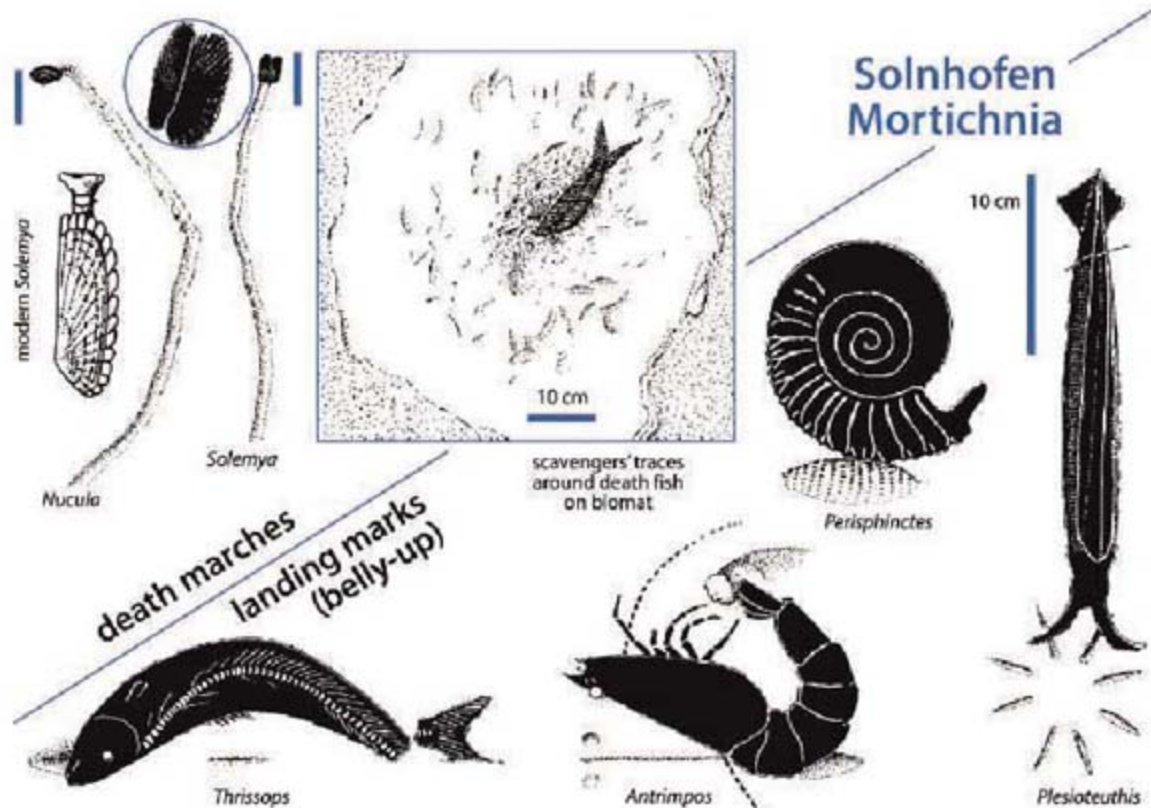
In the preface, Seilacher explains that the book is not intended to be a comprehensive text on ichnology. Instead, he aims for it to encourage the training of observational skills and of a “method of morphological thinking in terms of processes that could easily be transferred to any other subject matter.” Nevertheless, the book will prove an indispensable aid to anyone teaching trace fossils at the university level. To that end, the annotated reference lists occurring at regular intervals throughout the book will be quite helpful. The emphasis is heavily on the trace-making activity of marine invertebrates in soft sediments, but there are also sections on vertebrate traces and on various sedimentary structures that might mistakenly be attributed to the activity of organisms. Seilacher includes the majority of the more common and meaningful ichnogenera, although the naming of trace fossils is not an important theme of the book. (It should also be noted that the criteria for defining ichnotaxa vary widely among different trace fossil workers.) The author does not treat trace fossils on hard substrates, and he refers readers to other sources for discussion on ichnofabrics—the broader look at the sediment structure resulting from bioturbation and an increasingly important branch of trace fossil analysis over the past several decades.

Trace Fossil Analysis will be cherished by ichnologists, even though they already know what to expect. But it will be particularly

Trace Fossil Analysis

by Adolf Seilacher

Springer, Berlin, 2007.
240 pp. \$69.95, £38.50.
ISBN 9783540472254.



Solnhofen stories. Many of the biogenic structures in the Upper Jurassic lithographic limestones from southern Germany record “the last movements (or even postmortem convulsions) of the trace makers preserved together with them.”

The reviewer is in the Área de Paleontología, Facultad de Ciencias, Universidad de Extremadura, 06071 Badajoz, Spain. E-mail: soren@unex.es

handy to nonspecialists, who may not have the time, wish, or opportunity to track down Seilacher's original publications (some of which are in hard-to-find volumes). Nonspecialists should, however, keep in mind that such are the communicative powers of Seilacher's drawings and text that one can easily forget that these are interpretations—albeit ingenious ones and probably more often than not correct. This stimulating book documents the wonders that can be achieved by the eye and pen of a fertile mind.

References

1. B. Rasmussen, S. Bengtson, I. R. Fletcher, N. J. McNaughton, *Science* **296**, 1112 (2002).
2. A. Seilacher, P. K. Bose, F. Pflüger, *Science* **282**, 80 (1998).

10.1126/science.1166220

SCIENCE POLICY

What Can Science Do for the President?

Gregory A. Good

Consider a tale of two United States presidents and their approaches to science policy advice. The first preferred advisers who honestly disagreed with him and with each other, but who advised him with the best interests of the country at heart. The second preferred advisers who told him what he wanted to hear. The first preferred advisers who were skeptical of technological fixes; the second, advisers who thought technology could answer most challenges. The first preferred advisers with backgrounds in academia; the second, advisers from industry. The first president doubted the advice of ideologues and religionists; the second used their advice to form science policy on issue after issue. The first respected free and open debate; the second formed policy behind closed doors and presented carefully censored reports to the public.

The second U.S. president above is clearly George W. Bush. Readers may be surprised, however, to find that the first is General Dwight David Eisenhower, who in 1957 estab-

The reviewer is at the Department of History, West Virginia University, Morgantown, WV 26506-6303, USA. From January 2009, he will be at the Center for History of Physics, American Institute of Physics. E-mail: greg.good@mail.wvu.edu

lished the President's Science Advisory Committee (PSAC).

Zuoyue Wang's *In Sputnik's Shadow: The President's Science Advisory Committee and Cold War America* reminds us in rich detail of various ways in which U.S. presidents, especially in the mid- and late 20th century, have obtained advice on science. Wang (a historian at California State Polytechnic University, Pomona) focuses on the period from the Eisenhower administration to that of Richard Nixon but glances backward and forward. Despite these glances, his book is neither a prescription nor a diatribe but rather a careful and nuanced historical analysis. Readers looking for simple answers to where American science policy should go next need to look elsewhere. In Wang's book they will instead find a fully developed and complex historical analysis.

Eisenhower created PSAC in the midst of the Cold War, soon after the Soviet Union's October 1957 launch of Sputnik. Eisenhower charged the committee with advising him mainly on science and technology relevant to defense and nuclear weapons—or more to the point, relevant to arms control. Presidents before Eisenhower had sought advice from scientists, through either the National Academy of Sciences or ad hoc arrangements, but PSAC was intended to regularize the process. In addition, during World War II the Office of Scientific Research and Development, the Radiation Lab, and the Manhattan Project had fundamentally altered the culture of physics in the United States.

A recurrent theme throughout the book concerns the dual nature of science in American politics: science in policy versus policy for science. This seemingly cryptic phrase has a simple, direct meaning. Presidents realize that to forge policies regarding defense, energy, etc., government needs competent advice about science and technology, and PSAC provided such expert advice. Scientists have another interest, namely the funding and promotion of their research and their institutions. As Wang encapsulates the distinction: what can science do for the government versus what can government do for science? PSAC scientists recognized that these two perspectives are inextricably linked, and committee members often linked the country's



After Sputnik. Lee DuBridge (second from the left) and Vice President Richard Nixon hold a model of Explorer 1 at Caltech's Jet Propulsion Laboratory (1958). DuBridge would later serve as Nixon's science adviser to the president.

policy interests with the self-interest of their science. Aware of the distinction, Wang narrates many efforts of PSAC to “blur the boundary.”

Wang also emphasizes the balance that PSAC scientists tried to maintain between technological enthusiasm and technological skepticism. They insistently included technological limitations, environmental and social risks, and policy implications in their analyses—as in those regarding nuclear-powered airplanes, the supersonic transport, antiballistic missiles (ABM), and pesticide use. Wang notes “theirs was not an argument against technology, but one for appropriate technology, for a broadened concept of technological rationality that encouraged technological development not for its own sake but for its benefits in achieving social, political, cultural, and economic goals in a democratic society.”

The demise of PSAC came during the Nixon years, in large part through tensions magnified by the ABM debate. Nixon first distanced himself from his science adviser, Lee DuBridge, and ultimately, just weeks after the 1972 election, decided to dissolve the Office of Science and Technology and with it the committee. The decision then took six months to be finalized. As Wang suggests, PSAC's closing occurred at least in part because Nixon did not want the broader technological rationality that previous presidents had favored. He resented disagreement from his advisers.

Wang provides the scientific community and policy-makers with a most timely reminder of the positive roles that scientists can play in an open society. We can only hope that Barack Obama will turn a page and not let ideology, personal beliefs, or party politics interfere with his seeking of sound science advisement. *In Sputnik's Shadow* offers a history that both policy-makers and scientists should heed well.

10.1126/science.1165661

OCEANS

Smithsonian Swims in New Direction

Lekelia D. Jenkins

Although many factors led me to become a marine scientist, one was definitely the Smithsonian Institution's National Museum of Natural History (NMNH). I fondly remember childhood class trips to the aging marine hall. The exhibition was dim and musty, but the sheer wealth of knowledge held there made each visit a fresh and educational experience (even as an adult). I wondered whether the Sant Ocean Hall has the depth of knowledge to inspire a new generation of scientists as the earlier displays had inspired me.

Rare and wondrous but smaller than life serves as a good description of not only the giant squid highlighted in the new hall but also the exhibit itself. Although the display of two giant squid specimens is indeed worth seeing, the preserved quality of these fascinating and elusive creatures is disappointing. A plaque above the slightly decayed carcass of the larger, 7.3-m-long specimen explains that it has shrunk as a result of preservation and is substantially smaller than its original size.

Likewise, the heralded ocean-themed hall—a first for the Smithsonian—does not quite meet heightened expectations. The Smithsonian raised \$80 million for the ambitious project, including \$22 million from the National Oceanic and Atmospheric Administration (NOAA), the exhibit's cosponsor. At over 2100 m², the Ocean Hall is the NMNH's largest permanent exhibition. Nonetheless, it can display only a small portion of the Smithsonian's 30 million specimens of ocean organisms (the largest marine collection in the world). The material is organized around the themes of how the ocean has changed over time and how marine ecosystems vary across habitat types. Using 30 "human connections" stories (which are linked to critical ocean issues), the exhibit also attempts to show visitors that "the ocean is a global system essential to all life—including yours." However,

The reviewer is a AAAS Science and Technology Policy Fellow (http://fellowships.aaas.org/03_Directory/03_List_AZ.shtml#), 1220 East-West Highway, #216, Silver Spring, MD 20910, USA. E-mail: kiki.jenkins@gmail.com. The views expressed are the reviewer's own and do not represent those of any supporting organization.

because there is no clear path through the exhibit and the pithy signage is disparate and often poorly placed, the themes break down and the displays are incongruous.

The Ocean Hall incorporates a number of interactive video components that curators can update through the expected 30-year lifetime of the exhibit.

Sant Ocean Hall

Carole Baldwin, Sharon Katz Cooper, Brian Huber, Jill Johnson, Elizabeth Musteen, and Michael Vecchione, Exhibit Team

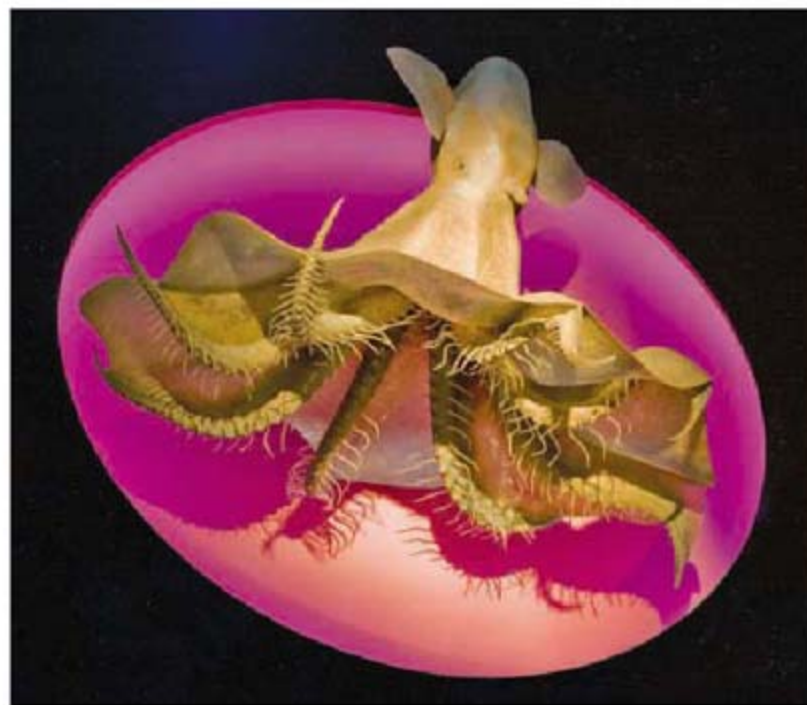
National Museum of Natural History, Smithsonian Institution, Washington, DC.
http://ocean.si.edu/ocean_hall/

For instance, one interactive kiosk simulates ocean management, allowing visitors to manipulate parameters such as fishing controls, aquaculture controls, and monitoring and then see the effects of their decisions on the ecosystem and stakeholders. The most frequently updated part of the hall will be the two Ocean Today Kiosks, video displays that offer visitors captivating two-minute summaries on a variety of contemporary ocean topics. These well-conceived kiosks, maintained by NOAA, will be regularly refreshed with new videos (30 story lines are currently in production), and they will soon feature a ticker-type crawl with the latest ocean news. But because they have poorly functioning directional speakers and are situated in an obstructed corner, the kiosks probably will not be able to shoulder the duty of keeping the entire Ocean Hall timely and relevant.

Visitors will be entertained by some impressive marvels, such as a living coral reef and a 14-m-long replica of Phoenix, a particular North Atlantic right whale, *Eubalaena glacialis*. The 1500-gallon coral aquarium houses fish, live coral, anemones, and other organisms that were all grown in captivity or collected in a sustainable manner. Visitors also cluster in engaging areas such as the Global Ocean Systems gallery. In this room, an animated six-foot sphere aptly tutors viewers on complex oceanic processes, such as the formation of the continents.

But these attractions are small islands of excitement in a sea of last-century displays of fossils, corpselike models, and pale dead fish in

jars that museum-goers quickly pass. These attempts to incorporate the museum's extensive collection into the hall are disharmonious anachronisms, given the technological scaffold of the exhibit. A video or interactive program could help visitors place the specimens within the larger conceptual context of the display and understand the value of preserved specimens to science. By presenting more actively posed models (such as the exquisite model of a dumbo octopus, *Cirrothauma magna*, with tentacles coiled in midpropulsion), the exhibit could have worked in aspects of the biomechanics of marine organisms. Also, the designers might have borrowed from one of the best aspects of the museum's Mammal Hall, the use of specimens in lifelike assemblages to communicate ecological information. For example, grouping of models or specimens could have provided insight into food webs. The implicit as well as explicit imparting of information would have added depth to the exhibit, making it more appealing to a wider audience.



Model display. The dumbo octopus *Cirrothauma magna*.

By far the highlight of the entire hall is the Ocean Explorer Theater. Here, in a video with vivid cinematography, a diverse cast of scientists describes with sincere awe their experience of discovery as they descend to the sea floor in a deep-sea submersible. The video moved me on an emotional level, reaffirming both why I love being a marine scientist and the powerful draw of the deep blue as our last natural frontier. I have no doubt that the theater and other effective parts of the exhibit will help inspire the next generation of marine researchers. The Sant Ocean Hall, although not all that I had anticipated, is still rare and wondrous.

10.1126/science.1167002

RESEARCH ETHICS

Certificates of Confidentiality and Compelled Disclosure of Data

Laura M. Beskow,^{1,2*} Lauren Dame,^{2,3} E. Jane Costello⁴

Ethical principles and professional codes of conduct require that researchers protect research participants' privacy, as well as the confidentiality of their data (1, 2). Certificates of Confidentiality are intended to help meet these obligations by preventing forced disclosure of identifiable data during legal proceedings (3). A recent case indicates that the protection Certificates offer is uncertain.

Certificates are authorized by federal law and granted by units of the U.S. Department of Health and Human Services for research collecting information that, if disclosed, could have adverse consequences or damage subjects' financial standing, employability, insurability, or reputation. The current law states that with a Certificate, "persons engaged in biomedical, behavioral, clinical, or other research ... may not be compelled in any Federal, State, or local civil, criminal, administrative, legislative, or other proceedings to identify such individuals" (4).

Although Certificates are commonly believed to offer "nearly absolute privacy protection" (5), there is a remarkable paucity of evidence on which to base such conclusions. In one of the only reported court opinions, *People v. Newman* (6), a Certificate successfully prevented disclosure of the identities of participants in a drug treatment program despite a grand jury subpoena in a murder investigation. Both sides in this case assumed that confidentiality protections granted under the law were absolute; the dispute focused on whether other legislation (7) repealed these protections. The Court held that the other legislation did not do so, but provided little analysis of the scope of a Certificate's protections.

We describe a criminal case that

reached the North Carolina Court of Appeals, in which research data collected under a Certificate were subpoenaed by the defense in an attempt to impeach the credibility of a prosecution witness. The outcome raises concerns about the protections Certificates provide and has implications for research that depends on participants' confidence that sensitive information will be protected.

Case Presentation

In the early 1990s, Duke University Health System (DUHS) researchers began a longitudinal study of psychiatric disorders and the need for mental health services among rural and urban youth (the "Study"). Researchers obtained a Certificate from the National Institute of Mental Health because they planned to gather information about psychosocial adversities, substance abuse, illegal behaviors, and genetic traits.

The challenge to the Study's Certificate arose in 2004 from a criminal proceeding in which the defendant was charged with indecent liberties with a minor and statutory rape. His attorney believed that a prosecution witness was a Study participant and requested a court order directing DUHS to supply all Study records about the witness. The court granted this request, noting that the defendant was entitled to the records for any exculpatory evidence they might contain. Although the order directed that the records remain confidential unless used at trial or sentencing, it allowed them to be read by the state's chief investigating officer, the witness, the District Attorney's office staff, the defendant and his wife, the Public Defender's office staff, the Assistant Public Defender, and any expert the defendant or state might consult (8).

The judge issued this order without knowledge of the Certificate; DUHS first learned of the attempt to obtain Study records upon receiving the subpoena. DUHS filed a motion for a protective order, asserting that the records were protected by

A recent court case suggests that the privacy of research subjects may not be fully protected by Certificates of Confidentiality.

a Certificate and should not be disclosed. DUHS also argued that the person whose records were sought was not the alleged victim; therefore, Study records were unlikely to contain exculpatory evidence. DUHS took no position regarding whether the witness was a Study participant. On the basis of its review of the motions, an affidavit from the Principal Investigator (PI), and arguments made at the hearing, the court vacated its initial order and granted DUHS' motion, but instructed DUHS to maintain a sealed copy of the records until the final resolution of the case.

A review of the hearing transcript (9) shows that the judge regarded the defendant's request to access Study records as a routine discovery motion and was unfamiliar with Certificates. He told DUHS that he had not realized "what kind of egg [he was] cracking open," but "obviously it had lit a fire under somebody." Further, although DUHS and the PI argued the critical importance of upholding the Certificate, the

The full legal effect of Certificates of Confidentiality remains unclear.

judge seemed most swayed by the argument that the defense was unlikely to find exculpatory evidence. Thus, despite the Certificate, the court weighed other interests and issued the protective order only after deeming the defendant's reasons for seeking the records insufficient.

The defendant was tried and convicted of all charges. Months later, the defendant's appellate lawyer filed a motion requesting access to the sealed records. A hearing was held before the same judge. This time, however, he ordered that the records be given to defense counsel and shared with the state, suggesting that it would be puzzling to ask the appellate court to decide if the records were relevant when the defense attorney arguing their relevance had never seen them (10). Arguments based on their contents could only be made in a separate sealed brief.

DUHS filed a notice of appeal, asserting

¹Duke Translational Medicine Institute, Duke University, Durham, NC 27710, USA. ²Duke Institute for Genome Sciences and Policy, Duke University, Durham, NC 27708, USA. ³Duke University School of Law, Durham, NC, 27708, USA. ⁴Developmental Epidemiology Program, Department of Psychiatry and Behavioral Sciences, Duke University Medical Center, Durham, NC 27710, USA.

*Author for correspondence. E-mail: laura.beskow@duke.edu

the Certificate and citing *People v. Newman* as particularly relevant, arguing that participants “must be given genuine assurances of confidentiality for investigators to obtain candid, meaningful, and wide participation in the study” (11). DUHS also argued that the defendant had failed to show that the documents were relevant to his defense. Pursuant to the court order, however, DUHS delivered the documents to the defendant’s appellate counsel.

The defendant’s brief contained a sealed appendix based on the Study records. In the unsealed portion, the defendant argued that *Newman* did not govern this situation because “[*Newman*] involves the State seeking information for use in a criminal prosecution as opposed to [this] case which involves a criminal defendant who has been afforded the Constitutional right to due process and confrontation to gain favorable and material information for his defense” (12). After hearing from DUHS and defense counsel, the Court of Appeals concluded that the Study records were not material. It vacated the order granting defense counsel access, but confidentiality had already been compromised. The Court specifically declined to consider DUHS’ argument that the confidentiality of the records was statutorily privileged (13) and, thus, failed to address whether the Certificate would have protected the records, had they been material to the defendant’s case.

Discussion

Certificates have gained prominence over the past decade. In 2002, the National Institutes of Health (NIH) announced a new policy encouraging broader use of Certificates (14). The National Cancer Institute recommends that biorepositories consider obtaining a Certificate (15), and NIH suggests as part of its data-sharing policy that Certificates be obtained for genome-wide association studies (16, 17).

Given such reliance on Certificates, their effectiveness in preventing forced disclosure deserves rigorous evaluation. Because the U.S. case law system relies heavily on precedent, attorneys and judges will review previously decided cases when considering how to handle future legal demands for research data. In the case presented here, the Certificate helped convince the court, after vigorous legal intervention, to refrain from ordering broad disclosure of Study records, permitting instead restricted disclosure to attorneys for use under seal, but did not provide absolute protection. This highlights

several important issues.

First, requests for research data may arise from legal proceedings unrelated to a study’s focus. A PI or institution may unexpectedly receive a subpoena and need swiftly to engage a lawyer with appropriate expertise. When notified of a Certificate dispute, the Office of the NIH Legal Advisor provides citation to the statute and case law of which it is aware, but does not ordinarily involve itself in third-party litigation or provide legal advice to non-NIH entities.

Second, a Certificate is granted to the research institution, not the PI, and their interests may not be identical. In this case, the PI felt a moral obligation to protect participants’ data; DUHS agreed and was willing to go to court. But an institution could decide that a costly legal battle is unwarranted or might be unwilling to defy court-ordered disclosure, even if the PI wants to do so.

Third, seeking to enforce a Certificate may result in some disclosure, even if data are not released. For some research, simply revealing the fact of a person’s participation could itself cause adverse consequences. But institutions or investigators who refuse to follow a court order may be found in contempt, resulting in fines or imprisonment.

Fourth, parties in both criminal and civil lawsuits have rights to obtain material relevant to their case. Courts have broad powers to enforce these rights, and they attempt to resolve disputes by balancing each side’s interests. When doing so, courts may give insufficient weight to society’s interest in protecting research records. Further, when the attempt to obtain study records comes from a criminal defendant, a Certificate may be especially vulnerable if the records could affect a defendant’s Constitutional rights to a fair trial or to confront and cross-examine witnesses. In this case, the court did not find that the facts implicated these rights, but a future case could raise the key question of when a defendant’s Constitutional rights overcome the statutory protection offered by a Certificate. Finally, attempts by the government itself to obtain study records may raise particularly difficult challenges if the records are considered relevant to “national security.” Since 9/11 and the passage of the Patriot Act (18), government agencies claim increasingly broad legal powers to obtain confidential information, and researchers may have great difficulty resisting disclosure.

Elucidating Certificates’ practical utility in preventing compelled disclosure is a critical area for future study. Empirical evidence about how frequently research data are subpoenaed, and what happens when investigators assert a Certificate to protect data, is needed to help set realistic expectations about Certificates’ role and value. In the meantime, the full legal effect of Certificates remains unclear, and caution is warranted when representing the impact of a Certificate to potential research participants.

References and Notes

1. Advisory Committee, Office for Human Research Protections, DHHS, *Recommendations on Confidentiality and Research Data Protections*, www.hhs.gov/ohrp/nhrpac/documents/nhrpac14.pdf.
2. National Commission for the Protection of Human Subjects of Biomedical and Behavioral Research, *The Belmont Report: Ethical Principles and Guidelines for the Protection of Human Subjects of Research* (Government Printing Office, Washington, DC, 1979).
3. Certificates of Confidentiality kiosk, NIH, <http://grants.nih.gov/grants/policy/coc/>.
4. *Public Health Service Act*, §301(d), 42 USC §241(d).
5. P. M. Currie, *IRB* 27, 7 (2005).
6. *People v. Newman*, 32 NY2d 379, 298 NE2d 651, 345 NYS2d 502 (1973), cert. denied, 414 US 1163 (1973).
7. *Drug Abuse Office and Treatment Act*, 21USC §1101 (1972), Public Law 92-255.
8. *Order for Disclosure: Duke University Health System*, 29 July 2004.
9. Transcript of the hearing on Duke’s Motion for Protective Order, 8 August 2004, p. 9.
10. Transcript of hearing on defendant’s Motion for Review of Sealed Documents for Appellate Review, 25 April 2005.
11. Brief of Appellant/Subpoenaed Non-Party Duke University Health System, Inc., *State of North Carolina v. Bradley*, Case No. COA05-1167, NC Court of Appeals, filed 4 January 2006, p. 16.
12. Defendant-Appellee’s Brief, *State of North Carolina v. Bradley*, Case No. COA05-1167, NC Court of Appeals, filed 4 January 2006, p. 17.
13. *State of North Carolina v. Bradley*, 179 NC App 551, 634 SE2d 258 (2006).
14. NIH announcement on Certificates of Confidentiality, <http://grants.nih.gov/grants/guide/notice-files/NOT-OD-02-037.html>.
15. *National Cancer Institute Best Practices for Biospecimen Resources* (NCI, NIH, Bethesda, Md, 2007); http://biospecimens.cancer.gov/global/pdfs/NCI_Best_Practices_060507.pdf.
16. *Policy for Sharing of Data Obtained in NIH Supported or Conducted Genome-Wide Association Studies (GWAS)*, <http://grants.nih.gov/grants/guide/notice-files/NOT-OD-07-088.html>.
17. *Genome-Wide Association Studies (GWAS), NIH Points to Consider*; http://grants.nih.gov/grants/gwas/gwas_ptc.pdf.
18. *Uniting and Strengthening America by Providing Appropriate Tools Required to Intercept and Obstruct Terrorism Act of 2001 (USA PATRIOT Act)*, Public Law 107-56; 115 Stat. 272 (2001).
19. Supported in part by a grant from the NIH Clinical and Translational Science Award 1UL1RR024128-01 to Duke University. None of the authors has any conflict of interest, financial or otherwise, to declare. The authors thank J. McCall for editorial assistance and W. E. Freeman and L. E. Wolf for their input.

10.1126/science.1164100

CHEMISTRY

A Sideways Glance at Chemical Reactivity

David A. Blank

Chemical reactions can often be described with surprisingly few variables, such as the highest energy barrier that is crossed and the nature of any brief stops in energy valleys along the way from reactants to products (see the figure, top panel). However, if the goal is to describe the choreography of chemical reactions and not just their rates, then a more complete description is needed that includes details such as whether the low-energy path widens or narrows as the reaction proceeds. The vast area between the stable points on this energy landscape dictates how a reaction takes place but is usually the most challenging piece to survey (see the figure, middle panel). On page 1073 of this issue, Takeuchi *et al.* (1) have reexamined the well-studied photoisomerization of stilbene, which is representative of a broad class of reactions that includes the photochemistry of vision (2, 3). They map out previously hidden parts of the landscape through direct measurements of vibrational motions that occur in parts of the molecule that are not directly involved in the twisting of its double bond.

Starting around 1930, chemical reactions were described in terms of a potential energy surface that depicted how the energy of the molecules increases or decreases as bonds are broken, made, or deformed (4, 5). Since then, much effort has been focused on finding ways to experimentally measure and computationally access the potential energy surface. Experimental studies are especially challenging in that the reacting molecules spend an extremely short time in the unstable regions, so the majority of the experimental observations are made on relatively stable molecules, which in some cases may be only the reactants and products. One analogy is that we are trying to describe what the players are doing at a tennis match on the basis of seeing the ball only when it hits the court or a racket, not when it is in flight.

The unstable regions can be probed by finding connections between what goes on there and more stable states. For example, optical spectroscopic methods excite the mol-

ecules from stable ground states to electronic excited states. The absorption of light can probe the difference between ground and excited states, and, if done at enough points on the ground-state surface, can allow us to map out the excited-state surface (see the figure, bottom panel). The reaction described by Takeuchi *et al.* actually takes place on the excited-state surface, and the ground-state surface provides an initial point of reference.

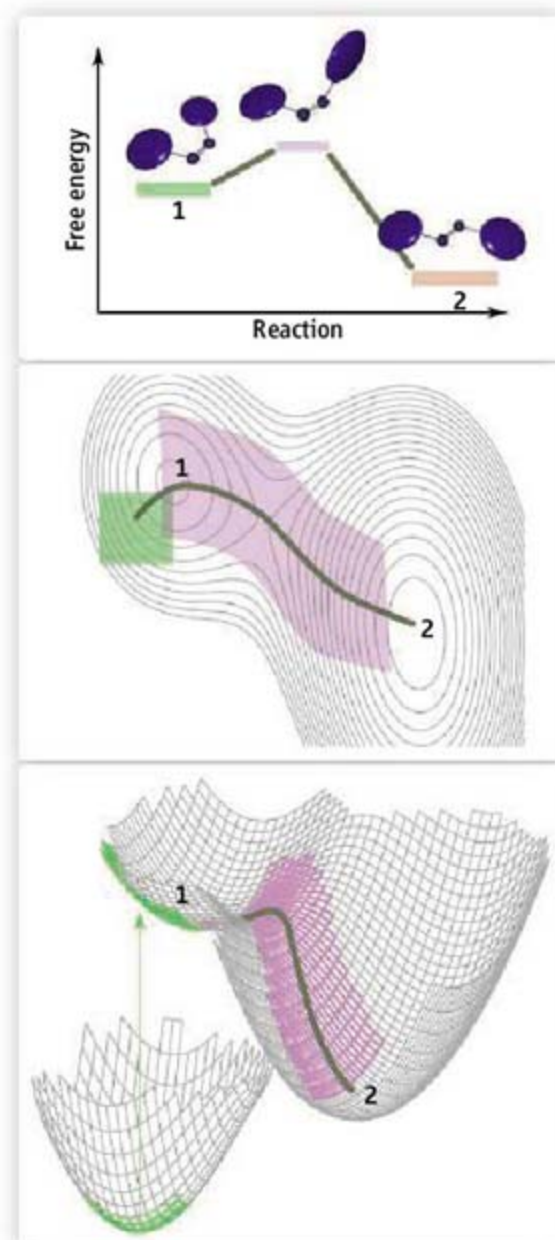
However, light absorption as a probe of the excited-state surface is limited in its access because the electronic changes occur on a much faster time scale than the response of the heavier nuclei. In the energy landscape, there is no movement along the horizontal direc-

Ultrafast spectroscopy allows us to see what happens to parts of a molecule not directly involved in a chemical reaction.

tions that represent the distances between nuclei, so the transitions are described as “vertical.” Thus, when *cis*-stilbene is photoexcited, the bonding pattern of its molecular orbitals now favors the *trans* arrangement around the double bond, and the nuclear coordinates try very quickly to “catch up” to this new stable point (to invoke our tennis match, this vertical transition is the racket deforming the ball). The accessible part of the upper surface, directly above the region of stability on the reference surface, is called the Franck-Condon region (illustrated as the green area in the bottom panel of the figure).

Spectroscopic methods that use more than one absorption or emission event, or both, and that have time resolution comparable to the time spent between the stable regions (10^{-13} to 10^{-12} s), can be used to probe directly the unstable regions of the potential energy surfaces (6). In the simplest implementation, a light pulse excites the reactant onto the upper surface in the Franck-Condon region. After a short delay, a second light pulse can be used to report on the progress of the reaction. This type of experiment can map the narrow path followed from 1 to 2, referred to as the reaction coordinate (illustrated with olive green in the figure). Takeuchi *et al.* take the next step by adding an additional dimension to the probe. They not only follow the reaction coordinate (the twisting of the double bond) but also measure changes in vibrations of other bonds in the molecule as the twisting proceeds.

Takeuchi *et al.* map the changes in topology around the reaction coordinate and fill



Degrees of realism in depicting chemical reactions. In all of these depictions, reactants (green regions) convert into products by moving quickly along a reaction coordinate (olive green and pink regions). (Top) A simple view of the energy barriers encountered along the reaction coordinate, which reflects the changes in one bond. For stilbene, the double bond must break to allow the phenyl rings to rotate, and the coordinate is the rotation angle. (Middle) The energy landscape for two degrees of freedom (more than one bond's motion) in a chemical reaction. Many more coordinates are often included, and depictions are slices in two dimensions. (Bottom) In a photoreaction, the changes in nuclear coordinates can occur along a second upper surface that represents an electronic excited state.

Department of Chemistry, University of Minnesota, 207 Pleasant Street SE, Minneapolis, MN 55455, USA. E-mail: blank@umn.edu

in the pieces of the landscape shown in pink. Their method is directly related to the time-resolved probing of vibrations by means of resonance Raman spectroscopy, as previously reported by Mathies and co-workers (7, 8). The main difference is that Takeuchi *et al.* probe the vibrational motions in time rather than frequency, which has the practical result of lowering the frequency of the vibrations that can be accessed. Thus, they can observe the evolution of a vibrational motion of the carbon-carbon bond framework at frequencies around 200 cm^{-1} during the isomerization reaction, which represents nuclear motions with a period of 1.6×10^{-13} s.

This lower-frequency motion is similar in time scale to the motion along the reaction

coordinate, and the curvature of the potential energy surface along these two dimensions is comparable. It provides details of how the phenyl rings move and twist as they settle into the extended trans conformation, which previously was viewed as a spectator to the motion rather than as part of the action. The complementary computational study in the report highlights the necessity of combining theory and experiment when mapping out these potential energy surfaces.

The report by Takeuchi *et al.* adds to our understanding of a specific class of chemical reactions by providing a new perspective on a model photoisomerization. Their study takes us beyond the question of “how fast” and to the more demanding question of “which way” at

the level of the entire molecule. Although the method presented is technically demanding, it could be applied to a wide variety of photoinitiated reactions, including those that take place in complex environments such as proteins.

References

1. S. Takeuchi *et al.*, *Science* **322**, 1073 (2008).
2. C. Dugave, L. Demange, *Chem. Rev.* **103**, 2475 (2003).
3. M. V. der Horst, K. Hellingwerf, *Acc. Chem. Res.* **37**, 13 (2004).
4. W. Heitler, F. London, *Z. Phys.* **44**, 455 (1927).
5. H. Eyring, M. Polanyi, *Z. Phys. Chem. Abt. B* **12**, 279 (1931).
6. G. R. Fleming, *Chemical Applications of Ultrafast Spectroscopy* (Oxford Univ. Press, Oxford, 1986).
7. P. Kukura *et al.*, *Science* **310**, 1006 (2005).
8. P. Kukura *et al.*, *Annu. Rev. Phys. Chem.* **58**, 461 (2007).

10.1126/science.1166563

BEHAVIOR

A Bilingual Agenda

Marc D. Hauser¹ and Thomas Bever²

When we transform thoughts into speech, we do something that no other animal ever achieves. Children acquire this ability effortlessly and without being taught, as though discovering how to walk. Damage to specific areas of the brain that are critical to language shows the profound selectivity of cerebral organization, underlining the exquisite biological structure of language and its computational features. Recent advances bring new insights into the neurogenetic basis of language, its development, and evolution, but also reveal deep holes in our understanding.

There are about 7000 living languages spoken in the world today, characterized by both exceptional diversity as well as significant similarities. Despite many controversies in the field, many linguistic scholars generally agree on two points (1–8). Language as a system of knowledge is based on genetic mechanisms that create the similarities observed across different languages, culturally specific experience that shapes the particular language acquired, and developmental processes that enable the growth and expression of linguistic knowledge. Also, the neural systems that allow us to acquire and process our knowledge of language are separate from

those underlying our ability to communicate.

To fulfill a bilingual agenda—study of the computational systems inherent to language—we must address the rules and constraints that underlie a mature speaker’s knowledge of language; how these rules and constraints are acquired; and whether they are mediated by language-specific mechanisms. We also need to distinguish which rules and constraints are shared with other animals and how they evolved, and to ask how knowledge of language is used in communicative expressions.

There has been little research linking the formal linguistic principles that describe the mature speaker’s knowledge of language to the evolutionary, neurobiological, and developmental factors that lead to their instantiation in the adult mind. These principles include computational devices such as hierarchies and dependencies among syntactic categories (e.g., the relationship between determiners such as “the” and “a” followed by nouns), recursive and combinatorial operations, and movement of parts of speech and phrases (e.g., to create a question, many languages move constructions such as “what” or “where” to the front of the sentence). This gap is slowly narrowing, but the separation remains great. It is thus important to clarify the appropriate targets of analysis. In particular, examination of the evolutionary, neurobiological, and developmental aspects of language often focuses narrowly on speech, or in some cases, on the separate issue of commu-

Neurobiology and genetics are helping to generate insights about the evolution of language.

nication. Instead, these aspects should be considered in light of the principles discussed, helping to align formal approaches to linguistics with the biological sciences.

Formal approaches to examine linguistic structure are marked by disagreement about the necessary or sufficient computations required to create the expressed languages of the world. Some linguists argue that linguistic form relies on abstract, generative operations that allow phrases and sentences (syntactic structures) to interface with meanings (the semantic system) to create a categorization (lexical terms) in which single words and groups of words convey a specific meaning. Such lexical terms then interface with speech sounds (phonology) to create expressed words in speech or sign. Language has been suggested as an optimal solution to the syntactic-semantic interface, achieved by a small number of computational operations. By comparison, current evolutionary models suggest that the variation in animal body form can be explained by different activation patterns for a few master genes during development. The corresponding idea in linguistics is that the cross-cultural variation in expressed human languages can be explained by a universal set of mental operations, some specific to language, others shared across domains including music, mathematics, and morality (4, 9).

Comparative evolutionary studies suggest that birds, rodents, and primates compute some components of human grammatical

¹Department of Psychology, Human Evolutionary Biology, Harvard University, Cambridge, MA 02138, USA. ²Departments of Linguistics, Psychology and Cognitive Science Program University of Arizona, Tucson, AZ 85721, USA. E-mail: mdh@wjh.harvard.edu

competence, but cannot attach this capacity to their own communication systems (10–12). For example, birds and primates can compute a first-degree finite state grammar, where elements in a string of sounds have specific orders, each predicted by simple statistical associations. This grammar is one of the simplest within a hierarchy of computational operations of increasing complexity and expressive power (10, 13). The biggest puzzle, however, is why nonhuman animals cannot integrate these computational capacities with their capacity to communicate. So, although songbirds can combine different notes into a variety of songs, they don't integrate this combinatorial capacity with conceptual abilities to create sounds with varied meaning. Understanding what neural connections are absent, or poorly developed, may help account for this evolutionary bottleneck, and explain why human infants readily produce an infinite variety of meaningful expressions.

Damage to Broca's area and Wernicke's area in the human brain results in distinct patterns of language loss, suggesting that properties of the neocortex make language unique to humans. Artificial language studies show that these cortical areas execute the computations that obey language universals (the principles accessed by all languages, such as specific word orders), but other brain areas are also activated by these computations (14, 15). In fact, different cortical areas may compute different kinds of grammars, but such localization does not provide insight into linguistic theories aimed at uncovering principles that guide the mature state of language competence and its acquisition during development.

Does language have its own dedicated brain circuits, or is much or all of this circuitry shared across domains (such as music and language)? For example, language and music rely on hierarchical representations, make use of combinatorial and recursive computations, and generate serially represented structures. But does each domain recruit a general-use ensemble of these processes or does each domain have its own set of processes? Further studies of selective brain damage and brain-imaging experiments should be informative.

Genes associated with particular linguistic deficits can help pinpoint the molecular basis for language, and link issues in evolution with those in development. Yet, we are far from understanding how normal genes are associated with linguistic features. When the gene *FOXP2* was linked to families with a particular language deficit, it seemed that genomics might account for linguistic structure. But the

relationship between *FOXP2* and language turns out to be weak. For example, *FOXP2* exists in songbirds and echo-locating bats; although songbirds have richly structured sound systems that might be properly characterized by a finite state grammar, such grammars are not hierarchically structured, lack syntactic categories (e.g., nouns and determiners), and do not productively generate meaningful variation. Further, the disorders associated with *FOXP2* in humans include articulatory disabilities and are not clearly syntactic, semantic, or computational (16, 17). The weak connection between *FOXP2* and these aspects



of language should not, however, come as a surprise given that most gene-phenotype relationships involving complex phenotypes (such as language) are weak. Nonetheless, by breaking language down into its component parts and finding potential homologs in other animals (especially those that can be genetically manipulated), we may better understand the evolution, development, and neurobiological breakdown of linguistic function.

Current research on hemispheric lateralization (division of the brain into left and right halves) and language acquisition provides one example of how interdisciplinary work relates to specific theories in linguistics. All right-handed people have strong left-hemisphere lateralization of syntactic function. However, classic investigations of aphasia—the inability to produce or comprehend language—reveal that familiarly “mixed” right-handers (right-handers with left-handed family members) show more right-hemisphere involvement in language than pure right-handers (18, 19). Thus, in familiarly mixed right-handers, the right hemisphere's involvement in language may be specific to lexical representations (20).

Familiarly mixed right-handers access individual words more readily than global sentence structure, whereas the reverse is true of familiarly pure right-handers (21). Their critical period for language learning is also earlier than that of familiarly pure right-handers (22), which suggests that mixed right-handers are more likely to base their language learning on the acquisition of words as opposed to syntactic structure. These findings are supported by brain-imaging research showing that familiarly pure right-handers have left-hemisphere activation during lexical access, whereas familiarly mixed right-handers show more bilateral hemisphere activation (23). At the same time, all subjects show left-hemisphere activation for syntactic processes. This confirms the basic hypothesis that mixed right-handers have more distributed representations of lexical knowledge.

What are the implications of such population-level differences in lexical use, access, and representation for linguistic theory? In recent decades, syntacticians have struggled with the role of the lexicon in syntactic architectures. Proposals range from the traditional view that the lexicon is distinct from the computations of syntax, to the view that syntax itself is driven by lexical structures. The observed variability in how the lexicon is accessed and represented suggests that it is indeed a biologically separable component of linguistic knowledge.

Brain imaging, genomics, and new methods for comparative studies have provided the means for better understanding the shared and uniquely human components of language. As some linguists argue, the variation in linguistic form among the world's languages may be as superficial as the variation in animal body forms. The superficiality arises, in each case, because of universal computations that provide the necessary suite of developmental programs to generate the variation. As the biolinguistic agenda advances, however, new generations of linguists will be required to translate their formalisms into testable experiments by biologists and psychologists. For example, language deploys recursive operations and generates hierarchical representations with specific configurations. It is not yet clear how to design experiments to test whether nonlinguistic organisms can acquire these representations, or what factors limit either their acquisition or implementation into communicative expression. Conversely, psychologists and biologists will need to be sensitive to the limitations of their methods and the extent to which they can test linguistic theories. Thus, neuropsychological studies showing deficits in language need

to be accompanied by comparable tests in non-linguistic domains to show that they are language-specific deficits. And studies using brain imaging must acknowledge that localization of function does not provide explanatory power for the linguist attempting to uncover principles underlying the speaker's knowledge of language. These cautions aside, the biolinguistic approach is clearly benefiting from modern technologies to advance our knowledge of what language is, how it is represented, and where it came from.

References

1. M. A. Arbib, *Behav. Brain Sci.* **28**, 105 (2005).
2. E. Bates, *Discuss. Neurosci.* **10**, 136 (1994).
3. T. G. Bever, in *Cognition and Language Development*, R. Hayes, Ed. (Wiley, New York, 1970), pp. 277–360.
4. N. Chomsky, *Linguist. Inq.* **36**, 1 (2005).
5. T. W. Deacon, *The Symbolic Species: The Coevolution of Language and the Brain* (Norton, New York, 1997).
6. R. Jackendoff, *Foundations of Language* (Oxford Univ. Press, New York, 2002).
7. E. H. Lennenberg, *Biological Foundations of Language* (Wiley, New York, 1967).
8. S. Pinker, *Language Learnability and Language Development* (Harvard Univ. Press, Cambridge, MA, 1984).
9. C. Boeckx, M. Piatelli-Palmerini, *Linguist. Rev.* **22**, 447 (2005).
10. W. T. Fitch, M. D. Hauser, *Science* **303**, 377 (2004).
11. T. Q. Gentner, K. M. Fenn, D. Margoliash, H. C. Nusbaum, *Nature* **440**, 1204 (2006).
12. R. A. Murphy, E. Mondragon, V. A. Murphy, *Science* **319**, 1849 (2008).
13. N. Chomsky, *Syntactic Structures* (Mouton, the Hague, 1957).
14. A. Friederici *et al.* *Proc. Nat. Acad. Sci.* **103**, 2458 (2006).
15. M. Musso *et al.*, *Nat. Neurosci.* **6**, 774 (2003).
16. W. Enard *et al.*, *Nature* **418**, 869 (2002).
17. S. Haesler *et al.*, *J. Neurosci.* **24**, 3164 (2004).
18. A. R. Luria, *Traumatic Aphasia* (Mouton, the Hague, 1969).
19. J. T. Hutton, N. Arsenina, B. Kotik, A. R. Luria, *Cortex* **13**, 195 (1977).
20. T. G. Bever, C. Carrithers, W. Coward, D. J. Townsend, in *From Neurons to Reading*, A. Galaburda, Ed. (MIT Press, Cambridge, MA, 1989).
21. D. J. Townsend, C. Carrithers, T. G. Bever, *Brain Lang.* **78**, 308 (2001).
22. D. S. Ross, T. G. Bever, *Brain Lang.* **89**, 115 (2004).
23. S. Chan, thesis, University of Arizona (2007).

10.1126/science.1167437

BIOCHEMISTRY

RT Slides Home...

Stefan G. Sarafianos¹ and Eddy Arnold²

For HIV to replicate inside human cells, it must convert its single-stranded RNA genome into double-stranded DNA that can be integrated into the host genome (1). This formidable task is achieved by HIV reverse transcriptase (RT), a multifunctional enzyme that has RNA-dependent and DNA-dependent DNA polymerase activities to synthesize minus and plus DNA strands, ribonuclease H (RNase H) activity to degrade the RNA strand of the RNA-DNA replication intermediate, a strand displacement activity to remove the remaining RNA and DNA fragments to allow synthesis of the plus DNA strand, and a strand transfer activity to move newly synthesized DNA within or between templates. Although 20 years of crystallographic and biochemical studies have illuminated the molecular details of the chemistry of DNA synthesis, there have been relatively few insights into how RT finds the end of the nucleic acid substrate where it begins DNA synthesis, how it displaces nucleic acid fragments, or where and how it executes masterful leaps when transferring DNA between templates. On page 1092 of this issue, Liu *et al.* (2) describe elegant single-molecule fluorescence resonance energy transfer (FRET) experiments that provide a view of RT at work. They show that RT has a remarkable

ability to slide on nucleic acid duplexes, rapidly shuttling between the two ends and flipping into the polymerase-competent binding mode when needed.

Important structural features of RT (3, 4) and its molecular interactions with substrates and inhibitors have been elucidated through extensive crystallographic studies (4–7). HIV RT is an asymmetric heterodimer composed of p66 and p51 subunits that have identical amino termini. The p66 subunit has enzymatic activity, containing the spatially distinct polymerase and RNase H active sites, whereas the smaller p51 subunit plays a structural role. The p66 polymerase domain comprises four subdomains: fingers, palm, thumb, and connection. Although p51 folds into the same subdomains as the polymerase domain of p66, the positions of the subdomains relative to each other are different in p66 and p51.

In this study, Liu *et al.* use a single-molecule FRET assay to measure the position and orientation of RT relative to its nucleic acid substrate. They immobilized nucleic acid labeled at one end of the template or primer strand with the FRET acceptor fluorophore, Cy5, and immersed it in a solution containing RT molecules labeled with a FRET donor dye, Cy3, attached either at the RNase H domain or at the fingers domain of the p66 subunit. By monitoring the FRET efficiency, they were able to determine the enzyme's position on the nucleic acid substrate during each binding event. The same team (groups of Zhuang and Le Grice) recently used this approach to show that RT can rapidly switch between two orientations when it binds duplexes containing the

To access its target sites, HIV reverse transcriptase slides and flips on nucleic acid substrates.

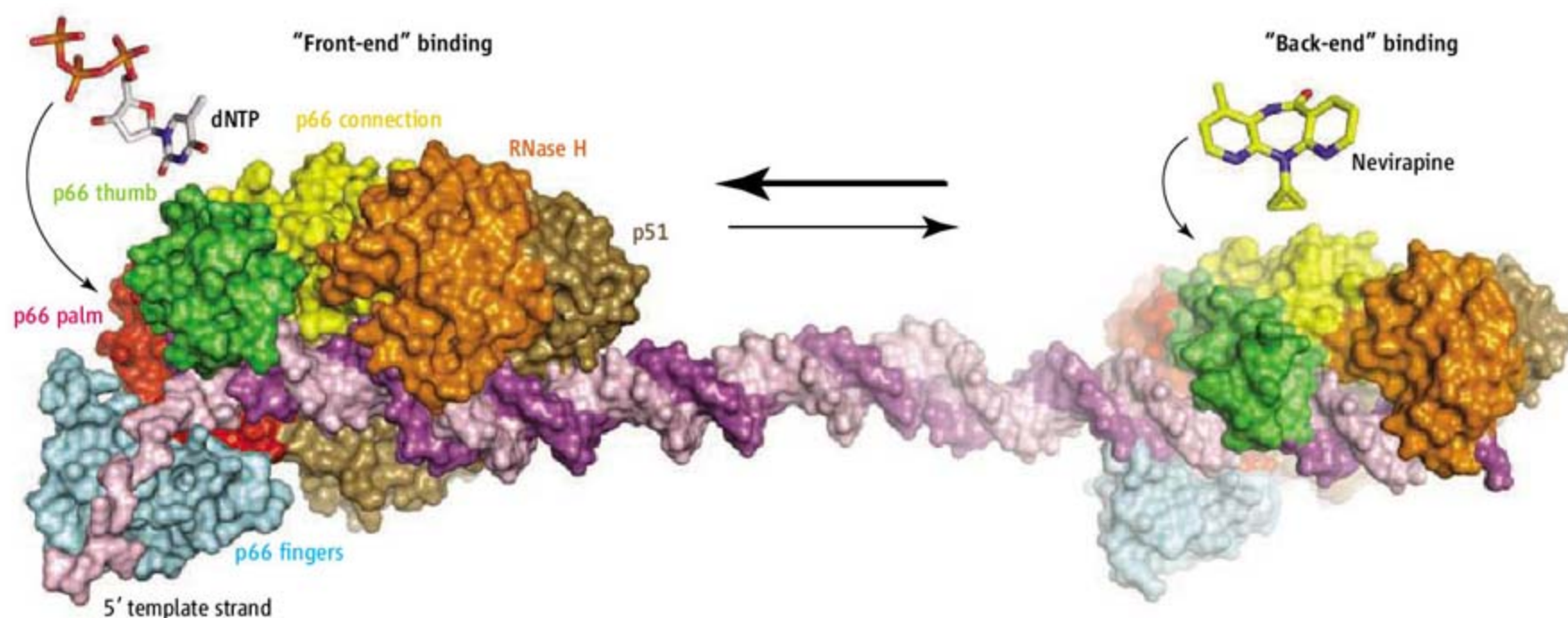
unique polypurine RNA sequences that are primers for plus-strand synthesis (8). Now they show that the enzyme can slide between opposite termini on long duplexes and that the flipping and sliding kinetics are altered in the presence of nevirapine, a non-nucleoside inhibitor of HIV RT (NNRTI).

Here, the authors pose the question: How does RT efficiently locate the 3' terminus of nascent DNA on a long duplex substrate so that it can extend it? This question is particularly important because HIV RT has relatively low processivity and must frequently locate the polymerization site after dissociation. Also, RT cleaves RNA-DNA hybrids at many different sites, and it is not well understood how it accesses these sites (9, 10).

In answer to these questions, Liu *et al.* initially showed that RT binds an oligonucleotide that is the same size as its nucleic acid binding cleft (19 base pairs) only in the configuration that places its polymerase site at the 3' end of the primer ("front-end" binding). However, when RT binds longer RNA-DNA (or DNA-DNA) substrates (38 or 56 base pairs), there is an equilibrium between front-end and back-end binding that favors front-end binding (see the figure). Therefore, the enzyme can stably bind either to the front end of the hybrid, poised for DNA extension, or to the back end, placing the RNase H domain close to the 3' of the RNA (or DNA) template.

By following changes in FRET over time, Liu *et al.* were able to detect repeated transitions between front- and back-end bound states within a single binding event, suggesting that shuttling can occur between these

¹Christopher S. Bond Life Sciences Center, Department of Molecular Microbiology and Immunology, University of Missouri, 1201 Rollins Street, Columbia, MO 65211, USA.
²Center for Advanced Biotechnology and Medicine, Department of Chemistry and Chemical Biology, Rutgers University, 679 Hoes Lane, Piscataway, NJ 08854, USA. E-mail: sarafianos@missouri.edu; arnold@cabm.rutgers.edu



RT slides on a nucleic acid substrate without dissociating. Binding at the 3' primer end (front-end binding) is favored over binding at the other end. However, in the presence of deoxyribonucleotide triphosphate (dNTP), RT becomes locked in a front-end binding conformation, whereas in the presence of

nevirapine it shifts toward back-end binding. p66 (fingers in cyan, palm in red, thumb in green, connection in yellow, RNase H in orange) and p51 (brown) are the large and small subunits of the RT heterodimer bound to an RNA-DNA template (pink) primer (magenta).

states without dissociation (see the figure). The shuttling is a thermally driven diffusion process that does not require energy from nucleotide hydrolysis. RT can cleave RNA at multiple positions within a DNA-RNA hybrid (9), and the sliding function of RT may provide a mechanism by which the enzyme can rapidly access these cleavage sites.

The authors also identified factors that modulated the ability of the enzyme to slide on the nucleic acid substrate. A cognate nucleotide favors front-end binding in the polymerization mode (see the figure); in contrast, the NNRTI nevirapine destabilized the polymerization binding mode, presumably because it binds at the base of the p66 thumb subdomain of RT and affects its ability to grasp the nucleic acid. On the basis of these results, Liu *et al.* conclude that for RT to escape from the polymerization mode, a relaxation of the fingers-thumb grip is likely to be required.

Other nucleic acid binding proteins are also thought to use a one-dimensional sliding diffusion along the nucleic acid to locate their targets (references 38 to 42 in Liu *et al.*). However, RT may add a twist to this mechanism. A tantalizing finding in the Liu *et al.* paper is that RT may bind the “wrong” way on the nucleic acid and still find its way to the 3'-OH of the nascent DNA, where it flips into the polymerization-competent orientation. This surprising trick may be used by RT to increase its efficiency of binding in a polymerization-competent mode.

This unexpected property challenges our assumptions of RT gripping the nucleic acid in

a single defined way, and highlights a remarkable flexibility that may be the hallmark of multifunctional enzymes. Nonetheless, it is consistent with the ability of the RT fingers and thumb subdomains to undergo large conformational changes during the polymerization reaction. This finding may also shed light on how the enzyme is able to jump from one RNA genome to another during reverse transcription, resulting in increased recombination rates and evolutionarily important genome diversity. Interestingly, unlike RT, viral RNA-dependent RNA polymerases with related architecture for polymerase catalysis appear to form structures reminiscent of tightly closed rings (11) that ensure unidirectional synthesis (either replication or transcription) after initiation.

Dissociated RT does not simply have to relocate the polymerization site during strand displacement synthesis. It may have to locate disrupted polymerization sites where the primer terminus has been displaced from the template by the competing nontemplate strand. The authors' data suggest that sliding allows RT to efficiently access the disrupted polymerization site and assist primer-template annealing, thereby facilitating RNA strand displacement synthesis.

In another striking experiment, Liu *et al.* used the single-molecule FRET method to observe a single RT molecule carrying out processive DNA synthesis or pausing in real time, as indicated by plateaus in the single-molecule FRET. This remarkable technical achievement bodes well for future studies that could focus on the mechanisms by which RT translocates or pauses on nucleic acid substrates.

The Liu *et al.* report vividly illustrates that RT has a remarkable dynamic flexibility that contributes to more efficient replication by allowing it to bind nucleic acids in multiple conformations and to slide over long distances toward the ends of the nucleic acid duplexes. Future challenges will be to enhance the complexity of the system by including components that are known to affect the efficiency and outcome of the polymerization reaction. For example, how might the sliding and flipping functions be affected on genomic RNA with considerable secondary structure? Also, what is the mechanism by which the nucleocapsid protein affects the strand transfer and processivity functions of RT (12, 13)?

References

1. J. M. Coffin, S. H. Hughes, H. E. Varmus, *Retroviruses* (Cold Spring Harbor Laboratory Press, Cold Spring Harbor, NY, 1997).
2. S. Liu, E. A. Abbondanzieri, J. W. Rausch, S. F. J. Le Grice, X. Zhuang, *Science* **322**, 1092 (2008).
3. L. A. Kohlstaedt, J. Wang, J. M. Friedman, P. A. Rice, T. A. Steitz, *Science* **256**, 1783 (1992).
4. A. Jacobo-Molina *et al.*, *Proc. Natl. Acad. Sci. U.S.A.* **90**, 6320 (1993).
5. J. Ren *et al.*, *Nat. Struct. Biol.* **2**, 293 (1995).
6. H. Huang, R. Chopra, G. L. Verdine, S. C. Harrison, *Science* **282**, 1669 (1998).
7. S. G. Sarafianos *et al.*, *EMBO J.* **20**, 1449 (2001).
8. E. A. Abbondanzieri *et al.*, *Nature* **453**, 184 (2008).
9. J. J. DeStefano, L. M. Mallaber, P. J. Fay, R. A. Bambara, *Nucleic Acids Res.* **21**, 4330 (1993).
10. M. Wisniewski, M. Balakrishnan, C. Palaniappan, P. J. Fay, R. A. Bambara, *J. Biol. Chem.* **275**, 37664 (2000).
11. Y. Tao, D. L. Farsetta, M. L. Nibert, S. C. Harrison, *Cell* **111**, 733 (2002).
12. J. C. You, C. S. McHenry, *J. Biol. Chem.* **269**, 31491 (1993).
13. L. Rodriguez-Rodriguez, Z. Tsuchihashi, G. M. Fuentes, R. M. Bambara, P. J. Fay, *J. Biol. Chem.* **270**, 15005 (1995).

CLIMATE CHANGE

Understanding Glacier Flow in Changing Times

Richard B. Alley,¹ Mark Fahnestock,² Ian Joughin³

Unexpected accelerations in outlet glaciers of the Greenland and Antarctic ice sheets in the last decade, in response to processes not fully understood, prompted the Intergovernmental Panel on Climate Change (IPCC) Fourth Assessment to conclude that poorly characterized uncertainties prevented a best estimate or upper bound on sea-level rise. These changes in ice sheet outlet glaciers come at a time when smaller glaciers and ice caps are wasting quickly as well. The focus of present glacier research must be the rapid reduction of the uncertainty identified by the IPCC. Rapid progress will require identification of the most relevant of the recent changes, effective moves toward understanding the controlling physics, and careful consideration of the differing time scales involved. We briefly review recent changes with a view toward an effective path forward.

About 6 years ago, Zwally *et al.* discovered that lubricating surface meltwater can reach the base of the Greenland Ice Sheet, thereby speeding up summer ice flow (1). Subsequent work confirms the broad picture of seasonal lubrication (2) but shows that annual motion is enhanced only by 10 to 20% (3). More important, the fast outlet glaciers responsible for most of the ice discharge to the ocean are relatively insensitive to summer melt, making it unlikely that enhanced seasonal lubrication will destabilize the ice sheet (2).

Meltwater drainage to the bed can play a second and possibly more important role, however, speeding ice flow by delivering heat rapidly to the bed. The water in surface lakes (see the figure) can wedge open crevasses, fracturing through to the bed catastrophically (4). Were this phenomenon to spread inland in a warming world, it would deliver sufficient heat to thaw areas where the bed is currently frozen (5). In this event, twofold accelerations would not be surprising, with the slight chance of an order-of-magnitude or more locally if extensive regions with soft sedi-

ments were to thaw (6). Some issues remain: Reliable mapping of the basal characteristics of regions now frozen but that might thaw is unavailable, and our present understanding is not sufficient to tell us whether inland migration of melting will be accompanied by the changes in ice flow required to open cracks beneath any new lakes.

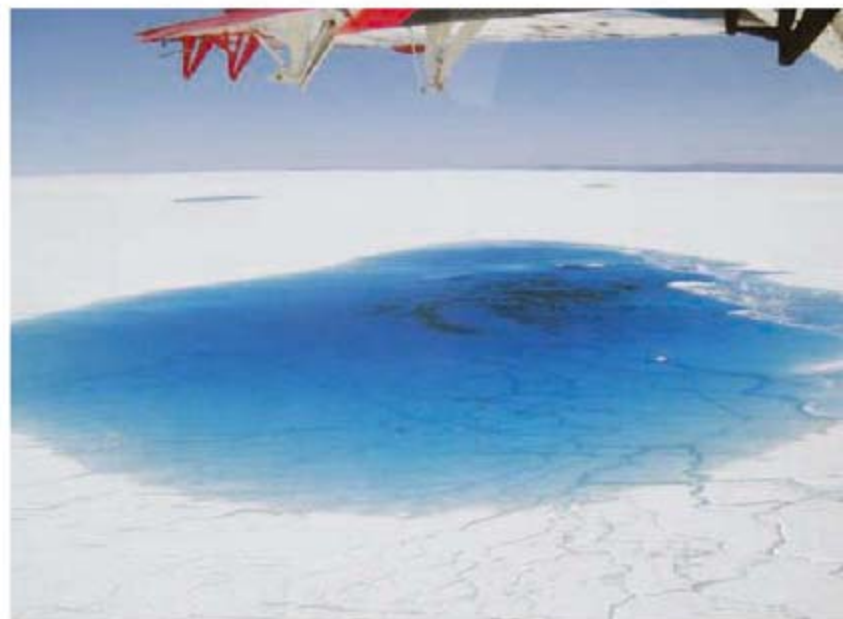
Lakes exist not only on top of but also beneath the ice. Increasingly seen to be widespread and dynamic, these subglacial lakes occur at and may be linked to the upglacier limit of rapid ice flow (7). However, release of stored lake water in outburst floods (8) does not seem to have major ice-flow effects. It is even possible that an ice sheet with more subglacial lakes will be less variable, because the lakes focus water drainage in space and time and thus reduce lubrication overall.

Far more ominous for future sea levels are the changes that originate where ice meets ocean. Ice shelves, the floating-but-still-attached parts of the ice sheets extending over the ocean, restrain the nonfloating ice through friction with local bedrock highs or with fjord walls. Because ice shelves are near sea level and in contact with the ocean, they are the elements of the coupled sheet-shelf system that are most susceptible to warming. Extensive surface melting can fill surface crevasses and destroy an ice shelf through the same fracture process that allows surface lakes to drain to the bed (9). Furthermore, even small changes in water temperature below the ice shelf can speed basal melting by roughly 10 meters per year for each 1°C warming (10).

Such wasting of shelves has no direct effect on sea level, but the loss of restraint and associated acceleration of inland flow to the ocean has triggered doublings of flow speed, with one change reaching eightfold (11). Large diurnal changes in flow speed of Antarctic ice streams feeding ice shelves occur in response to the small changes in loading at the ends caused by the tides (12),

Subannual lurches of the Greenland and Antarctic ice sheets may reduce uncertainties about climate change effects on sea-level rise.

showing that these ice streams will respond rapidly if the buttressing from their ice shelves is reduced. Ice shelves are far less prevalent in Greenland than in Antarctica, but loss of floating and grounded ice at marine-terminating outlet glaciers has had similarly large effects (13). Present seasonal acceleration in the flow speed of Jakobshavn Glacier in Greenland begins in response to loss of sea ice damming the fjord. This commences well



Lakes on the western flank of the Greenland Ice Sheet. The nearest lake is roughly 1500 m across and 10 m deep. Meltwater from these lakes can drain catastrophically into the ice sheet, causing brief but strong local disturbance of the ice flow. More important, these drainage events establish a meltwater pathway from surface to bed. Inland migration of this phenomenon might thaw now-frozen regions of the ice-sheet bed and speed up flow. The wing of a De Havilland Twin Otter occupies the top of the frame.

before the springtime onset of surface melt (14).

In the absence of validated models incorporating these processes, scientists have turned to a range of ice-flow scaling exercises and back-of-the-envelope estimates to constrain estimates of future ice-sheet contributions to sea-level change (see supporting online material). Although these estimates are instructive and useful, there is a lack of strong convergence among them, and a wide range of possible answers remains.

Progress toward more rigorously quantitative estimates will not be easy. When each major new project turns up something unexpected, we can be confident that the field is undersampled. For decades, the major atmo-

¹Department of Geosciences and Earth and Environmental Systems Institute, Pennsylvania State University, University Park, PA 16802, USA. E-mail rba6@psu.edu ²Institute for the Study of Earth, Oceans, and Space, University of New Hampshire, Durham, NH 03824, USA. ³Polar Science Center, Applied Physics Laboratory, University of Washington, Seattle, WA 98105-6698, USA.

sphere-ocean general-circulation modeling groups have assumed that ice sheets are static, white mountain ranges; reversing this approach by having such groups develop sophisticated treatments of ice sheets would unleash great talent on this crucial problem. Such a modeling effort, however, must be coordinated tightly with remote-sensing, field- and laboratory-based efforts to understand the processes that control ice flow.

Perhaps the key uncertainty remains the interaction between the ice and its underlying bed, which controls how basal velocity will change as ice-sheet stresses evolve. Geophysical exploration is essential but, realistically, cannot sample everything. Inversions from remotely sensed data provide modern snapshots (15) but do not elucidate the dependence of basal velocity on changing stress. If we wait for the ice sheets to evolve through a wide enough range of stresses, then we or some future generation of glaciologists will retrodict changes rather than predict them usefully.

Fortunately, the lake drainages, calving events, tidal responses, and other recently observed phenomena discussed above are exciting the ice sheet, providing short-period samples of a wide range of stress and lubrication states and the associated velocity

response necessary to characterize the system. Such short-period changes, however, are so fast that they have been difficult to observe fully and may involve elastic responses that are not captured by comprehensive ice-flow models. A more holistic approach that uses appropriately designed experiments that assimilate ground-based and remotely sensed data into improved models may provide the improved understanding needed to constrain future sea-level changes.

Although crucial, such experiments are increasingly difficult, as field efforts are eliminated or delayed in the face of rising fuel costs (16). The U.S. National Aeronautics and Space Administration's Decadal Survey missions addressing ice [the Ice, Cloud, and land Elevation Satellite II (ICESAT-II) and the Deformation, Ecosystem Structure, and Dynamics of Ice (DESDynI) mission] are a number of years from providing data to replace those endangered by failing satellites and access limitations. In the interim, this gap could be partly closed through closer coordination and improved data distribution among the various space agencies that operate the international constellation of remote-sensing spacecraft.

For a student of ice flow, these are exciting times, with the pace of discovery seemingly

accelerating. For a student of policy, the possibility looms of a fifth IPCC assessment lacking projections of sea-level rise sufficiently constrained for effective policy design. Wise choices may yet beat this unpleasant outcome. A coupled observation and modeling approach that lets the ice sheets tell us the answer may be the quickest path.

References

1. H. J. Zwally *et al.*, *Science* **297**, 218 (2002).
2. I. Joughin *et al.*, *Science* **320**, 781 (2008).
3. R. S. W. van de Wal *et al.*, *Science* **321**, 111 (2008).
4. S. B. Das *et al.*, *Science* **320**, 778 (2008).
5. B. R. Parizek, R. B. Alley, *Quat. Sci. Rev.* **23**, 1013 (2004).
6. R. B. Alley, I. M. Whillans, *Science* **254**, 959 (1991).
7. R. E. Bell *et al.*, *Nature* **445**, 904 (2007).
8. H. A. Fricker *et al.*, *Science* **315**, 1544 (2007).
9. T. A. Scambos *et al.*, *J. Glaciol.* **46**, 516 (2000).
10. E. Rignot, S. S. Jacobs, *Science* **296**, 2020 (2002).
11. E. Rignot *et al.*, *Geophys. Res. Lett.* **31**, L18401 (2004).
12. S. Anandakrishnan *et al.*, *Geophys. Res. Lett.* **30**, 1361 (2003).
13. I. M. Howat *et al.*, *Science* **315**, 1559 (2007).
14. I. Joughin *et al.*, *J. Geophys. Res.* **113**, F01004 (2008).
15. I. Joughin *et al.*, *J. Geophys. Res.* **109**, B09405 (2004).
16. E. Kintisch, *Science* **321**, 1142 (2008).

Supporting Online Material

www.sciencemag.org/cgi/content/full/322/5904/1061/DC1

SOM Text

References

10.1126/science.1166366

MICROBIOLOGY

A Protein Pupylation Paradigm

Sohini Mukherjee¹ and Kim Orth²

Tuberculosis, a devastating infectious disease caused by *Mycobacterium tuberculosis* (*Mtb*), is a global health threat that presently afflicts one-third of the world's population. The culprit bacterium is an obligate and persistent pathogen that maintains viability, in a latent state, within phagocytes—cells that ingest foreign materials and microorganisms—that reside in the lungs of humans. Treating tuberculosis requires prolonged antibiotic therapy that can result in multidrug-resistant *Mtb* strains. Because the bacterium is highly infectious, grows extremely slowly, and is difficult to manipulate genetically, the discovery of new drugs to combat *Mtb* infection is challenging. Thus, identifying *Mtb* components as potential drug targets is one

of the key approaches to developing new tuberculosis therapies. On page 1104 of this issue, Pearce *et al.* (1) report the discovery of a protein (Pup) in *Mtb* that modifies other bacterial proteins to target them for degradation. The process is similar to that in eukaryotes, in which the protein ubiquitin modifies proteins and targets them for proteolysis (see the figure). The discovery of this process in prokaryotes opens the door to further characterizing a protein regulatory mechanism that could be targeted by pathogen-specific drugs.

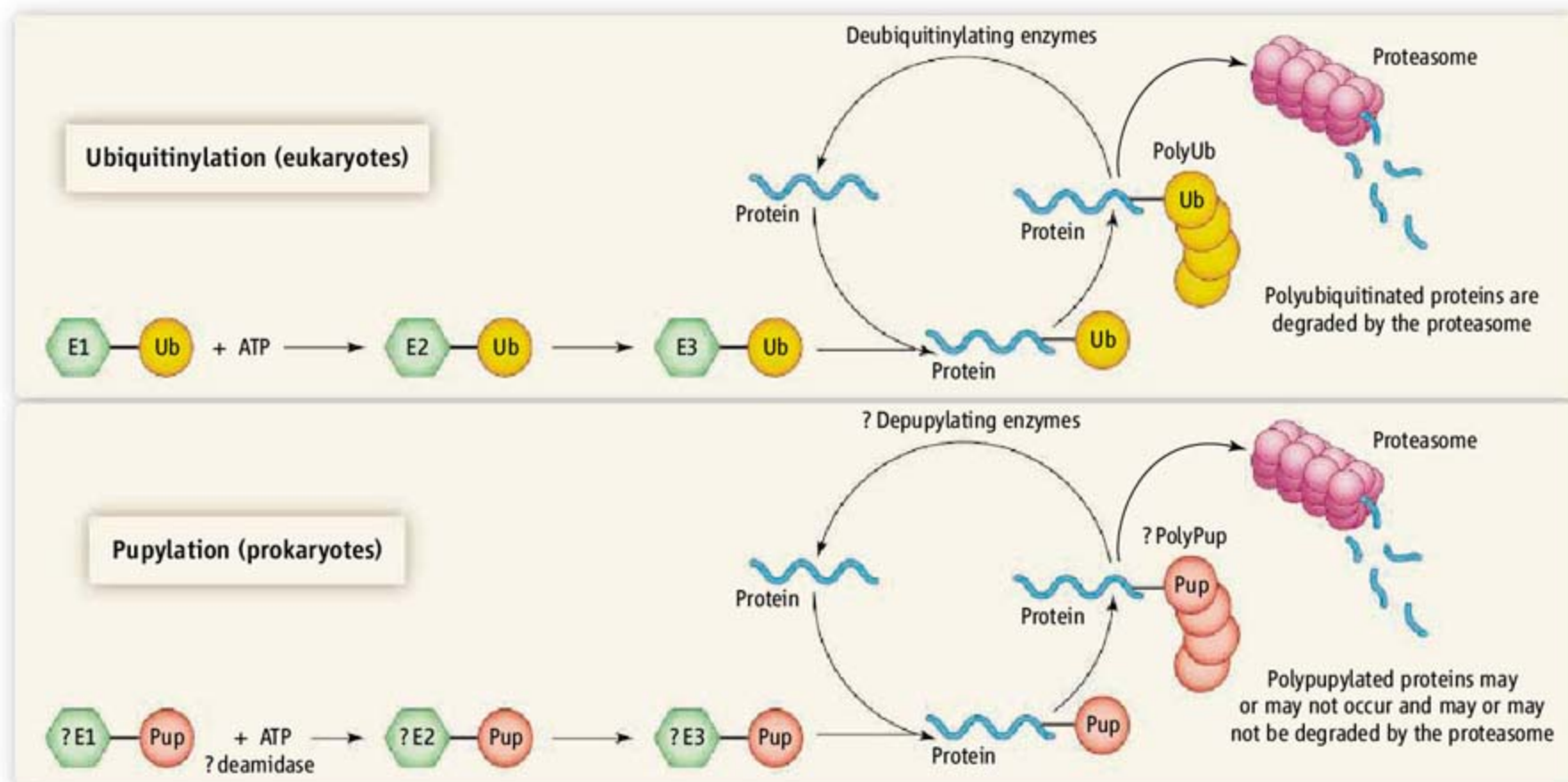
The proteasome is an adenosine 5'-triphosphate (ATP)-dependent protein degradation complex present in eukaryotes, as well as in several archaeobacterial and eubacterial species, including *Mtb* (2). The *Mtb* proteasome system, however, is not well characterized, and its functions remain elusive. Nitric oxide, an important signaling molecule, slows the growth of *Mtb*; genetic inactivation of an enzyme that produces

Tagging proteins with ubiquitin molecules so that they will be degraded in the proteasome is not a mechanism unique to eukaryotes.

nitric oxide (inducible nitric oxide synthase) increases the susceptibility of mice to *Mtb* infection (3). Two *Mtb* proteins, *Mycobacterium* proteasomal adenosine triphosphatase (ATPase) and proteasome accessory factor A, were identified in screens for factors that increase susceptibility of the bacterium to the lethal effects of nitric oxide. *Mycobacterium* proteasomal ATPase forms hexamers and exhibits ATPase activity similar to that of the eukaryotic ATPases involved in proteasome function (3). ATPase activity is required for the recognition, unfolding, and translocation of substrates into the proteasomal core in eukaryotes. *Mtb* bacteria that are resistant to nitric oxide, and consequently exhibit increased virulence in mice, require proteasomal activity, thereby linking protein degradation to pathogenesis. Interestingly, autophagy, another form of protein degradation in eukaryotes, is linked to a mechanism that inhibits the survival of *Mtb* within host cells independent of nitric oxide (4).

¹Department of Immunology, University of Texas Southwestern Medical School, Dallas, TX 75230, USA.

²Department of Molecular Biology, University of Texas Southwestern Medical School, Dallas, TX 75230, USA. E-mail: kim.orth@utsouthwestern.edu



Degradation parallels. Proteins in eukaryotes and prokaryotes are similarly modified by the small proteins ubiquitin (Ub) and Pup, respectively, targeting them for destruction by the proteasome. However, the specific mechanisms are likely to be different.

To understand how proteins are targeted for degradation in *Mtb*, Pearce *et al.* successfully defined the proteasome system in the bacterium, identified the first prokaryotic ubiquitin-like protein, and discovered a mechanism for activating and conjugating this protein to its substrates based on a unique chemistry. The authors identified Pup, a 6.9-kD protein, while searching for potential binding partners for *Mycobacterium* proteasomal ATPase. The carboxyl-terminal sequence (Gln-Lys-Gly-Gly-Gln) of Pup is very similar to the motif (X-X-Gly-Gly, where X is any amino acid) found at the end of most ubiquitin-like proteins. The carboxyl terminus of ubiquitin-like proteins is processed to expose the Gly-Gly portion of the motif, which prepares it for conjugation to substrates. The carboxyl-terminal glycine can covalently link, via an isopeptide bond, to a lysine in the target protein (5).

Pearce *et al.* demonstrate that Pup must become activated as well, but the enzymatic activity responsible for its conversion to an active form remains to be identified. As well, enzymes that conjugate activated Pup to substrates—similar to the ligases (E1, E2, and E3) that conjugate ubiquitin to substrates—have not been identified either. By contrast, homologs of the proteasome core and associated ATPases have been identified in *Mtb* (and in other bacteria). This suggests that the mechanism of attachment of Pup to substrates is different from that of eukaryotes, or that the *Mtb* enzymes involved share little amino acid

similarity with their eukaryotic counterparts. Undetectable amounts of Pup-conjugated proteasome substrates in strains of *Mtb* that lack functional proteasome accessory factor A hint at the involvement of this factor in the modification process.

Pearce *et al.* used mass spectrometry to characterize Pup activation and its conjugation to a *Mtb* proteasome substrate. The authors demonstrate the formation of an isopeptide bond between a lysine residue on the substrate and the carboxyl terminus of Pup—an event called “pupylation.” Strikingly, although Pup has a penultimate Gly-Gly motif, the linkage giving rise to pupylation is atypical in that Pup is attached to a substrate via a glutamate within a Gln-Lys-Gly-Gly-Glu motif. Clearly, this mechanism is distinct from ubiquitination in at least two ways (6). Pup protein is not proteolytically activated to reveal a carboxyl-terminal Gly-Gly motif that is used in the subsequent conjugation step. Also, the amino acid at the carboxyl terminus of Pup that is conjugated to the target protein is glutamate, not glutamine. This supports the authors’ hypothesis that Pup is deamidated before or during conjugation to substrates. Similar to ubiquitin, the activated form of Pup is covalently attached to a specific lysine residue of a proteasome substrate. Thus, although pupylation differs from ubiquitination in terms of the mechanism of conjugation, it appears to affect the demise of target proteins through a similar process of proteasome-mediated degradation.

Besides protein degradation, pupylation may have other functional consequences for proteins, ranging from subcellular sorting to secretion. For example, unlike eukaryotes, bacteria do not have subcellular organelles or a nuclear membrane, yet certain proteins need to be properly localized for bacteria to be viable and proliferate. Like eukaryotic ubiquitination, NEDDylation, or SUMOylation, the discovery of this prokaryotic posttranslational protein modification raises many questions about how proteins are targeted for pupylation. Like ubiquitin, does Pup get removed from proteins and recycled? Also, the enzymes that use this unique chemistry for conjugation may represent candidates for drug targeting. Most importantly, the study by Pearce *et al.* presents an exciting new paradigm for protein regulation by bacteria.

References and Notes

1. M. J. Pearce, J. Mintseris, J. Ferreyra, S. P. Gygi, K. H. Darwin, *Science* **322**, 1104 (2008); published online 2 October 2008 (10.1126/science.1163885).
2. A. Lupas, P. Zwickl, W. Baumeister, *Trends Biochem. Sci.* **19**, 533 (1994).
3. M. J. Pearce *et al.*, *EMBO J.* **25**, 5423 (2006).
4. M. G. Gutierrez *et al.*, *Cell* **119**, 753 (2004).
5. E. S. Johnson, *Annu. Rev. Biochem.* **73**, 355 (2004).
6. K. H. Ventii, K. D. Wilkinson, *Biochem. J.* **414**, 161 (2008).
7. K.O. is an Arnold and Mabel Beckman Young Investigator, a Burroughs Wellcome Investigator, and a W. W. Caruth Jr. Scholar. S.M. is a Helen Hay Whitney Postdoctoral Fellow.

10.1126/science.1166485

Physiographic Control on the Development of *Spartina* Marshes

Gerardo Fragoso^{1*} and Tom Spencer²

Spartina grasses, which form extensive marshes throughout the temperate world and often constitute the lowest vascular cover relative to sea level, have been prominent in the development of current ideas on coastal wetland development and response to physiographic change. Over the past five decades, a substantial body of research has indicated that *Spartina* production is primarily regulated by submergence and the resulting edaphic conditions (1–3). The physical sedimentary environment is in turn considered to affect production through its effect on marsh-surface elevation relative to sea level. However, our results working with *Spartina anglica* (2) show that production and marsh perennation are controlled by variation in surface level relative to the plant's meristematic base and are not hindered by prolonged submergence (4). Experimental ground-level displacement above the original marsh surface resulted in displacement of *Spartina*'s basal meristematic zone to a higher base (Fig. 1) consistently located about 2 cm below the new surface, from which a new clonal cohort emerged, leaving below the old base with its earlier, senescent cohort.

Although accretion is known to foster production, the effect has been attributed to the ameliorating effects of increased elevation on the putative negative impact of increased submergence, from sea-level rise, on plant vigor (5). However, orthogonal disaggregation of surface-level displacement and submergence conditions shows that, after taking into account the effect of submergence, growth was significantly greater in plants subject to upward surface-level displacement of only 2.5 cm than in plants in control treatments, whereas plant growth after a reduction in surface level of 1.0 cm was significantly lower than that in controls. In turn, after the effect of surface-level changes was taken into account, plants under continuous submergence showed significantly greater growth than those under intermittent inundation, whereas no significant difference in shoot growth occurred under continuous submergence whether the growing medium was aerated or stagnant. Although *Spartina* establishes perennial marshes, perennation depends chiefly on vegetative reproduction of individual clonal modules, which have a life span of 1 or 2 years (2). We suggest that basal-meristem displacement provides the basis of marsh perennating strategy because an accretionary environment enables

regular meristematic, and therefore vegetative, renewal. In turn, with a location only about 2 cm below ground surface required for basal-meristem establishment, even a small degree of erosion can expose the basal zone, hindering production. We thus suggest that production of clonal cohorts from the same, aging base in poor sedimentary environments leads to marsh senescence.

The applicability of our findings to other marsh plants remains to be tested. However, the morphological and paradigmatic parallels between *S. anglica*, its genetic parents, and other low-lying rhizomatous halophytes suggest that this mechanism may be involved more generally in the process of marsh development. Analysis of *Spartina* marshes has shown that marsh distribution is not related to sea level, although confirming that primary forcing is exerted by a then-undetermined factor regulated by tidal range (2, 6). Our findings indicate that the sedimentary

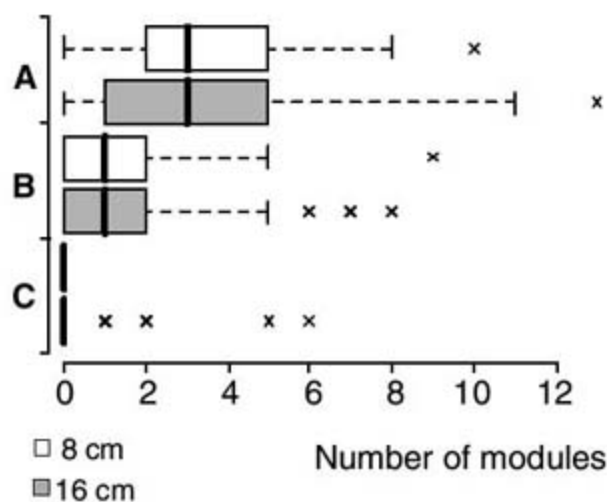


Fig. 1. Number of clonal modules (i.e., shoots and buds) per stem produced from (A) the new basal meristematic zone, counted as the first "node," which consisted of a nodular agglomeration formed consistently at ~2 cm from the new surface, regardless of treatment; (B) second and third nodes below the base; and (C) fourth and lower nodes in *S. anglica* plants subjected to surface displacement of 8 and 16 cm above the original marsh surface. Results are presented as box plots (9), each consisting of a box, divided at the median, whose left- and right-hand sides are drawn at the lower and upper quartiles. Dotted lines are drawn from the lower and upper quartiles to the smallest and largest observations within 1.5 interquartile ranges of each side of the box. All further values are plotted individually (x). Abundant roots of different diameters, ranging down to small filaments, also emerged from the new base. Modules forming from subsequent individual nodes below the base (nodes 2, 3, 4, etc.) were separated by internodal stem sections >1 cm long.

environment, which is tidally regulated, directly controls production and vegetative renewal, whereas prolonged submergence does not hinder growth of vegetative modules that emerge from new basal meristems. Edaphic products of submergence, such as interstitial sulfide, apparently deleterious in hydroponic conditions, have been found to be innocuous or even beneficial in solid substrate (7). Moreover, susceptibility to hypoxic conditions has been observed when experimental subjects are short forms (8), which commonly grow in poor accretionary environments and are therefore likely to originate from aging meristematic bases. Sedimentation and submergence often operate collinearly in the field: Stagnant areas are often sediment-starved, and sedimentary-active areas are often well drained. Thus, correlational observations may attribute the effects of sedimentary conditions on production to submergence unless both variables are experimentally disaggregated. When measured across several marshes, data on production and on sulfide distributions show no consistent relationship, with greater differences occurring between, rather than within, marshes (7). Our findings may also provide an explanation for the phenomenon of *Spartina* die-back, the causes for which have remained elusive for more than half a century (2, 3, 7). Although marsh production is known to be affected by a wide variety of both bottom-up and top-down factors, current theory of marsh ecology holds that stress from submergence is a major control. Our results suggest that plant responses to changes in sedimentary conditions determine marsh development and survival in the short term, independently of long-term changes in relative sea level.

References and Notes

1. A. C. Redfield, *Science* **147**, 50 (1965).
2. A. J. Gray, D. F. Marshall, A. F. Raybould, *Adv. Ecol. Res.* **21**, 1 (1991).
3. P. J. Goodman, W. T. Williams, *J. Ecol.* **49**, 391 (1961).
4. Further information on methods and data are available as supporting material on Science Online.
5. I. A. Mendelsohn, N. L. Kuhn, *Ecol. Eng.* **21**, 115 (2003).
6. K. L. McKee, W. H. Patrick Jr., *Estuaries* **11**, 143 (1988).
7. J. T. Morris, C. Haley, R. Krest, in *Biological and Environmental Chemistry of DMSP and Related Sulfonium Compounds*, R. Kiene, P. Visser, M. Keller, G. Kirst, Eds. (Plenum, New York, 1996), pp. 87–95.
8. J. T. Morris, J. W. H. Dacey, *Am. J. Bot.* **71**, 979 (1984).
9. J. W. Tukey, *Exploratory Data Analysis* (Addison-Wesley, Reading, MA, 1977).
10. We thank H. Gillett, A. Hayes, F. Hughes, J. Scharlemann, M. Tester, and H. Viles for helpful discussions and support.

Supporting Online Material

www.sciencemag.org/cgi/content/full/322/5904/1064/DC1

Materials and Methods

Tables S1 and S2

2 May 2008; accepted 9 September 2008

10.1126/science.1159973

¹United Nations Environmental Programme–World Conservation Monitoring Centre (UNEP-WCMC), 219 Huntingdon Road, Cambridge CB3 0DL, UK. ²Cambridge Coastal Research Unit, Department of Geography, University of Cambridge, Cambridge CB2 3EN, UK.

*To whom correspondence should be addressed. E-mail: gerardo.fragoso@unep-wcmc.org

Reconstruction of Zebrafish Early Embryonic Development by Scanned Light Sheet Microscopy

Philipp J. Keller,^{1,2*} Annette D. Schmidt,² Joachim Wittbrodt,^{1,2,3,4*} Ernst H.K. Stelzer¹

A long-standing goal of biology is to map the behavior of all cells during vertebrate embryogenesis. We developed digital scanned laser light sheet fluorescence microscopy and recorded nuclei localization and movement in entire wild-type and mutant zebrafish embryos over the first 24 hours of development. Multiview in vivo imaging at 1.5 billion voxels per minute provides “digital embryos,” that is, comprehensive databases of cell positions, divisions, and migratory tracks. Our analysis of global cell division patterns reveals a maternally defined initial morphodynamic symmetry break, which identifies the embryonic body axis. We further derive a model of germ layer formation and show that the mesendoderm forms from one-third of the embryo's cells in a single event. Our digital embryos, with 55 million nucleus entries, are provided as a resource.

Model systems such as *Caenorhabditis elegans* and *Ciona intestinalis* lend themselves well to comprehensive analyses at the cellular level, for example, by conventional microscopy (1, 2). However, global studies of complex vertebrate species encounter technical limitations. Whereas the formation of single organs has been reconstructed by imaging and tracking nuclear fluorescent proteins for several hours (3–6), obtaining quantitative morphogenetic data representing the full embryos over the entire time course of embryogenesis remains a major challenge.

For comparison, 671 cells need to be followed during *C. elegans* embryogenesis, whereas the analysis of complex vertebrate embryos requires the simultaneous tracking of tens of thousands of cells. High spatiotemporal resolution, ultralow photobleaching rates, and an excellent signal-to-noise ratio are crucial. In order to follow the nuclei of the 16,000 cells of an 18-hour-old zebrafish embryo, a volume of 1000 by 1000 by 1000 μm^3 must be recorded at least once every 90 s because nuclei move several micrometers per minute. In order to reliably detect all nuclei, the set of images must be acquired at a step size of no more than 3 μm along the *z* axis, resulting in ~350 images per time point. In addition, an image size of at least 1500 by 1500 pixels is necessary to elucidate nuclear morphologies. Thus, the observation must be

performed at a continuous imaging speed of at least 10 million volume elements (voxels) per second. A dynamic range of at least 12 bit covers the varying expression levels of genetically encoded markers. At the same time, photobleaching and phototoxicity (7) must be minimized to ensure the physiological development of the embryo. Finally, the embryo's central yolk cell is opaque at physiological wavelengths; therefore, imaging along multiple directions is needed to capture the development of the entire embryo.

The most widely applied advanced fluorescence imaging techniques rely on confocal and multiphoton microscopes, which provide three-dimensional resolution but lack the combination of high-speed imaging and low phototoxicity required for the fast recording of entire embryos over long periods of time. They are also unsuited for multiview imaging (8). To overcome some of these limitations, we recently introduced light sheet–based technologies to biological imaging (SPIM) (9). With these microscopes, the specimen is illuminated along a single plane with a sheet of light that is typically generated via a set of

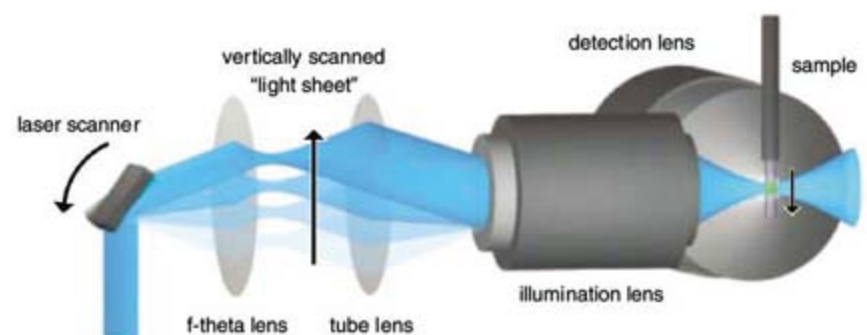
apertures and by focusing a collimated beam with a cylindrical lens. This arrangement provides three-dimensional optical sectioning and reduces the energy load on the specimen (9–11).

Digital scanned laser light sheet fluorescence microscopy. To achieve the imaging speed and quality for recording entire embryos, we developed digital scanned laser light sheet fluorescence microscopy (DSLM) (fig. S1). The idea behind DSLM is to generate a “plane of light” with a laser scanner that rapidly moves a micrometer-thin beam of laser light vertically and horizontally through the specimen (Fig. 1 and movie S1).

This approach has several advantages over standard light sheet microscopy. First, DSLM illuminates each line in the specimen with the same intensity, a crucial prerequisite for quantitative imaging of large specimens (fig. S2). Second, in contrast to standard light sheet–based microscopy, DSLM does not rely on apertures to form the laser profile, which reduces optical aberrations and thereby provides an exceptional image quality. Third, the entire illumination power of the light source is focused into a single line, resulting in an illumination efficiency of 95% as compared with ~3% in standard light sheet microscopy. Fourth, DSLM allows to generate intensity-modulated illumination patterns (structured illumination) (12), which can be used to enhance the image contrast in highly light-scattering specimens, such as large embryos. Furthermore, DSLM combines (i) an imaging speed of 63 million voxels per second, (ii) a signal-to-noise ratio of 1000:1 at a lateral and axial resolution of 300 and 1000 nm, respectively, and (iii) ultralow excitation energies confined to a single plane (1.7 μJ at 488 nm passing each plane in our zebrafish experiments) (8).

In order to analyze zebrafish embryonic development, we recorded stacks of ~400 images (2048 by 2048 pixels each) in intervals of 60 or 90 s and along two opposing directions (Fig. 2 and movies S2 and S3). The embryos were embedded in agarose, kept at a constant temperature (26.5°C) [see (13) for developmental stages] throughout the experiment, and exhibited normal development (8). Nuclei were labeled at the one-cell stage by mRNA injection of H2B-eGFP, a fusion protein of human histone-2B and the en-

Fig. 1. Digital scanned laser light sheet microscopy. The laser beam illuminates the specimen from the side and excites fluorophores along a single line. Rapid scanning of a thin volume and fluorescence detection at a right angle to the illumination axis provides an optically sectioned image (movie S1). The f-theta lens converts the tilting movement of the scan mirror into a vertical displacement of the laser beam. The tube lens and the illumination objective focus the laser beam into the specimen, which is positioned in front of the detection lens.



¹Cell Biology and Biophysics Unit, European Molecular Biology Laboratory (EMBL), Meyerhofstrasse 1, D-69117 Heidelberg, Germany. ²Developmental Biology Unit, EMBL, Meyerhofstrasse 1, D-69117 Heidelberg, Germany. ³Institute of Zoology, Department for Developmental Physiology, University of Heidelberg, INF 230, D-69120 Heidelberg, Germany. ⁴Institute of Toxicology and Genetics, Karlsruhe Institute of Technology (KIT), Post Office Box 3640, D-76021 Karlsruhe, Germany.

*To whom correspondence should be addressed. E-mail: keller@embl.de (P.J.K.), wittbrodt@embl.de (J.W.)

hanced green fluorescent protein (GFP) reporter, which localizes to chromatin (14). This presents an effective marker for cell positions and cell divisions because changes in chromatin density can be directly observed. Imaging was performed for 24 hours, providing about 400,000 images per embryo.

We measured nuclear fluorescence intensities and found that steady-state GFP concentrations are reached at ~12 hours post fertilization (hpf), owing to the limited stability of the injected mRNA. However, despite continuous imaging for another 12 hours, the fluorescence intensity levels remained constant. This indicates a negligible photobleaching rate in DSLM high-speed live imaging (fig. S3). We applied comparable experimental settings in state-of-the-art confocal and two-photon fluorescence microscopes. The embryo was exposed to a factor of 5600 more energy in the confocal (9.6 mJ at 488 nm passing each plane) and to a factor of 10^6 more energy in the two-photon fluorescence microscope (1.7 J at 930 nm passing each plane) (8). Thus, DSLM allows for a comprehensive, quantitative analysis of zebrafish embryonic development, over periods longer than 24 hours, with high spatiotemporal resolution and ultralow phototoxicity.

The digital embryo. To efficiently handle the large amounts of microscopy data, we developed a parallelized image segmentation pipeline, i.e., a set of software modules that automatically detects nuclei in the raw images by using large-scale computer networks (at the European Molecular Biology Laboratory, EMBL; and Karlsruhe Institute of Technology, KIT) (fig. S4). Image segmentation was performed by (i) recursive refinement of the three-dimensional shapes and internal structures of objects detected in the microscopy data (fig. S5), (ii) subsequent filtering of these objects according to the morphological characteristics expected for nuclei, and (iii) an analysis of the identification rate for each nucleus throughout time (8). Because of the high signal-to-noise ratio of the DSLM data, we obtained a robust average segmentation efficiency of 97% during the first 10 hours of embryogenesis and an average of 90% during late gastrulation (8). The microscopy data acquired along the two opposing directions were segmented separately and subsequently combined into a complete data set by a fusion algorithm (8). A “digital embryo” was derived for each experiment and constitutes a comprehensive database of the positions, sizes, and fluorescence intensities of 92% of the nuclei in the entire embryo (determined by manual controls) (8) throughout early embryogenesis from early cleavage stages up to the onset of heartbeat (Fig. 2 and movie S3). The algorithms, furthermore, provide 99.5% efficiency in converting these nuclear positions into migratory tracks, corresponding to an error per 200 time points or 3 to 5 hours (8). We pro-

cessed seven 24-hour time-lapse recordings of zebrafish embryogenesis and obtained developmental blueprints with 55 million nuclear data entries, including a reconstruction of the zebrafish *one-eyed pinhead* mutant (*MZoop*) (15). Our data on zebrafish embryogenesis from 1.5 to 30 hpf are presented as time-lapse movies of the microscopy recordings (movies S2, S4, S7, and S12) and as movies of the reconstructions (movies S3, S5, S8, and S13). Further analysis of the digital embryos (8) provides a detailed description of morphogenetic and developmental processes at subcellular resolution (fig. S3), spatiotemporal coordinates and polarity of cell divisions (movie S10 and Fig. 3B and fig. S6), global nuclear population statistics (figs. S3 and S6), embryo-to-embryo variability in morphogenetic key parameters (fig. S7), and cell tracking throughout development (movies S9, S11, S14, and S15 and Fig. 3A).

The digital embryos provide direct quantitative access to a global analysis of cell and tissue behavior, as shown below. In order to visualize morphogenetic domains, we tracked individual cell movements up to somitogenesis stages and color-encoded the information on directionality (movies S9, S14, and S15 and Fig. 3A). This analysis identifies morphogenetic movements during development (emboly, epiboly, convergence, and extension) and provides a global, quantitative perspective of their interplay.

Early morphodynamic symmetry-breaking. Nuclear β -catenin is one of the earliest markers for the future dorsal side of the embryo (~512-cell stage) (16, 17), which raises the question of whether morphodynamic symmetry-breaking also occurs at this early time point. We mapped and analyzed the three-dimensional patterns and polarity of early cell divisions in five embryos during 1.5 to 7 hpf [all experiments were per-

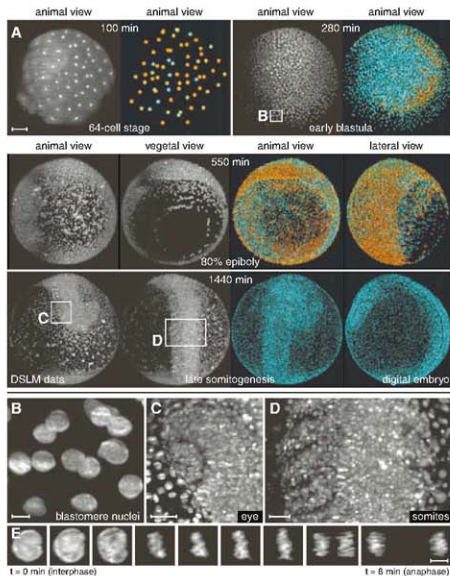


Fig. 2. Imaging and reconstruction of zebrafish embryogenesis. (A) Maximum-intensity projections (left) and digital embryo reconstructions (right) of nuclear-labeled wild-type zebrafish embryo (movies S2 and S3) at the indicated times and developmental stages. Color code: movement speeds (0 to 1.2 $\mu\text{m}/\text{min}$, cyan to orange). Images are Lucy-Richardson-deconvolved (10 iterations). Zeiss C-Apochromat $10\times/0.45$. Scale bar, 100 μm . (B to D) Insets and parts) Frames of close-ups on (A), demonstrating subcellular resolution of various areas of the developing embryo. Enlargements scale bar, 10 μm (B), 30 μm (C and D). (E) Nuclear morphology of a dividing blastomere from movie S7 (intensity-normalized). Scale bar, 10 μm . *t*, time.

formed at 26.5°C [13]) (movie S10). Whereas planes of cell division are evenly distributed [fig. S6b; in contrast to the asymmetry in gas-

trulation [18, 19], a symmetry break in the spatiotemporal pattern occurs at the 512-cell stage (movie S10 and Fig. 4A). Initially, cell divisions

follow 3-min-long radial waves, originating in the embryonic center. After the 512-cell stage, two circular peripheral waves break this radial symmetry (Fig. 4, A and B, and fig. S8 and movie S10). They occur during division cycles 10 to 13 at an angle that correlates with the future body axis (Fig. 4B).

To investigate whether the break of radial symmetry can also be related to nuclear densities, we determined the nuclear counts in small volumes around the animal pole. This analysis indicates a divergence commencing at 5 hpf, i.e., two hours after the symmetry break in cell division patterns, but still before the morphological signs of shield formation at the onset of convergence (8 hpf) (Fig. 4C). Between 5 and 8 hpf, reduced cell proliferation rates in the future embryonic shield result in lower cell densities dorsally (rather than dorsal compaction) (20, 21) and, thereby, indicate the position of the future body axis.

Thus, by dissecting the three-dimensional pattern of cell divisions in the entire embryo, we reveal an early morphodynamic symmetry break, concomitant with the nuclear localization of β -catenin, that allows an early prediction of the orientation of the body axis, preceding the midblastula transition (22).

A model of hypoblast formation. In addition to enabling the analysis of global quantitative studies, the digital embryos allow us to focus on confined morphogenetic events. We investigated the formation of the hypoblast, the inner cell layer, which gives rise to mesoderm and endoderm. The formation of the hypoblast is known to result from internalization of cells (emboly) of the outer layer (epiblast) during gastrulation and stretching and thinning of cell sheets over the yolk (epiboly) (23). Our data

Fig. 3. Cell tracking and detection of cell divisions in the digital embryo. (A) Microscopy data (right half of embryo: animal view, maximum projection) and digital embryo (left half of embryo) with color-encoded migration directions (see movie S9). Color code: dorsal migration (cyan), ventral migration (green), toward or away from body axis (red or yellow), toward yolk (pink). (B) Dividing cells (red) and their daughter cells (blue). See movie S10 and fig. S6b for complete coverage (1.7 to 6.7 hpf). Yellow, red, and gray overlays indicate progression of the peripheral cell division waves during division cycle 12 (arrows show direction of peripheral waves; $t_0 = 216$ min, see also Fig. 4).

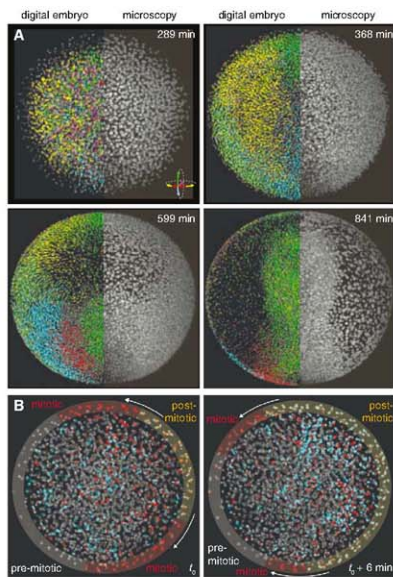
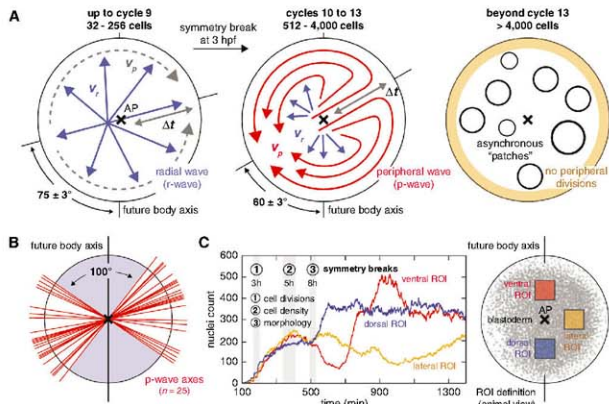


Fig. 4. Symmetry-breaking of the global cell division pattern. (A) Illustration of the cell division patterns during early zebrafish embryogenesis: fast radial waves (cycles 1 to 9, progression speed v_r), slow circular peripheral waves (cycles 10 to 13, progression speed v_p), and asynchronous cell-division patches (cycles 14+). Errors are indicated as SEM. A quantification of the parameters v_r , v_p , and the time shift Δt between radial and peripheral waves is provided in fig. S8. (B) Symmetry axes of 25 peripheral waves (20 slow waves in cycles 10 to 13 and 5 fast waves in cycle 9; $n = 5$ embryos). Of the 25 waves, 92% occurred at an angle of 45 to 90° to the future body axis. (C) Nuclei counts in three 110 by 110 μm^2 domains (future dorsal, ventral, and lateral) reveal the first symmetry break in cell densities at 5 hpf. The symmetry break in the cell division pattern (3 hpf) precedes the symmetry break in cell densities (5 hpf) and the first morphogenetic symmetry break (onset of convergence, 8 hpf).



reveal a pronounced “embolic wave” of internalization and regional differences in modes of internalization (Fig. 5 and fig. S9 and movies S14 and S15).

Starting at 5.8 hpf (40% epiboly at 26.5°C) (13) and lasting for 2 hours, ~1550 cells (34% of all cells) internalize around the perimeter of the blastopore to form the mesendoderm (Fig. 5

and fig. S9). After this time window, we did not observe any further cells moving from epiblast to hypoblast.

Internalizing cells follow the path of a wave, which stretches inward toward the yolk cell, reaches a peak height of 50 μm before rolling over, touches the deep cells situated closer to the animal pole (Fig. 5, green cell population, and movie S16), and completes epiboly at 7.5 hpf. Whereas cells internalize around the entire perimeter, the wave is most prominent dorsally. The onset of internalization is synchronized along the blastopore (fig. S9, c and d), but the folding-over at the dorsal shield takes 30 min longer than at other locations along the blastopore. As a consequence of this dorsally pronounced emboly, the dorsal leading edge of epiboly lags behind in its vegetal approach (movie S14).

Modes of internalization (24), either involution (synchronously flowing sheets as in amphibian gastrulation) or ingression (cells individually sinking inward), have been subject to intense discussion (25, 26). To determine whether modes of internalization vary regionally, we generated “internalization maps” for the dorsal and ventral hemispheres (fig. S9a). An analysis of time shifts between internalization events around the blastopore reveals that asynchronous internalization and radial intercalation of single cells in the shield region disrupt the internalization pattern on the dorsal hemisphere [fig. S9, b and c; supporting previous single cell-tracking studies (27, 28)]. On the ventral hemisphere, however, mesendoderm internalization occurs exclusively in a synchronous manner (fig. S9, b and e), reminiscent of involution (24) or an intermediate mechanism termed “synchronized ingression” (23, 29).

In dorso-anterior regions on the animal hemisphere, internalized cells move antiparallel to epiblast cells toward the animal pole for ~100 min (Fig. 5, purple and yellow cell populations; movie S14). In contrast, internalized cells in the ventral hemisphere change direction within 30 min after internalization and migrate toward the vegetal pole (Fig. 5 and movies S15 and S16).

Unlike gastrulation in *Xenopus* (30), a continuous rolling internalization with hypoblast cells moving toward the animal pole does not occur as epiboly proceeds to the vegetal hemisphere (movie S16). Instead, hypoblast cells follow a well-defined leading edge and move parallel to epiblast cells toward the vegetal pole (movie S14, xz slice).

A comparative reconstruction of the zebrafish *MZoepe* mutant quantitatively describes its deficiency in forming mesendoderm (15, 27): Whereas ~1550 cells internalize via the embolic wave in the wild-type embryo, the *MZoepe* digital embryo (movies S4 and S5) reveals merely ~60 internalizing cells in the entire embryo during the same time period (movie S6). This visualization shows that the oversized epiblast (15) forms through convergence and absence

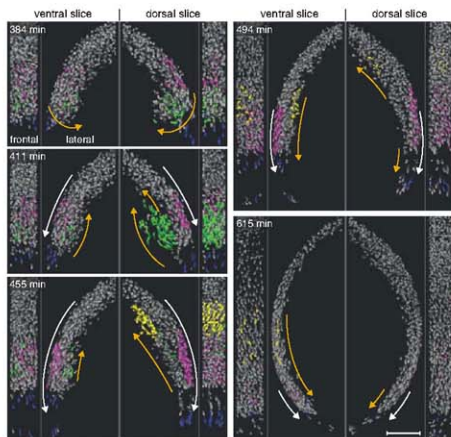
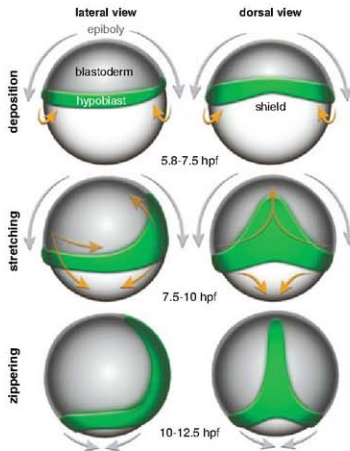


Fig. 5. Mesendoderm internalization and migration in dorsal and ventral hemispheres. Frontal and lateral views of slices on dorsal (shield region, right) and ventral hemispheres (opposite of shield, left). Four cell populations were tracked (movie S16): green or yellow nuclei in the early or late embolic wave, blue nuclei at the leading edge of epiboly, and noninternalizing pink nuclei. Orange and white arrows indicate hypoblast and epiblast cell movements. Scale bar, 100 μm .

Fig. 6. A model of mesendoderm formation in zebrafish. The hypoblast forms in a single synchronized internalization wave around the entire circumference (“deposition”). On the dorsal side, internalized cells become distributed along the entire future body axis (“stretching”). On the ventral side, the internalized ring of hypoblast cells moves toward the vegetal pole. The ring closes at the vegetal pole (“zipping”) and completes the formation of the hypoblast. Orange arrows indicate hypoblast cell movements. Gray arrows indicate epiboly.



of internalization and dorsal stretching (movies S5 and S6). Convergence is highly abnormal and prolonged, with ventral cells moving across the animal pole toward the epiblast's center (movie S6).

In conclusion, we show that wild-type hypoblast cells are deposited in a single embolic wave that occurs before epiboly moves the blastopore to the vegetal hemisphere. The embryo is therefore split into a dorso-anterior domain characterized by antiparallel movements of germ layers and a dorso-posterior domain, where the parallel migration of epi- and hypoblast stretches the hypoblast. In the trunk and tail regions, parallel germ layer migration and convergence and/or extension move the mesendoderm, deposited in a ring around the blastopore, to an axial position, closing the blastopore dorsally from anterior to posterior like a zipper.

Our analysis puts previous cell-tracking studies (31, 32) into a global perspective. Regarding mesendoderm formation in zebrafish, a three-stage model is proposed (Fig. 6): Mesendoderm forms by (i) global deposition in a single event, (ii) dorsal stretching, and (iii) antero-posterior “zippering.”

Different modes of internalization characterize the initial deposition, with synchronous events (involution and/or synchronized ingression) occurring on the ventral side, and disruption of synchrony (asynchronous ingression and/or radial intercalation) on the dorsal side. Our analysis of the entire embryo describes the migratory behavior of 92% of all cells throughout gastrulation and leads to a comprehensive model that complements and partially revises the general view of zebrafish gastrulation (30, 33). In particular, our finding of a single embolic event contradicts the current assumption of a continuous internalization during epiboly (30, 33–35).

Conclusions. We developed and applied DSLM as a fluorescence microscopy system for the high-speed in vivo observation of embryonic development at subcellular resolution, which enabled cell tracking in the entire early zebrafish embryo. Applying the automated image segmentation pipeline provides a “digital embryo” that visualizes complex developmental events in a global context. We demonstrate application of the method to a quantitative reconstruction of early cell division patterns. This analysis reveals an initial morphodynamic symmetry break, before the onset of zygotic transcription, coinciding with the embryonic body axis. We also follow germ layer formation on a quantitative level and provide a comprehensive model of hypoblast formation in zebrafish embryos. We show that the mesendoderm forms from one-third of the embryo's cells in a single embolic event by means of regionally different modes of internalization.

Our digital embryos constitute complex data sets with information about millions of nuclear positions, as well as thousands of cell tracks and

cell divisions per embryo. These data are publicly available in a central repository as a resource for further analyses (36).

Detailed recordings of embryonic development will allow the measurement and the modeling of the mechanical forces that drive morphogenesis, e.g., by complementing existing data with information about membrane dynamics. Further applications range from the construction of databases of organ development (using tissue-specific fluorescent lines) and the analysis of mutant phenotypes (37–39) to the quantification of the variability of vertebrate cell lineages. Moreover, with its high-throughput and high-content capabilities DSLM presents a powerful tool for systems biology and enables complete in vivo reconstructions of gene expression dynamics that incorporate the steadily growing number of gene and enhancer trap lines (40–42). In addition, DSLM should be suitable for analyses of entire mouse, chicken, and *Xenopus* early embryogenesis—the unfavorable light-scattering tissue properties of *Xenopus* can be partially overcome by DSLM's intrinsic structured illumination and multiview imaging capabilities. The comparison of individuals within species and across species borders might allow us to reveal the conserved and emerging morphogenetic rules of embryogenesis.

References and Notes

1. J. E. Sulston, E. Schierenberg, J. G. White, J. N. Thomson, *Dev. Biol.* **100**, 64 (1983).
2. P. Lemaire, *Science* **312**, 1145 (2006).
3. Y. Hirose, Z. M. Varga, H. Kondoh, M. Furutani-Seiki, *Development* **131**, 2553 (2004).
4. M. Rembold, F. Loosli, R. J. Adams, J. Wittbrodt, *Science* **313**, 1130 (2006).
5. S. J. England, G. B. Blanchard, L. Mahadevan, R. J. Adams, *Development* **133**, 4613 (2006).
6. S. G. Megason, S. E. Fraser, *Cell* **130**, 784 (2007).
7. R. Y. Tsien, L. Ernst, A. Waggoner, in *Handbook of Biological Confocal Microscopy*, J. B. Pawley, Ed. (Springer, New York, 2006), pp. 338–352.
8. Materials and methods are available as supporting material on *Science* Online.
9. J. Huisken, J. Swoger, F. Del Bene, J. Wittbrodt, E. H. Stelzer, *Science* **305**, 1007 (2004).
10. P. J. Keller, F. Pampaloni, E. H. Stelzer, *Curr. Opin. Cell Biol.* **18**, 117 (2006).
11. P. J. Keller, F. Pampaloni, E. H. Stelzer, *Nat. Methods* **4**, 843 (2007).
12. M. A. Neil, R. Juskaitis, T. Wilson, *Opt. Lett.* **22**, 1905 (1997).
13. K. K. Hisaoka, H. I. Battle, *J. Morphol.* **102**, 311 (1958).
14. T. Kanda, K. F. Sullivan, G. M. Wahl, *Curr. Biol.* **8**, 377 (1998).
15. K. Gritsman *et al.*, *Cell* **97**, 121 (1999).
16. S. Schneider, H. Steinbeisser, R. M. Warga, P. Hausen, *Mech. Dev.* **57**, 191 (1996).
17. S. T. Dougan, R. M. Warga, D. A. Kane, A. F. Schier, W. S. Talbot, *Development* **130**, 1837 (2003).
18. M. L. Concha, R. J. Adams, *Development* **125**, 983 (1998).
19. Y. Gong, C. Mo, S. E. Fraser, *Nature* **430**, 689 (2004).
20. R. M. Warga, C. Nusslein-Volhard, *Dev. Biol.* **203**, 116 (1998).
21. B. Schmitz, I. A. Campos-Ortega, *Roux Arch. Dev. Biol.* **203**, 374 (1994).

22. D. A. Kane, C. B. Kimmel, *Development* **119**, 447 (1993).
23. L. Solnica-Krezel, *Curr. Biol.* **15**, R213 (2005).
24. J. P. Trinkaus, *Cells into Organs: The Forces That Shape the Embryo* (Prentice-Hall, Englewood Cliffs, NJ), ed. 2, 1984.
25. D. Kane, R. J. Adams, in *Pattern Formation in Zebrafish*, L. Solnica-Krezel, Ed. (Springer, Heidelberg, 2002).
26. L. A. Rohde, C. P. Heisenberg, *Int. Rev. Cytol.* **261**, 159 (2007).
27. J. A. Montero *et al.*, *Development* **132**, 1187 (2005).
28. J. Shih, S. E. Fraser, *Development* **121**, 2755 (1995).
29. R. J. Adams, C. B. Kimmel, in *Gastrulation: From Cells to Embryo*, C. D. Stern, Ed. (Cold Spring Harbor Laboratory Press, Cold Spring Harbor, NY, 2004), pp. 305–316.
30. L. Wolpert, *Principles of Development* (Oxford Univ. Press, New York, ed. 3, 2007).
31. D. C. Myers, D. S. Sepich, L. Solnica-Krezel, *Dev. Biol.* **243**, 81 (2002).
32. D. S. Sepich, C. Calmelet, M. Kiskowski, L. Solnica-Krezel, *Dev. Dyn.* **234**, 279 (2005).
33. S. F. Gilbert, *Developmental Biology* (Sinauer Associates, Sunderland, MA, ed. 8, 2006).
34. R. M. Warga, C. B. Kimmel, *Development* **108**, 569 (1990).
35. G. Pezeron *et al.*, *Curr. Biol.* **18**, 276 (2008).
36. Movies and zebrafish digital embryos can be downloaded at www.embl-heidelberg.de/digitalembryo
37. D. A. Kane *et al.*, *Development* **123**, 47 (1996).
38. C. P. Heisenberg, M. Tada, *Semin. Cell Dev. Biol.* **13**, 471 (2002).
39. D. S. Sepich, L. Solnica-Krezel, *Methods Mol. Biol.* **294**, 211 (2005).
40. S. Ellingsen *et al.*, *Development* **132**, 3799 (2005).
41. S. Parinov, I. Kondrichin, V. Korzh, A. Emelyanov, *Dev. Dyn.* **231**, 449 (2004).
42. K. Asakawa *et al.*, *Proc. Natl. Acad. Sci. U.S.A.* **105**, 1255 (2008).
43. We thank U. Liebel, M. Alef, and M. Wahlers for excellent KIT/EMBL computer cluster support; the EMBL mechanical workshop for custom hardware; A. Riedinger and G. Ritter for custom electronics; F. Härle and A. Riedinger for custom microscope operating software; W. Dilling for technical drawings; M. Knop, K. Brown, K. Khairy, J. Martinez, D. Gilmour, and C.-P. Heisenberg for critical manuscript comments; L. Centanin for immunostained medaka embryos; C.-P. Heisenberg for MZoop mutants; S. Terjung for Leica SP5 support; G. Giese for Zeiss LSM 510 NLO support. Financial support: EU-FP6-STREP Plurigenes, DFG SFB-488 (J.W.); Studienstiftung des deutschen Volkes (P.J.K.); Hartmut Hoffmann-Berling International Graduate School of Molecular and Cellular Biology, HBIGS (A.D.S.). Contributions: P.J.K. outlined the digital embryo project, designed and built the DSLM, recorded the microscopy data, developed the image processing pipeline, performed the reconstructions and drafted the manuscript. A.D.S. developed the biological methods, performed the biological preparations, contributed to project planning and participated in the writing of the manuscript. E.H.K.S. outlined the DSLM development, cosupervised the project, and participated in manuscript preparation. P.J.K., A.D.S., and J.W. analyzed the digital embryos. J.W. guided the biological research, cosupervised the project, and participated in the writing of the manuscript.

Supporting Online Material

www.sciencemag.org/cgi/content/full/1162493/DC1

Materials and Methods

Figs. S1 to S9

References

Movies S1 to S16

30 June 2008; accepted 1 October 2008

Published online 9 October 2008;

10.1126/science.1162493

Include this information when citing this paper.

Kinetics of Individual Nucleation Events Observed in Nanoscale Vapor-Liquid-Solid Growth

B. J. Kim,¹ J. Tersoff,² S. Kodambaka,^{2*} M. C. Reuter,² E. A. Stach,^{1†} F. M. Ross^{2†}

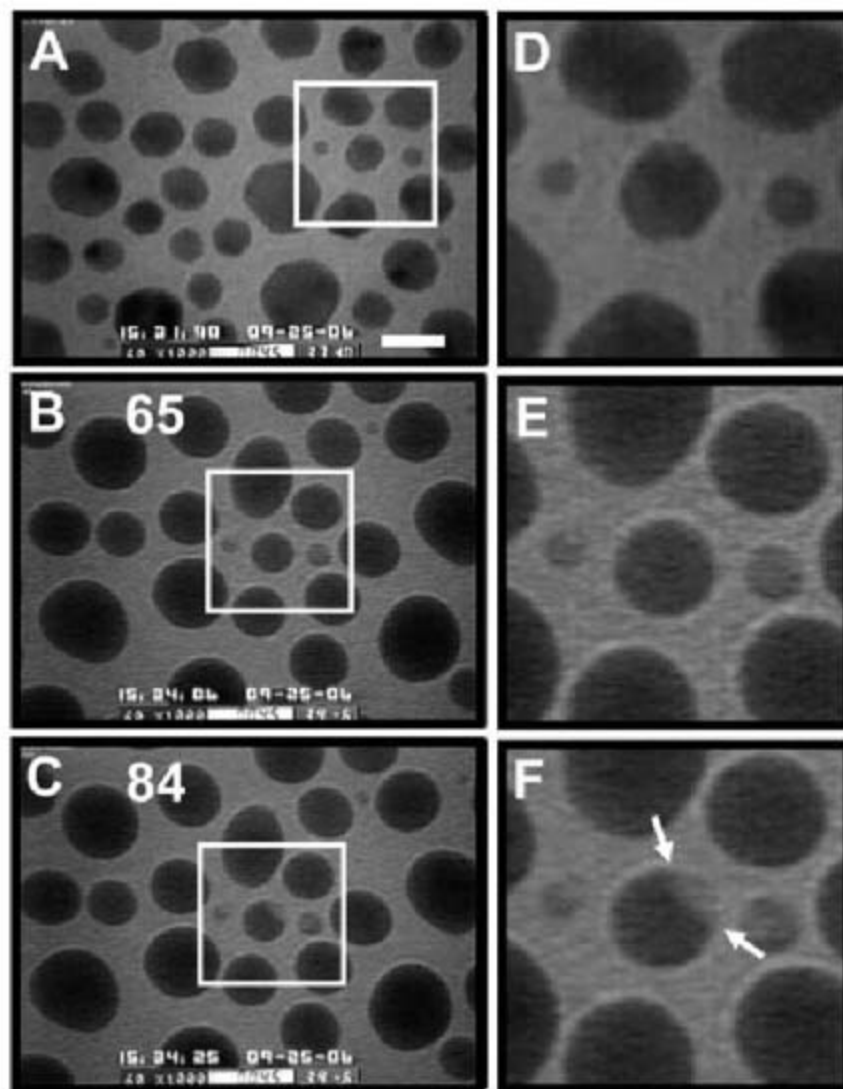
We measured the nucleation and growth kinetics of solid silicon (Si) from liquid gold-silicon (AuSi) catalyst particles as the Si supersaturation increased, which is the first step of the vapor-liquid-solid growth of nanowires. Quantitative measurements agree well with a kinetic model, providing a unified picture of the growth process. Nucleation is heterogeneous, occurring consistently at the edge of the AuSi droplet, yet it is intrinsic and highly reproducible. We studied the critical supersaturation required for nucleation and found no observable size effects, even for systems down to 12 nanometers in diameter. For applications in nanoscale technology, the reproducibility is essential, heterogeneity promises greater control of nucleation, and the absence of strong size effects simplifies process design.

Nucleation is central to all types of growth phenomena, but it is a fleeting event and thus difficult to observe in detail. Phase transitions in macroscopic samples typically involve a large number of distinct nucleation events, and the properties of the final material (such as grain-size distribution) are determined by the statistical ensemble of nucleation events. However, systems that are sufficiently small will transform by a single nucleation event. This raises issues such as statistical variability and size effects (1–3). These classic issues take on new urgency in the context of nanoscale technology, in which an entire functional structure such as a nanowire transistor may depend on a single nucleation event. Only recently, using innovative microscopy techniques, has it become feasible to study individual nucleation events in nanoscale systems (4–10).

We used ultrahigh-vacuum transmission electron microscopy (UHV-TEM) to examine the growth of Si from a AuSi eutectic liquid, a system of particular relevance for the initial stages of nanowire growth by the vapor-liquid-solid process (VLS) (11) and one in which devices such as wrap-gate field-effect transistors have been demonstrated (12–14). By comparing quantitative measurements of nucleation and growth with a simple kinetic model, we determined the critical supersaturation of Si in AuSi required for nucleation and explained in detail the subsequent growth kinetics. Hofmann *et al.* (10) recently reported in situ observations of nucleation and growth in a similar system, addressing the

“incubation time” for nucleation, which primarily reflects the vapor-liquid kinetics and is not sensitive to the nucleation process. Here, we have extracted key information about the nucleation process itself, which allows us to examine size effects and reproducibility, both of which are important for a fundamental understanding of nucleation and for reliable fabrication of nanowires for applications.

Fig. 1. (A to C) Bright-field images extracted from a video obtained during nucleation of Si from polycrystalline Au clusters at 525°C and 4×10^{-6} torr disilane. Scale bar, 20 nm. (A) Image acquired before opening the leak valve, showing polycrystalline Au particles, as indicated by their faceted shapes and by the interparticle variations in their bright-field contrast. (B) Image acquired after 65 s, showing the formation of the liquid AuSi alloy as reflected by the rounded shapes in projection and the disappearance of crystalline contrast. (C) Image acquired after 84 s, showing the appearance of a Si nucleus with lighter contrast at the edge of one AuSi droplet. (D to F) Enlarged images of the boxed regions of (A) to (C), respectively. Arrows in (F) indicate the interface between liquid AuSi and solid Si.



Experiments were carried out in a UHV-TEM that is equipped with facilities for introducing the reactive gas disilane (Si_2H_6) to a heated sample while it remains under observation (15–17). Nucleation and growth kinetics of Si were observed in nanoscale Au crystallites supported on an electron-transparent amorphous SiN_x membrane. Figure 1 shows a series of images as a function of disilane exposure time, showing the initial transformation of polycrystalline Au islands (Fig. 1A) into eutectic droplets of AuSi (Fig. 1B), followed by the appearance of Si nuclei (Fig. 1C). Enlargements in Fig. 1, D to F, show one reaction sequence in more detail, and movies S1 and S2 illustrate a complete video sequence and a magnified view of a single nucleation event. The general behavior is consistent with that reported in (10), but we took advantage of time-resolved measurements to focus on the kinetics of the initial nucleation. In all cases, we found that Si nucleation occurs at the edge of the droplet, which suggests that this is the energetically favorable location that minimizes the nucleation barrier (18). At later times, the Si nuclei grew into elongated wires. We did not analyze this stage of growth because of the random wire direction and geometry, but instead focused on the regime in which the nuclei are still small particles within the AuSi droplets.

Figure 2A shows a representative series of images of a Si nucleus after formation, and Fig. 2,

¹School of Materials Engineering and Birck Nanotechnology Center, Purdue University, West Lafayette, IN 47907, USA.

²IBM Research Division T. J. Watson Research Center, Yorktown Heights, NY 10598, USA.

*Present address: Department of Materials Science and Engineering, University of California Los Angeles, Los Angeles, CA 90095, USA.

†To whom correspondence should be addressed. E-mail: eastach@purdue.edu (E.A.S.); fmross@us.ibm.com (F.M.R.)

B and C, shows quantitative measurements of the radius r (defined in the figure caption) versus time t of this and several other nuclei obtained at 525°C from droplets of different volumes at two different pressures. The data show that after disilane was introduced at $t = 0$, a certain time elapsed (the incubation time) before the solid Si nucleus appeared. Each nucleus initially grew very rapidly but within a few seconds reached a crossover point (C), after which the growth slowed down. This crossover is visibly sharper at lower pressures, as seen by comparing Fig. 2, B and C. Larger droplets show a longer incubation time, as expected from scaling arguments (10, 19), and also show a larger initial jump in nucleus size.

To model these kinetics, we used the fact that disilane cracking on the droplet surface results in a steady supply of Si into the droplet, which causes the Si fraction within the droplet to increase continuously. This initially results in a transition from solid pure Au to a liquid AuSi alloy. As more Si is supplied, the mole fraction of Si in the AuSi liquid alloy increases. At thermodynamic equilibrium, solid Si would appear when the AuSi composition (c) reaches the Si liquidus composition at the growth temperature (c_0). However, for growth on a substrate different from Si, there is a nucleation barrier to form the new crystalline Si phase. As a result, the liquid becomes supersaturated with Si before nucleation. With increasing supersaturation, the nucleation barrier decreases, until solid Si finally nucleates and quickly captured most of the excess Si in the liquid in a rapid growth spurt (10). Subsequently, growth continues more slowly, at a rate determined by the steady external Si supply from the disilane vapor.

We explain this behavior with a simple kinetic model, in which the AuSi droplet and the

growing solid Si nucleus are each assumed to maintain a constant shape. The rate of Si addition to the droplet is proportional to PA , where A is the exposed surface area of the droplet and P is the nominal disilane pressure (19). The droplets were treated as independent, consistent with annealing experiments that show that surface diffusion of Au and Si on the substrate is not appreciable over the time of the experiment (20). Nucleation occurs at a time t_n when the composition is $c_n (>c_0)$. Once the solid nucleates, it grows rapidly, and we assumed that by the time it is large enough to be visible, the Gibbs-Thomson effect of interfacial curvature can be neglected. This means that the nucleus captures Si from the liquid at a rate proportional to $c - c_0$ per unit area.

From these assumptions, we derived (17) the following equation for the evolution of the linear dimension r of the Si particle with time, valid when r is small as compared with R :

$$\frac{dr}{dt} = k_{LS} \left[\alpha(c_n - c_0) + k_{VL} \frac{P}{R} (t - t_n) - \left(\frac{r}{R} \right)^3 \right] \quad (1)$$

with initial condition $r = 0$ at $t = t_n$. R is the linear dimension of the AuSi droplet at the time of nucleation. The first term, $c_n - c_0$ in Eq. 1, reflects the initial growth rate at t_n . The second and third terms (P/R and r^3/R^3) represent the effect of c increasing because of Si addition from the vapor and decreasing because of Si capture by the nucleus. The three parameters controlling growth in Eq. 1 are the geometry-weighted supersaturation $\alpha(c_n - c_0)$ and the vapor-liquid and liquid-solid rate constants k_{VL} and k_{LS} , respectively (which also include geometric factors); details are given in (17). The geometric factors cannot be

determined directly because we only have images of the droplets in projection.

Although the assumptions are highly idealized, we found that Eq. 1 gives an excellent description of the data, as illustrated in Fig. 2. We measured 33 nucleation events with droplet radii ranging from 6 to 24 nm, temperatures from 470° to 585°C, and pressures from 3.5×10^{-7} to 4.0×10^{-6} torr. The complete set of data, and fits to Eq. 1, are shown in fig. S1. It can be seen that Eq. 1 automatically captures and quantifies our qualitative observations regarding the role of system size and growth rate. It predicts that larger droplets give later nucleation with larger jumps. It also predicts that the crossover is sharper at lower pressure, which is confirmed by examination of the complete set of data and fitted curves. We initially fitted each curve independently and confirmed that the resulting values for k_{LS} and k_{VL} were consistent for all droplets at a given temperature T , as expected. The values for the geometry-weighted supersaturation, $\alpha(c_n - c_0)$, were, surprisingly, also the same. We therefore fitted the entire data set for each T with a single value of each parameter. Figure 3 shows the fitted values of k_{LS} , k_{VL} , and $\alpha(c_n - c_0)$.

The most dramatic aspect of the growth kinetics is the initial jump, which gives a direct visualization of the supersaturation as the nucleus captures the excess Si from the supersaturated liquid. Because the jump is quite sudden as compared with the incubation time and the subsequent slow growth, it is useful to consider Eq. 1 in the limit of large k_{LS} , giving

$$\frac{r^3}{R^3} \approx \alpha(c_n - c_0) + k_{VL} \frac{P}{R} (t - t_n) \quad (2)$$

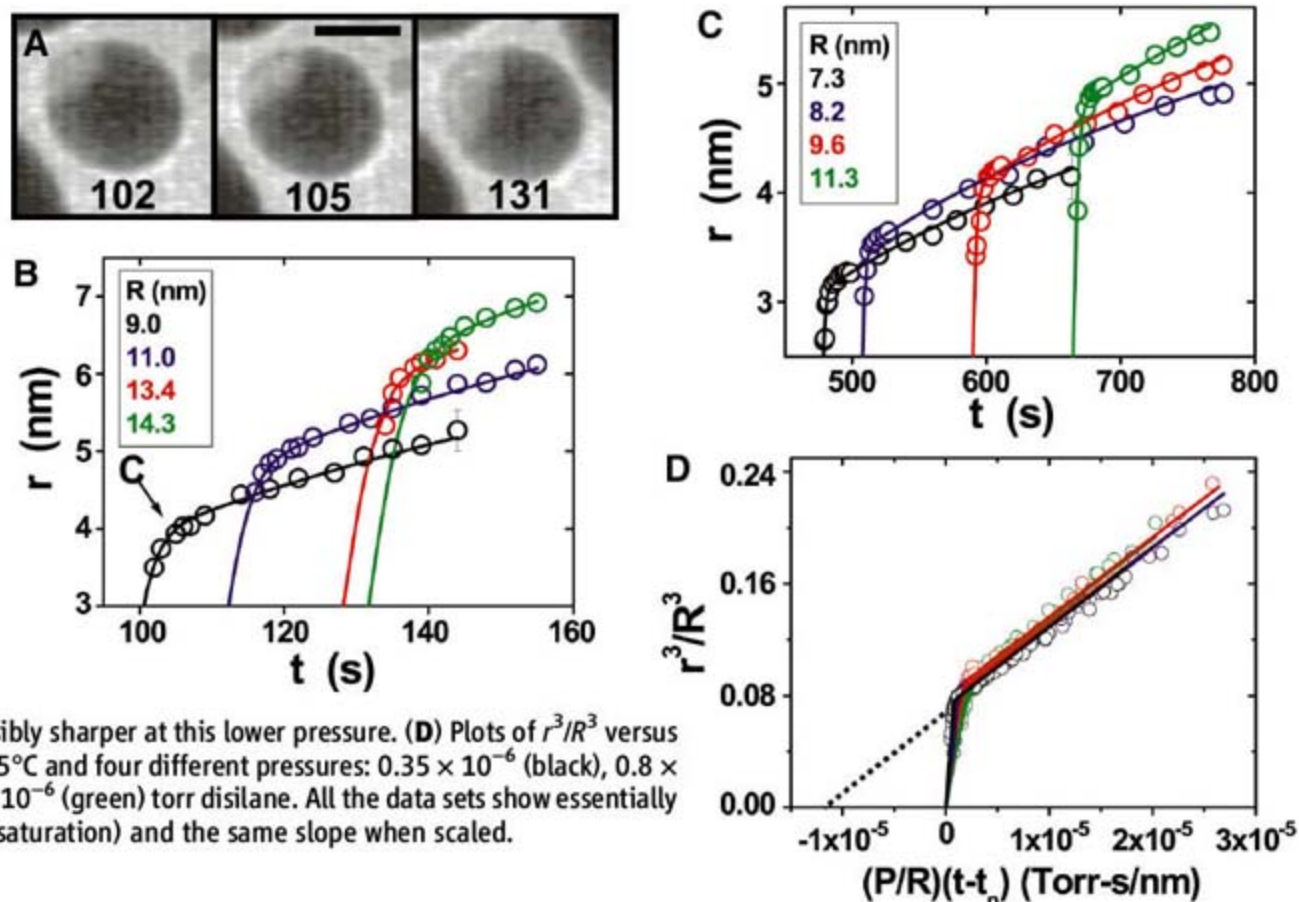
In this limit, Si nucleates at t_n and “instantly” jumps to size $r = [\alpha(c_n - c_0)]^{1/3} R$. Subsequently,

Fig. 2. (A) Images of a growing Si nucleus acquired at the times specified, recorded during deposition at 525°C and 4×10^{-6} torr. Scale bar, 10 nm.

(B) Linear dimension r of several Si nuclei versus time t for droplets of different initial radius R (as indicated in the box) during the same growth experiment. Approximating the nucleus image by an ellipse, r is calculated as the geometric mean of the semi-major and semi-minor axes; that is, the radius of a circle with an equivalent area. The “C” marks the crossover point (see text) of the data set from the droplet shown in (A); the middle image was recorded at this time. Solid curves are fits using Eq. 1. The error bar indicates measurement errors of ~5%.

(C) Plots and fits of r versus t at $T = 525^\circ\text{C}$ and $P = 8 \times 10^{-7}$ torr. In

comparison with (B), the crossover is visibly sharper at this lower pressure. **(D)** Plots of r^3/R^3 versus $(P/R)(t - t_n)$ for all nuclei analyzed at 525°C and four different pressures: 0.35×10^{-6} (black), 0.8×10^{-6} (blue), 1.5×10^{-6} (red), and 4.0×10^{-6} (green) torr disilane. All the data sets show essentially the same jump (that is, the same supersaturation) and the same slope when scaled.



its volume ($\propto r^3$) grows linearly with time because of the steady supply of Si from the vapor phase. Equation 2 predicts that if we plot r^3/R^3 versus $(P/R)(t - t_n)$ for all the measurements at a given temperature, the data should collapse onto a single curve. This is confirmed in Fig. 2D for data obtained from different experiments at a fixed temperature of 525°C and covering a wide range of disilane pressures and droplet sizes. All the data sets show essentially the same jump (that is, the same supersaturation) and the same slope. This is an important test of the model and the assumptions underlying Eqs. 1 and 2. In particular, the collapse of the data onto a single curve confirms that there is no strong dependence of any of the model parameters, such as the shape factors, rate constants, and supersaturation, on P or on R , the system size.

Size effects in nucleation have been studied for decades. Until recently, the only observed size effects were attributed to defects or impurities

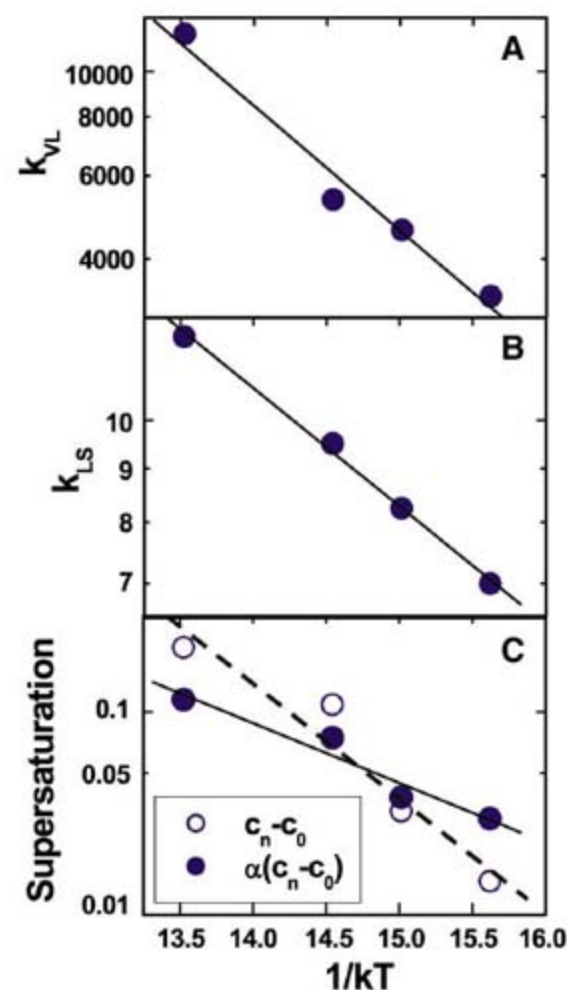


Fig. 3. (A to C) Parameter values versus temperature, shown on Arrhenius plots. These values are determined by fitting the entire data set shown in fig. S1, E to H. The solid and dashed lines are linear least-squares fits. (A) Vapor-liquid rate constant k_{VL} . (B) Liquid-solid rate constant k_{LS} . (C) Supersaturation at nucleation; solid circles indicate the parameter $\alpha(c_n - c_0)$ obtained directly from the fitting of Eq. 1 and open circles indicate the absolute supersaturation $c_n - c_0$ based on extrapolation from the growth kinetics after the jump. The two analyses exhibit a similar trend, in that the supersaturation at nucleation increases strongly with temperature.

(1, 3, 21), although the possibility of intrinsic size effects due to the number of available sites was also considered (21). The extrinsic size effects disappeared when the system was so small that it contained no impurities (1, 3, 21). More recently, there have been reports of dramatic intrinsic size effects, with substantial changes in the fundamental phase diagram even for systems as large as 60 nm in diameter (5, 22–24). It therefore was surprising to find no effect in our own data, with diameters between 12 and 40 nm.

Thermodynamics predicts that the liquidus concentration c_0 shifts by an amount roughly proportional to γ/R , whereas size effects on c_n are expected to be negligibly small by comparison (17). Here, γ involves geometrically weighted differences of the respective interfacial energies in the system, so it is highly system-dependent and has not to our knowledge been determined for any VLS system. Thus, we could not predict the magnitude of size effect expected, so we focused on the size scaling. For each temperature, our data span roughly a factor of 2 in size, so whatever size effects occur at our smallest size should be reduced by half at our largest size. Figure 2D shows that the scatter in jump height is very small; more quantitatively, we estimate that changes in $\alpha(c_n - c_0)$ due to size are not more than 0.005 (0.5%), otherwise they would be observable as a systematic trend above the scatter. We therefore found a lack of sensitivity to size over the important range used to form nanowires for device applications, which is helpful for predictably engineering small structures.

Furthermore, we found that nucleation systematically occurs at the droplet edge, indicating that it is heterogeneous, with both surface and interface playing a role. This implies that the supersaturation needed for nucleation, and possibly even the extent of size effects, could be rather different on another substrate and could be altered by appropriate pretreatment of the substrate. Yet the nucleation is intrinsic, being highly reproducible from drop to drop. Both facts are favorable for technological applications; reproducibility is essential for large-scale integration, and the role of the substrate in nucleation suggests opportunities for control via substrate engineering.

We now discuss the numerical values and physical importance of the fitted parameters. If we knew the three-dimensional shapes, and hence the geometric factors, the results in Fig. 3 would correspond to direct measurements of the two rate constants k_{VL} and k_{LS} and the critical supersaturation $c_n - c_0$. Even without this knowledge, we can determine the temperature dependences of the physical parameters if we assume that the shapes are independent of temperature. The kinetic rate constants are expected to be thermally activated, and indeed the measured values are consistent with this (Fig. 3). The slope for k_{VL} gives an activation energy of about 0.61 eV for the dissociative adsorption of disilane, in agreement with previous work (19).

The slope for k_{LS} gives an activation energy of about 0.26 eV for incorporation of Si from the AuSi liquid into the Si crystal. And the parameter $\alpha(c_n - c_0)$ ranges from 3 to 12%, increasing with temperature.

The unknown geometrical factors are expected to be of order 1. But their presence causes uncertainty in extracting supersaturation from the parameter $\alpha(c_n - c_0)$. However, we can estimate the supersaturation without knowledge of the geometrical factors by using an entirely different approach (17). It relies on the assumption that the rate of addition of Si to the droplet is approximately constant over time and can be determined from the time to reach c_0 (the x intercept of the dotted line in Fig. 2D). In Fig. 3C, we show values of supersaturation calculated using this approach. The results are similar to the results from the direct fitting, and the ratio (which ideally should be α) is of order 1, as expected for reasonable geometries. Both data sets in Fig. 3C show a similar trend with temperature. There is a difference in the slope, which could arise if the α values depend on temperature (such as via the drop contact angle) or if there are other systematic deviations from our simplifying assumptions. In any case, two quite different approaches lead to the same conclusion, namely that the supersaturation at nucleation increases strongly with temperature.

The temperature dependence of the supersaturation is intriguing. We are not aware of prior results that explain this, and we can only speculate about the mechanism. The required supersaturation is controlled largely by the interfacial free energy of the Si nucleus (2), so the temperature dependence of $c_n - c_0$ is likely to track the temperature dependence of this energy. The results are consistent with an Arrhenius behavior, with the smaller values at low temperature suggesting a reduced interface energy at low temperature. Temperature-dependent interface energies may be related to a temperature-dependent near-surface ordering that has recently been observed in AuSi (25) or to hydrogen coverage at the Si-vapor interface, which could depend on T via thermally activated disilane-cracking and H desorption.

We have shown detailed measurements of a nucleation and growth phenomenon, exploring the phase diagram of a nanoscale system at constant temperature and varying composition. The growth kinetics are explained by the buildup of a substantial supersaturation before nucleation. The lack of any change in supersaturation with system size suggests that the phase diagram has no appreciable size dependence in this system, at least down to ~ 12 nm in diameter.

We believe that the results shown here are of fundamental interest in advancing the theoretical understanding of nucleation in nanoscale systems, a phenomenon that is of importance in materials design for nanotechnology and in crystal growth and phase transformations. The results are particularly relevant to the growth of nano-

wires from liquid eutectic droplets, the most common route of nanowire formation. A detailed understanding of nucleation and growth kinetics will help in engineering nanostructures for applications such as sensors, transistors, and logic circuits (26), in which size dependence, incubation times, and the reliability of nucleation itself must all be controlled for the successful fabrication of each nanoscale device.

References and Notes

1. D. Turnbull, R. E. Cech, *J. Appl. Phys.* **21**, 804 (1950).
2. D. Turnbull, J. C. Fisher, *J. Chem. Phys.* **17**, 71 (1949).
3. J. H. Perepezko, J. L. Sebright, P. G. Höckel, G. Wilde, *Mater. Sci. Eng. A* **326**, 144 (2002).
4. Y. Wu, P. Yang, *J. Am. Chem. Soc.* **123**, 3165 (2001).
5. P. W. Sutter, E. A. Sutter, *Nat. Mater.* **6**, 363 (2007).
6. B. Kalache, P. R. I. Cabarrocos, A. Fontcuberta i Moral, *Jpn. J. Appl. Phys.* **45**, L190 (2006).
7. T. Clement, S. Ingole, S. Ketharanathan, J. Drucker, S. T. Picraux, *Appl. Phys. Lett.* **89**, 163125 (2006).
8. K. C. Lu *et al.*, *Nano Lett.* **7**, 2389 (2007).
9. S. K. Eswaramoorthy, J. M. Howe, G. Muralidharan, *Science* **318**, 1437 (2007).
10. S. Hofmann *et al.*, *Nat. Mater.* **7**, 372 (2008).
11. R. S. Wagner, W. C. Ellis, *Appl. Phys. Lett.* **4**, 89 (1964).
12. C. Thelander *et al.*, *Mater. Today* **9**, 28 (2006).
13. V. Schmidt *et al.*, *Small* **2**, 85 (2006).
14. O. Hayden *et al.*, *Small* **3**, 230 (2007).
15. M. Hammar, F. K. LeGoues, J. Tersoff, M. C. Reuter, R. M. Tromp, *Surf. Sci.* **349**, 129 (1996).
16. F. M. Ross, J. Tersoff, M. C. Reuter, *Phys. Rev. Lett.* **95**, 146104 (2005).
17. Materials and methods are available as supporting material on Science Online.
18. R. P. Sear, *J. Phys. Condens. Matter* **19**, 033101 (2007).
19. S. Kodambaka, J. Tersoff, M. C. Reuter, F. M. Ross, *Phys. Rev. Lett.* **96**, 096105 (2006).
20. To establish this, we measured Au crystallite sizes and AuSi droplet sizes during annealing without growth. We did not observe appreciable changes in size, even for the smallest particles, which shows that Ostwald ripening need not be considered in these experiments.
21. T. Takahashi, W. A. Tiller, *Acta Metall.* **17**, 643 (1969).
22. J. G. Lee, H. Mori, *Phys. Rev. Lett.* **93**, 235501 (2004).
23. E. Sutter, P. Sutter, *Nano Lett.* **8**, 411 (2008).
24. H. Adhikari, A. F. Marshall, C. E. D. Chidsey, P. C. McIntyre, *Nano Lett.* **6**, 318 (2006).
25. O. G. Shpyrko *et al.*, *Science* **313**, 77 (2006).
26. W. Lu, C. M. Lieber, *J. Phys. D Appl. Phys.* **39**, R387 (2006).
27. We acknowledge A. Ellis and K. B. Reuter of IBM for their assistance with experimental aspects of this work, M. Comer of Purdue with assistance in image analysis, and financial assistance from NSF under grant DMR-0606395.

Supporting Online Material

www.sciencemag.org/cgi/content/full/322/5904/1070/DC1

Materials and Methods

Figs. S1 and S2

Movie S1 and S2

21 July 2008; accepted 17 October 2008

10.1126/science.1163494

Spectroscopic Tracking of Structural Evolution in Ultrafast Stilbene Photoisomerization

Satoshi Takeuchi,¹ Sanford Ruhman,² Takao Tsuneda,³ Mahito Chiba,⁴ Tetsuya Taketsugu,⁵ Tahei Tahara^{1*}

Understanding a chemical reaction ultimately requires the knowledge of how each atom in the reactants moves during product formation. Such knowledge is seldom complete and is often limited to an oversimplified reaction coordinate that neglects global motions across the molecular framework. To overcome this limit, we recorded transient impulsive Raman spectra during ultrafast photoisomerization of *cis*-stilbene in solution. The results demonstrate a gradual frequency shift of a low-frequency spectator vibration, reflecting changes in the restoring force along this coordinate throughout the isomerization. A high-level quantum-chemical calculation reproduces this feature and associates it with a continuous structural change leading to the twisted configuration. This combined spectroscopic and computational approach should be amenable to detailed reaction visualization in other photoisomerizing systems as well.

Molecular rearrangements in chemical reactions occur on a time scale comparable to nuclear vibrational periods (i.e., from 10 fs to 1 ps). This time scale is now accessible with advanced ultrafast vibrational spectroscopy (1), but, in almost all studies, we only observe structures in stationary (excited) states and the population transfer from one state to the other. Continuous changes of the molecular structure are seldom observed, especially for large polyatomic molecules. This situation often limits our understanding to a level of an oversimplified reaction coordinate (RC). To map

structural evolution and elucidate true RCs, it is crucial to track molecular vibrations during reactions, which characterize the global motions of the whole molecule. Recently, femtosecond infrared spectroscopy has provided highly time-resolved vibrational spectra, but the technique is practically limited to the >1000 cm⁻¹ region (2). Conventional spontaneous Raman is only applicable to picosecond or slower processes, because long and narrow-band pulses are utilized to achieve sufficient frequency resolution (<15 cm⁻¹). This drawback in time resolution was improved by the introduction of a stimulated Raman process with femtosecond pulses (3). With the use of this technique, geometric changes of the retinyl chromophore in visual pigments were uncovered by monitoring hydrogen out-of-plane wagging vibrations in the 800- to 1000-cm⁻¹ region (4). Common to these frequency-domain Raman approaches, however, is the challenge of observing low-frequency vibrations, given disturbance from strong Rayleigh scattering. Here we report a fem-

tosecond resonance Raman probing at the impulsive limit to follow the low-frequency spectral change accompanying structural evolution in a *cis*-*trans* photoisomerization in solution.

Femtosecond transient impulsive Raman spectroscopy is explained as a combined pump-probe and time-domain Raman technique using three laser pulses (5, 6), as shown in Fig. 1A (7). In this experiment, we first generate a reactive excited-state molecule by a pump pulse (P_1). After a certain delay (ΔT), we introduce an ultrashort pulse (P_2) resonant with the excited-state absorption and impulsively induce a vibrational coherence of Raman active modes, which is driven by two frequency components contained in the spectrum of the P_2 pulse. In other words, the P_2 pulse initiates the motion of a nuclear wave packet in the reactive excited state. The third pulse (P_3) monitors the excited-state absorption, whose intensity is modulated by the nuclear wave-packet motion. Fourier transformation of the resultant beating feature in the time-resolved absorption provides a spectrum of the molecular vibration with a detectable range reaching into the low-frequency terahertz region, which is inaccessible by other frequency-domain methods. For long-lived stationary states, this time-domain measurement gives vibrational information equivalent to that obtainable from conventional frequency-domain Raman (8, 9). However, for structurally evolving states in a picosecond, this method can afford vibrational spectra with the best possible time- and frequency-resolutions that are determined only by the vibrational coherence time of the transients.

Stilbene is an extensively studied paradigm of ultrafast olefinic photoisomerization (Fig. 1B). In particular, *cis*-stilbene exhibits nearly barrierless bond twisting in the excited state that is complete within ~1 ps (10–15). The photoisomerization mechanism of *cis*-stilbene has been often discussed on the basis of a traditional one-dimensional (1D) potential energy surface (PES) along the torsional coordinate of the cen-

¹Molecular Spectroscopy Laboratory, RIKEN, 2-1 Hirosawa, Wako 351-0198, Japan. ²Institute of Chemistry, Hebrew University, Jerusalem 91904, Israel. ³School of Engineering, University of Tokyo, Tokyo 113-8656, Japan. ⁴National Institute of Advanced Industrial Science and Technology, Tsukuba 305-6568, Japan. ⁵Graduate School of Science, Hokkaido University, Sapporo 060-0810, Japan.

*To whom correspondence should be addressed. E-mail: tahei@riken.jp

tral C=C bond in the first singlet electronic excited (S_1) state (Fig. 1A) (16). The S_1 PES is believed to have a rather flat feature on the cis side, where the excited molecule persists for ~ 1 ps as an isomerization precursor showing strong $S_n \leftarrow S_1$ absorption in the 600- to 700-nm region (here, S_n is a higher-lying electronic excited state). Then, the molecule migrates to an S_1/S_0 conical intersection and relaxes to either the trans (product) or cis isomer in the ground (S_0) state. However, spectroscopic studies have pointed to the inadequacy of this 1D rigid-twist model that does not take into account, for example, out-of-plane deformations of the ethylenic moiety (17, 18). Pyramidalization of one ethylenic carbon ($sp^2 \rightarrow sp^3$ change of hybridization) was recently claimed to be essential in the structure at the S_1/S_0 conical intersection, indicating the importance of the multidimensionality of PES (19). For elucidation of the true RC of the polyatomic molecule, it is crucial to track the structural evolution by taking a temporal series of spectroscopic snapshots of the molecule.

To achieve this aim, we acquired femtosecond impulsive Raman data of *cis*-stilbene over the course of the isomerization. Figure 1C presents a time-resolved $S_n \leftarrow S_1$ absorption in the absence of the P_2 pulse after excitation with the 267-nm P_1 pulse. This signal shows a 1.3-ps decay, reflecting a decrease in the S_1 population due to internal conversion/isomerization (11–13, 15). With irradiation by the P_2 pulse (11 fs, 620 nm) after a delay ΔT , the $S_n \leftarrow S_1$ absorption instantaneously changes, because the P_2 pulse resonantly excites a fraction of the S_1 molecules to the S_n state. The difference between the $S_n \leftarrow S_1$ absorption signals measured with and without the P_2 pulse gives time-resolved impulsive Raman data, which include information about the nuclear wave-packet motion induced by the P_2 pulse. With the P_2 pulse tuned in rigorous resonance with absorption of the isomerization precursor, this impulsive Raman measurement selectively monitors the photoisomerization process, and the signal contribution from a minor photocyclization to 4a,4b-dihydrophenanthrene is negligible (20). We measured time-resolved impulsive Raman signals in hexadecane at three delays ($\Delta T = 0.3, 1.2,$ and 2 ps) to examine the temporal change of S_1 vibrational structure (Fig. 2A). A strong beating feature is observed in each trace, which reflects the nuclear wave-packet motion induced in S_1 *cis*-stilbene at each delay. A contribution from the S_n state is excluded because its lifetime is shorter than the damping time of the beating. The other features of the observed traces are represented by three exponential decay components that reflect the population dynamics after the P_1 and P_2 irradiation (21).

The inset of Fig. 2A shows the beating features extracted from the data by subtraction of the population component. Their Fourier transform power spectra (Fig. 2B) represent vibrational spectra of S_1 *cis*-stilbene at the three ΔT delays. At $\Delta T = 0.3$ ps, a broad band appears near 240

cm^{-1} , together with several weak bands at 411, 533, and 752 cm^{-1} . As the only band showing exceptionally large Raman intensity in the 200- to 300- cm^{-1} region, the predominant 240- cm^{-1} band is characteristic of S_1 *cis*-stilbene; hence, it is straightforwardly associated with a broad band observed near 229 cm^{-1} in a picosecond frequency-domain Raman study (22). This vibration has been assigned to a mode that involves the motion of phenyl-C=C bending, ethylenic C=C torsion, and phenyl torsion. The nuclear wave-packet motion due to the same mode was also observed in previous ultrafast uv-pump/vis-probe measurements in this laboratory (23), which detected the nuclear wave-packet motion induced directly by photoexcitation.

The present Raman measurements reveal that the center frequency of the 240- cm^{-1} motion considerably downshifts with increasing ΔT delay, diminishing from 239 cm^{-1} ($\Delta T = 0.3$ ps) to 224 cm^{-1} (1.2 ps) to 215 cm^{-1} (2 ps). This large frequency downshift is directly apparent in the raw time-domain data. As shown in the inset of Fig. 2A, the intensity maxima of the three beating components gradually shift in time, manifesting a lengthening of the oscillation period with increasing delay. The data reveal that the frequency of the 240- cm^{-1} mode substantially changes while the isomerization proceeds. In other words, the 240- cm^{-1} mode probes the structural

evolution of the molecule as a spectator through a large anharmonic coupling to the isomerization coordinate.

To confirm that the frequency downshift is directly related to the isomerization process, we carried out the same measurements in methanol, where the isomerization is accelerated and proceeds with a time constant of 0.48 ps (13, 15). The data obtained at $\Delta T = 0.3, 0.7,$ and 1.1 ps (Fig. 2, B and C) show that the 240- cm^{-1} mode exhibits a clear frequency downshift in methanol also. Figure 2D compares the temporal change of the center frequency of the mode in the two solvents. Clearly, the rate of the frequency downshift is higher in methanol than in hexadecane. With the change of solvent from hexadecane to methanol, the isomerization rate increases by a factor of 2.7 (0.77 to 2.08 ps^{-1}), and the rate of the frequency downshift nearly doubles (14 versus 27 cm^{-1}/ps). This strong correlation confirms that the frequency downshift of the 240- cm^{-1} mode arises from the structural evolution relevant to the isomerization of S_1 *cis*-stilbene.

Linear fits to the frequency shifts observed in the two solvents both extrapolate to the same initial frequency ($242 \pm 2 \text{ cm}^{-1}$) at zero delay (24). We independently evaluated the initial frequency of this mode in a uv-pump/vis-probe experiment (23) (where the nuclear wave-packet motion was directly induced by $S_1 \leftarrow S_0$ photo-

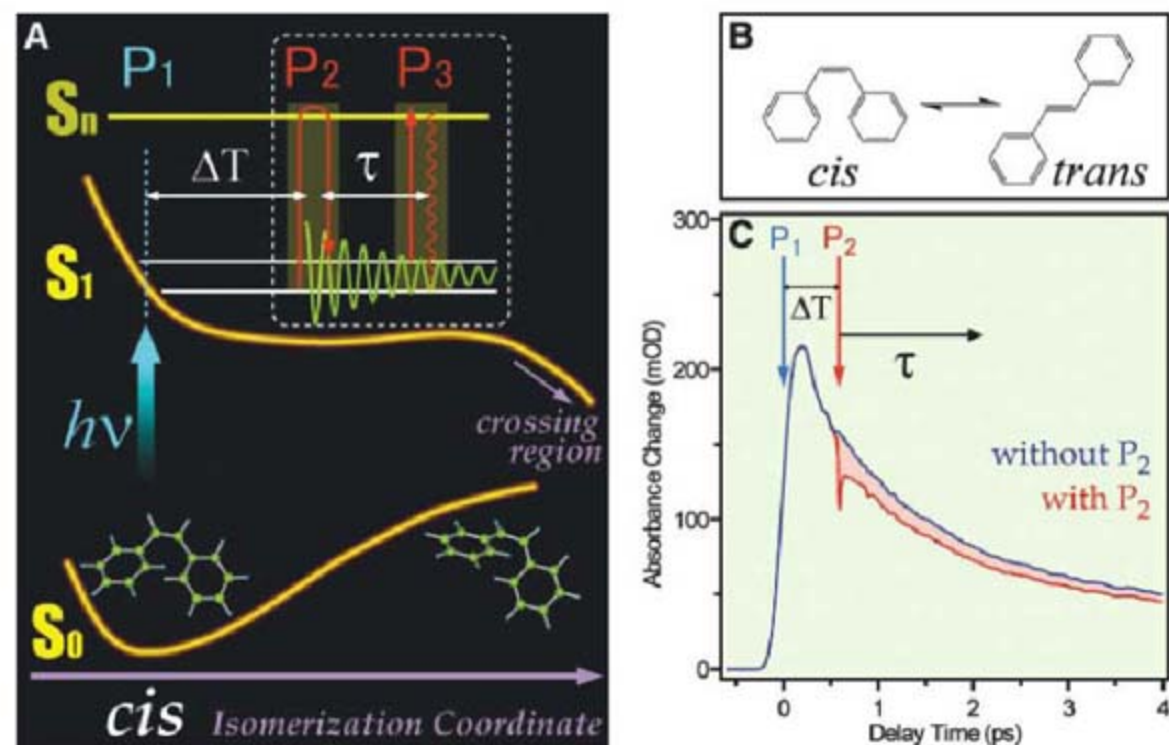


Fig. 1. (A) Schematic illustration of the S_0 , S_1 , and S_n PESs of *cis*-stilbene against the isomerization coordinate, together with a sequence of three laser pulses used in the measurements. The first pulse (P_1 ; 267 nm, 150 fs) photoexcites S_0 *cis*-stilbene in solution and generates the reactive S_1 state. It does not efficiently generate vibrational coherences in the S_1 molecule because of its relatively long duration. After a delay ΔT , the second ultrashort pulse (P_2 ; 620 nm, 11 fs), which is resonant with the $S_n \leftarrow S_1$ transient absorption, is applied to generate a nuclear wave packet in the S_1 state. The third pulse (P_3 ; 620 nm, 11 fs) is used to monitor time-resolved $S_n \leftarrow S_1$ absorption signals. h , Planck's constant; ν , frequency; τ , delay time for impulsive Raman measurements. (B) Photoisomerization reaction of stilbene between the *cis* and *trans* isomers. (C) Typical time-resolved traces of the $S_n \leftarrow S_1$ absorption of *cis*-stilbene measured with and without the P_2 pulse. The difference between the two traces, shaded in red, gives a time-resolved impulsive Raman signal, which contains information about the S_1 wave-packet motion induced by the P_2 pulse. mOD, milli-optical density.

excitation) and found it to be $231 \pm 3 \text{ cm}^{-1}$ in both nonpolar (cyclohexane) and polar (methanol) solvents (25), which is 11 cm^{-1} lower than the value obtained from the extrapolation of the frequency shift after $\Delta T = 0.3 \text{ ps}$. This discrepancy indicates that the frequency of this mode first exhibits an upshift as the wave packet evolves on the S_1 surface. In fact, we observed a shortening of the oscillation period in the uv-pump/vis-probe experiment (23), which demonstrates that the frequency upshift occurs within

the vibrational coherence time. After this initial upshift, the mode shows a frequency downshift as observed in the present impulsive Raman experiment.

The vibrational period of the 240-cm^{-1} mode is approximately equal to 140 fs, which is well separated from the time scale of the isomerization (1.3 ps in hexadecane). Thus, the nuclear motion along the 240-cm^{-1} coordinate (q) can adjust adiabatically during the relatively slow temporal evolution of nuclear configurations due to the

isomerization, with the instantaneous frequency of the 240-cm^{-1} mode decreasing as the isomerization proceeds. In other words, the vibrational force constant of the 240-cm^{-1} mode (k) decreases as the isomerization coordinate (Q) changes through the following anharmonic coupling relation (where V is potential energy)

$$\frac{\partial k}{\partial Q} = \frac{\partial}{\partial Q} \left(\frac{\partial^2 V}{\partial q^2} \right) = \frac{\partial^3 V}{\partial q^2 \partial Q} \neq 0 \quad (1)$$

Because the force constant is given by the curvature of the S_1 PES along the 240-cm^{-1} coordinate (q), the present results reveal that the shape of the S_1 PES changes along the isomerization coordinate (26), as illustrated in Fig. 3B. The experiment shows that the structure of S_1 *cis*-stilbene continuously evolves within the S_1 lifetime. It is noteworthy that the “averaged” frequency measured in a picosecond frequency-domain Raman study (229 cm^{-1}) (22) lies in the middle of the range of the frequency shift ($239 \rightarrow 215 \text{ cm}^{-1}$) observed here.

To associate the experimental observation with actual structural changes in S_1 *cis*-stilbene, we calculated the PES and vibrational structure by density functional theory (DFT) and time-dependent DFT (TDDFT) using the Becke 1988 exchange + one-parameter progressive correlation functionals with long-range correction (27). The calculation gave a nonplanar optimized structure (C_2 symmetry) for S_0 *cis*-stilbene because of steric hindrances: The two phenyl groups are largely tilted ($\phi_{\beta\alpha 12} \approx 40^\circ$), although the ethylene moiety is nearly planar ($\theta_{1\alpha\alpha'1'} \approx 5^\circ$). At this S_0 geometry, an optically allowed transition to the S_1 state, with a highest occupied molecular orbital \rightarrow lowest unoccupied molecular orbital single-excitation character, was calculated at 4.90 eV, which agrees well with the experimental value (4.48 eV). Two almost-dark states were computed to lie above this bright S_1 state. The S_1 character, as well as the state ordering, is consistent with a recent calculation (28).

Starting from the S_1 state with the structure optimized for the S_0 state (Franck-Condon point), we gradually changed the geometry along the negative direction of mass-weighted energy gradients calculated at every point and searched the minimum energy path on the S_1 PES. The RC, s , is defined as the path length along the thus-obtained minimum energy path ($s = 0$ at the initial Franck-Condon point). Figure 4A depicts the change of the S_0 and S_1 energies along the RC. The S_1 energy first decreased rapidly ($s < 0.5$) and then exhibited a slower decrease ($s > 0.5$). This energy change reflects the biphasic structural evolution of the S_1 state. As shown in Fig. 4C, the initial structural change (Q_{init}) in $s < 0.5$ is dominated by a prompt stretch of the central C=C bond due to $\pi\pi^*$ electronic excitation and an out-of-plane motion of the two ethylenic hydrogens. In the later region of $s > 0.5$, the two ethylenic hydrogens gradually move in opposite directions to a greater extent so that the

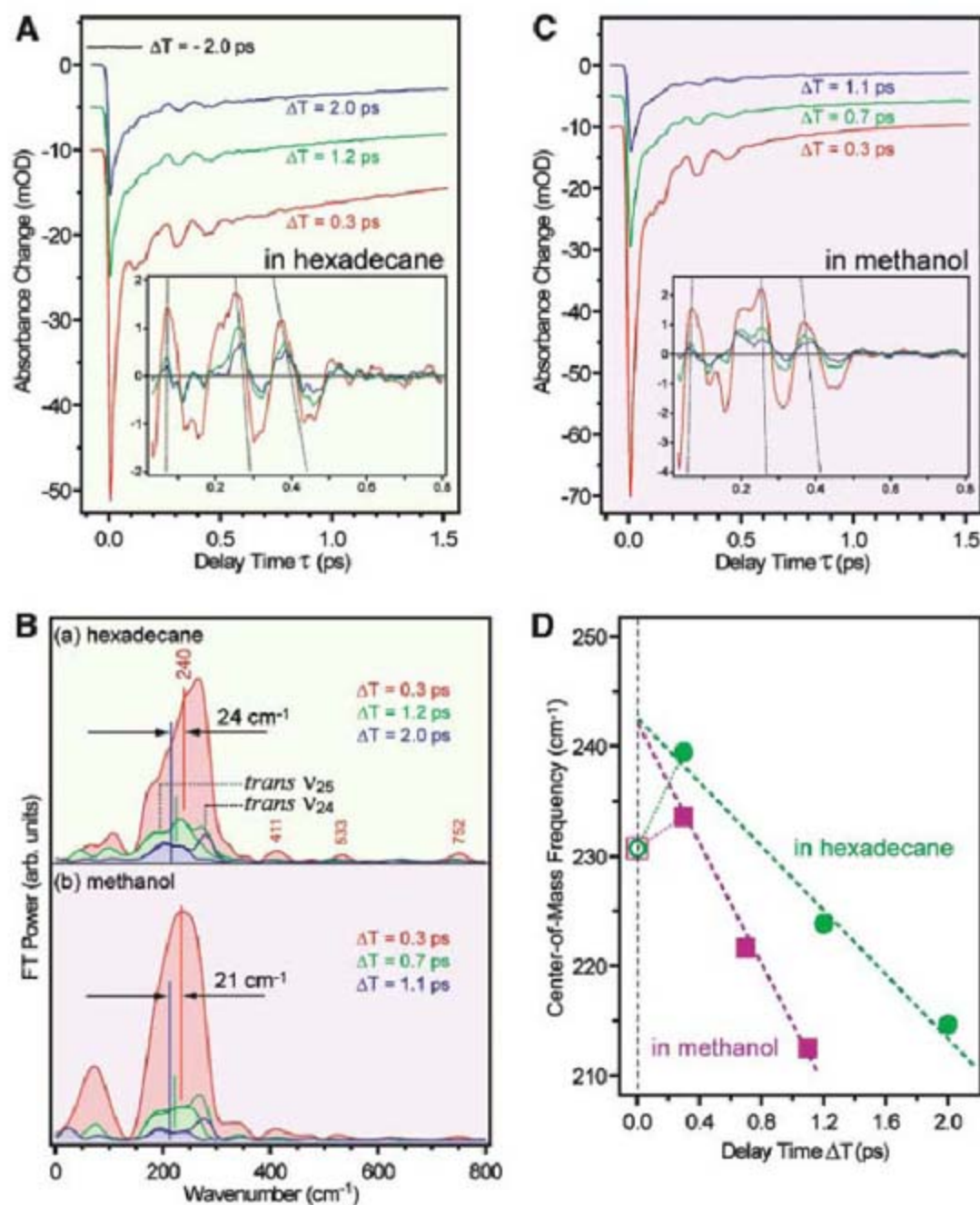
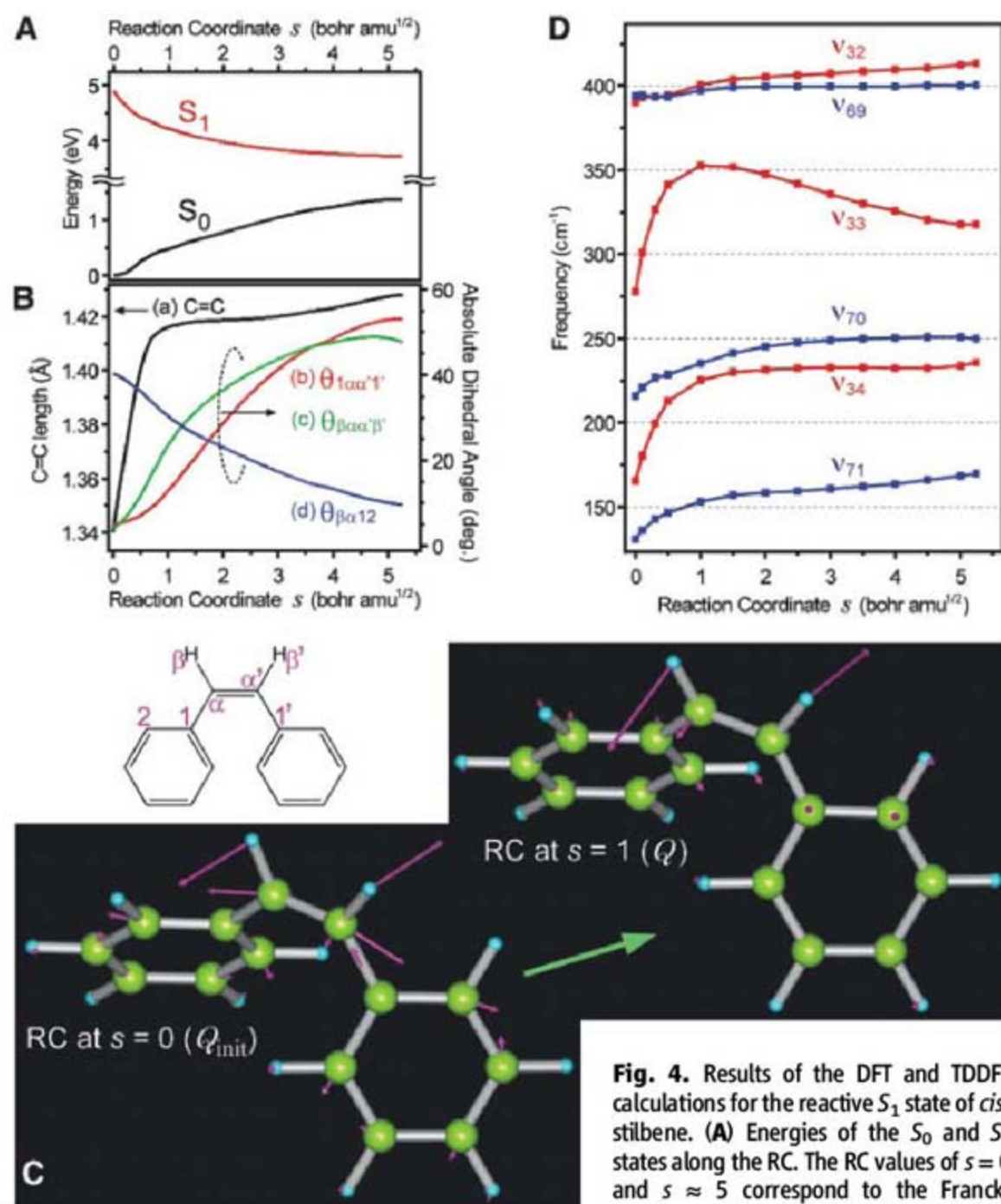
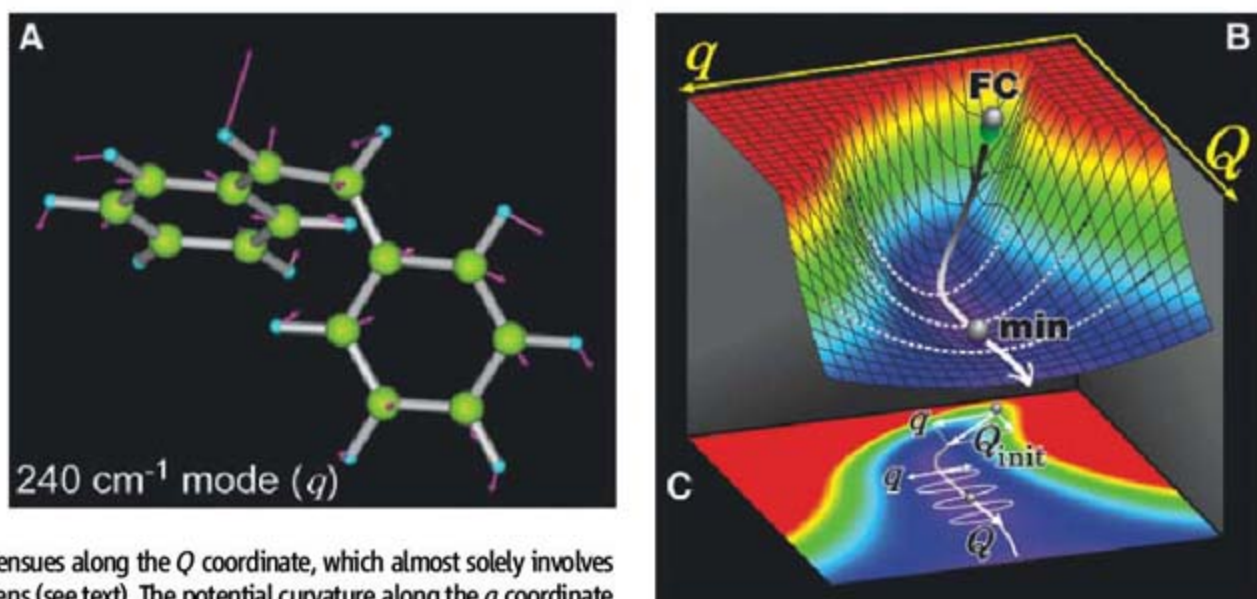


Fig. 2. Experimental results of the time-resolved impulsive Raman spectroscopy of *cis*-stilbene in two solvents. (A and C) Time-resolved impulsive Raman signals measured at three different ΔT delays in hexadecane and methanol, respectively. The measurements were carried out at room temperature with 0.02 mol dm^{-3} stilbene concentrations. The insets show the beating components obtained after subtraction of the population components. The dotted lines connect the corresponding maxima of the three beating components, and their tilt with time indicates that the oscillation period becomes longer with increasing ΔT delay. (B) Fourier transform (FT) power spectra of the beating components obtained at the three ΔT delays in (a) hexadecane and (b) methanol. Pure spectra of S_1 *cis*-stilbene (represented as the bands shaded in red, green, and blue for the three delays) were obtained after subtraction of weak bands due to the ν_{24} and ν_{25} modes of S_1 *trans*-stilbene (30) from the raw Fourier transform spectra represented by solid curves. The center-of-mass frequency of each *cis*-stilbene spectrum is indicated by a vertical line, which clearly shows a frequency downshift with time. (D) Plots of the center-of-mass frequency against ΔT delay for the two solvents. The rate of the frequency downshift after $\Delta T = 0.3 \text{ ps}$, evaluated from the slope of this plot, is $14 \text{ cm}^{-1}/\text{ps}$ in hexadecane and $27 \text{ cm}^{-1}/\text{ps}$ in methanol.

Fig. 3. (A) Nuclear motions of the 240-cm^{-1} mode at the geometry near the energy minimum on the S_1 PES ($s = 5$). (B) Schematic illustration of the S_1 PES of *cis*-stilbene against the isomerization coordinate (Q) and 240-cm^{-1} coordinate (v_{33} mode, q) together with (C) the corresponding contour plot, which are drawn on the basis of the understanding obtained in the present study. The *cis*-stilbene molecule excited at the Franck-Condon point (FC) first shows a rapid structural change along a steep route (Q_{init}) that mainly involves a stretching of the central C=C bond with out-of-plane motion of the two ethylenic hydrogens. Then, a slower structural evolution toward the minimum point of the S_1 PES (min) ensues along the Q coordinate, which almost solely involves out-of-plane motion of the two ethylenic hydrogens (see text). The potential curvature along the q coordinate (indicated by dotted curves) becomes smaller as the molecule evolves along the isomerization coordinate.



minima in the S_1 state, respectively. (B) Geometrical parameters against the RC. (a) Ethylenic C=C bond length; (b to d) dihedral angles. The atomic labeling is indicated below the figure. (C) RC vectors at $s = 0$ and $s = 1$, corresponding to Q_{init} and Q , respectively. (D) Calculated frequencies of several low-frequency modes of S_1 *cis*-stilbene against the RC. All the frequencies were scaled by a factor of 0.97. Vibrational modes with A and B symmetries are shown in red and blue, respectively.

twisting angle ($\theta_{\beta\alpha\alpha'\beta'}$) of the C=C bond increases and the tilt angle ($\phi_{\beta\alpha12}$) of the phenyl group decreases (17, 18) (Fig. 4B). Consequently, a twisted structure having $\theta_{\beta\alpha\alpha'\beta'} \approx 49^\circ$ and $\phi_{\beta\alpha12} \approx 10^\circ$ is attained at $s \approx 5$, which corresponds to a very shallow potential minimum leading to the conical intersection. The substantial twisting around the C=C bond is achieved mainly by the out-of-plane motion of the ethylenic hydrogens without extensive motion of the phenyl rings. This twisting motion in the second phase, which actually characterizes the isomerization, cannot be fully detected by the analysis of resonance Raman spectra of the S_0 state (17), because it only sees the nuclear motions occurring within a very short electronic coherence time of the $S_1 \leftarrow S_0$ transition (a few tens of femtoseconds).

To calculate the instantaneous vibrational frequency during the structural evolution of S_1 *cis*-stilbene, we evaluated the force-constant matrix at different points along the RC and obtained the frequencies of the instantaneous normal modes. The calculated frequencies of six low-frequency modes are plotted against RC in Fig. 4D. Among these modes, the v_{33} mode is uniquely assignable to the 240-cm^{-1} vibration observed in the experiment, on the basis of the frequency and Raman activity of this mode (29). The initial nuclear motion in $s < 0.5$ (Q_{init}) involves a substantial component parallel to the v_{33} coordinate (q), and this motion is smoothly connected to the v_{33} mode in the second phase ($s > 0.5$) (Fig. 3C). After a steep increase from 278 to 353 cm^{-1} , the v_{33} frequency substantially decreases down to 318 cm^{-1} at the twisted geometry at $s = 5$. This behavior of the v_{33} frequency almost perfectly reproduces the frequency shift of the 240-cm^{-1} mode observed experimentally, including the initial upshift measured by the ultrafast uv-pump/vis-probe measurement (23). The agreement strongly bolsters our conclusion that the present experiment tracks the structural evolution of *cis*-stilbene during the isomerization through accompanying changes in the vibrational structure. The frequency differences between the

experiment and computation are attributed to the normal coordinate analysis (harmonic approximation) applied to the highly anharmonic S_1 PES.

We thus achieved direct experimental tracking of the continuous structural evolution of a reacting polyatomic molecule by monitoring the evolving frequency of a spectator wave packet. The spectator frequency showed a gradual downshift over the course of the isomerization through a large anharmonic coupling to the isomerization coordinate. This observation arises from the gradual twisting of the olefinic moiety, realized by the out-of-plane motion of the two ethylenic hydrogens with minimal change in the molecular volume. The global molecular rearrangements visualized here lead to the structure at the S_1/S_0 conical intersection, which may be accompanied with further pyramidalization of one ethylenic carbon (19). Femtosecond time-domain Raman spectroscopy offers effective probing of complicated multidimensional RC of polyatomic molecules that cannot be tracked by conventional vibrational spectroscopy.

References and Notes

- M. D. Fayer, *Ultrafast Infrared and Raman Spectroscopy* (Marcel Dekker, New York, 2001).
- J. Herbst, K. Heyne, R. Diller, *Science* **297**, 822 (2002).
- P. Kukura, D. W. McCamant, R. A. Mathies, *Annu. Rev. Phys. Chem.* **58**, 461 (2007).
- P. Kukura, D. W. McCamant, S. Yoon, D. B. Wandschneider, R. A. Mathies, *Science* **310**, 1006 (2005).
- U. Banin, S. Ruhman, *J. Chem. Phys.* **99**, 9318 (1993).
- S. Fujiyoshi, S. Takeuchi, T. Tahara, *J. Phys. Chem. A* **107**, 494 (2003).

- Materials and methods are available as supporting online material on Science Online.
- G. Cerullo *et al.*, *J. Phys. Chem. A* **107**, 8339 (2003).
- T. Hornung, H. Skenderovic, M. Motzkus, *Chem. Phys. Lett.* **402**, 283 (2005).
- M. Sumitani, N. Nakashima, K. Yoshihara, *Chem. Phys. Lett.* **68**, 255 (1979).
- S. Abrash, S. Repinec, R. M. Hochstrasser, *J. Chem. Phys.* **93**, 1041 (1990).
- D. C. Todd *et al.*, *J. Chem. Phys.* **93**, 8658 (1990).
- S. T. Repinec, R. J. Sension, A. Z. Szarka, R. M. Hochstrasser, *J. Phys. Chem.* **95**, 10380 (1991).
- R. J. Sension, A. Z. Szarka, R. M. Hochstrasser, *J. Chem. Phys.* **97**, 5239 (1992).
- D. C. Todd, G. R. Fleming, *J. Chem. Phys.* **98**, 269 (1993).
- J. Saltiel, *J. Am. Chem. Soc.* **90**, 6394 (1968).
- A. B. Myers, R. A. Mathies, *J. Chem. Phys.* **81**, 1552 (1984).
- H. Petek *et al.*, *J. Phys. Chem.* **94**, 7539 (1990).
- J. Quenneville, T. J. Martinez, *J. Phys. Chem. A* **107**, 829 (2003).
- J. M. Rodier, A. B. Myers, *J. Am. Chem. Soc.* **115**, 10791 (1993).
- The first component is due to instantaneous electronic response of S_1 *cis*-stilbene. The second 70-fs decay corresponds to the $S_n \rightarrow S_1$ internal conversion that occurs after the $S_n \leftarrow S_1$ excitation by the P_2 pulse. The third component decays with the S_1 lifetime. The appearance of this long-lasting component suggests that a fraction of the S_n molecules does not go back to the S_1 state but follows other relaxation routes (permanent bleaching) (6).
- W. M. Kwok *et al.*, *J. Raman Spectrosc.* **34**, 886 (2003).
- K. Ishii, S. Takeuchi, T. Tahara, *Chem. Phys. Lett.* **398**, 400 (2004).
- The initial frequency was obtained by the linear fit as the intercept at zero delay, and it was separately evaluated as 243.1 ± 2.3 cm^{-1} in hexadecane and 241.1 ± 1.6 cm^{-1} in methanol. On the average, we determined the common initial frequency as 242 ± 2 cm^{-1} .
- We made Fourier transform analysis of a beating feature observed in the $S_n \leftarrow S_1$ transient absorption and

- obtained its power spectrum that shows an intense band corresponding to the 240- cm^{-1} vibration. The center-of-mass frequency of the band was evaluated as 231 ± 3 cm^{-1} in both cyclohexane and methanol.
- S. Pedersen, L. Banares, A. H. Zewail, *J. Chem. Phys.* **97**, 8801 (1992).
- H. Iikura, T. Tsuneda, T. Yanai, K. Hirao, *J. Chem. Phys.* **115**, 3540 (2001).
- R. Improta, F. Santoro, *J. Phys. Chem. A* **109**, 10058 (2005).
- As already reported, the 240- cm^{-1} vibration exhibits a high Franck-Condon activity in the $S_1 \leftarrow S_0$ transition, indicating that it is a totally symmetric, Raman-active mode showing a large S_0/S_1 potential displacement (23). Among the totally symmetric candidate modes in Fig. 4D (ν_{32} , ν_{33} , ν_{34}), the initial frequencies of the ν_{33} and ν_{34} modes are close to 240 cm^{-1} . We found that the S_1/S_0 potential displacement along the ν_{33} mode is largest: Absolute potential gradients at $s = 0$, which reflect the potential displacement, were calculated as 0.0036 (ν_{32}), 0.0076 (ν_{33}), and 0.0033 (ν_{34}) hartree/(bohr \cdot amu $^{1/2}$), respectively (where amu stands for atomic mass unit). Therefore, we assigned the ν_{33} mode to the 240- cm^{-1} vibration observed experimentally.
- K. Iwata, H. Hamaguchi, *J. Phys. Chem. A* **101**, 632 (1997).
- This work was supported in part by Grant-in-Aid for Science Research on Priority Area (no. 19056009) from the Ministry of Education, Culture, Sports, Science, and Technology of Japan. S.T. acknowledges financial support by a Grant-in-Aid for Scientific Research (B) (no. 19350017) from the Japan Society for the Promotion of Science (JSPS). T. Tahara and S.R. acknowledge the JSPS invitation fellowship program.

Supporting Online Material

www.sciencemag.org/cgi/content/full/322/5904/1073/DC1
Materials and Methods
References

23 May 2008; accepted 15 September 2008
10.1126/science.1160902

Random Tiling and Topological Defects in a Two-Dimensional Molecular Network

Matthew O. Blunt,¹ James C. Russell,¹ María del Carmen Giménez-López,² Juan P. Garrahan,¹ Xiang Lin,² Martin Schröder,² Neil R. Champness,^{2*} Peter H. Beton^{1*}

A molecular network that exhibits critical correlations in the spatial order that is characteristic of a random, entropically stabilized, rhombus tiling is described. Specifically, we report a random tiling formed in a two-dimensional molecular network of *p*-terphenyl-3,5,3',5'-tetracarboxylic acid adsorbed on graphite. The network is stabilized by hexagonal junctions of three, four, five, or six molecules and may be mapped onto a rhombus tiling in which an ordered array of vertices is embedded within a nonperiodic framework with spatial fluctuations in a local order characteristic of an entropically stabilized phase. We identified a topological defect that can propagate through the network, giving rise to a local reordering of molecular tiles and thus to transitions between quasi-degenerate local minima of a complex energy landscape. We draw parallels between the molecular tiling and dynamically arrested systems, such as glasses.

The tiling of surfaces with simple polygons has fascinated scientists, mathematicians, and artists in both ancient and modern cultures. The mathematical rules that govern the formation of periodic tilings, in which tiles are regularly placed on a surface, have been extensively studied and provide the foundation for the clas-

sification of crystalline materials. More recently, the discovery of quasi-crystals has inspired great interest in aperiodic tilings, which exhibit symmetries that are not compatible with translational order (1–5). It is also possible to form tilings in which translational symmetry is absent by using simple tile shapes such as the rhombus with internal an-

gles of 60° and 120°. Rhombus, or lozenge, tilings lead to a particularly rich range of arrangements, which may be periodic, but random nonperiodic tilings are also permitted (6, 7) and have attracted great interest because of their relevance to mixing algorithms (8, 9), antiferromagnetism (10, 11), and entropic models of quasi-crystals (12–15).

We show that a rhombus tiling may be realized experimentally in a two-dimensional arrangement of organic molecules adsorbed on graphite. Specifically, we studied the molecule *p*-terphenyl-3,5,3',5'-tetracarboxylic acid (TPTC) (Fig. 1A), which was synthesized as described in (16). The choice of molecule was motivated by the placement of carboxylic acid groups that promote directional intermolecular hydrogen bonding. For TPTC, these groups stabilize two possible relative placements of neighboring molecules, which we refer to as the parallel (Fig. 1B) and arrowhead (Fig. 1C) configurations. Small quantities of a saturated solution of TPTC in nonanoic acid were applied to a freshly cleaved highly oriented pyro-

¹School of Physics and Astronomy, University of Nottingham, University Park, Nottingham NG7 2RD, UK. ²School of Chemistry, University of Nottingham, University Park, Nottingham NG7 2RD, UK.

*To whom correspondence should be addressed. E-mail: neil.champness@nottingham.ac.uk (N.R.C.); peter.beton@nottingham.ac.uk (P.H.B.)

lytic graphite (HOPG) substrate, and images of the interface between HOPG and the TPTC solution were acquired by using a scanning tunneling microscope (STM) [see (16) for full experimental details]. The samples were prepared and imaged

at room temperature. Nonanoic acid has been identified as a suitable solvent by Lackinger *et al.* (17, 18) in their investigations of trimesic and related acids, and the properties of molecular networks stabilized by noncovalent interactions such

as hydrogen bonding have been reviewed by a number of authors (19–21). There have also been recent studies of molecules functionalized with multiple carboxylic acid groups, similar to TPTC (22–24).

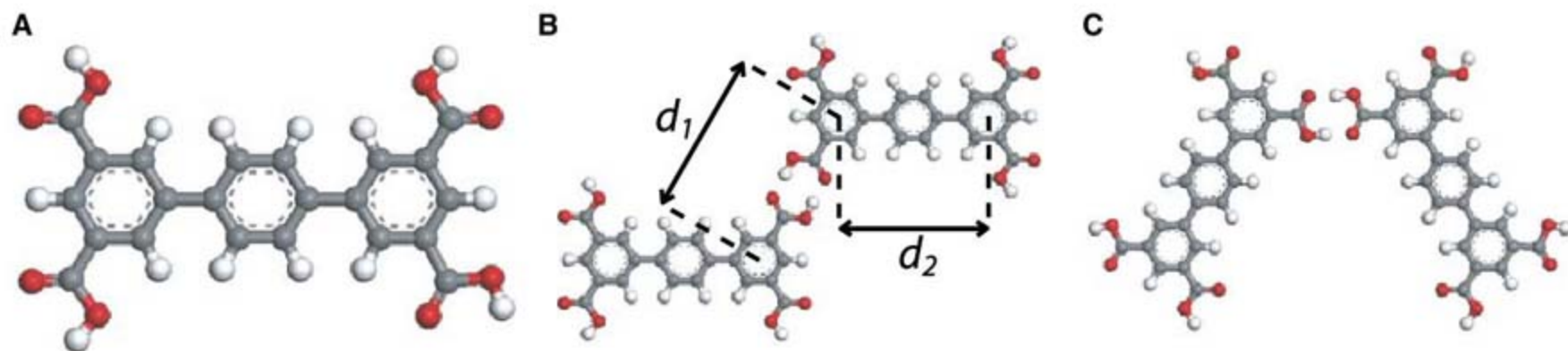
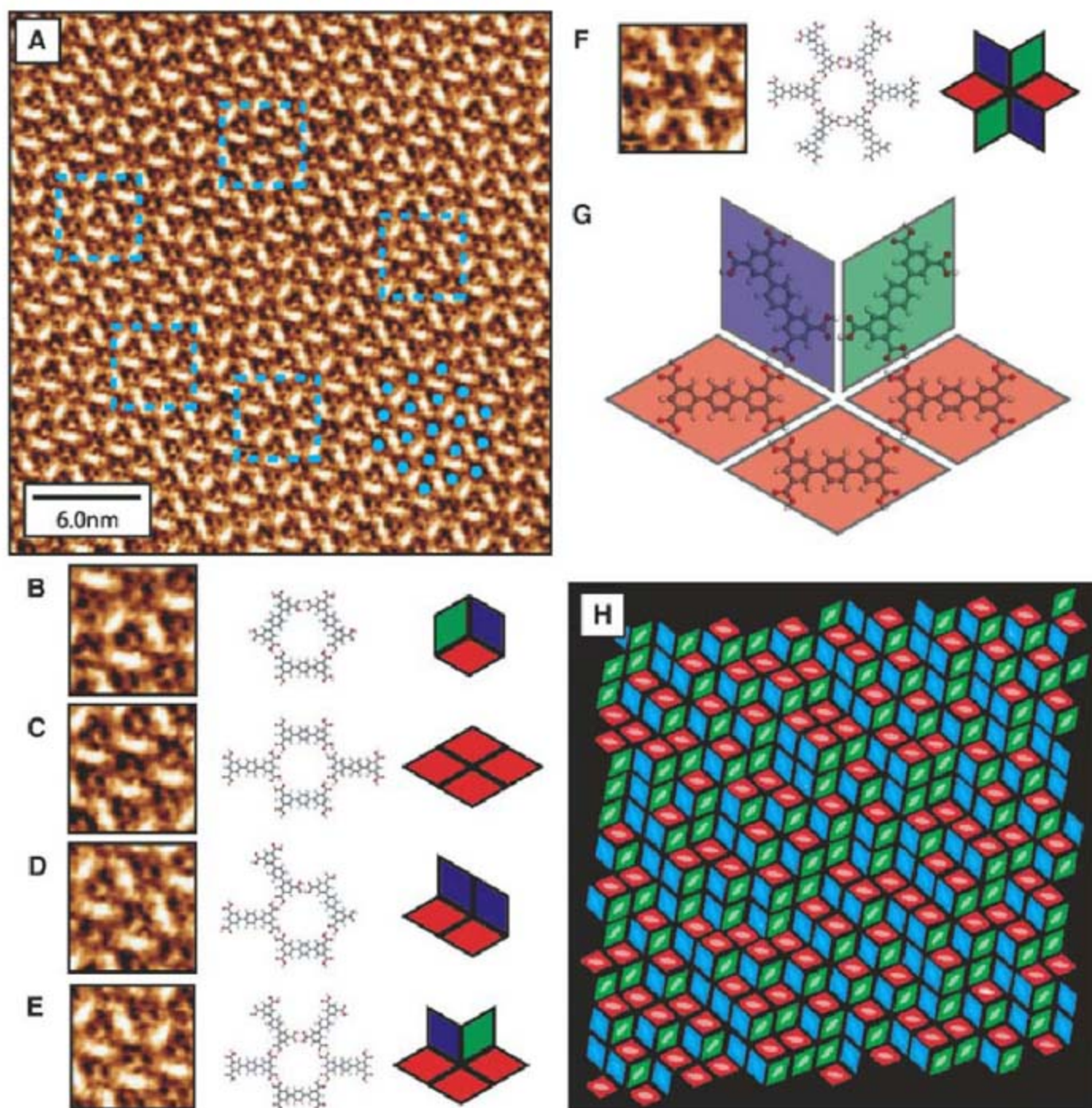


Fig. 1. (A) Molecular structure of TPTC. Two possible arrangements for a pair of TPTC molecules linked via a carboxylic acid–carboxylic acid hydrogen bond, (B) with the long axes of both molecules parallel to each other, and (C) with one molecule rotated by 60° with respect to the other.

Marked on (B) are the calculated distances (16) between two phenyl rings of different TPTC molecules taken across a carboxylic–carboxylic hydrogen bond (d_1), and the distance between the two end phenyl rings of a single TPTC molecule (d_2).

Fig. 2. (A) STM image of a typical area of TPTC network at the nonanoic acid/HOPG interface. The group of three phenyl rings constituting the backbone of the TPTC molecules appear as bright rodlike features in the image. The hexagonal orientational order of the structure is highlighted by the group of blue dots in the lower right-hand corner of the image, marking the location of dark contrast regions in the image (depressions/pores in the network). (B to F) Molecular ball and stick diagrams and tiling representations for the five possible arrangements of TPTC molecules around a network pore. Also shown are magnified STM image examples of each pore type from (A); the locations of the magnified regions are marked in (A) by blue dashed squares. Scanning conditions of (A) were tunneling current (I_t) = 0.015 nA and tip voltage (V_t) = 1200 mV. (G) Enlarged version of the molecular arrangement shown in (E). The equivalent tiling representation is shown as a transparent overlay, which highlights the location of the carboxylic acid–carboxylic acid hydrogen bonds at the midpoint of edges between tiles. (H) Corresponding tiling representation of (A). The coloration of (H) represents the three possible orientations of rhombi within the tiling (red, green, and blue). Idealized representations of the molecular positions are shown faintly in the tiling.



A typical area of the TPTC network adsorbed on the HOPG surface is shown in Fig. 2A. The terphenyl backbones of the molecules appear as bright rodlike features, and the molecular arrangement is unusual because it exhibits hexagonal orientational order but no translational symmetry. The hexagonal order may be discerned from the array of blue dots overlaid on dark contrast features (corresponding to depressions or pores) in Fig. 2A and, using calibration scans of the graphite substrate, we found that the hexagonal array has a period of $16.6 \pm 0.8 \text{ \AA}$ oriented at an angle of $\pm 6^\circ$ to the HOPG substrate (16). Although the pores are regularly arranged, the molecular network enclosing them is not translationally ordered. Figure 2, B to F, shows that the molecular arrangements enclosing different pores (highlighted areas in Fig. 1A) are hexagons formed by a varying number of molecules.

For example, Fig. 2B shows a hexagon formed by three molecules with edges that alternate between a terphenyl backbone and a carboxylic acid-carboxylic acid junction. Figure 2, C and D, shows two alternative hexagonal arrangements formed by the junction of four molecules with two edges formed by the terphenyl backbone. Similarly, the junction in Fig. 2E is formed by five molecules with one terphenyl edge, and the junction in Fig. 2F is formed by six molecules with no terphenyl edges. The lengths of the hydrogen-bonded and terphenyl edges (equivalent to d_1 and d_2 as defined in Fig. 1B) are calculated to be 9.6 and 8.7 \AA [the intermolecular binding energy $E_{\text{HB}} = 0.80 \text{ eV}$ is calculated to be the same for the parallel and arrowhead arrangements (16)], giving estimated widths of the hexagons in Fig. 2 ranging from 15.8 \AA (Fig. 2B) to 16.6 \AA (Fig. 2F), which is in good agreement with the measured periodicity. The molecular array shown in Fig. 2A may be built by combining these five structural units in an arrangement that exhibits orientational symmetry but no translational order.

The network may be mapped onto a tiling by replacing each molecule with a rhombus [see (25)

for another example linking molecular arrays to tiling problems]. Each molecule in the network points along one of three high-symmetry directions, and we have chosen, for clarity, to represent these three molecular orientations as rhombi with different colors. To illustrate the tiling, we have converted each of the hexagonal structural units discussed above into rhombi (Fig. 2). The representations of the junctions in Fig. 2, B to F, correspond to vertices where three, four, five, or six rhombi meet. These diagrams also show that, at a molecular level, the mapping is possible because the intermolecular bonds between neighboring molecules are located at the midpoint of the rhombus edges (Fig. 2G). We suggest that this symmetry is key to identifying other candidate molecules that might form similar networks.

The molecular network displayed in Fig. 2A can be mapped into rhombi, and the resultant tiling is shown in Fig. 2H. The mapping directly accounts for the presence of orientational symmetry combined with an absence of translational order because the rhombus vertices (pores in the STM images) fall on a hexagonal lattice, even though the arrangement of rhombi is not ordered. Thus, we demonstrate that the molecular array is equivalent to a rhombus tiling.

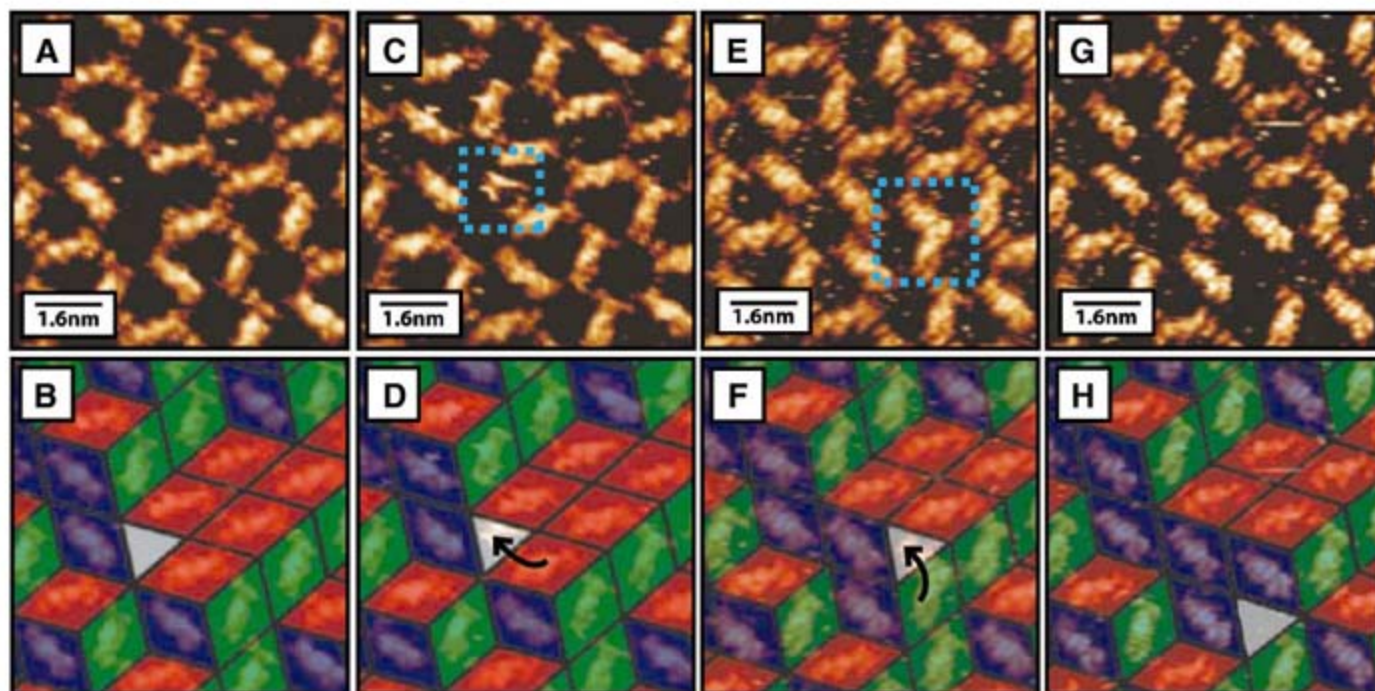
We also observed tiling defects in the form of triangular voids enclosed completely by rhombi (Fig. 3). These voids are topological defects that occur in two states of effective "charge" corresponding to triangles pointing either "up" or "down" and have been considered theoretically but have not previously been observed (26–28). We observed $\sim 3 \times 10^{-3}$ defects per adsorbed molecule and may unequivocally distinguish these voids from other less intrinsically interesting defects, such as vacancies. The triangular defects have been observed to propagate through the network, as shown in Fig. 3, C to H. This movement results in a rearrangement of a single molecule (or tile) within the network. Figure 3, C and F, shows a comparison of images before and after such a transition, in which, as expected, effective

charge is conserved. The triangular defect undergoes a second movement between Fig. 3, E and G. In our images, this transition appears to be mediated by the temporary presence of an additional species at the defect site, as highlighted in Fig. 3, C and E, possibly an additional TPTC molecule temporarily bound by hydrogen bonding. Although it is difficult to determine the exact details of the atomistic mechanism for defect movement, this sequence of images shows that defect propagation through the network gives rise to a reordering of molecular tiles and facilitates a transition between different local energy minima.

To determine whether the observed rhombus tilings are ordered or random, we followed previous theoretical studies (10, 12) and introduced an effective height $h(x,y)$ at each vertex (x,y) . The height was calculated with the scheme shown in Fig. 4A, in which a displacement along a rhombus edge leads to a change in height of ± 1 . By arbitrarily choosing an origin with zero height, it is possible to define $h(x,y)$ for all vertices of a perfect (defect-free) tiling. Within this scheme, a tiling may be visually considered as a perspective of the surface of a simple cubic lattice when viewed along a (111) direction. More formally, the rhombus tiling is equivalent to the projection of an irregular surface of a three-dimensional simple cubic crystal onto a (111) plane of the cubic lattice. A map of effective height of the STM image (Fig. 2A) is shown in Fig. 4C.

Within the random tiling hypothesis (11), the tilings may be analyzed by introducing an effective free energy G , which, assuming that all vertex types (shown in Fig. 2) are degenerate, is determined entirely by an entropic contribution and is given by $G = (K_0/2) \int |\nabla h|^2 dx dy$. This contribution is equivalent to the energy of a deformed surface with elastic constant K_0 . The gradient ∇h corresponds to the projection in the (x,y) plane of the normal to the representative surface. The tilings that are generated by this free energy have a height representation for which $\langle \nabla h \rangle = 0$, that is, a surface which on average is flat and par-

Fig. 3. (A, C, E, and G) STM images showing two separate movements of a single defect through the network structure. (B, D, F, and H) Tiling representation of the network structure during the defect motion. The effective rearrangements of rhombi in the tiling are marked by the black arrows in (D) and (F). Transient image artifacts observed within the defect site before defect motion are highlighted by blue dashed squares [(C) and (E)]. Scanning conditions for all images were $I_t = 0.021 \text{ nA}$ and $V_t = 1200 \text{ mV}$.



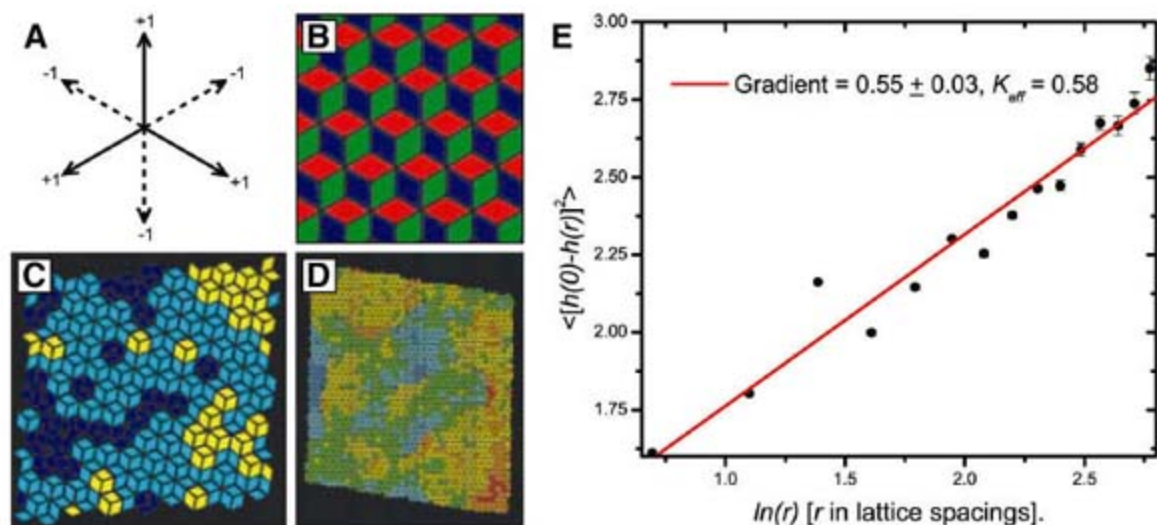


Fig. 4. (A) Scheme for evaluating height function of a tiling. A displacement from a vertex along three of the possible directions leads to an increase in height by 1 as shown; a displacement along the other three directions leads to a decrease by 1. (B) A schematic showing a flat undeformed representative surface to be compared with the (111) surface of a simple cubic crystal. (C) Height representation of tiling in Fig. 2. Here the height of a tile is calculated as the average over its four vertices; different heights are represented as different colors. (D) Height map of one of the large area scans (100 nm by 100 nm) used to generate correlation function [see (16) for more details]. (E) Dependence of correlation on separation demonstrating logarithmic dependence. Scanning conditions for all images were $I_t = 0.015$ nA and $V_t = 1200$ mV.

allel to a (111) plane of the projected cubic lattice, which is equivalent to a requirement that equal numbers of tiles are oriented in each of the three possible directions. Fluctuations in height with wavevector \mathbf{k} are expected with a Fourier spectrum $h(\mathbf{k}) \propto K_0^{-1} |\mathbf{k}|^{-2}$. In two dimensions, this spectrum leads to logarithmic spatial correlations in $h(x,y)$, $C(r) = \langle [h(0) - h(r)]^2 \rangle = (\pi K_0)^{-1} \ln(r) + c$, where c is a constant and, for the maximally random rhombus tiling, $K_0 = \pi/9$ (10, 12).

We calculated the height correlation function $C(r)$ from STM images that had been converted to a height representation (Fig. 4D). The fraction of tiles pointing in the three directions is in the ratio 1:1:1, within statistical error, and thus the condition $\langle \nabla h \rangle = 0$ is satisfied [see (16) for tile maps and ratios of tile orientations]. It is not possible to solely specify $h(x,y)$ in the presence of triangular void defects because the line integral of $h(x,y)$ along a closed path around a triangular void gives a nonzero value corresponding to the winding number of the defect (in this case, ± 3). However, it is possible to unambiguously calculate the contributions to the height correlation function in regions that do not enclose defects. Our method for calculating $C(r)$ is based on this approach and provides reliable data for $r \leq r_d$, the average defect separation.

As shown in Fig. 4E, the measured $C(r)$ has the expected logarithmic dependence on r , corresponding to the critical correlations of a random rhombus tiling (12). The effective elasticity of the tiling may be extracted from the prefactor of the logarithm. We find $K_{\text{eff}} = 0.58 \pm 0.03$, or equivalently $K_{\text{eff}}/K_0 \sim 1.7$.

The enhancement of the elastic constant over the expected value K_0 is explained as a breaking of the exact degeneracy in local bonding arrangements, with a small energetic preference for the

arrowhead (Fig. 1C) configuration. This difference in energy results in an energy cost for vertices that have neighboring tiles in the parallel configuration (Fig. 2, C to E). These vertices [which are not present on the idealized undeformed (111) representative surface, for which molecules are exclusively in the arrowhead arrangement (Fig. 4B)] are associated with local changes in height $\nabla h \neq 0$, leading to an energetic contribution to the free energy in addition to the purely entropic term discussed above. These effects lead to an increase in the effective elastic constant K_{eff} in G .

This explanation is consistent with results by Alet *et al.* (29) for closed packed dimers on the square lattice with aligning interactions, in which there is a critical phase with an effective elasticity that increases with increasing interaction strength Δ [and an eventual phase transition to an ordered phase for $\Delta \sim kT$ (T , temperature), where other terms become relevant in the free energy G (29)]. In the context of our experiments, Δ characterizes the energy difference between the parallel and arrowhead configurations. Our finding of logarithmic correlations with K_{eff} close to K_0 , to within a factor 2, confirms that our system is in the random tiling regime and therefore $\Delta < kT$ (0.03 eV). This very small value of energy, comparable with the uncertainty in our calculation of E_{HB} , highlights the delicate balance required for entropically stabilized randomness in the rhombus tiling.

Although the above analysis of the spatial distribution of tiles is based on the equilibrium free energy G , it is clear that the tilings are frozen, with minimal temporal evolution, in one local minimum of a complex energy landscape. The system is dynamically arrested, similar to a glass, and all tile movements are activated with an energy cost that is expected to scale with the number of intermolecular hydrogen bonds that must be broken. Triangular defects, which mediate the only tile

rearrangements that have been experimentally observed, have the lowest activation barrier because only three bonds must be broken in order to move a molecule directly adjacent to a defect. Other tile rearrangements, such as the 60° rotation of the hexagonal unit in Fig. 2B, often considered in the context of mixing algorithms for perfect (defect-free) random tilings (8), require six bonds to be broken and would be expected to be exponentially suppressed. The observation of the propagation of localized defects as a mechanism for transitions between different local energy minima is highly reminiscent of dynamically facilitated models of glass formers (30, 31). Our results demonstrate the potential of molecular tilings as model systems for the study of glasses and provide an interesting alternative to the random molecular networks recently identified by Otero *et al.* as glassy systems (32).

Our results show that, once formed, tilings are trapped in one of a large number of quasi-degenerate locally stable states that can rearrange through defect migration. Overall, the connection between rhombus tiling and molecular architecture, through the approximate equality $d_1 \sim d_2$, leads to design rules for a general class of analogous molecular networks in two and three dimensions that can provide novel model systems for the study of random structural arrangements and dynamically arrested materials.

References and Notes

1. D. Shechtman, I. Blech, G. Gratias, J. W. Cahn, *Phys. Rev. Lett.* **53**, 1951 (1984).
2. D. Levine, P. J. Steinhardt, *Phys. Rev. Lett.* **53**, 2477 (1984).
3. G. Onoda, P. J. Steinhardt, D. J. DiVincenzo, J. E. S. Socolar, *Phys. Rev. Lett.* **60**, 2653 (1988).
4. J. Ledieu *et al.*, *Phys. Rev. Lett.* **92**, 135507 (2004).
5. J. Yuhara *et al.*, *Phys. Rev. B* **70**, 024203 (2004).
6. M. E. Fisher, *Phys. Rev.* **124**, 1664 (1961).
7. P. Kasteleyn, *J. Math. Phys.* **4**, 287 (1963).
8. D. B. Wilson, *Ann. Appl. Probab.* **14**, 274 (2004).
9. H. Cohn, R. Kenyon, J. Propp, *J. Am. Math. Soc.* **14**, 297 (2001).
10. H. W. J. Blote, H. J. Hilhorst, *J. Phys. A* **15**, L631 (1982).
11. R. Moessner, S. L. Sondhi, E. Fradkin, *Phys. Rev. B* **65**, 024504 (2002).
12. C. L. Henley, in *Quasicrystals, the State of the Art*, D. P. DiVincenzo, P. J. Steinhardt, Eds. (World Scientific, Singapore, 1999), p. 459.
13. M. Widom, D. P. Deng, C. L. Henley, *Phys. Rev. Lett.* **63**, 310 (1989).
14. N. Destainville, *Phys. Rev. Lett.* **88**, 030601 (2002).
15. A. S. Keys, S. C. Glotzer, *Phys. Rev. Lett.* **99**, 235503 (2007).
16. Materials and methods and additional data are available as supporting material on Science Online.
17. M. Lackinger, S. Griessl, W. A. Hechl, M. Hietschold, G. W. Flynn, *Langmuir* **21**, 4984 (2005).
18. S. J. H. Griessl *et al.*, *Langmuir* **20**, 9403 (2004).
19. S. de Feyter, F. C. de Schryver, *J. Phys. Chem. B* **109**, 4290 (2005).
20. J. V. Barth, G. Costantini, K. Kern, *Nature* **437**, 671 (2005).
21. F. Rosei *et al.*, *Prog. Surf. Sci.* **71**, 95 (2003).
22. H. Zhou *et al.*, *J. Am. Chem. Soc.* **129**, 13774 (2007).
23. M. Blunt *et al.*, *Chem. Commun.* 2304 (2008).
24. M. Li *et al.*, *Angew. Chem. Int. Ed.* **47**, 6717 (2008).
25. M. Pivetta, M. C. Blum, F. Patthey, W. D. Schneider, *Angew. Chem. Int. Ed.* **47**, 1076 (2008).
26. M. E. Fisher, J. Stephenson, *Phys. Rev.* **132**, 1411 (1963).

27. J. Linde, C. Moore, M. G. Nordahl, *Discrete Mathematics and Theoretical Computer Science Proceedings AA (DM-CCG)* 23 (2001).
28. W. Krauth, R. Moessner, *Phys. Rev. B* 67, 064503 (2003).
29. F. Alet *et al.*, *Phys. Rev. Lett.* 94, 235702 (2005).
30. G. H. Fredrickson, H. C. Andersen, *Phys. Rev. Lett.* 53, 1244 (1984).
31. J. P. Garrahan, D. Chandler, *Proc. Natl. Acad. Sci. U.S.A.* 100, 9710 (2003).
32. R. Otero *et al.*, *Science* 319, 312 (2008).
33. We thank the UK Engineering and Physical Sciences Research Council (EPSRC) for financial support under grant EP/D048761/01. J.P.G. was supported by EPSRC grant GR/S54074/01. M.S. acknowledges receipt of a Royal Society Wolfson Merit Award.

Supporting Online Material

www.sciencemag.org/cgi/content/full/322/5904/1077/DC1

Materials and Methods

Figs. S1 to S4

References

16 July 2008; accepted 6 October 2008

10.1126/science.1163338

Observing the Creation of Electronic Feshbach Resonances in Soft X-ray–Induced O₂ Dissociation

Arvinder S. Sandhu,^{1*†} Etienne Gagnon,^{1*} Robin Santra,^{2,3} Vandana Sharma,¹ Wen Li,¹ Phay Ho,² Predrag Ranitovic,⁴ C. Lewis Cocke,⁴ Margaret M. Murnane,^{1‡} Henry C. Kapteyn¹

When an atom or molecule is ionized by an x-ray, highly excited states can be created that then decay, or autoionize, by ejecting a second electron from the ion. We found that autoionization after soft x-ray photoionization of molecular oxygen follows a complex multistep process. By interrupting the autoionization process with a short laser pulse, we showed that autoionization cannot occur until the internuclear separation of the fragments is greater than approximately 30 angstroms. As the ion and excited neutral atom separated, we directly observed the transformation of electronically bound states of the molecular ion into Feshbach resonances of the neutral oxygen atom that are characterized by both positive and negative binding energies. States with negative binding energies have not previously been predicted or observed in neutral atoms.

The ability to reveal fast correlated electronic dynamics with ultrafast x-rays has attracted considerable interest in recent years. In general, some of the fastest electronic processes involve highly excited states. Autoionization after photoionization of an electron from an atom, molecule, or solid is a good example of one such process (1–8). Autoionization is an important electronic many-body problem in molecules, and the electrons and ions produced also contribute to radiation damage in materials and biological systems (9). In the autoionization of a deep inner-shell hole, an electron from a higher energy level fills the hole, while a second outer (Auger) electron is ejected, carrying away excess energy. Auger decay from a deep inner-shell hole is always energetically allowed, both in isolated atoms and molecules. In this case, the molecular environment generally plays a minor role. In contrast, autoionization of an inner-valence vacancy in an isolated atom is often energetically forbidden. For example, the 2s¹2p⁴ ²P inner-valence state of O⁺ lies 40 eV above the ground state of atomic oxygen but 9 eV below the O²⁺ ground state and can therefore only

decay radiatively; that is, by emitting a photon. However, in polyatomic systems, autoionization after inner-valence ionization can be energetically allowed because the molecular environment can play a role. Because the two final-state charges in a molecular dication do not have to sit on one atom, the Coulomb repulsion between the holes is reduced, and thus the double ionization threshold is lowered.

Interatomic Coulombic decay (ICD) in the Ne dimer, for instance, is a prominent example in which the molecular environment plays a major role in autoionization and has received much recent attention (1, 2, 10). In ICD in Ne, autoionization of a 2s hole relies on energy transfer between the two Ne atoms and thus preferentially takes place near the equilibrium separation of the atoms of the neutral Ne dimer. Molecular oxygen (O₂) can also autoionize after photoionization in the inner-valence region (4–6). However, O₂ does not follow the paradigm provided by ICD, in which autoionization occurs when the atoms are in proximity. Rather, Feifel *et al.* (4) performed a high-resolution coincident electron study of O₂ and concluded that the atomiclike character of the autoionization spectrum indicates that the decay takes place at large interatomic distances, which is in stark contrast to ICD. However, these experiments did not have any time resolution: Without the ability to observe intermediate states, it was not possible to uncover the mechanism for autoionization to fully understand what was happening.

In this work, we irradiated an O₂ molecule with a few-femtosecond x-ray pulse to create

superexcited states of the O₂⁺ molecular ion. We then used an ultrafast laser pulse to follow how this superexcited state evolves into an autoionizing state. We achieved this by interrupting the autoionization with an ultrafast laser pulse at different times during the process. First, we found that autoionization cannot occur until the molecular fragments are well-separated, by distances of >30 Å. Second, we found that the autoionizing state forms 300 fs after x-ray irradiation and emerges as a negative binding-energy Feshbach resonance. The use of ultrafast x-rays and lasers (11), in combination with a triple-coincidence detection scheme, allowed us to directly observe the onset of these negative binding-energy Feshbach autoionizing states. Before this work, the existence of negative binding-energy states in neutral atoms was not anticipated. Third, by providing an explanation for the atomic nature of the autoionization lines observed in O₂, we were able to highlight the dramatic difference between the roles of the molecular environment in ICD in van der Waals dimers and molecular autoionization, in which the presence of a molecular field can suppress, rather than enhance, autoionization. Finally, we showed that we can manipulate superheated, metastable, autoionizing states before they decay and actively influence, with a strong field, whether a superexcited state will have the opportunity to decay or not. This capability raises the possibility of coherent manipulation of highly excited quantum states, even when their energies lie above the ionization potential. Autoionization after soft x-ray photoionization of O₂ is thus a much more complex multi-step process than in the case of N₂, with which in recent studies we used an ultrafast soft x-ray pump combined with an infrared probe to study electron shakeup processes (12, 13).

Several studies have reported the existence of negative binding energy states in multiply charged molecular ions (anions) (14–16). A particular electronic state is considered to have a negative binding energy when the kinetic energy of an ejected photoelectron is greater than the single-photon energy used for the ionization step. This means that the electronic state must be higher in energy than the ionization channel being considered. A state with negative binding energy must therefore be metastable. The repulsive Coulomb barrier in multiply charged anions supports long-lived shape resonances (metastable states that decay by tunneling through a potential barrier), which because of their long lifetime are easy to detect experimentally. To date, states with negative electron-binding energy were thought to be

¹JILA, University of Colorado at Boulder, Boulder, CO 80309, USA. ²Argonne National Laboratory, Argonne, IL 60439, USA.

³Department of Physics, University of Chicago, Chicago, IL 60637, USA. ⁴J. R. MacDonald Lab, Department of Physics, Kansas State University, Manhattan, KS 66506, USA.

*These authors contributed equally to this work.

†Present address: Department of Physics, University of Arizona, Tucson, AZ 85721-0081, USA.

‡To whom correspondence should be addressed. E-mail: margaret.murnane@colorado.edu

a feature only of multiply charged anions because of the presence of a repulsive Coulomb barrier.

Feshbach resonances occur in compound systems such as atoms, molecules, nuclei, or quarkonia, when a bound state in a closed channel can decay into a continuum state in an open channel via interchannel coupling. The nature of the channels and the nature of the interchannel coupling depend on the system under consideration. If at least one of the partners in a collision process, for example, is itself a compound system, one cannot necessarily characterize a collision entirely in terms of the relative motion of two collision partners within an effective collision potential because the internal degrees of freedom of the systems may be dynamically involved in the collision. Feshbach resonances have been known since Herman Feshbach formalized them in the 1950s (17). Initially, the Feshbach resonance picture was used to describe nuclear collisions. However, more generally any autoionizing state generated by removing an inner-shell electron is a Feshbach resonance, and therefore these states underlie Auger, Coster-Kronig, or ICD decay. In recent years, Feshbach resonances have been exploited in ultracold collisions, in which the collision energy is very small (18, 19). In these systems, the relative position of the open and closed channels can be adjusted by using a variable magnetic field. This provides a simple knob to control the collisional properties of an ultracold gas.

The experimental setup and schematic of the molecular autoionization process are shown in Fig. 1. The output from an ultrafast Ti:sapphire amplifier system producing ~ 2 -mJ pulses with ~ 30 fs duration, at a repetition rate of 2 kHz, was split into pump and probe beams. (12, 13) The pump beam (~ 1.2 mJ) was used to generate an ultrashort (< 10 fs) soft x-ray pump beam with a photon energy of 42.7 eV (full width at half maximum ≈ 1.5 eV) through high-order harmonic upconversion. The net photon flux, after filtering out the visible laser and selecting a single harmonic with a pair of multilayer mirrors, was $\sim 10^6$ photons per pulse or 2×10^9 photons/s. The probe beam (~ 0.8 mJ) was time-delayed and recombined with the soft x-ray pump beam in the interaction region, which provided a means to dynamically probe the autoionization process. This infrared (IR) probe beam passed through an optical chopper with a 50% duty cycle, which allowed us to normalize our data on a shot-to-shot basis. The IR probe beam was focused onto the O_2 sample with a 75-cm lens to an intensity of 4.9×10^{12} W/cm 2 . The target O_2 gas was cooled and confined with a supersonic jet expansion employing a 30- μ m nozzle. The cold supersonic portion of the jet was selected using a 300- μ m skimmer placed ~ 13 mm from the gas nozzle. The gas density in the interaction region was estimated to be $\sim 10^{11}$ to 10^{12} cm $^{-3}$. A cold-target recoil ion momentum spectroscopy (COLTRIMS)-based reaction microscope collected reaction fragments with high

efficiency (solid angle $\sim 4\pi$) for both electrons and ions for each laser shot.

Figure 2 shows electron and ion kinetic energy spectra acquired with our coincident ion/electron detectors for the case of soft x-ray illumination of O_2 . For these spectra, an electron was detected in coincidence with two O^+ ions. By requiring that the two ions have nonzero kinetic energy release and zero total momentum, we ensured that both ions came from the same molecule. The broad feature centered at ≈ 1.8 eV in the electron-energy spectrum in Fig. 2 corresponded predominantly to the photoelectron (one-photon single ionization) and to electrons

produced via direct one-photon double ionization. The width of this feature was partly determined by the distribution of binding energies of the various autoionizing states of O_2^+ that are populated (4). More electronic states are excited than one might expect based on the number of initially occupied orbitals. This is an example of the breakdown of the molecular orbital picture for inner-valence electrons (20).

The electron-energy peak appearing at ≈ 0.5 eV is consistent with the A1 and A2 autoionization lines of O_2 that were identified by Feifel *et al.* (4). (Other, less prominent autoionization lines are merged with the photoelectron

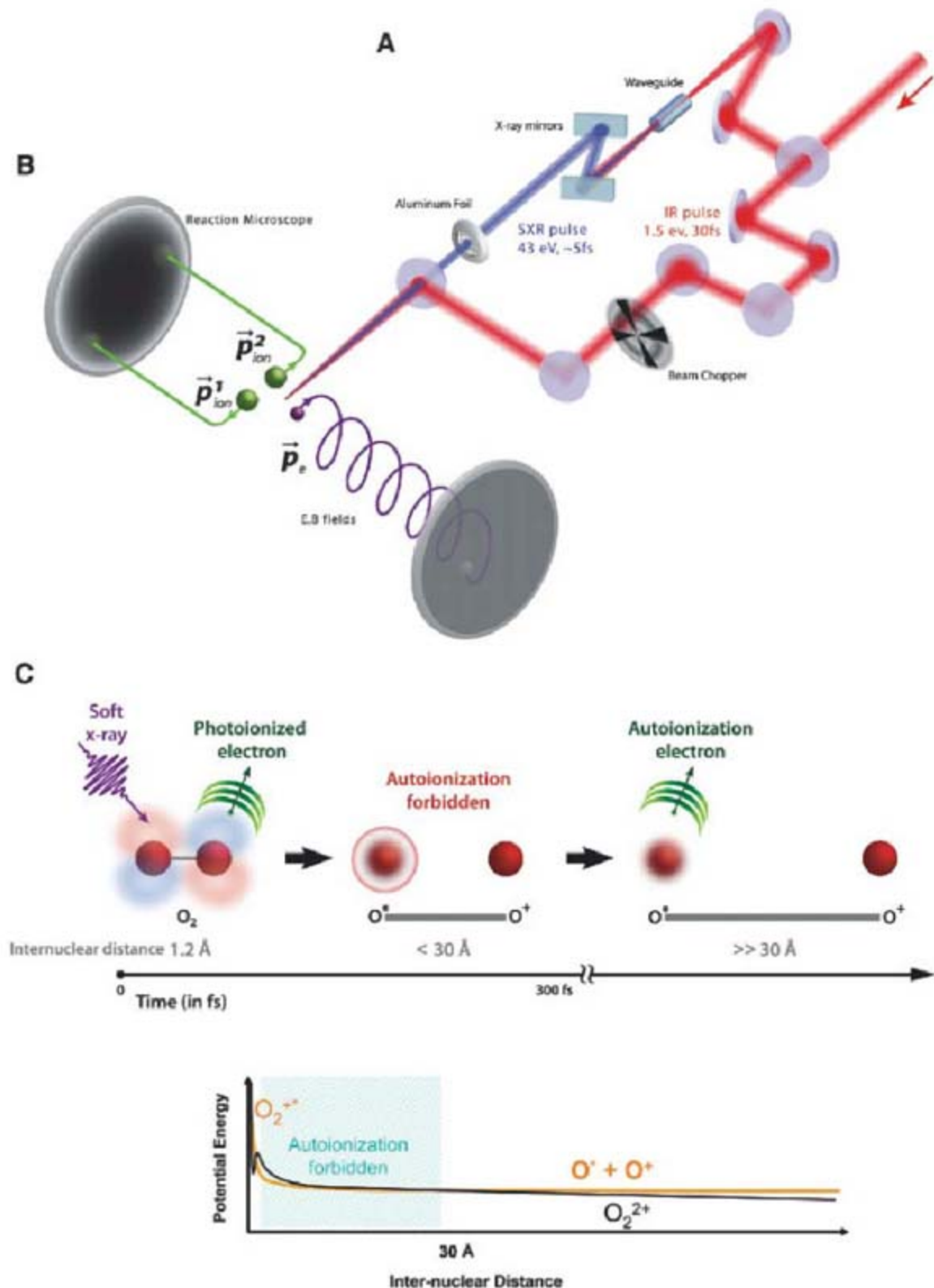


Fig. 1. (A) Schematic of the experimental setup in which a soft x-ray beam photoionizes the O_2 molecule while an IR probe beam interrupts the autoionization in order to follow the dynamics. E.B. fields, electric and magnetic fields, respectively; SXR, soft x-ray beam. (B) COLTRIMS reaction microscope. (C) Schematic of the multistep photoionization, dissociation, and autoionization of O_2 . Autoionization is forbidden until the autoionizing state emerges as a negative-binding energy Feshbach resonance at internuclear separations of 30 Å or greater.

distribution.) As pointed out in (4), the A1 and A2 autoionization lines observed are so narrow that the electronic decay process must be taking place in the dissociation limit, in which the atomic fragments are well separated. Specifically, the A1 line corresponds to the $2s^2 2p^3(^4D^o)3p^1(^3D)$ state of atomic oxygen. In this state, which is 0.43 eV above the ground state of O^+ $2s^2 2p^3(^4S^o)$, the $3p$ electron is bound to the $2s^2 2p^3(^3D^o)$ excited-state ion core (Fig. 3B). This $2s^2 2p^3(^3D^o)$ excited state of O^+ is a closed channel for autoionization because this transition is energetically forbidden; there is simply insufficient energy for the autoionizing electron to be ejected, leaving behind O^+ in the first excited state. Thus, the $2s^2 2p^3(^4S^o)$ ground state of O^+ is the only open channel into which the autoionizing state can decay. The necessary change in the electronic configuration of the ion core (channel coupling) that must accompany autoionization is mediated by the

electron-electron and spin-orbit interactions; in the absence of spin-orbit coupling, that is, when the total orbital angular momentum L and the total spin S are good quantum numbers, autoionization would be forbidden. As described above, relaxation via channel coupling is precisely the required characteristic of a Feshbach resonance. The A2 line corresponds to the $2s^2 2p^3(^2D^o)3p^1(^3F)$ [autoionization LS-allowed] and $2s^2 2p^3(^2P^o)3s^1(^3P^o)$ (autoionization LS-forbidden) states of atomic oxygen. They lie 0.48 and 0.51 eV, respectively, above the O^+ ground state.

The kinetic energy release (KER) of the two detected O^+ ions shown in Fig. 2 was obtained by considering only those counts that were associated with the autoionization electrons (electrons with energies between 0 and 1 eV in Fig. 2). The structure of this KER spectrum [see (5) for a similar measurement] can be understood using the O_2^+ electron-binding energies (4), the atomic

autoionization electron energies, and the O_2^+ dissociation limits (21). These parameters allow the assignment of the strongest KER peaks between 4.9 and 7.5 eV in Fig. 2 to events associated with the quasimolecular A1 and A2 autoionization lines. Therefore, after O_2 is ionized by a 43-eV soft x-ray photon, a highly excited O_2^+ is formed. The molecular cation dissociates into an ion O^+ and an excited oxygen atom O^* . From the narrow observed autoionization lines (4), the superexcited oxygen atom autoionizes only after dissociation, resulting in a second O^+ ion.

This brings us to an obvious question: Why does autoionization not happen at short interatomic distances? Because the presence of a neighboring ion breaks the spherical symmetry, there should be no need for spin-orbit coupling in order to drive LS-forbidden autoionization. Autoionization could then conceivably be as fast as molecular dissociation. An answer to this question is suggested by Fig. 3, which shows a few of the lowest-lying potential energy curves of O_2^+ [see (21) for further curves] as well as the autoionizing state (orange line). We calculated the potential energy curves using the *ab initio* program package COLUMBUS (22–24), employing the high-quality Gaussian basis set cc-pV5Z (25) in combination with a multiconfiguration self-consistent-field calculation followed by a multireference configuration-interaction calculation. In Fig. 3A, we plot the region near the Franck-Condon window (1.16 to 1.27 Å) with respect to the vibrational ground state of O_2 . At a photon energy of 42.7 ± 0.75 eV, a typical photoelectron energy of ≈ 2 eV or higher (Fig. 2) implies that, within the Franck-Condon window, the majority of associated O_2^+ states can only decay into the $X^1\Sigma_g^+$ channel. The corresponding predissociating vibrational states of O_2^+ below

Fig. 2. Coincident electron and ion ($O^+ + O^+$) kinetic energy spectra in the presence of the soft x-ray field alone (triple coincidence detection). The detected electrons include the autoionizing electrons (lower energy, ≈ 0.5 eV) and the photoelectrons (higher energy). $h\nu_{\text{exc}}$, soft x-ray photo energy.

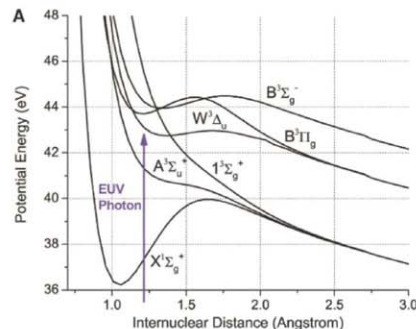
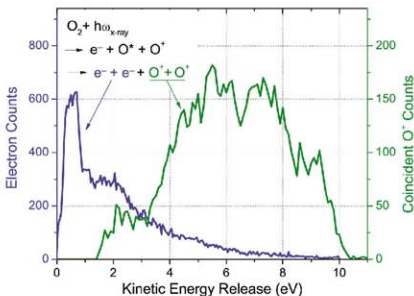
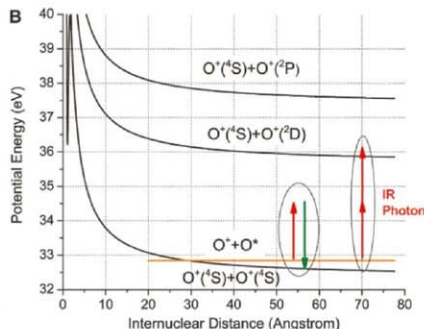


Fig. 3. (A) Potential energy curves of O_2^+ for short internuclear distances near the Franck-Condon window. Each curve is labeled by conventional spectroscopic notation that indicates the symmetry of the state. (B) Potential energy curves [same as in (A)] shown for large internuclear distances. The orange line shows the energy of the ground-state oxygen ion $O^+(^4S)$ plus



an autoionizing oxygen atom (corresponding to the A2 autoionizing line). Absorption of a single IR photon (red arrows) ionizes the Feshbach autoionizing state, leaving the system in the ground state of O_2^+ . This process results in a photoelectron energy (green arrow) greater than the incident IR photon energy.

vibrational levels $v = 13$ are very long-lived (26) and do not contribute to the coincidence signal considered here. The known potential energy curves of O_2^+ in the inner-valence regime are all highly repulsive (27). Therefore, unless autoionization into quasi-bound states on the X curve has already taken place (if spin-allowed), the potential energy of O_2^+ would be expected to drop below all O_2^{2+} curves. Fast dissociation would therefore occur, and the O_2^+ curves would then become essentially flat. However, autoionization will still remain energetically forbidden until the O_2^+ curves (Fig. 3B, orange line) cross one or more O_2^{2+} curves for a second time. As shown in Fig. 3B, in the case of the O_2^+ potential energy curves correlating to a ground-state O^+ ion and an excited oxygen atom that are associated, for example, with the A2 autoionization line, the crossing point with

the $O^+(^1S^o) + O^+(^1S^o)$ curve lies at ≈ 30 Å. Only for interatomic distances greater than this is autoionization energetically allowed. In view of the ion KER shown in Fig. 2, for these ion velocities it should take between 220 and 280 fs to reach this crossing point.

We have experimental and theoretical [see supporting online material (SOM) text] evidence that this scenario is correct. Figure 4 displays electron-energy spectra, measured in coincidence with two O^+ ions, for various time delays between the soft x-ray pump and IR probe pulses. At time delays smaller than 300 fs, the coincidence rate is similar to the soft x-ray-only case. However, the A1/A2 autoionization feature at low electron energies is absent. At early time delays, the IR pulse suppresses atomic autoionization partly by producing dissociative O_2^{2+} at

short interatomic distance, thus giving rise to a shift of the KER toward larger values, and partly by transferring population to states that do not contribute to the coincidence signal (SOM text and figs. S1 and S2). Two new features begin to appear at time delays around 300 fs: a peak at ≈ 2 eV of electron energy and a peak near zero electron energy. We interpret these features in terms of the mechanisms indicated in Fig. 3B. After the dissociation of O_2^+ has reached the crossing point at internuclear separations around 30 Å as described earlier (for each electronic state there is a somewhat different crossing point), we have an O ion and an excited oxygen atom born into a Feshbach resonance state. Absorption of a single IR photon of energy 1.55 eV from this Feshbach state liberates a photoelectron of energy ≈ 2 eV, which shows that this state has a negative binding energy with respect to the ground state of O^+ . Two-photon absorption yields a photoelectron energy of ≈ 0.1 eV, corresponding to excitation to the first excited state of O^+ , as shown in Fig. 3B. The width of the observed features is largely determined by the resolution of our apparatus and by the bandwidth of our laser. There may also be a contribution from above-threshold ionization.

The negative and positive binding-energy features move to slightly higher energy at longer time delays. This is due to the fact that the O_2^+ potential energy curves on which the nuclear wave packet travels before IR ionization are flat, whereas the O_2^{2+} potential energy curves are influenced by the ion-ion Coulomb repulsion (Fig. 3B). At time delays of 1000 fs, a small shoulder appears in the electron-energy spectra around ≈ 0.5 eV, where the soft x-ray-only spectra are peaked. As mentioned earlier, autoionization of one of the two resonances that contribute to the A2 line is LS-allowed, with an expected lifetime of the order of 1 ps (28). It is probable that this shoulder is due to LS-allowed autoionization preceding the IR probe pulse. The lifetime of resonances whose autoionization is LS-forbidden is expected to be on the order of 1 ns, in competition with radiative decay. This translates to an autoionization efficiency of less than unity. The IR probe efficiently ionizes the Feshbach resonance states, thus leading to a higher coincidence rate than in the soft x-ray-only case, as confirmed in Fig. 4.

Given our findings, it is interesting to compare autoionization in van der Waals dimers with the same process in small covalently bound molecules. Both Ne_2 and O_2 can in principle autoionize within the Franck-Condon window. The reason is the same in both cases: It takes less energy to form a dication with one positive charge on one atom and a second positive charge on the other atom than it takes to form a dication with two positive charges localized on a single atom. However, the real difference between the Ne dimer and O_2 is the following: The inner-valence potential energy curves of the neon dimer cation are very flat; therefore, the Ne atoms do not separate until interatomic Coulombic decay has taken place because dissociation of the inner-

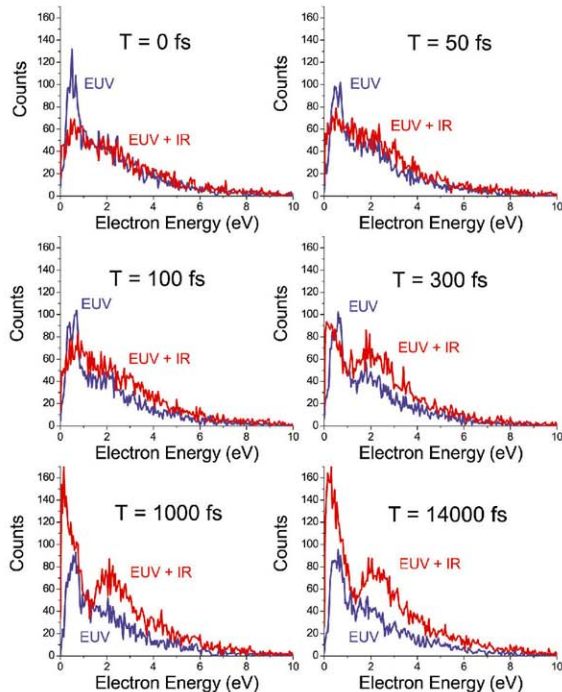


Fig. 4. Electron-energy spectra acquired in triple coincidence ($O^+ + O^+ + \text{electron}$) by varying the time delay (T) between the soft x-ray pump and IR probe pulses. Soft x-ray-only spectra are shown for comparison. Near time zero, the presence of the IR field suppresses autoionization. For times >300 fs, the presence of the IR field enhances ionization by ionizing the Feshbach resonance before autoionization or radiative decay has time to occur (Fig. 3B).

valence-ionized Ne dimer is slow in comparison to ICD. The flatness of the inner-valence potential energy curves, which enables ICD at essentially all interatomic distances and prevents ultrafast dissociation, is specific to van der Waals systems. In real molecules such as O₂, electron-correlation effects are stronger. The adiabatic potential energy curves in the inner-valence regime are not flat and have many avoided crossings associated with steep dissociative curves. Real molecules can rapidly dissociate and convert electronic energy into kinetic energy of the dissociating fragments.

Finally, without triple-coincidence COLTRIMS experiments to locate the curve-crossing region and moment of onset of the Feshbach autoionizing state, accurate modeling of these superexcited states would not have been possible. Generally, electronic-structure methods, even for excited states, have made substantial progress. However, the inner-valence regime remains challenging because of the large number of electronic states involved and because of the considerable role that electronic many-body effects play in this highly excited energy regime.

We have uncovered the onset of an electronic Feshbach resonance and the existence of negative binding-energy states in neutral atoms. We

show that it is possible to actively manipulate superexcited states above the ionization potential by interrupting autoionization with a strong femto-second laser field. These findings should be applicable to autoionizing states in small molecules.

References and Notes

1. R. Santra, J. Zobeley, L. S. Cederbaum, N. Moiseyev, *Phys. Rev. Lett.* **85**, 4490 (2000).
2. T. Jahnke *et al.*, *Phys. Rev. Lett.* **93**, 163401 (2004).
3. T. Jahnke *et al.*, *J. Electron Spectrosc. Relat. Phenom.* **141**, 229 (2004).
4. R. Feifel, J. H. D. Eland, D. Edvardsson, *J. Chem. Phys.* **122**, 144308 (2005).
5. S. Hsieh, J. H. D. Eland, *J. Phys. At. Mol. Opt. Phys.* **29**, 5795 (1996).
6. S. D. Price, J. H. D. Eland, *J. Phys. At. Mol. Opt. Phys.* **24**, 4379 (1991).
7. L. Miaja-Avila *et al.*, *Phys. Rev. Lett.* **101**, 046101 (2008).
8. M. Drescher *et al.*, *Nature* **419**, 803 (2002).
9. B. Boudaiffa, P. Cloutier, D. Hunting, M. A. Huels, L. Sanche, *Science* **287**, 1658 (2000).
10. A. Kuleff, L. S. Cederbaum, *Phys. Rev. Lett.* **98**, 083201 (2007).
11. A. Rundquist *et al.*, *Science* **280**, 1412 (1998).
12. E. Gagnon *et al.*, *Science* **317**, 1374 (2007).
13. E. Gagnon *et al.*, *Rev. Sci. Instrum.* **79**, 063102 (2008).
14. J. Yang *et al.*, *J. Chem. Phys.* **128**, 091102 (2008).
15. A. Dreuw, L. S. Cederbaum, *Phys. Rev. A* **63**, 012501 (2000).
16. X.-B. Wang, L.-S. Wang, *Nature* **400**, 245 (1999).

17. H. Feshbach, *Ann. Phys.* **5**, 357 (1958).
18. C. A. Regal, C. Ticknor, J. L. Bohn, D. S. Jin, *Nature* **424**, 47 (2003).
19. S. Jochim *et al.*, *Science* **302**, 2101 (2003).
20. L. S. Cederbaum *et al.*, *J. Phys. B* **10**, L549 (1977).
21. M. Lundqvist, D. Edvardsson, P. Baltzer, M. Larsson, B. Wannberg, *J. Phys. At. Mol. Opt. Phys.* **29**, 499 (1996).
22. H. Lischka, R. Shepard, F. B. Brown, I. Shavitt, *Int. J. Quantum Chem. Symp.* **15**, 91 (1981).
23. R. Shepard *et al.*, *Int. J. Quantum Chem. Symp.* **22**, 149 (1988).
24. H. Lischka *et al.*, *Phys. Chem. Chem. Phys.* **3**, 664 (2001).
25. T. H. Dunning, *J. Chem. Phys.* **90**, 1007 (1989).
26. R. I. Hall, *et al.*, *Phys. Rev. Lett.* **68**, 2751 (1992).
27. Y. Hikosaka, *et al.*, *J. Chem. Phys.* **119**, 7693 (2003).
28. P. M. Dehmer, W. L. Luken, W. A. Chupka, *J. Chem. Phys.* **67**, 195 (1977).
29. We thank J. H. D. Eland and B. Krassig for helpful discussions. We acknowledge support for this work from NSF through the Physics Frontiers Centers Program and from the Office of Basic Energy Sciences, Office of Science, U.S. Department of Energy (DOE) (H.C.K. and M.M.M. under grant DOE DE-FG02-99ER14982; R.S. and P.H. under contract DE-AC02-06CH11357).

Supporting Online Material

www.sciencemag.org/cgi/content/full/322/5904/1081/DC1

SOM Text
Figs. S1 and S2

References

11 August 2008; accepted 15 October 2008
10.1126/science.1164498

Photosynthetic Control of Atmospheric Carbonyl Sulfide During the Growing Season

J. E. Campbell,^{1,†} G. R. Carmichael,² T. Chai,³ M. Mena-Carrasco,^{4,5} Y. Tang,² D. R. Blake,⁶ N. J. Blake,⁶ S. A. Vay,⁷ G. J. Collatz,⁸ I. Baker,⁹ J. A. Berry,¹⁰ S. A. Montzka,¹¹ C. Sweeney,¹² J. L. Schnoor,¹ C. O. Stanier²

Climate models incorporate photosynthesis-climate feedbacks, yet we lack robust tools for large-scale assessments of these processes. Recent work suggests that carbonyl sulfide (COS), a trace gas consumed by plants, could provide a valuable constraint on photosynthesis. Here we analyze airborne observations of COS and carbon dioxide concentrations during the growing season over North America with a three-dimensional atmospheric transport model. We successfully modeled the persistent vertical drawdown of atmospheric COS using the quantitative relation between COS and photosynthesis that has been measured in plant chamber experiments. Furthermore, this drawdown is driven by plant uptake rather than other continental and oceanic fluxes in the model. These results provide quantitative evidence that COS gradients in the continental growing season may have broad use as a measurement-based photosynthesis tracer.

Parameterizations of carbon-climate feedbacks in climate models are based on climate sensitivities for photosynthesis and respiration that are highly uncertain (1–3). Measurement-based estimates of photosynthesis or respiration fluxes at large scales (>10⁴ km²) are needed to investigate these feedback mechanisms. Whereas photosynthesis and respiration-flux estimates have been made using eddy flux (4, 5) and isotope techniques (6), robust tools for investigating these processes at large scales are currently lacking.

Recent work suggests potential for the use of atmospheric carbonyl sulfide (COS) as a photosynthesis tracer, on the basis of similarities observed between COS and CO₂ in a global air-monitoring network (7). The similarities are attributable to the simultaneous uptake of COS and CO₂ in photosynthetic gas exchange by terrestrial plants (8). COS has also been studied as a source of stratospheric aerosol (9, 10), with recent reports suggesting that COS is a major source and that its contribution may be closely linked to continental surface fluxes (11, 12).

Past models of COS plant uptake assume a 1:1 relation between relative uptake of COS and net primary productivity (NPP) (13–16). This relation was challenged by plant chamber (8) and atmospheric measurement studies (7), which suggest a new model of uptake that is related to photosynthesis [gross primary productivity (GPP)] and yields four to six times the uptake of the NPP-based models. COS uptake is related to GPP because atmospheric COS and CO₂ diffuse at similar rates into stomata, dissolve at similar rates into intercellular plant water, and are consumed by photosynthesis enzymes (17, 18). COS is taken up preferentially to CO₂ because

¹Department of Civil and Environmental Engineering, University of Iowa, Iowa City, IA 52242, USA. ²Center for Global and Regional Environmental Research, University of Iowa, Iowa City, IA 52242, USA. ³Science and Technology Corporation, Hampton, VA 23666, USA. ⁴Department of Environmental Engineering, Universidad Andrés Bello, Santiago, Chile. ⁵Molina Center for Energy and the Environment, Massachusetts Institute of Technology, Cambridge, MA 02139, USA. ⁶Department of Chemistry, University of California, Irvine, CA 92697, USA. ⁷NASA Langley Research Center, Hampton, VA 23681, USA. ⁸Biospheric Sciences Branch, NASA-Goddard Space Flight Center, Greenbelt, MD 20771, USA. ⁹Department of Atmospheric Science, Colorado State University, Fort Collins, CO 80523, USA. ¹⁰Department of Global Ecology, Carnegie Institution of Washington, Stanford, CA 94305, USA. ¹¹Global Monitoring Division, National Oceanic and Atmospheric Administration (NOAA) Earth System Research Laboratory, Boulder, CO 80305, USA. ¹²Cooperative Institute for Research in Environmental Sciences, University of Colorado, Boulder, CO 80304, USA.

*Present address: College of Engineering, University of California, Merced, CA 95344, USA.

†To whom correspondence should be addressed. E-mail: ecampbell3@ucmerced.edu

photosynthesis enzymes transform one-third of the dissolved CO₂ in leaf water but irreversibly transform most of the dissolved COS (19, 20). The remainder of the dissolved CO₂ diffuses back to the atmosphere. The chamber studies suggest a GPP-based uptake model

$$F = GPP \cdot \frac{[COS]}{[CO_2]} \cdot V_{COS/CO_2} \quad (1)$$

where *F* is COS plant uptake, *GPP* is the photosynthetic uptake of CO₂ by terrestrial plants, [COS]/[CO₂] is the ratio of ambient concentrations, and *V*_{COS/CO₂} is the leaf-scale relative uptake measured during plant chamber experiments.

This GPP-based model was found in recent work to be qualitatively consistent with variations of global atmospheric measurements, suggesting that the total atmospheric lifetime of COS is only 1.5 to 3 years (7, 21). However, it remains to be determined whether atmospheric COS measurements are quantitatively consistent with GPP-based plant uptake.

To provide a quantitative test of the relation between GPP and atmospheric COS, we compared atmospheric COS measurements from an airborne experiment with two simulations from a three-dimensional atmospheric transport model; one simulation was driven by the GPP-based uptake, and the second was driven by the NPP-based uptake. The airborne experiment, the Intercontinental Chemical Transport Experiment–North America (INTEX-NA), included 1741 daytime measurements of COS over continental North America between the surface and 12 km in altitude during July and August 2004. The experiment also included measurements of CO₂ (22) and many other species (23). We compared these INTEX-NA observations to the NOAA Earth System Research Laboratory (NOAA/ESRL) airborne observations made during July and August of 2005, 2006, and 2007 (7). To interpret the INTEX-NA observations, we simulated COS and CO₂ concentrations over North America for the INTEX-NA period (24, 25). The COS simulations were driven by plant uptake, soil sinks, and ocean and anthropogenic sources (direct and indirect). We calculated GPP-based plant uptake (Eq. 1) by scaling regional GPP fluxes (26) by leaf-scale relative uptake estimates. The NPP-based uptake and other surface fluxes were taken from a recent inventory of gridded surface fluxes (14). We simulated CO₂ concentrations using ecosystem, ocean, and anthropogenic surface fluxes. See the supporting online material (SOM) for details on observations and model simulations.

The persistent vertical drawdown (Fig. 1) and variability (Fig. 2) in the boundary layer are well represented by the GPP model, whereas the NPP model performs poorly. Plant uptake was found to be dominant over other sources and sinks in the continental COS budget during the growing season (Fig. 3), a necessary condition for the use of COS as a photosynthesis tracer. These results are discussed below.

The mean modeled and measured CO₂ concentrations along the INTEX-NA flight paths (Fig. 1A) show the expected net uptake of CO₂ and boundary-layer mixing during the growing season (27). The agreement between the observed and modeled drawdown indicates that atmospheric

mixing is well represented in the model. Whereas model underestimation in the 2- to 5-km altitude range may suggest some deficiencies in the simulated mixing, there is only a 10% difference between the observed and modeled estimates of the column-integrated drawdown (21).

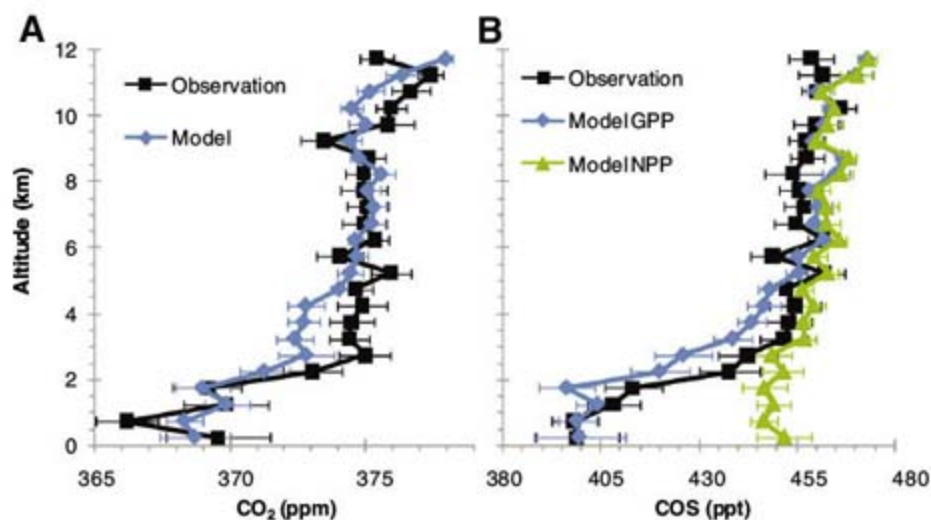
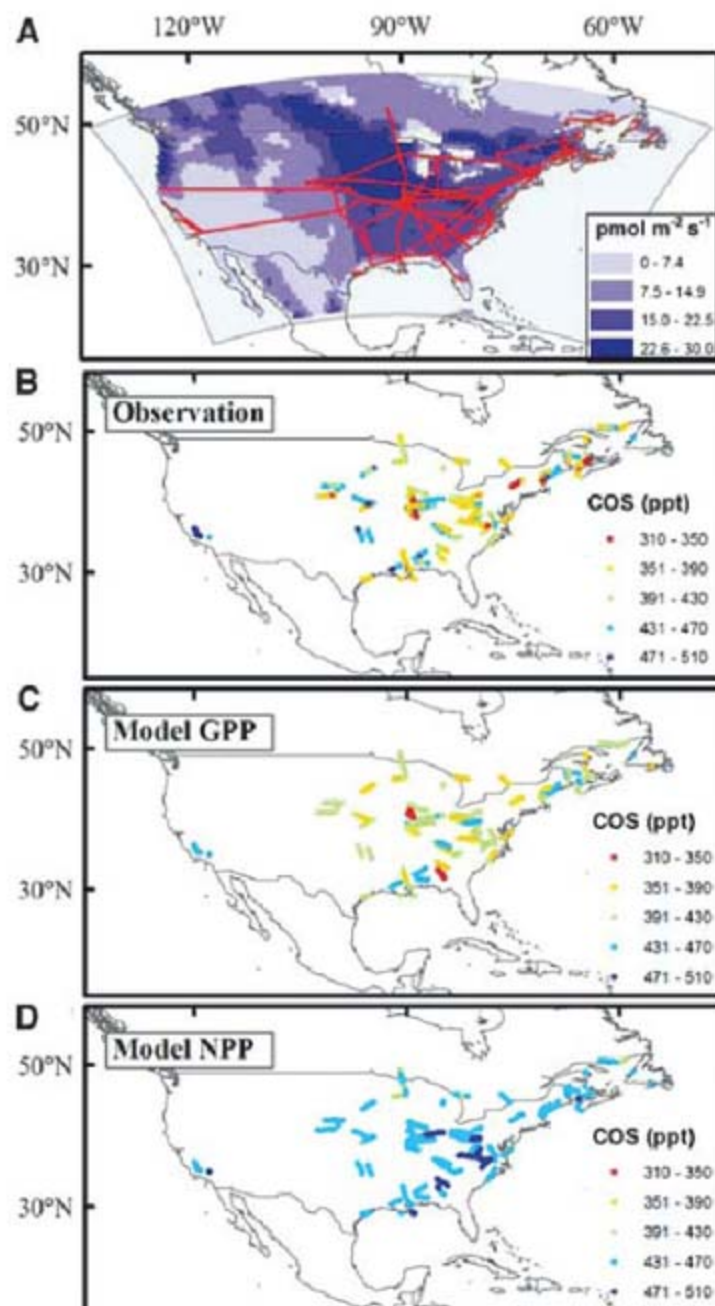


Fig. 1. Vertical profiles of COS and CO₂ along INTEX-NA flight paths. Mean concentrations for all continental INTEX-NA data for CO₂ (A) and COS (B) (error bars indicate ± 95% CI, *n* = 70 average observations in each bin). Model results were interpolated to time and location of each observation. ppm, parts per million.

Fig. 2. COS plant uptake flux and boundary-layer concentrations. (A) COS plant uptake flux (mean July 2004) calculated by scaling modeled GPP by leaf-relative uptake. See SOM for details. Continental INTEX-NA DC8 flight paths (red lines) are shown within the model domain (gray box). (B to D) Modeled and observed atmospheric COS concentrations at all continental sampling points under 2 km in altitude above sea level (ASL).



The mean COS vertical profile (from the 1741 INTEX-NA samples) also shows considerable drawdown in the boundary layer (Fig. 1B). The INTEX-NA concentration drawdown (difference between 6 to 8 km and 0 to 2 km in altitude) of 59.9 ± 8.9 parts per thousand (ppt) [mean \pm 95% confidence interval (CI), $n = 50$ vertical profiles] for sampling in July and August of 2004 is consistent with the NOAA/ESRL drawdown of 55.9 ± 19.0 ppt (mean \pm 95% CI, $n = 12$ airborne sites) for sampling in July and August of 2005 through 2007. The NPP model largely underestimates the observed drawdown as expected (13, 16), whereas the GPP model has good agreement with the observed drawdown. As with CO₂, some deficiencies in the GPP model are apparent in the 2- to 5-km altitude range. However, there is only a 15% difference between

the observed and GPP model estimates of the column-integrated drawdown (21). The column-integrated drawdown for the observed data was 4.2 times the NPP model estimate (21). Sensitivity analysis showed that the drawdown estimates are robust with respect to boundary condition uncertainty (21).

Maps of INTEX-NA boundary-layer COS concentrations show considerable variability in the boundary-layer observations (SD = 39 ppt), and this variability is similar to that in the GPP model (SD = 34 ppt) but much larger than that in the NPP model (SD = 24 ppt) (Fig. 2). The GPP model captures much of the observed variability in the boundary-layer COS concentrations with a correlation coefficient of 0.71 ($n = 440$). This GPP model performance is similar to the a priori performance in CO₂ studies that use a model-

observations analysis to infer surface-flux estimates (28). The variability in the GPP model is largely driven by the magnitude of the plant uptake and caused by the mixing of background air with boundary-layer air that is depleted of COS (21).

The combined evidence from the concentration drawdown, column-integrated drawdown, boundary-layer variation, CO₂ profiles, and NOAA/ESRL data are consistent with the GPP-based model rather than the NPP-based model. Next, we consider the relative influence of the different surface fluxes on the COS airborne samples using transport simulations driven by only one surface flux at a time (Fig. 3A). Anthropogenic COS emissions (direct and indirect) are concentrated in the eastern United States but result in a boundary-layer enhancement that is less than one-third of the vegetative drawdown (21). The COS soil up-

Fig. 3. Tropospheric drawdown for observed and modeled concentrations along continental INTEX-NA flight paths. Tropospheric drawdown of COS (A) and CO₂ (B), for total (left bracket) and modeled components (right bracket) as the difference between mean 6- to 8-km and 0- to 2-km altitude ASL concentrations for all continental INTEX-NA data (error bars indicate \pm 95% CI, $n = 50$ vertical profiles). Anth, anthropogenic; Photo, photosynthesis; Resp, ecosystem respiration; BC, boundary condition. Positive drawdown is removal from the atmosphere, and negative drawdown is a source to the atmosphere. Individual component drawdowns (right bracket) are based on multiple atmospheric transport model simulations using only one flux at a time as input and fixed boundary conditions.

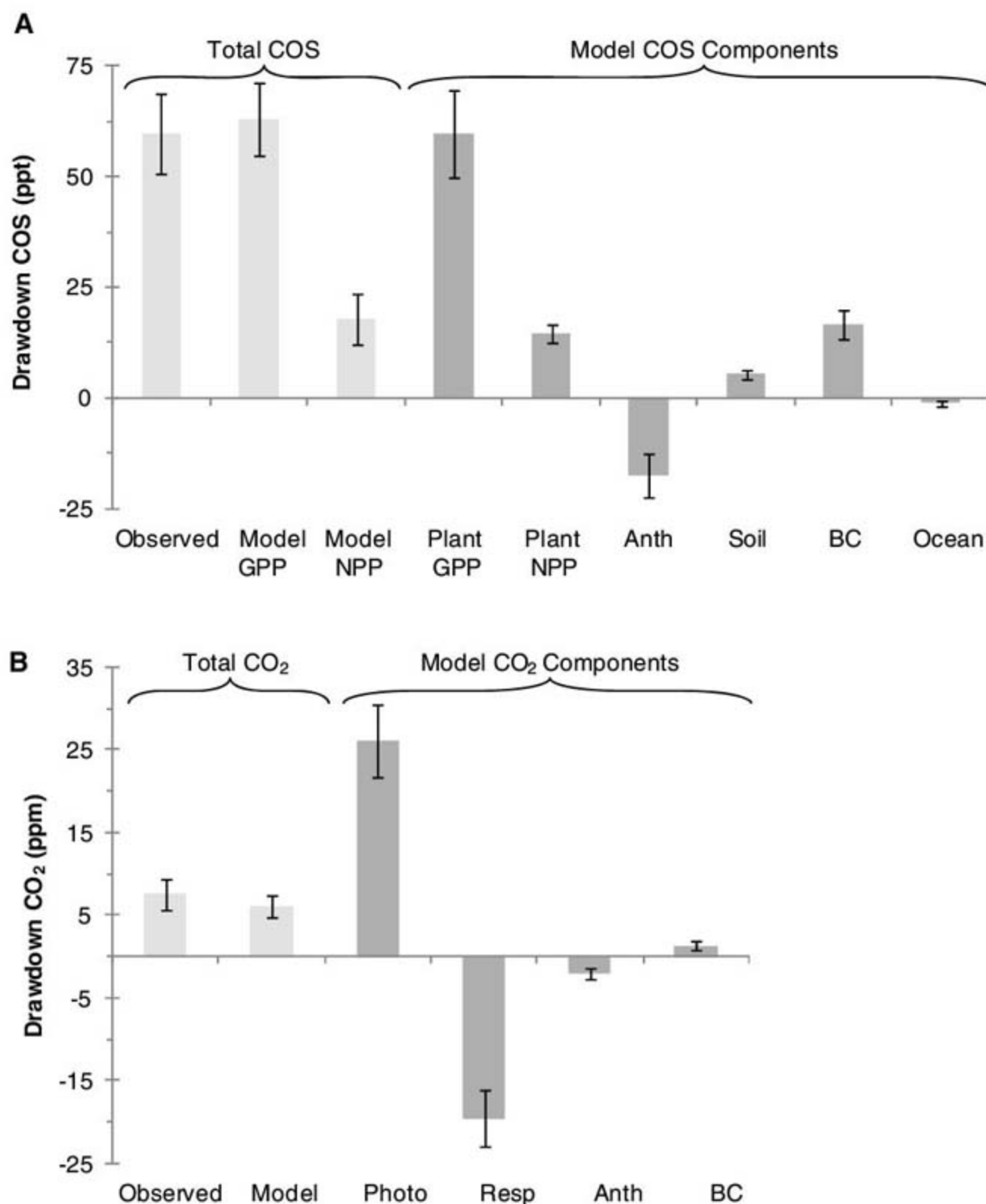
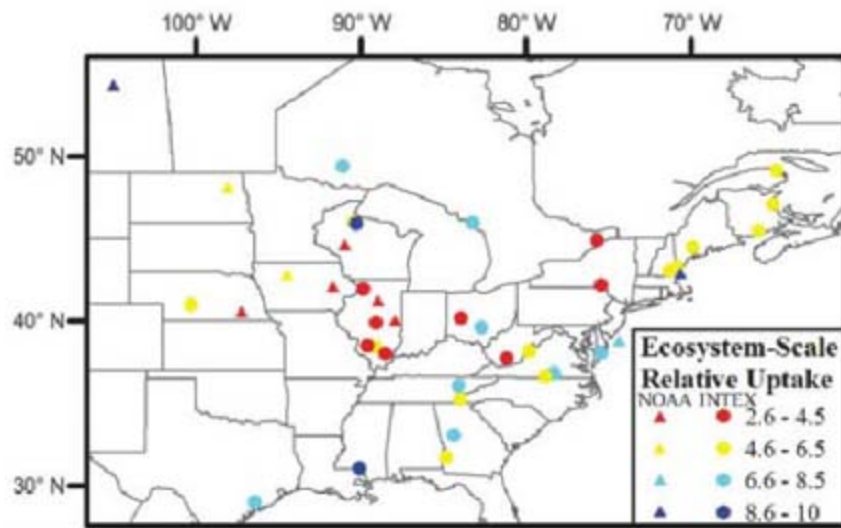


Fig. 4. Observed ERU of COS to CO₂ from INTEX-NA and NOAA/ESRL measurements. ERU is the normalized drawdown of COS relative to the normalized drawdown of CO₂, calculated from the difference between airborne observations in the 0- to 2-km and 6- to 8-km altitude bins. Samples were taken in July and August 2004 for INTEX-NA (circles) and July and August of 2005 through 2007 for NOAA/ESRL (triangles). Repeated vertical profiles at the same location are shown as a single average. (See SOM for details.)



take is <10% of the plant uptake, which is consistent with available field observations (29). Although ocean fluxes are a large source globally (14), they have only a small influence on the vertical profile for the continental growing season. There may be large missing sources in the global COS budget that could be important in relation to plant uptake for some regions (8). However, the good agreement of modeled and observed COS during INTEX-NA suggests that these missing sources are not located in North America during the growing season. Whereas the COS drawdown is dominated by plant uptake, the CO₂ drawdown has offsetting influences of photosynthesis and respiration components that are many times the net CO₂ drawdown (Fig. 3B). These offsetting components make it challenging to apply CO₂ measurements to separately investigate photosynthesis and respiration, reinforcing the need for a tracer such as COS.

This evidence that continental-scale variations of atmospheric COS over North America are driven by the COS/photosynthesis relation suggests the potential use of COS as a carbon-cycle tracer. One tracer application is to estimate the ratio of GPP CO₂ fluxes relative to net ecosystem exchange (NEE) CO₂ fluxes using relations between simultaneous observations of COS and CO₂. For vertical profile observations, a useful relation is the ecosystem-scale relative uptake (ERU), which is the ratio of the relative drawdown of COS to CO₂ (7, 21). When plant uptake is the dominant flux, the ERU is proportional to the ratio of GPP/NEE with a proportionality constant that is the leaf-scale relative uptake. The INTEX-NA and NOAA/ESRL observations have a mean ERU of 5.7 ± 0.6 (mean \pm SD, $n = 31$ vertical profiles, July and August 2004) and 5.7 ± 2.1 (mean \pm SD, $n = 10$ airborne sites, July and August of 2005 through 2007), respectively. For a mean continental leaf-scale relative uptake of 2.2 (21), these ERU values imply a GPP/NEE ratio of 2.6, which is similar to estimates of GPP/NEE of crops during mid-growing season from eddy-flux studies (5, 7, 30). Both INTEX-NA and NOAA/ESRL observations show lower ERU values over

the mid-continent where C4 corn is extensive (Fig. 4). This regional depression in ERU could reflect a decrease in the ratio of GPP/NEE for C4 corn plants that has also been observed in eddy covariance studies of the North American growing season (5). Alternatively, lower leaf-scale relative uptake values have been hypothesized for C4 plants (7, 8) and we suggest that the leaf-scale relative uptake and the ratio of GPP/NEE for C4 plants be explored more widely. Although the ERU could also be influenced by a regional anthropogenic COS source, the anthropogenic source relative to the plant uptake is rather weak in this region (21).

Another tracer application is to estimate the photosynthesis CO₂ flux with the use of an inverse analysis (31) of the COS model concentration error. Inverse analyses must consider multiple sources of model error, including transport parameterizations, different surface fluxes, boundary conditions, and representation error. For the COS inversion, the two flux parameters, other than GPP (Eq. 1), must be well constrained, and the COS fluxes other than plant uptake must be well known or relatively small, as may be the case for the continental growing season. One flux parameter, the concentration ratio parameter (Eq. 1), is well constrained by observations and has an observed variability of <10% in the INTEX-NA boundary-layer samples ($n = 440$). The other flux parameter, leaf-scale relative uptake, may be more uncertain because of the dependence on plant type and growth conditions, but the success of the simple leaf-scale uptake mapping used in this work is promising (21). Knowledge of leaf-scale uptake could be improved with additional plant chamber and ambient studies in support of efforts to recover GPP values.

The results presented here suggest global COS plant uptake and vertical gradients that are more than four times those predicted in previous global models (14–16). This finding implies a large missing source in the global COS budget (7, 8) and large uncertainty in how previous global models have predicted the transfer of COS to the stratosphere. Applications of the GPP

model at a global scale should help to resolve uncertainties in COS budgets and could improve our understanding of the relation between COS surface fluxes and stratospheric aerosol. However, the most intriguing application may be to recover GPP and ecosystem respiration information by inverse analysis of atmospheric COS measurements.

References and Notes

- P. M. Cox, R. A. Betts, C. D. Jones, S. A. Spall, I. J. Totterdell, *Nature* **408**, 184 (2000).
- C. B. Field, D. B. Lobell, H. A. Peters, N. R. Chiariello, *Annu. Rev. Environ. Resour.* **32**, 1 (2007).
- P. Friedlingstein et al., *J. Clim.* **19**, 3337 (2006).
- P. Ciais et al., *Nature* **437**, 529 (2005).
- E. Falge et al., *Agric. For. Meteorol.* **113**, 53 (2002).
- D. R. Bowling, P. P. Tans, R. K. Monson, *Global Change Biol.* **7**, 127 (2001).
- S. A. Montzka et al., *J. Geophys. Res.* **112**, D09302 (2007).
- L. Sandoval-Soto et al., *Biogeosciences* **2**, 125 (2005).
- M. Chin, D. D. Davis, *J. Geophys. Res.* **100**, 8993 (1995).
- P. J. Crutzen, *Geophys. Res. Lett.* **3**, 73 (1976).
- J. Notholt et al., in *SPARC Assessment of Stratospheric Aerosol Properties (ASAP)*, L. Thomason, T. Peter, Eds. (World Meteorological Organization World Climate Research Programme, Toronto, 2006), pp. 29–76.
- J. Notholt et al., *Science* **300**, 307 (2003).
- N. J. Blake et al., *J. Geophys. Res.* **113**, D09590 (2008).
- A. J. Kettle, U. Kuhn, M. von Hobe, J. Kesselmeier, M. O. Andreae, *J. Geophys. Res.* **107**, 4658 (2002).
- A. J. Kettle et al., *Atmos. Chem. Phys.* **2**, 343 (2002).
- E. Kjellström, *J. Atmos. Chem.* **29**, 151 (1998).
- G. Protoschill-Krebs, J. Kesselmeier, *Bot. Acta* **105**, 206 (1992).
- G. Protoschill-Krebs, C. Wilhelm, J. Kesselmeier, *Atmos. Environ.* **30**, 3151 (1996).
- G. D. Farquhar et al., *Nature* **363**, 439 (1993).
- R. J. Francey, P. P. Tans, *Nature* **327**, 495 (1987).
- Materials and methods are available as supporting material on Science Online.
- Y. H. Choi et al., *J. Geophys. Res.* **113**, D07301 (2008).
- H. B. Singh, W. H. Brune, J. H. Crawford, D. J. Jacob, P. B. Russell, *J. Geophys. Res.* **111**, D24501 (2006).
- J. E. Campbell et al., *Tellus B* **59B**, 199 (2007).
- G. R. Carmichael et al., *J. Geophys. Res.* **108**, 8823 (2003).
- S. C. Olsen, J. T. Randerson, *J. Geophys. Res.* **109**, D02301 (2004).
- C. Gerbig et al., *J. Geophys. Res.* **108**, 4757 (2003).
- D. M. Matross et al., *Tellus B Chem. Phys. Meteorol.* **58**, 344 (2006).
- M. Steinbacher, H. G. Bingemer, U. Schmidt, *Atmos. Environ.* **38**, 6043 (2004).
- A. E. Suyker, S. B. Verma, G. G. Burba, T. J. Arkebauer, *Agric. For. Meteorol.* **131**, 180 (2005).
- C. D. Rodgers, *Inverse Methods for Atmospheric Sounding: Theory and Practice* (World Scientific, Singapore, 2000), p. 238.
- We thank J. Kettle for COS flux data and C. Tebaldi, J. Dungan, T. Campbell, and D. Campbell for critical comments on the manuscript. This research was supported by a NASA Earth System Science Graduate Fellowship, Center for Global and Regional Environmental Research, NOAA Office of Oceanic and Atmospheric Research contribution to the North American Carbon Program, NASA INTEX, and NSF Information Technology Research grants. NOAA observations of COS and CO₂ were made possible by the assistance of P. Tans, C. Sweeney, L. Miller, T. Conway, P. Lang, C. Siso, and B. Hall.

Supporting Online Material

www.sciencemag.org/cgi/content/full/322/5904/1085/DC1

Materials and Methods

SOM Text

Figs. S1 to S5

Tables S1 to S3

References

31 July 2008; accepted 17 October 2008

10.1126/science.1164015

A Female *Homo erectus* Pelvis from Gona, Ethiopia

Scott W. Simpson,^{1,2} Jay Quade,³ Naomi E. Levin,^{4,5} Robert Butler,⁶ Guillaume Dupont-Nivet,⁷ Melanie Everett,^{8,9,10} Sileshi Semaw^{9,10*}

Analyses of the KNM-WT 15000 *Homo erectus* juvenile male partial skeleton from Kenya concluded that this species had a tall thin body shape due to specialized locomotor and climatic adaptations. Moreover, it was concluded that *H. erectus* pelvis were obstetrically restricted to birthing a small-brained altricial neonate. Here we describe a nearly complete early Pleistocene adult female *H. erectus* pelvis from the Busidima Formation of Gona, Afar, Ethiopia. This obstetrically capacious pelvis demonstrates that pelvic shape in *H. erectus* was evolving in response to increasing fetal brain size. This pelvis indicates that neither adaptations to tropical environments nor endurance running were primary selective factors in determining pelvis morphology in *H. erectus* during the early Pleistocene.

The modern human pelvis is uniquely modified to accommodate both bipedal locomotion and the birthing of large-brained offspring (1, 2). The earliest known fossil hominid adult pelvis are from small-bodied females (such as the 3.2-million-year-old *Australopithecus afarensis* specimen A.L. 288-1an/ao and the ~2.5- to 2.8-million-year-old *Au. africanus* specimen Sts14) that show anatomical adaptations to bipedal locomotion yet lack obstetric specializations. By the early Pleistocene, *Homo erectus* exhibited an absolute and relative increase in brain size, suggesting that the parturition of a large-brained fetus may have imposed novel selection on its pelvis. Few early *Homo* fossil pelvis fragments exist (3), and it is the 1.53-million-year-old juvenile male skeleton (KNM-WT 15000) from Kenya that has been central in assessing *H. erectus* pelvic morphology and body shape (4). The transversely narrow pelvis and torso reconstructed for this individual were suggested to be adaptations that enhanced locomotor effectiveness and thermoregulatory homeostasis in more open, semi-arid tropical environments (4, 5). Estimates of female birth canal dimensions based on this fossil have been interpreted to suggest that *H. erectus* lacked derived obstetric modifications in the pelvis and that its small birth canal limited neonatal brain size (3, 6) to a maximum of ~230 ml. This, in turn, was argued to have resulted in the birth of de-

velopmentally immature offspring that experienced rapid postnatal brain growth requiring a modern human-like degree of maternal investment and child-rearing behaviors (6).

Here we describe a nearly complete early Pleistocene adult female *H. erectus* pelvis and last lumbar vertebra (BSN49/P27a-d) from the upper Busidima Formation (7, 8), dated 1.8 to <0.16 million years ago (Ma), in the Gona Paleanthropological Research Project study area in the Afar Regional State, Ethiopia (Fig. 1). The BSN49 site is stratigraphically located between the Silbo Tuff (0.751 ± 0.022 Ma) and the base of the C1r polarity chron (1.778 Ma) (fig. S1). Con-

sideration of the range of observed sediment accumulation rates in the Busidima Formation narrows the likely age of the fossil to 0.9 to 1.4 Ma (8). To date, *H. erectus* is the only hominid known from the early Pleistocene deposits in the Afar Depression. Early Acheulean artifacts are common at the BSN49 stratigraphic level. Analyses of carbon and oxygen stable isotopes from pedogenic carbonates and herbivore enamel from the BSN49 level indicate a semi-arid environment with a landscape dominated by C4 grasses and grazing herbivores (8).

The pelvis (Fig. 2) includes the sacrum and both os coxae with the first complete pubis from the early Pleistocene. Most of its distortion was produced by in situ fracture and carbonate cementation of the displaced fragments. The complete pelvis was reconstructed from high-resolution plaster casts. Despite minor residual asymmetry, the major functionally relevant dimensions and articular surfaces required little or no reconstruction and can be considered reliable for anatomical interpretation and mensuration (8).

The adult BSN49/P27 pelvis is transversely broad with laterally flaring ilia and anteriorly positioned acetabulocristal buttresses, long pubic rami, and a wide sciatic notch, which are all plesiomorphic characters shared with the australopithecines, other early (3) and middle (9, 10) Pleistocene *Homo*, and Neandertals (11). The fossils attributable to *H. erectus* or early *Homo* [including KNM-WT 15000, KNM-ER 1808,

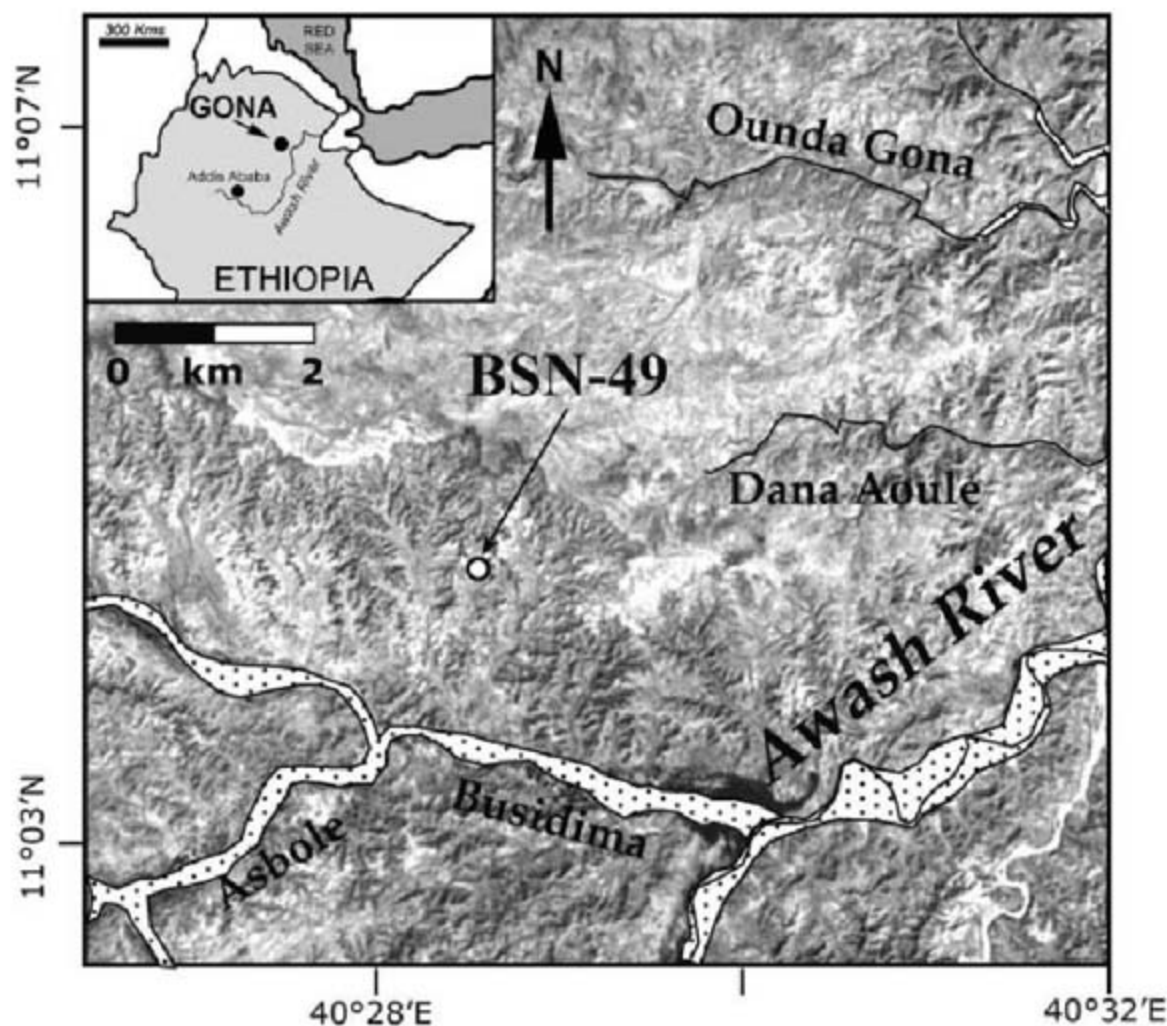


Fig. 1. Location of site BSN49. See (8) for additional information on site stratigraphy and tuff geochemistry.

¹Department of Anatomy, Case Western Reserve University School of Medicine, Cleveland, OH 44106-4930, USA.

²Laboratory of Physical Anthropology, Cleveland Museum of Natural History, Cleveland, OH 44106, USA. ³Department of Geosciences/Desert Laboratory, University of Arizona, Tucson, AZ 85721, USA. ⁴Department of Geology and Geophysics, University of Utah, Salt Lake City, UT 84112, USA. ⁵Division of Geological and Planetary Sciences, California Institute of Technology, MC 100-23, Pasadena, CA 91125, USA. ⁶Department of Physics, University of Portland, Portland, OR 97203-5798, USA. ⁷Faculty of Geosciences, Utrecht University, Budapestlaan 17, 3584 CD Utrecht, Netherlands. ⁸Department of Geological Sciences, Indiana University, Bloomington, IN 47407, USA. ⁹The Stone Age Institute, 1392 West Dittmore Road, Gosport, IN 47433, USA. ¹⁰Center for Research into the Anthropological Foundations of Technology (CRAFT), Indiana University, Bloomington, IN 47405, USA.

*To whom correspondence should be addressed. E-mail: ssemaw@indiana.edu

KNM-ER 3228, OH28, and UA-173/404+UA-466 (3, 12)] span the early Pleistocene in Africa and exhibit laterally flaring ilia, wide (in terms of modern males) greater sciatic notches, tall thin pubic symphyseal faces, small auricular surfaces, and anteriorly placed iliac pillars. Except for overall size, the BSN49/P27 specimen is anatomically similar to these pelvis fossils (8). The BSN49/P27 pelvis shares with *Homo* such diagnostic characters (8) as an anteroposteriorly broadened birth canal, a thickened acetabulocrystal buttress (iliac pillar), a sigmoid-shaped anterior inferior iliac spine, a shelf formed by attachment of the reflected head of the rectus femoris muscle, deepened fossa for the gluteus medius muscle, an increased height of the posterior ilium with an expanded retroauricular area, and angular elevation and anterior projection of the superior pubic rami (13). As in other *Homo* sacra, the BSN49/P27 alae are anteroposteriorly broad with marked periauricular excavation and a robust and projecting sacral tuberosity indicating a well-developed interosseous sacroiliac ligament complex: features that readily distinguish *Homo* from the australopithecines (8).

The BSN49/P27 acetabulae are small, with an estimated femoral head diameter of 33.4 to 36.8 mm (8)—substantially smaller than the femoral head of other early Pleistocene specimens [such as KNM-WT 15000: 44.9 mm (14)]. Regressions estimating femur length and stature based on the major load-bearing articular surfaces of the pelvis (8) predict a stature for the BSN49/P27 individual of 1.20 to 1.46 m, markedly shorter than the 1.85 m adult stature estimated for the male KNM-WT 15000 individual (4). Although *H. erectus* is widely characterized as apomorphically exhibiting an increase in stature and reduction in stature dimorphism, the data supporting this idea are surprisingly meager. With the recent discovery of *H. erectus* crania and postcrania from smaller individuals [such as KNM-OL 45500 (15), KNM-ER 42700 (16), and Dmanisi (17, 18)], it is apparent that body size range in *H. erectus* has been underestimated, and a size “Rubicon” should not be part of the species diagnosis (16). The presence of very wide greater sciatic notches (8) and subpubic angle (table S5), everted ischia, rectangular pubic bodies with a ventral arc, a subpubic concavity, a large sacral angle (19), a nonprojecting sacral promontory, a symmetrically oval pelvic inlet, and a preauricular sulcus are all traits diagnostic of a female pelvis. Thus, the BSN49/P27 pelvis is from a short-statured *H. erectus* adult female.

The BSN49/P27 pelvis is obstetrically capacious for such a short-statured individual. The fossil’s inlet circumference is within modern female ranges (8). The obstetrically important bispinous (pelvic midplane) and bitubercular (pelvic outlet) transverse breadths of BSN49/P27 are greater than in most modern females (Fig. 3) (8). Size-normalized comparisons and multivariate analyses of the pelvic inlet and midplane demonstrate the obstetrically derived shape of the BSN49/P27 birth canal (Fig. 3, C and D) (8).

Humans are unusual among the hominoids in having a near identity in size between the neonatal head and the birth canal dimensions that places both mother and neonate at substantial risk of a traumatic birth. When these anatomical relationships in humans were used to estimate neonatal head size in *H. erectus*, it was seen that the BSN49/P27 pelvis was capable of birthing an offspring with estimated maximal brain volume of up to 315 ml (8)—over 30% greater than previously predicted from the KNM-WT 15000 pelvis (6), although this value is similar to growth-based estimates (20). Neonatal brain size was approximately 30 to 50% (the mean ratio is 34 to 36%) of early Pleistocene *H. erectus* adult brain size [~600 to 1067 ml (mean = 880 ml, $n = 18$ crania)] (21), an intermediate value between that of chimpanzees (~40%) and modern humans (~28%) (20). This new estimate of *H. erectus*

neonatal brain size, in tandem with the revised age at death (~0.5 to 1.5 years) of the child’s cranium from Peming (Mojokerto), Indonesia (<1.81 Ma) (22), suggests that *H. erectus* had a prenatal brain growth rate similar to that of humans but a postnatal brain and somatic growth rate intermediate between that of chimpanzees and humans (23).

The enlarged neonatal brain in *H. erectus* required a concomitant increase in the dimensions of their bony birth canal. Two nonexclusive means of enlarging birth canal size beyond the primitive *Australopithecus* condition (1) are an increase in female body size [larger females can have isometrically larger pelvises (24)] or developmentally mediated changes in pelvic shape resulting in pelvic sexual dimorphism. Given this individual’s short stature with a capacious birth canal and characteristically female pelvic shape,

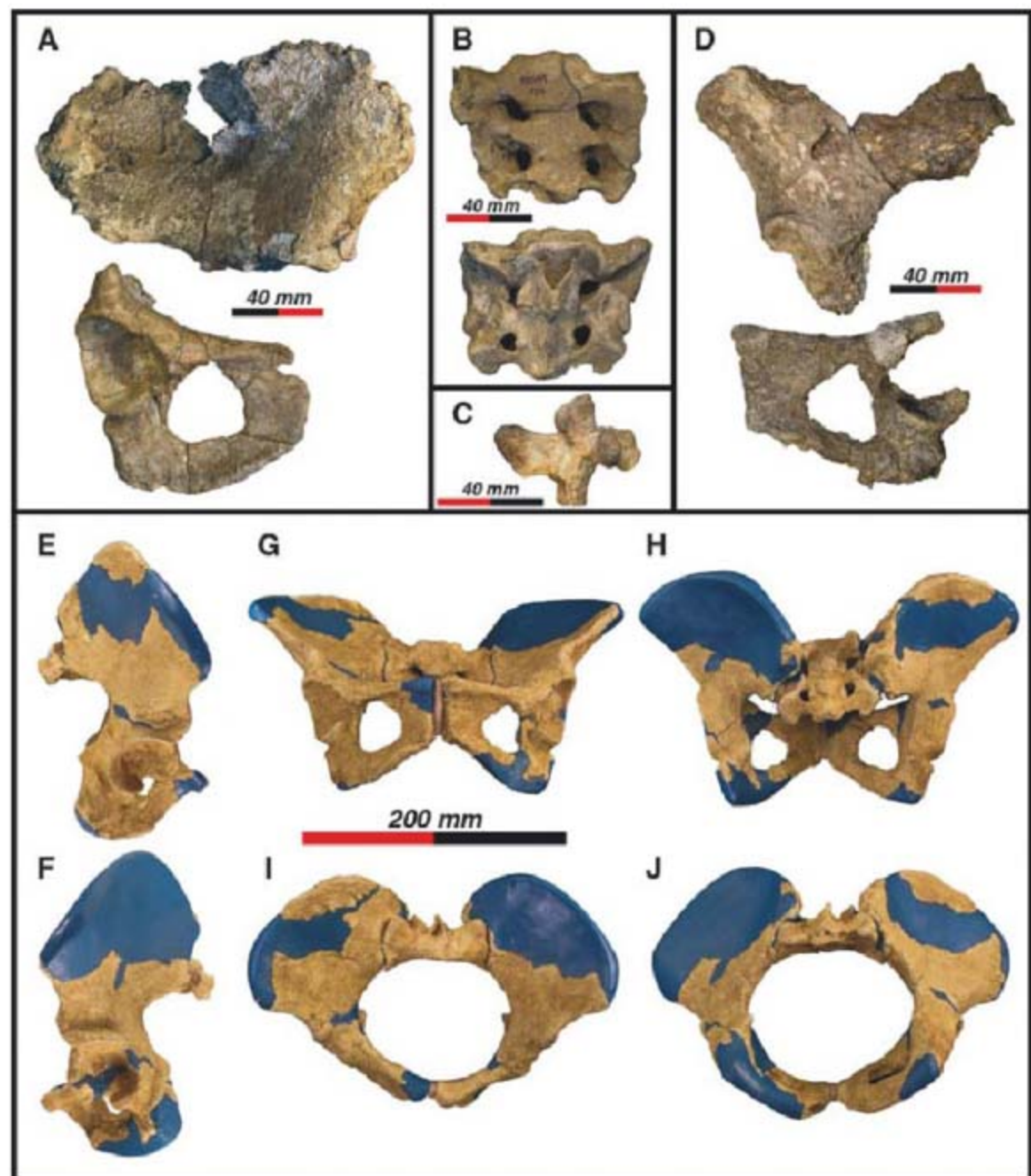


Fig. 2. Illustrations of major elements of the BSN49/P27 pelvis and lumbar vertebra and reconstruction of the pelvis. (A) Right os coxa with posterolateral view of the ilium and anterolateral view of an ischiopubic fragment. (B) Anterior and posterior views of the sacrum. (C) Right lateral view of the lumbar vertebra. (D) Posterolateral view of the left ilium and anterolateral view of the left ischiopubic fragment. (E) Right lateral view. (F) Left lateral view. (G) Anterior view. (H) Posterior view. (I) Pelvic inlet. (J) Pelvic outlet. The blue portions of the cast indicate areas that have been reconstructed or restored. Scale bar for (A) to (D), 40 mm; scale bar for (E) to (J), 200 mm.

it is clear that the latter applies. This resulted in a recognizably dimorphic pelvis by the early Pleistocene, with females demonstrating the distinctive obstetric anatomy required to deliver a large-brained offspring. This derived anatomy indicates that the fetal cephalic-maternal pelvic disproportion, which directly affects reproductive success, was a significant selective factor on female pelvic morphology at that time.

This individual's absolutely wide bi-iliac breadth (288 mm) is greater than the mean width of modern females and males from eight diverse populations (8, 19, 25, 26), indicating that the BSN49/P27 individual had a very broad trunk. Its bi-iliac breadth is exceeded in the fossil record only by the very large middle and late Pleistocene pelvises from Atapuerca, Spain (9), Jinniushan, China (10), and Kebara, Israel (11), which are specimens that retain the primitive condition of laterally flaring ilia. The only ancient pelvis that does not exhibit marked lateral flare is the reconstructed KNM-WT 15000 pelvis, a reconstruction that has been questioned (3, 9).

Many anatomical changes in the human pelvis have occurred since the middle Pleisto-

cene, including a narrowing of the interacetabular distance; an increase in the anteroposterior breadth of the birth canal, with shorter, elevated pubic rami; and a decrease in the degree of iliac flaring, leading to a reduction of the bi-iliac breadth (13). Some authors have suggested that these anatomical adaptations had their roots in the early Pleistocene as a locomotor adaptation by *H. erectus* to endurance running (5). The BSN49/P27 pelvis does not exhibit any of these anatomical modifications or others proposed to be adaptive responses to this behavior, such as tall stature, enlarged acetabulae, or a narrow torso. Clearly, improving locomotor effectiveness, as exhibited by a relative and absolute increase in lower limb length, was a component of the early *Homo* adaptive complex. However, the earliest fossil evidence of the modern human pelvis is documented about 100,000 years ago from Skhul, Israel, indicating both the recency of this morphology and the historical stability of the plesiomorphic transversely broad pelvis.

Modern humans display a relation between body shape and ambient temperature and humidity, with individuals living in more temperate and

Arctic climates having absolutely and relatively broader torsos, and peoples in tropical arid/semi-arid areas possessing narrower trunks (27). The BSN49/P27 pelvis represents a short-statured, broad-hipped individual who would have had an extreme bi-iliac breadth/stature ratio characteristic of more temperate-adapted modern humans and not the tall narrow body form previously identified in *H. erectus* as an adaptation to tropical semi-arid environments (4, 8). Thus, although early *Homo* lived in a diversity of environments, because of their unique pelvic shape they did not exhibit the same ecogeographic patterns of body form as seen in modern humans (10).

The first *H. erectus* fossils were found over 100 years ago. Additional *H. erectus* remains have since been recovered from numerous sites spanning over a million years, thousands of miles, and a wide diversity of ecological zones. These fossils have documented a substantial increase in endocranial capacity in *H. erectus* over their Pliocene ancestors. Despite this rich history, few complete fossil postcrania (18) have been recovered, and basic features of *H. erectus* body shape remain poorly understood. The transversely broad torso, clearly evident in this short individual, requires reappraisal of some current models of locomotor and ecogeographic adaptations in African early Pleistocene *H. erectus*. It is now clear that the *H. erectus* pelvis retained many elements of its australopithecine heritage, although substantially modified by the demands of birthing large-brained offspring.

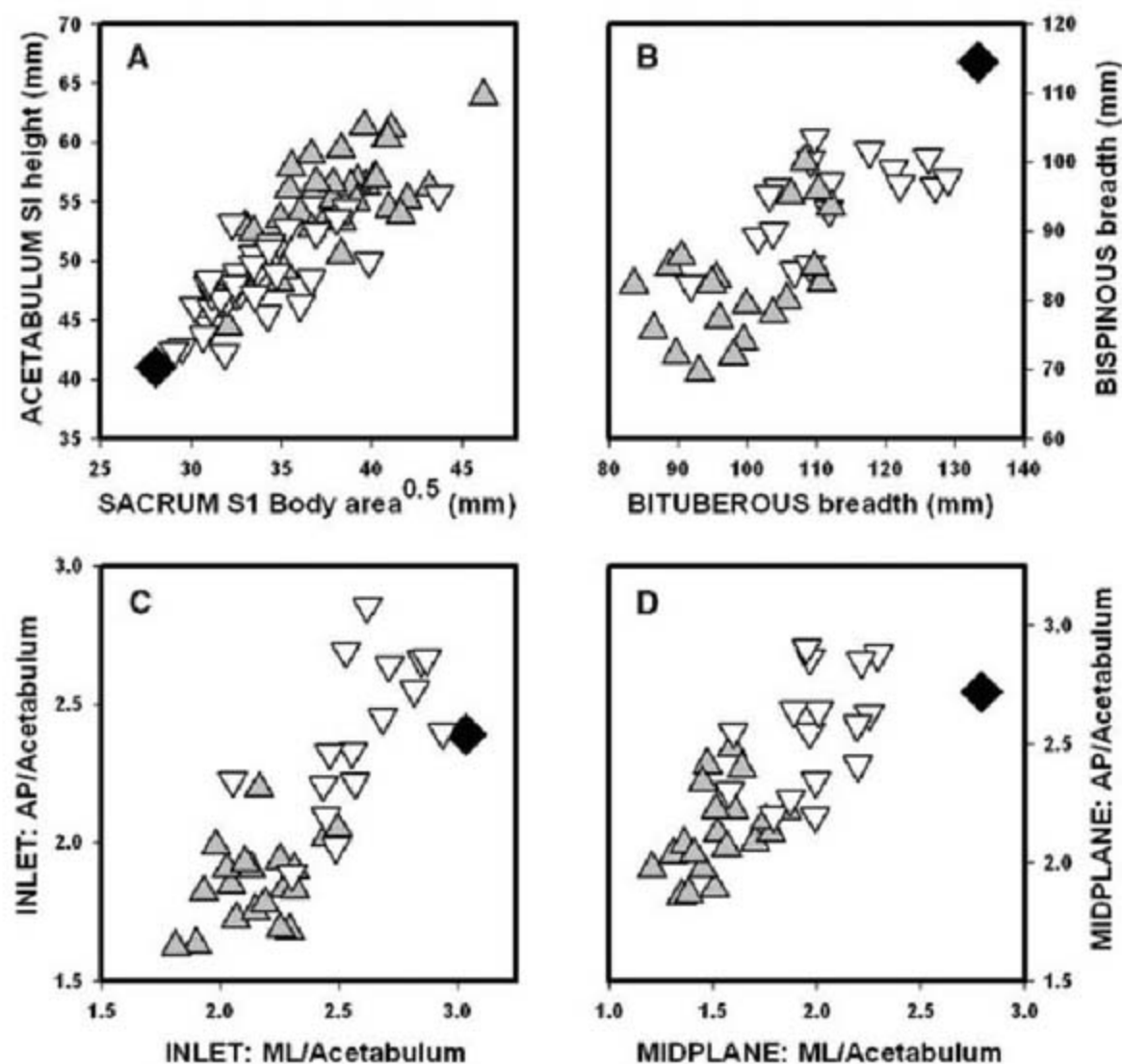


Fig. 3. Comparative pelvimetrics. (A) Plot of acetabulum superoinferior diameter with the square root of the sacral S1 body area (8). (B) Plot of bituberous breadth (pelvic outlet breadth) and bispinous breadth (pelvic midplane breadth). (C) Anteroposterior (AP) and mediolateral (ML) birth canal inlet dimensions normalized by acetabulum superoinferior diameter. (D) Anteroposterior and transverse birth canal midplane dimensions normalized by acetabulum superoinferior diameter. Human data are from The Hamann-Todd collection, Cleveland Museum of Natural History, Cleveland, Ohio. Open inverted triangles, females; gray triangles, males; black diamond, BSN49/P27.

References and Notes

1. C. O. Lovejoy, K. G. Heiple, A. H. Burstein, *Am. J. Phys. Anthropol.* **38**, 757 (1973).
2. R. G. Tague, C. O. Lovejoy, *J. Hum. Evol.* **35**, 75 (1998).
3. C. B. Ruff, *Am. J. Phys. Anthropol.* **98**, 527 (1995).
4. C. B. Ruff, A. Walker, in *The Nariokotome Homo erectus Skeleton*, A. Walker, R. Leakey, Eds. (Harvard Univ. Press, Cambridge, MA, 1993), pp. 234–265.
5. D. M. Bramble, D. E. Lieberman, *Nature* **432**, 345 (2004).
6. A. Walker, C. B. Ruff, in *The Nariokotome Homo erectus Skeleton*, A. Walker, R. Leakey, Eds. (Harvard Univ. Press, Cambridge, MA, 1993), pp. 221–233.
7. J. Quade et al., *Geol. Soc. Am. Bull.* **116**, 1529 (2004).
8. Materials and methods are available as supporting material on Science Online.
9. J.-L. Arsuaga et al., *Nature* **399**, 255 (1999).
10. K. Rosenberg, Z. Lü, C. B. Ruff, *Proc. Natl. Acad. Sci. U.S.A.* **103**, 3552 (2006).
11. Y. Rak, B. Arensburg, *Am. J. Phys. Anthropol.* **73**, 227 (1987).
12. L. Bondioli et al., *J. Hum. Evol.* **50**, 479 (2006).
13. C. O. Lovejoy, *Gait Posture* **21**, 95 (2005).
14. C. Ruff, *Am. J. Phys. Anthropol.* **133**, 698 (2007).
15. R. Potts et al., *Science* **305**, 75 (2004).
16. F. Spoor et al., *Nature* **448**, 688 (2007).
17. G. P. Rightmire, D. Lordkipanidze, A. Vekua, *J. Hum. Evol.* **50**, 115 (2006).
18. D. Lordkipanidze et al., *Nature* **449**, 305 (2007).
19. R. G. Tague, *Am. J. Phys. Anthropol.* **80**, 59 (1989).
20. J. DeSilva, J. Lesnik, *J. Hum. Evol.* **51**, 207 (2006).
21. R. L. Holloway, D. C. Broadfield, M. S. Yuan, *The Human Fossil Record: Brain Endocasts* (Wiley-Liss, Hoboken, NJ, 2004).
22. H. Coquegniot, J.-J. Hublin, F. Veillon, F. Houët, T. Jacob, *Nature* **431**, 299 (2004).
23. C. Dean et al., *Nature* **414**, 628 (2001).
24. R. G. Tague, *Am. J. Phys. Anthropol.* **127**, 392 (2005).

25. H. Correia, S. Balseiro, M. De Areia, *J. Comp. Hum. Biol.* **56**, 153 (2005).
26. D. Walrath, thesis, University of Pennsylvania, Philadelphia (1997).
27. C. B. Ruff, *Yearb. Phys. Anthropol.* **37**, 65 (1994).
28. The Gona Project thanks the Authority for Research and Conservation of Cultural Heritage of the Ministry of Culture and Tourism, and the National Museum of Ethiopia, for research permits and support. Support for this research was provided by the L. S. B. Leakey Foundation, National Geographic Society, Wenner-Gren Foundation, and NSF.

We are grateful for the overall support of K. Shick and N. Toth (co-directors of CRAFT). We appreciate the hospitality of the Afar administration at Semera and our Afar colleagues from Eloha. We thank Y. Haile-Selassie and L. Jellema (Cleveland Museum of Natural History) for allowing us to examine materials in their care. Discussions with and comments by C. O. Lovejoy, R. G. Tague, Y. Haile-Selassie, G. Suwa, T. White, G. WoldeGabriel, B. Latimer, B. Asfaw, S. Standen, R. Byrne, and anonymous reviewers were helpful. A. Admasu's help at the National Museum of Ethiopia is appreciated.

Supporting Online Material

www.sciencemag.org/cgi/content/full/322/5904/1089/DC1
Materials and Methods
SOM Text
Figs. S1 to S11
Tables S1 to S10
References

22 July 2008; accepted 14 October 2008
10.1126/science.1163592

Slide into Action: Dynamic Shuttling of HIV Reverse Transcriptase on Nucleic Acid Substrates

Shixin Liu,¹ Elio A. Abbondanzieri,¹ Jason W. Rausch,⁴ Stuart F. J. Le Grice,⁴ Xiaowei Zhuang^{1,2,3*}

The reverse transcriptase (RT) of human immunodeficiency virus (HIV) catalyzes a series of reactions to convert single-stranded viral RNA into double-stranded DNA for host cell integration. This process requires a variety of enzymatic activities, including DNA polymerization, RNA cleavage, strand transfer, and strand displacement synthesis. We used single-molecule fluorescence resonance energy transfer to probe the interactions between RT and nucleic acid substrates in real time. RT was observed to slide on nucleic acid duplexes, rapidly shuttling between opposite termini of the duplex. Upon reaching the DNA 3' terminus, RT can spontaneously flip into a polymerization orientation. Sliding kinetics were regulated by cognate nucleotides and anti-HIV drugs, which stabilized and destabilized the polymerization mode, respectively. These long-range translocation activities facilitate multiple stages of the reverse transcription pathway, including normal DNA polymerization and strand displacement synthesis.

Retroviral reverse transcriptase (RT) is a multifunctional enzyme that catalyzes conversion of the single-stranded viral RNA genome into integration-competent double-stranded DNA. RT possesses several distinct activities, including DNA- and RNA-dependent DNA synthesis, DNA-directed RNA cleavage, strand transfer, and strand displacement synthesis, all of which are required to complete the reverse transcription cycle (fig. S1) (1, 2). The enzyme first uses viral RNA as the template to synthesize minus-strand DNA (3, 4), and the resulting DNA/RNA hybrid is then cleaved by the ribonuclease H (RNase H) activity of RT to produce short RNA fragments hybridized to nascent DNA (5, 6). Specific RNA fragments, known as the polypurine tracts (PPTs), serve as primers for synthesis of plus-strand DNA from the minus-strand DNA template (7–9). Secondary structures present in the viral RNA genome, as well as the nontemplate strands hybridized to the DNA template, require RT to perform strand displacement synthesis during both minus- and plus-strand DNA synthesis (10–16).

As a major target for anti-HIV therapy, RT has been the subject of extensive research. Crystal structures, biochemical assays, and single-molecule analyses have suggested different modes of interaction between RT and nucleic acid substrates, providing snapshots of the nucleoprotein complexes that illuminate the functional mechanism of RT [e.g., (17–25)]. Nevertheless, how the enzyme-substrate complex acquires specific functional configurations and switches between different functional modes remains unclear. For example, how does RT efficiently locate the 3' terminus of nascent DNA on a long duplex substrate to initiate DNA polymerization? This question is particularly important for a low-processivity polymerase such as RT, which must frequently locate the polymerization site after dissociation (10, 26). Perhaps even more puzzling is how the dissociated RT locates the polymerization site during strand displacement synthesis, considering that the primer terminus may itself be displaced from the template by the competing nontemplate strand. Also, RT cleaves at many different sites within a DNA/RNA hybrid, but how it accesses these sites remains incompletely understood (21, 22). A dynamic visualization of RT interacting with different substrates will help us address these questions and gain a more complete understanding of its function.

In this work, we used fluorescence resonance energy transfer (FRET) (27, 28) to monitor in real time the action of individual HIV-1 RT molecules

and their interactions with various nucleic acid substrates. We specifically labeled RT with the FRET donor dye Cy3 at either the RNase H domain (H-labeled) or the fingers domain (F-labeled) of its catalytically active p66 subunit (fig. S2A) (2, 29, 30). A Glu⁴⁷⁸→Gln⁴⁷⁸ (E478Q) mutation was introduced to eliminate RNase H activity (31) and prevent degradation of the nucleic acid substrates during experiments. Nucleic acid substrates were labeled with the FRET acceptor dye Cy5 at various sites, specifically immobilized on a quartz surface, and immersed in a solution containing Cy3-labeled RT (fig. S2B) (2). Fluorescence from individual RT-substrate complexes was monitored with a total-internal-reflection fluorescence (TIRF) microscope by using an alternating laser excitation scheme (32). The observed FRET value allowed the binding configuration of the enzyme to be determined (fig. S2C) (2). Control experiments showed that neither dye labeling nor surface immobilization notably affected the enzyme activity (fig. S3) and that photophysical properties of the FRET dyes did not change appreciably when placed in proximity to the enzyme (fig. S4) (2).

To mimic substrates encountered by RT during minus-strand synthesis, we constructed a series of hybrid structures of various lengths, each consisting of a DNA primer and an RNA template with Cy5 attached to one of two sites: (i) near the 3' end of the RNA template, which we define as the back end of the hybrid ("back-labeled," Fig. 1, A to C), or (ii) near the 5' end of the RNA template and 3' end of the DNA primer, which we define as the front end ("front-labeled," fig. S5, B and C) (2). On a 19-base pair (bp) hybrid, a length chosen to approximate its footprint on nucleic acid duplexes (17, 33), RT bound in only one configuration: Binding of H-labeled RT to the back-labeled substrate yielded uniformly high FRET values (centered at 0.95) (Fig. 1A), indicating that RT bound with its RNase H domain close to the back end of the hybrid. Considering that the RNase H and polymerase active sites are at opposite ends of the substrate binding cleft of RT, this configuration places the polymerase active site of the RT over the 3' terminus of the DNA primer, consistent with the polymerization-competent binding mode observed in crystal structures (17, 18).

In contrast, two distinct binding modes were observed on longer DNA/RNA hybrids. H-labeled RT bound to back-labeled 38-bp hybrid yielded two FRET peaks centered at 0.95 and 0.39, re-

¹Department of Chemistry and Chemical Biology, Harvard University, Cambridge, MA 02138, USA. ²Department of Physics, Harvard University, Cambridge, MA 02138, USA. ³Howard Hughes Medical Institute, Harvard University, Cambridge, MA 02138, USA. ⁴HIV Drug Resistance Program, National Cancer Institute, Frederick, MD 21702, USA.

*To whom correspondence should be addressed. E-mail: zhuang@chemistry.harvard.edu

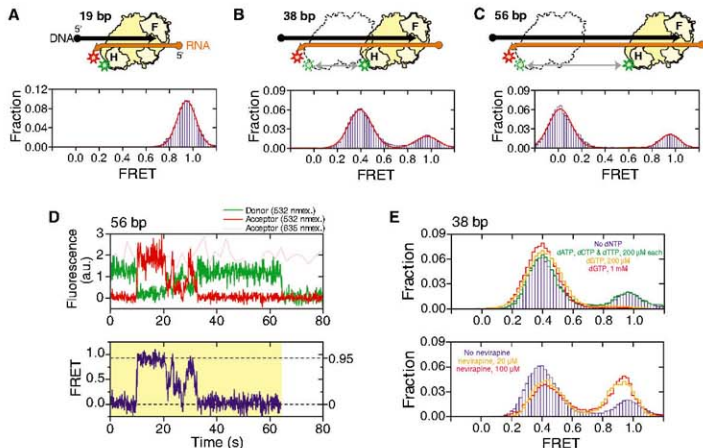
spectively (Fig. 1B). The FRET value of 0.39 is quantitatively consistent with RT binding in polymerization competent mode, in which the polymerase active site is located over the primer terminus at the front end of the hybrid, placing the Cy3 dye ~ 19 bp away from the Cy5 label. The high-FRET peak at 0.95 indicates an additional binding mode in which the RNase H domain is located near the back end of the hybrid, which apparently cannot support polymerase activity. The equilibrium constant between the front- and back-end binding states was 3.3:1. Moving the biotin from the 5' end of the DNA primer (i.e.,

near the back end of the hybrid) to the 5' end of the RNA template (i.e., near the front end) resulted in a nearly identical equilibrium constant (3.1:1), again suggesting a minimal effect of surface immobilization. These two binding modes at the front and back end of the hybrid were further confirmed by two additional FRET labeling schemes in which F-labeled or H-labeled RT was added to the front-labeled substrate (Fig. S5) (2). The two end-binding states also predict further separation of the two FRET peaks as the length of the hybridized region increases, which was experimentally confirmed with a 56-bp

hybrid. Binding of H-labeled RT to the back-labeled 56-bp hybrid produced two FRET peaks centered at 0 and 0.95, also with a ~ 3 :1 partition ratio (Fig. 1C).

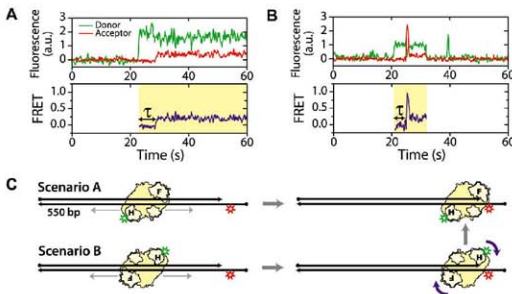
Taken together, these results indicate that the enzyme can stably bind either to the front end of the hybrid poised for DNA extension or to the back end, placing the RNase H domain close to the 3' end of the RNA template. The front-end binding state of RT should also support RNase H activity. The two binding modes were independent of hybrid sequence and the nature of the hybrid termini, that is, whether they feature recessed

Fig. 1. RT slides on nucleic acid substrates. (A to C) H-labeled RT (yellow) bound to a 19-bp (A), 38-bp (B), and 56-bp (C) back-labeled DNA (black)/RNA (orange) hybrid. F and H on the enzyme represent the fingers and RNase H domains, respectively. Circle and arrow on the nucleic acid strands represent 5' and 3' ends, respectively. Green and red stars indicate Cy3 and Cy5 dyes, respectively. The FRET histograms (blue) were fit with a single (A) or double (B) and (C) Gaussian peaks (red line). (D) Representative fluorescence (top) and FRET (bottom) time traces of RT bound to a 56-bp DNA/RNA hybrid at 12°C, showing gradual transitions between the 0 and 0.95 FRET states and the preferred intermediates near FRET ~ 0.3 to 0.5. The time resolution is 10 Hz. The green and red traces represent donor and acceptor fluorescence under 532-nm excitation, and the pink trace represents acceptor fluorescence under 635-nm excitation. The yellow shade marks a single RT binding event. a.u., arbitrary units. (E) Effects of nucleotides and nevirapine



on sliding. (Top) FRET histograms of RT bound to the 38-bp DNA/RNA hybrid in the absence of nucleotides (blue), in the presence of the cognate dGTP (orange and red), or noncognate nucleotides (green). The DNA primer was chain-terminated to prevent elongation. (Bottom) FRET histograms in the absence (blue) and presence of nevirapine (orange and red).

Fig. 2. Sliding of RT facilitates polymerization site targeting. H-labeled RT was added to a ~ 550 -bp DNA duplex with Cy5 attached near the front end. Binding of RT to the polymerization site at the duplex front end is expected to give a FRET value of 0.3. (A) Donor and acceptor fluorescence and corresponding FRET time traces of a typical binding event show a time delay (τ) between binding of RT and placing of RT at the polymerization site. (B) A binding event showing a transient 0.9 FRET state between the 0 and 0.3 FRET states, suggesting that RT arrived at the front end in an orientation that placed the RNase H domain close to the primer terminus and subsequently flipped to the polymerization orientation. The time resolution of the traces is 10 Hz. Cy5 fluorescence under direct 635-nm excitation (omitted for clarity) indicates that an active Cy5 is present during the whole detection time. Yellow shades in the FRET time traces mark individual RT binding events. The histogram of the time delay, τ , is shown in Fig. S9. (C) Schematic depiction of the two primer terminus search scenarios as suggested by traces in (A) and (B).



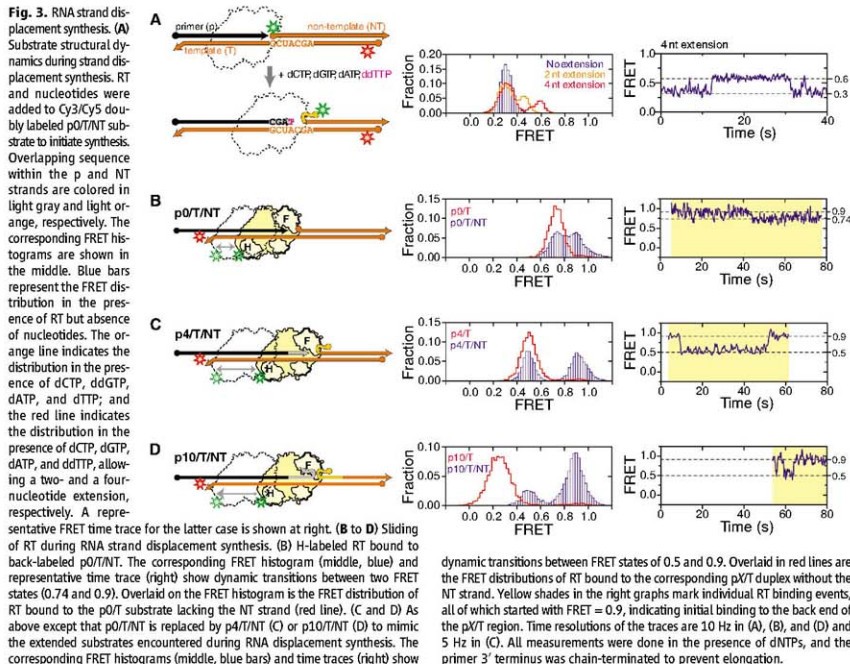
DNA or RNA (fig. S6) (2). They were also independent of whether the RNase H-inactivating E478Q mutation was introduced (fig. S5) (2). To further test whether sliding was a general activity of RT, we exchanged the RNA template in the DNA/RNA hybrid for a DNA template to emulate plus-strand DNA synthesis. RT was again observed to slide between the termini of the duplex DNA, although the transition rates between the two ends were different from those observed on the DNA/RNA hybrid (fig. S7) (2).

The FRET time traces of individual RT molecules showed repeated transitions between the front- and back-end bound states within a single binding event (Fig. 1D), suggesting shuttling between the two ends of the hybrid without dissociation. The FRET transitions between the two end states were not instantaneous but rather gradual, with preferred intermediate states in the middle of the hybrid (Fig. 1D and fig. S8, A and B) (2). Shuttling motion sped up as the temperature was raised (fig. S8C) but did not require nucleotide hydrolysis, suggesting that the movement is a thermally driven diffusion process. RT was previously observed to cleave RNA at multiple po-

sitions within a DNA/RNA hybrid (5, 21, 22) in a manner consistent with the end-binding states and the sliding intermediates observed here, suggesting that sliding may provide a mechanism for RT to rapidly access these cleavage sites.

It is remarkable that a polymerase could frequently slide away from the polymerization site. To explore what structural rearrangements within the enzyme may be required for this action, we tested the effects of small molecule ligands on sliding kinetics. Binding of a cognate nucleotide is expected to cause the fingers and thumb domains of RT to form a tighter grip around the primer terminus (3,4) and stabilize the polymerization state. To test the effect of nucleotide binding, we again used H-labeled RT and back-labeled 38-bp DNA/RNA hybrid but with 3'-dideoxyribonucleoside-terminated DNA primer to prevent DNA synthesis. Addition of 2'-deoxyguanosine 5'-triphosphate (dGTP), the next cognate nucleotide, significantly stabilized the low FRET front-end bound state (Fig. 1E), further supporting the notion that the front-end bound state reflects RT binding in the polymerization-competent mode. Kinetically, addition of 1 mM dGTP slowed down

the rate constant of front to back transitions ($k_{\text{front} \rightarrow \text{back}}$) by 12-fold without substantially affecting the reverse rate constant $k_{\text{back} \rightarrow \text{front}}$ (fig. S7C) (2). In contrast, addition of mismatched nucleotides [2'-deoxyadenosine 5'-triphosphate (dATP), 2'-deoxycytidine 5'-triphosphate (dCTP), and 2'-deoxythymidine 5'-triphosphate (dTTP)] did not significantly affect the transition kinetics (Fig. 1E). Another small molecule ligand tested was the nonnucleoside RT inhibitor (NNRTI), one of the major classes of anti-HIV drugs that inhibit DNA synthesis (30, 35). We measured the sliding dynamics of RT in the presence of nevirapine, a representative NNRTI. Interestingly, the effects of the drug were opposite to those of the cognate deoxyribonucleotide triphosphate (dNTP): Addition of nevirapine destabilized the front-end bound state of the enzyme (Fig. 1E) by increasing $k_{\text{front} \rightarrow \text{back}}$ without significantly altering $k_{\text{back} \rightarrow \text{front}}$ (fig. S8C) (2). Structurally, NNRTI and cognate dNTP have opposite effects on the conformation of RT near the polymerase active site (34, 35): Whereas nucleotide binding tightens the clamp of the fingers and thumb domains around the substrate, binding of NNRTI loosens



the clamp. Hence, our data suggest that relaxation of the fingers-thumb grip is likely required for RT to escape the polymerization site. Our observation that NNRTI promotes enzyme escape from the polymerization site also suggests an inhibitory mechanism for this class of drugs and explains why the inhibitory effect of NNRTI is stronger on long DNA synthesis than on short DNA synthesis (36).

Next, we probed potential functional roles of RT sliding on reverse transcription. Compared to cellular DNA polymerases, RT exhibits poor processivity, typically dissociating from the substrate after synthesizing only a few to a few hundred nucleotides (10, 26), despite a ~10-kb-long HIV genome (37). RT thus frequently encounters the challenge of having to locate the nascent DNA terminus to continue DNA synthesis. The ability of RT to slide on duplexes suggests an interesting mechanism of enzyme targeting by one-

dimensional search, a mechanism that has been proposed for target searching by transcription factors, RNA polymerase, and DNA repair enzyme (38–42). To test this possibility, we added H-labeled RT to a ~550-bp front-labeled DNA duplex (Fig. 2). Were RT to bind directly to the duplex front end, we would expect a FRET value of 0.3 immediately upon binding, corresponding to the ~19-bp distance expected between Cy3 and Cy5. Instead, we found that the majority of the binding events initiated with a FRET value of 0, reaching 0.3 only after a finite time delay (Fig. 2A and fig. S9). This observation indicates that the enzyme first bound to the DNA outside the polymerization site and subsequently moved to the primer terminus where polymerization takes place (Fig. 2C). Such a binding procedure will likely increase the polymerization target searching efficiency on long duplexes where the primer terminus constitutes only a tiny fraction of the duplex sub-

strate. However, if the enzyme can indeed bind in the middle of a duplex, the lack of directional cues may also lead to binding in the “wrong” orientation, such that the RNase H domain is poised closer than the polymerase domain to the 3' terminus of the primer (Fig. 2C). In this case, even after sliding to the front end, RT would not be properly positioned for DNA synthesis. This type of binding was indeed observed frequently (~48% of the time), as indicated by a high FRET state with FRET ~0.9, after the initial 0 FRET state (Fig. 2B). Remarkably, the high FRET state converted rapidly into the 0.3 FRET state *in situ* without dissociation (Fig. 2B), indicating that the enzyme flipped into the polymerization-competent orientation. The ability of RT to flip to the polymerization orientation once reaching the primer terminus without dissociation may further increase its target searching efficiency. Our data does not exclude a possibility that the enzyme may also flip in the middle of the duplex, although such flipping events should not lead to a net increase of target searching efficiency.

Hairpins and long duplexes present on the template strand during DNA synthesis require the polymerization machinery to perform strand displacement synthesis. Polymerization site targeting on these substrates may be even more challenging because, after enzyme dissociation, these template secondary structures could displace the nascent primer terminus to occlude the polymerization site. This is especially problematic in the case of intrastand RNA displacement during minus-strand synthesis because duplex RNA is more stable than a DNA/RNA hybrid (43, 44). To probe the structural dynamics of substrates encountered during RNA strand displacement synthesis, we designed a series of FRET-labeled triple-stranded substrates, each consisting of an RNA template (T) to which a complementary DNA primer (p) and RNA nontemplate strand (NT) were simultaneously hybridized, with the Cy3 and Cy5 dyes flanking the T/NT duplex region (Fig. 3A). We use the notation pX/T/NT to represent a substrate whose primer has been extended by *X* nucleotides. As expected, the FRET distributions for substrates with all *X* values displayed a peak at 0.3, identical to that observed for the nonextended p0/T/NT substrate (fig. S10), indicating that the T/NT duplex was fully annealed and that the extended DNA primers were not able to displace the NT RNA.

We then added RT and dNTPs to the p0/T/NT substrate to monitor substrate dynamics during displacement synthesis. In the absence of dNTP, a single FRET peak centered at 0.3 was again observed (Fig. 3A). After addition of dNTPs to initiate primer extension and selected dideoxynucleotide triphosphate (ddNTP) to terminate synthesis at specific positions, FRET was observed to increase because of unwinding of the T/NT duplex. The presence of dCTP, ddGTP, dATP, and dTTP supported a two-nucleotide addition, producing a higher FRET peak at 0.45 (Fig. 3A). This higher FRET peak further increased

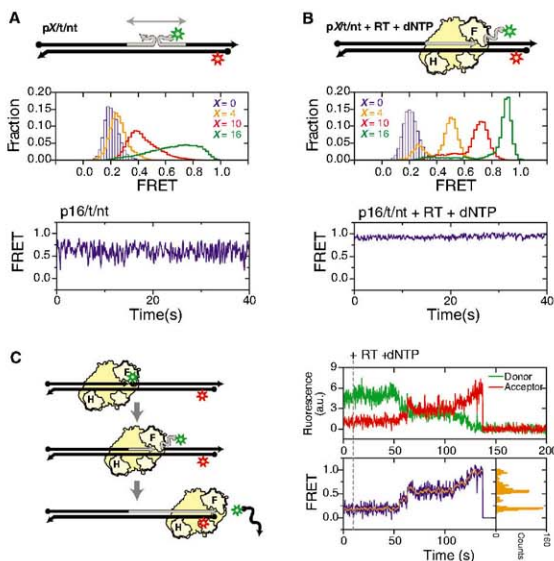


Fig. 4. DNA strand displacement synthesis. **(A)** Structural dynamics of the pX/nt substrates ($X = 0, 4, 10,$ and 16) consisting of all DNA strands. The corresponding FRET histograms are shown in the middle and a representative FRET time trace ($X = 16$) in the bottom. **(B)** As in **(A)** but in the presence of RT and dNTPs. The primers were terminated with a dideoxynucleoside to prevent elongation. **(C)** Single-molecule detection of DNA displacement synthesis. RT and dNTPs were added to the p0/nt substrate to initiate DNA synthesis *in situ*. FRET gradually increased as reaction progressed because of the unzipping of the nontemplate strand. Completion of the reaction was marked by the abrupt loss of the fluorescence signal because of dissociation of the donor labeled nontemplate strand. Plateaus were observed in the donor/acceptor fluorescence traces (top) and the FRET trace (blue trace in bottom left graph), indicating pausing events during synthesis. As a corollary, distinct peaks were observed in the histogram (bottom right inset) constructed from the FRET trace smoothed by 9-point average (orange trace in bottom left graph). Time resolutions are 16 Hz in **(A)** and **(B)** and 10 Hz in **(C)**.

to 0.6 in the presence of dCTP, dGTP, dATP, and ddTTP, which allowed a four-nucleotide extension (Fig. 3A). The FRET distribution agreed quantitatively with that observed for the pre-assembled, chain-terminated p4/T/NT substrate in the presence of RT and dNTPs (fig. S11) (2), confirming successful primer extension. FRET time traces of individual molecules showed repetitive transitions between the 0.6 and 0.3 FRET states (Fig. 3A), suggesting frequent reannealing of the T and NT strands.

One possible cause for T/NT reannealing is sliding of RT to the back end of the p/T hybrid, leaving its front end unbound. To test this experimentally, we added Cy3-labeled RT and dNTPs to Cy5-labeled pX/T/NT substrates, the primers of which were chain-terminated to prevent extension (Fig. 3, B to D). Indeed, transitions between a high and a relatively low FRET state were observed. The high FRET state (0.9) indicates proximity of RT to the back end of the p/T hybrid. The lower FRET states (0.74 for p0/T/NT and 0.5 for p4/T/NT) quantitatively agree with those observed for the p0/T and p4/T hybrids lacking the NT strand (Fig. 3, B and C), to which RT should predominantly bind at the front end in the presence of dNTPs. These results indicate that RT shuttles between the polymerization site and the back end of the substrate even during displacement synthesis.

In the absence of enzyme, a stable T/NT RNA duplex was formed (fig. S10) and no spontaneous annealing of the pX/T hybrid was observed in the FRET time traces. The low processivity of RT poses another question: How would the enzyme, after dissociation, locate the polymerization site (i.e., the front end of the primer/template hybrid) again if such a structure is rarely formed? The answer can be found in the FRET traces: The vast majority (~90%) of the binding events on the pX/T/NT substrates started at the back end with high FRET, with RT subsequently sliding forward to assume the front-end binding state with relatively low FRET (Fig. 3C, right). These observations suggest that sliding allows the enzyme to kinetically access the disrupted polymerization site and assist primer-template annealing, thereby facilitating RNA strand displacement synthesis.

Interestingly, on a substrate with a longer primer extension (p10/T/NT), FRET was also observed to switch between the same 0.9 and 0.5 states as observed for the p4/T/NT substrate (Fig. 3D). Had the primer/template hybrid fully annealed, binding of RT to the front end of the hybridized region would yield FRET values significantly lower than 0.5, as observed for the p10/T substrates lacking the NT strand (Fig. 3D). Similar results were found for the p5/T/NT substrate. These data indicate that RT was not able to slide all the way to the front end of the primer once the overlap between the p and NT strands exceeded four nucleotides. Moreover, the enzyme predominantly remained at the back end of the substrate. We thus expect the efficiency of strand displacement synthesis to drop accordingly. This was directly confirmed by an ensemble

primer extension assay, which revealed that primer extension primarily terminated after adding five nucleotides through RNA strand displacement synthesis (fig. S12A) (2). The exact termination sites were sequence-dependent, consistent with previous observations (16).

The energetic difference between the pX/T and T/NT duplexes observed during RNA strand displacement synthesis does not exist in DNA strand displacement synthesis because all strands involved in the latter case are DNA. To examine substrate dynamics during DNA strand displacement synthesis, we doubly labeled all DNA primer/template/nontemplate substrates (defined as pX/t/nt) with Cy3 and Cy5 (Fig. 4A). In contrast to the pX/T/NT counterparts, the FRET distributions were substantially broader for nonzero primer extension ($X = 4, 10, \text{ and } 16$), and rapid FRET fluctuations were observed in single-molecule traces (Fig. 4A). These observations suggest frequent exchanges between the primer and nontemplate strands for base-pairing with the template. After addition of RT and dNTPs to the substrates (chain-terminated to prevent primer extension), the FRET distribution predominantly assumed a high FRET value that consistently increased with X (Fig. 4B), suggesting that RT reached the front end of the p/t duplex and unwound the t/nt duplex. Even in the case of DNA displacement synthesis, the primer was rarely fully annealed to the template in the absence of a bound RT. It is likely that RT is also targeted to the polymerization site by first binding to the intact part of the primer/template duplex and subsequently sliding forward to unwind the nontemplate strand and anneal the primer. Because there is no substantial energy penalty for exchanging DNA base pairs, RT was thus able to access the primer terminus regardless of the length of the primer extension (Fig. 4B), consistent with RT's ability to perform displacement synthesis through long DNA duplexes (12). When RT and dNTPs were added to the non-terminated p0/t/nt substrate to support synthesis, an increase in FRET was observed as the nt strand was displaced (Fig. 4C). Once the FRET donor-labeled nt strand was fully displaced, a sudden drop in the total fluorescence signal reflected completion of the reaction (Fig. 4C). Rapid and complete DNA strand displacement synthesis was observed for nearly all molecules (fig. S12) (2). Frequent pausing was also observed during synthesis, indicated by plateaus in the single-molecule FRET trace (Fig. 4C). The origin of these kinetic pausing events and their relation to the preferred synthesis termination sites (23, 45) will be a subject of future investigation.

HIV-1 RT thus appears to be a highly dynamic enzyme that can spontaneously slide over long distances on DNA/RNA and DNA/DNA duplex structures, which facilitates multiple phases of reverse transcription, including targeting RT to the primer terminus for DNA polymerization, allowing the enzyme to rapidly access multiple sites within an RNA/DNA hybrid during viral RNA degradation, as well as displacing the nontem-

plate strand and annealing the primer terminus during displacement synthesis. The dynamic flexibility further extends into orientational conformations, allowing the enzyme to flip between opposite binding orientations that support different activities (21, 25). Flipping and sliding can be combined in a complex series of enzyme movements to enhance its efficacy: RT molecules originally bound in the opposite orientation were observed to spontaneously flip into the polymerization orientation after sliding to the primer terminus. It is remarkable that an enzyme could have such large-scale orientational and translational dynamics. This type of dynamic flexibility may be a general design principle for multifunctional enzymes like HIV RT, helping them to rapidly access different binding configurations required to accomplish different functions.

References and Notes

1. A. Telesnitsky, S. P. Goff, in *Retroviruses*, J. M. Coffin, S. H. Hughes, H. E. Varmus, Eds. (Cold Spring Harbor Laboratory Press, Cold Spring Harbor, NY, 1997), pp. 121–160.
2. Materials and methods are available as supporting material on Science Online.
3. D. Baltimore, *Nature* **226**, 1209 (1970).
4. H. M. Temin, S. Mizutani, *Nature* **226**, 1211 (1970).
5. J. P. Leis, I. Berkower, J. Hurwitz, *Proc. Natl. Acad. Sci. U.S.A.* **70**, 466 (1973).
6. J. Hansen, T. Schulze, W. Mellert, K. Moelling, *EMBO J.* **7**, 239 (1988).
7. J. K. Smith, A. Cywinski, J. M. Taylor, *J. Virol.* **49**, 200 (1984).
8. C. A. Omer, R. Resnick, A. J. Faras, *J. Virol.* **50**, 465 (1984).
9. W. I. Finston, J. J. Champoux, *J. Virol.* **51**, 26 (1984).
10. H. E. Huber, J. M. McCoy, J. S. Seehra, C. C. Richardson, *J. Biol. Chem.* **264**, 4669 (1989).
11. M. Hottiger, V. N. Podust, R. L. Thimmig, C. McHenry, U. Hubscher, *J. Biol. Chem.* **269**, 986 (1994).
12. S. H. Whiting, J. J. Champoux, *J. Virol.* **68**, 4747 (1994).
13. G. M. Fuentes, P. J. Fay, R. A. Bambara, *Nucleic Acids Res.* **24**, 1719 (1996).
14. Z. Suo, K. A. Johnson, *Biochemistry* **36**, 12459 (1997).
15. C. D. Kelleher, J. J. Champoux, *J. Biol. Chem.* **273**, 9976 (1998).
16. C. Lanciault, J. J. Champoux, *J. Biol. Chem.* **279**, 32252 (2004).
17. A. Jacobo-Molina et al., *Proc. Natl. Acad. Sci. U.S.A.* **90**, 6320 (1993).
18. S. G. Sarafianos et al., *EMBO J.* **20**, 1449 (2001).
19. S. G. Sarafianos et al., *EMBO J.* **21**, 6614 (2002).
20. W. Metzger, T. Hermann, O. Schatz, S. F. Le Grice, H. Heumann, *Proc. Natl. Acad. Sci. U.S.A.* **90**, 5909 (1993).
21. J. J. DeStefano, L. M. Mallaber, P. J. Fay, R. A. Bambara, *Nucleic Acids Res.* **21**, 4330 (1993).
22. M. Wisniewski, M. Balakrishnan, C. Palaniappan, P. J. Fay, R. A. Bambara, *J. Biol. Chem.* **275**, 37664 (2000).
23. J. Winshell, B. A. Paulson, B. D. Buelow, J. J. Champoux, *J. Biol. Chem.* **279**, 52924 (2004).
24. P. J. Rothwell et al., *Proc. Natl. Acad. Sci. U.S.A.* **100**, 1655 (2003).
25. E. A. Abbondanzieri et al., *Nature* **453**, 184 (2008).
26. K. J. Williams, L. A. Loeb, M. Fry, *J. Biol. Chem.* **265**, 18682 (1990).
27. L. Stryer, R. P. Haugland, *Proc. Natl. Acad. Sci. U.S.A.* **58**, 719 (1967).
28. T. Ha et al., *Proc. Natl. Acad. Sci. U.S.A.* **93**, 6264 (1996).
29. Z. Hostomsky, Z. Hostomska, T. B. Fu, J. Taylor, *J. Virol.* **66**, 3179 (1992).
30. L. A. Kohlstaedt, J. Wang, J. M. Friedman, P. A. Rice, T. A. Steitz, *Science* **256**, 1783 (1992).
31. J. W. Rausch, B. K. Sathyanarayana, M. K. Bona, S. F. Le Grice, *J. Biol. Chem.* **275**, 16015 (2000).

32. A. N. Kapanidis *et al.*, *Science* **314**, 1144 (2006).
 33. M. Gotte, G. Maier, H. J. Gross, H. Heumann, *J. Biol. Chem.* **273**, 10139 (1998).
 34. H. Huang, R. Chopra, G. L. Verdine, S. C. Harrison, *Science* **282**, 1669 (1998).
 35. J. Ren *et al.*, *Nat. Struct. Biol.* **2**, 293 (1995).
 36. Y. Quan, C. Liang, P. Inouye, M. A. Wainberg, *Nucleic Acids Res.* **26**, 5692 (1998).
 37. L. Ratner *et al.*, *Nature* **313**, 277 (1985).
 38. P. H. von Hippel, O. G. Berg, *J. Biol. Chem.* **264**, 675 (1989).
 39. H. Kabata *et al.*, *Science* **262**, 1561 (1993).
 40. M. Guthold *et al.*, *Biophys. J.* **77**, 2284 (1999).
 41. P. C. Blainey, A. M. van Oijen, A. Banerjee, G. L. Verdine, X. S. Xie, *Proc. Natl. Acad. Sci. U.S.A.* **103**, 5752 (2006).
 42. J. Elf, G. W. Li, X. S. Xie, *Science* **316**, 1191 (2007).
 43. K. B. Hall, L. W. McLaughlin, *Biochemistry* **30**, 10606 (1991).
 44. N. Sugimoto, S. Nakano, M. Yoneyama, K. Honda, *Nucleic Acids Res.* **24**, 4501 (1996).
 45. G. J. Klarmann, C. A. Schaubert, B. D. Preston, *J. Biol. Chem.* **268**, 9793 (1993).
 46. This work is supported in part by NIH (GM 068518 to X.Z.) and the Intramural Research Program of the Center for Cancer Research, National Cancer Institute (to

S.F.J.L.G.). X.Z. is a Howard Hughes Medical Institute investigator. E.A.A. is a Jane Coffin Childs postdoctoral fellow. Nevirapine was provided through the AIDS Research and Reference Reagent Program of NIH.

Supporting Online Material

www.sciencemag.org/cgi/content/full/322/5904/1092/DC1

Materials and Methods

Figs. S1 to S12

References

11 July 2008; accepted 24 September 2008

10.1126/science.1163108

Batf3 Deficiency Reveals a Critical Role for CD8 α ⁺ Dendritic Cells in Cytotoxic T Cell Immunity

Kai Hildner,^{1,2} Brian T. Edelson,¹ Whitney E. Purtha,³ Mark Diamond,¹ Hirokazu Matsushita,¹ Masako Kohyama,^{1,2} Boris Calderon,¹ Barbara U. Schraml,¹ Emil R. Unanue,¹ Michael S. Diamond,^{1,3} Robert D. Schreiber,¹ Theresa L. Murphy,¹ Kenneth M. Murphy^{1,2*}

Although *in vitro* observations suggest that cross-presentation of antigens is mediated primarily by CD8 α ⁺ dendritic cells, *in vivo* analysis has been hampered by the lack of systems that selectively eliminate this cell lineage. We show that deletion of the transcription factor *Batf3* ablated development of CD8 α ⁺ dendritic cells, allowing us to examine their role in immunity *in vivo*. Dendritic cells from *Batf3*^{-/-} mice were defective in cross-presentation, and *Batf3*^{-/-} mice lacked virus-specific CD8⁺ T cell responses to West Nile virus. Importantly, rejection of highly immunogenic syngeneic tumors was impaired in *Batf3*^{-/-} mice. These results suggest an important role for CD8 α ⁺ dendritic cells and cross-presentation in responses to viruses and in tumor rejection.

During antigen cross-presentation (1), antigens generated in one cell are presented by major histocompatibility complex (MHC) class I molecules of a second cell. It remains unclear whether all antigen presenting cells (APCs) use cross-presentation and whether this pathway plays a role in immune responses *in vivo* (2). Dendritic cells (DCs) are a heterogeneous group of APCs with two major subsets, plasmacytoid dendritic cells (pDCs) and conventional CD11c⁺ dendritic cells (cDCs) (3). Subsets of cDCs include CD8 α ⁺, CD4⁺, and CD8 α ⁻CD4⁻ populations that may exert distinct functions in immune responses. Evidence has suggested that CD8 α ⁺ cDCs are important for cross-presentation during infections but has its basis in *ex vivo* analysis (4–6) or *in vitro* antigen loading (7). Evidence both for and against a role for cross-presentation in responses against tumors has been reported (8–10).

Attempts have been made to study the *in vivo* role of DCs by selective depletion. Diphtheria toxin treatment can deplete all CD11c^{hi} cells in

one transgenic mouse model (11) but affects splenic macrophages and activated CD8⁺ T cells (12). Gene targeting of transcription factors (e.g., *Irf2*, *Irf4*, *Irf8*, *Stat3*, and *Id2*) has caused broad defects in several DC subsets, T cells, and macrophages (13). To identify genes regulating DC development, we performed global gene expression analysis across many tissues and immune cells (fig. S1A). *Batf3* (also known as *Jun dimerization protein p21SNFT*) (14) was highly expressed in cDCs, with low to absent expression in other immune cells and nonimmune tissues. Thus, we generated *Batf3*^{-/-} mice that lack expression of the *Batf3* protein (fig. S1, B to D).

In spleens of *Batf3*^{-/-} mice, we found a selective loss of CD8 α ⁺ cDCs, without abnormalities in other hematopoietic cell types or architecture (Fig. 1 and figs. S2 to S14). CD8 α ⁺ cDCs coexpress DEC205, CD24, and low levels of CD11b (3, 15). *Batf3*^{-/-} mice lacked splenic CD11c^{hi}CD8 α ⁺DEC205⁺ cells (Fig. 1A), showed a loss of CD11c^{hi}CD11b^{dull} cells and CD11c^{hi}CD8 α ⁺CD24⁺ cells (Fig. 1B), but had normal populations of CD4⁺ and CD8 α ⁻CD4⁻ cDC subsets (Fig. 1B). Lymph nodes and thymi of *Batf3*^{-/-} mice lacked CD8 α ⁺ DCs but had normal distributions of CD8 α ⁻CD11c⁺ cells (Fig. 1C). DEC205^{int} and DEC205^{hi} DCs were present in lymph nodes draining the skin of *Batf3*^{-/-} mice (Fig. 1C) and showed normal migration from skin to lymph node after topical application of fluorescein-5-isothiocyanate (fig. S3A). *Batf3*^{-/-} mice had normal development of pDCs (CD11c^{int}CD11b^{B220}⁺)

(fig. S3B), interstitial DCs of pancreatic islets (CD11c⁺CD8 α ⁻) (fig. S3, C and D), monocytes, neutrophils (fig. S3E), and SIGN-R1⁺ marginal zone and MOMA-1⁺ metallophilic macrophages (Fig. 2A). CD8 α ⁺ cDCs developed normally in heterozygous *Batf3*^{+/-} mice (fig. S4A) and were absent in *Rag2*^{-/-} *Batf3*^{+/-} mice (fig. S4B).

This loss of CD8 α ⁺ cDCs could result from a cell-autonomous hematopoietic defect or a cell-extrinsic requirement for *Batf3*. To distinguish these possibilities, we generated chimeras in which CD45.2⁺ *Batf3*^{+/-} or CD45.2⁺ *Batf3*^{-/-} bone marrow (BM) was transplanted into lethally irradiated CD45.1⁺CD45.2⁻ recipients (Fig. 2B). Upon reconstitution (fig. S5A), we found CD8 α ⁺ cDCs developed only from *Batf3*^{+/-} donor BM cell (Fig. 2B), indicating a cell-intrinsic hematopoietic defect in *Batf3*^{-/-} mice.

Treatment of mice with fms-like tyrosine kinase 3 (flt3) ligand-Fc (FL-Fc) increased the numbers of CD8 α ⁺ cDCs, CD8 α ⁻ cDCs, and pDCs in *Batf3*^{+/-} mice but failed to increase the number of CD8 α ⁺ cDCs in *Batf3*^{-/-} mice (Fig. 2C). *In vitro* culture of BM with FL generates cell populations corresponding to pDCs (CD11c⁺CD45RA⁺) and cDCs (CD11c⁺CD45RA⁻) (3, 16) (Fig. 2D). These *in vitro*-derived cDCs do not express CD8 α or CD4 but contain a CD24⁺Sirp- α ^{lo-int} population corresponding to CD8 α ⁺ cDC (16). *Batf3*^{+/-} or *Batf3*^{-/-} BM cells treated with FL produced similar ratios of pDCs and cDCs (Fig. 2D and fig. S5B). However, *Batf3*^{-/-} BM generated far fewer CD24⁺Sirp- α ⁻ cells compared with *Batf3*^{+/-} BM (Fig. 2D), corresponding to loss of CD8 α ⁺ cDCs. Lastly, DCs generated from *Batf3*^{-/-} BM were selectively deficient in Toll-like receptor (TLR) 3-induced interleukin (IL)-12 production (fig. S5C), a specific feature of CD8 α ⁺ cDCs (16). Similarly, CD11c⁺ cDCs from the spleens of *Batf3*^{-/-} mice were selectively deficient in TLR3-induced IL-12 production but had normal responses to TLR4 and TLR9 ligands (fig. S6A).

We next tested whether APCs from *Batf3*^{-/-} mice could prime CD4⁺ and CD8⁺ T cell responses. Similar proliferative responses of OT-II transgenic CD4⁺ T cells (17) occurred with soluble ovalbumin presented by *Batf3*^{+/-} and *Batf3*^{-/-} cDCs (fig. S6B). However, *Batf3*^{-/-} cDCs were defective in an assay for cross-presentation of cellular antigen to CD8⁺ T cells (2, 18) (Fig. 3A). OT-I T cells proliferated in response to *Batf3*^{+/-} cDCs cocultured with ovalbumin-loaded cells but failed to proliferate in response to *Batf3*^{-/-} cDCs in this assay.

¹Department of Pathology and Immunology, Washington University School of Medicine, 660 South Euclid Avenue, St. Louis, MO 63110, USA. ²Howard Hughes Medical Institute, Washington University School of Medicine, 660 South Euclid Avenue, St. Louis, MO 63110, USA. ³Departments of Medicine and Molecular Microbiology, 660 South Euclid Avenue, St. Louis, MO 63110, USA.

*To whom correspondence should be addressed. E-mail: kmurphy@wustl.edu

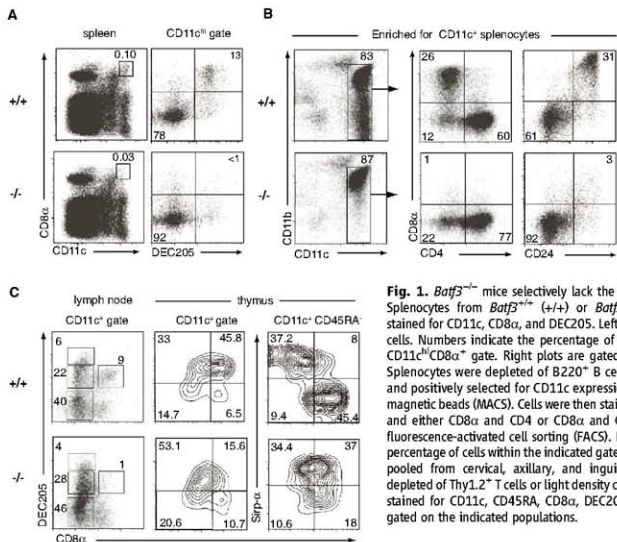


Fig. 1. *Batf3*^{-/-} mice selectively lack the CD8 α ⁺ DC subset. **(A)** Splenocytes from *Batf3*^{+/+} (+/+) or *Batf3*^{-/-} (-/-) mice were stained for CD11c, CD8 α , and DEC205. Left plots are gated on live cells. Numbers indicate the percentage of splenocytes within the CD11c⁺CD8 α ⁺ gate. Right plots are gated on CD11c⁺ cells. **(B)** Splenocytes were depleted of B220⁺ B cells and Thy1.2⁺ T cells and positively selected for CD11c expression by antibody-coated magnetic beads (MACS). Cells were then stained for CD11c, CD11b, and either CD8 α or CD4 or CD8 α and CD24 and analyzed by fluorescence-activated cell sorting (FACS). Numbers represent the percentage of cells within the indicated gates. **(C)** Lymph node cells pooled from cervical, axillary, and inguinal lymph nodes and depleted of Thy1.2⁺ T cells or light density cells of the thymus were stained for CD11c, CD45RA, CD8 α , DEC205, or Sirp- α . Plots are gated on the indicated populations.

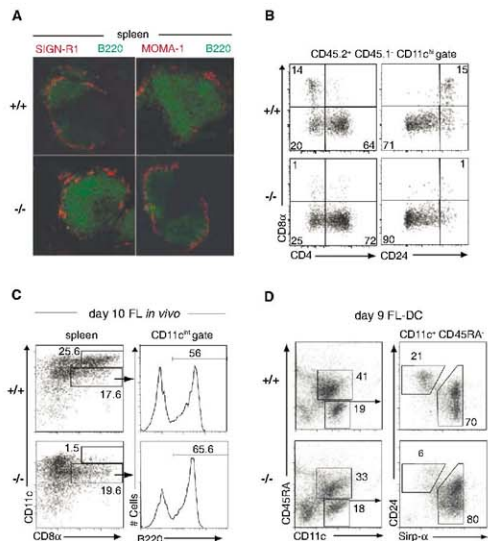


Fig. 2. Functional loss of CD8 α ⁺ cDCs in *Batf3*^{-/-} mice is cell-intrinsic to the hematopoietic system. **(A)** Frozen sections from *Batf3*^{+/+} (+/+) or *Batf3*^{-/-} (-/-) mice were stained for B220 (green) and SIGN-R1 (red) expression (left) or for B220 (green) and MOMA-1 (red) (right). **(B)** Irradiated F1(B6.SJL/J1295Ev) mice (CD45.1⁻CD45.2⁻) were reconstituted with 2×10^7 bone marrow cells from *Batf3*^{+/+} (+/+) or *Batf3*^{-/-} (-/-) CD45.1⁻CD45.2⁻ mice. After 10 weeks, donor cells (CD45.1⁻CD45.2⁻) were analyzed for CD11c, CD8 α , CD4, and CD24 expression. Shown are plots for CD8 α and CD4 (left) or CD8 α and CD24 (right) gated on CD11c⁺ donor-derived cells. Numbers represent the percentage of cells within the indicated gates. **(C)** *Batf3*^{+/+} (+/+) or *Batf3*^{-/-} (-/-) mice were treated intraperitoneally with 10 μ g FL-Fc. After 10 days, splenocytes were enriched for CD11c⁺ by MACS and stained for CD11c, CD8 α , and B220. Plots are gated on live cells (left) or CD11c⁺CD8 α ⁺ cells (right). Numbers represent the percentage of cells within the indicated gates. **(D)** *Batf3*^{+/+} (+/+) or *Batf3*^{-/-} (-/-) BM cells were cultured in FL (20 ng/ml) for 9 days, and nonadherent cells were analyzed for CD11c, CD45RA, CD24, and Sirp- α expression. Plots are gated on live cells (left) or CD11c⁺CD45RA⁺ cells (right).

We examined responses of *Batf3*^{-/-} mice to West Nile virus (WNV) (19, 20) (fig. S6). *Batf3*^{-/-} mice showed normal WNV-specific antibody responses (Fig. 3B) and memory B cell (fig. S6C) and CD4⁺ T cell responses (fig. S6D) but had a dramatic reduction in WNV-specific CD8⁺ T cell responses (Fig. 3C) and in vivo cytotoxic T lymphocyte (CTL) killing of WNV peptide-loaded target cells (fig. S7, A and B). *Batf3*^{-/-} mice lacked WNV-specific memory CD8⁺ T cells and had impaired formation of CD8⁺CD44^{hi}CD62L^{low} cells (fig. S7). Adoptive transfer of *Batf3*^{-/-} CD8⁺ T cells into *Rag2*^{-/-} mice generated normal WNV-specific CD8⁺ T cell response (Fig. 3D), but adoptive transfer of *Batf3*^{+/+} CD8⁺ T cells into *Batf3*^{-/-} *Rag2*^{-/-} mice generated an impaired WNV-specific CD8⁺ T cell response (fig. S7C). This shows that impaired

WNV-specific CTL responses in *Batf3*^{-/-} mice results from a defect of DCs rather than CD8⁺ T cells.

We challenged *Batf3*^{+/+} and *Batf3*^{-/-} mice with syngeneic fibrosarcomas that normally are rapidly rejected in a CD4⁺ and CD8⁺ T cell-dependent manner (21, 22) (fig. S8A). Two independent fibrosarcomas were rapidly rejected by *Batf3*^{+/+} mice but grew progressively in *Rag2*^{-/-} mice and *Batf3*^{-/-} mice (Fig. 4A and fig. S8, B and C). Moreover, *Batf3*^{-/-} mice failed to develop tumor-specific CTLs (Fig. 4B). Tumor-infiltrating CD8⁺ T cells, but not CD4⁺ T cells, were significantly reduced in *Batf3*^{-/-} mice (Fig. 4C). The failure of *Batf3*^{-/-} mice to reject these tumors was not due to defective natural killer cell development or function (figs. S2B and S9, A to C). We considered whether *Batf3*^{-/-} T cells have an intrinsic

dysfunction because overexpression studies had suggested *Batf3* might affect IL-2 transcription (14). Although *Batf3* overexpression reduces IL-2 reporter activity in Jurkat T cells (fig. S10B), *Batf3*^{-/-} CD4⁺ T cells showed normal IL-2 production (fig. S10D) and normal T helper cell (T_H) T_H1, T_H2, and T_H17 differentiation (figs. S10, C to E, and S11B). Lastly, *Batf3*^{-/-} CD8⁺ T cells showed normal allospecific effector responses (fig. S11A) and cytokine production (fig. S11B).

Other DC subsets may cross-present, although less efficiently than CD8α⁺ DCs (23–26), suggesting there may be residual cross-presentation capacity in *Batf3*^{-/-} mice. We therefore challenged mice by using reduced tumor-cell numbers, which might allow effective responses in the setting of reduced cross-presentation (fig. S8). Whereas 10⁴

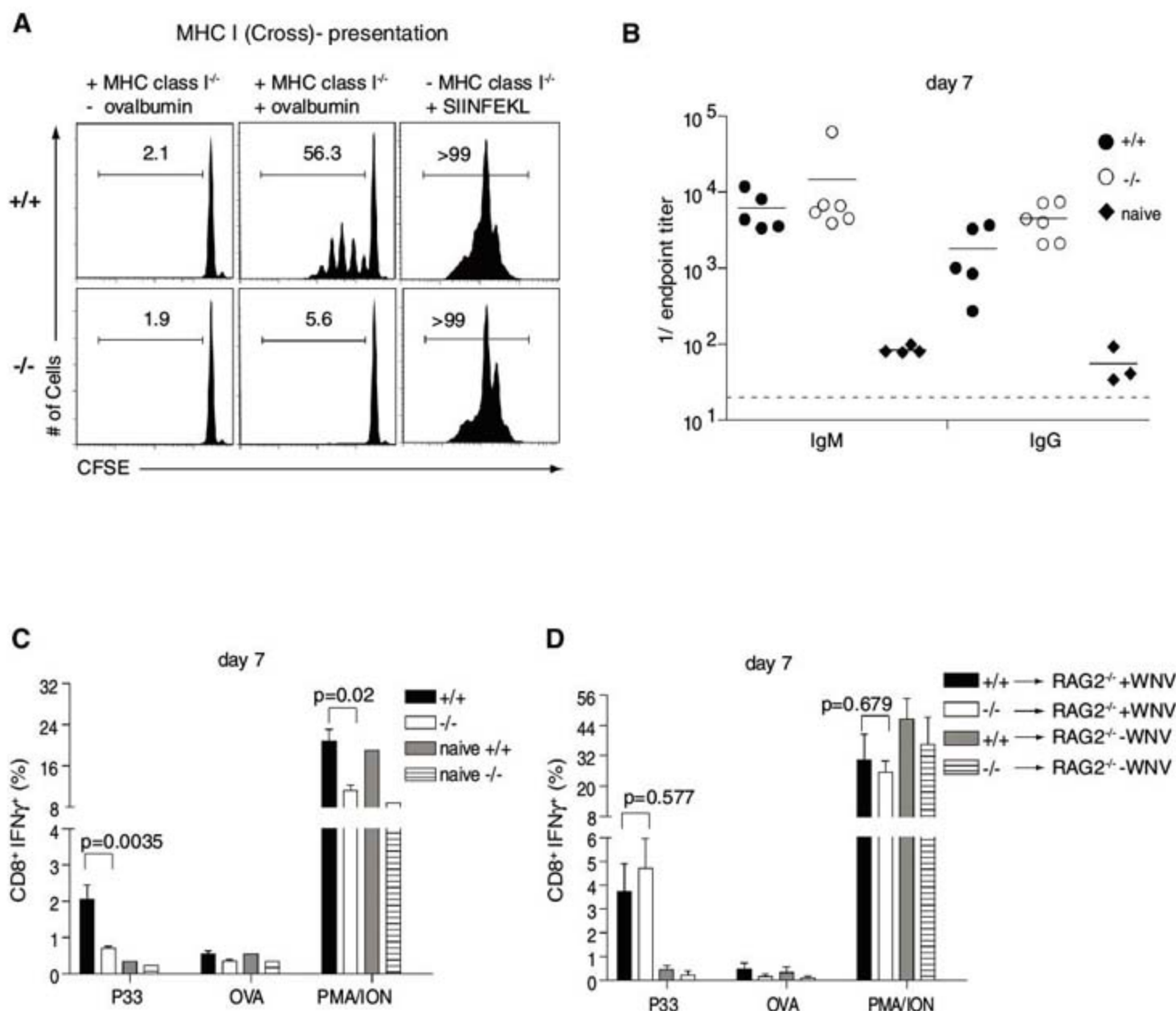
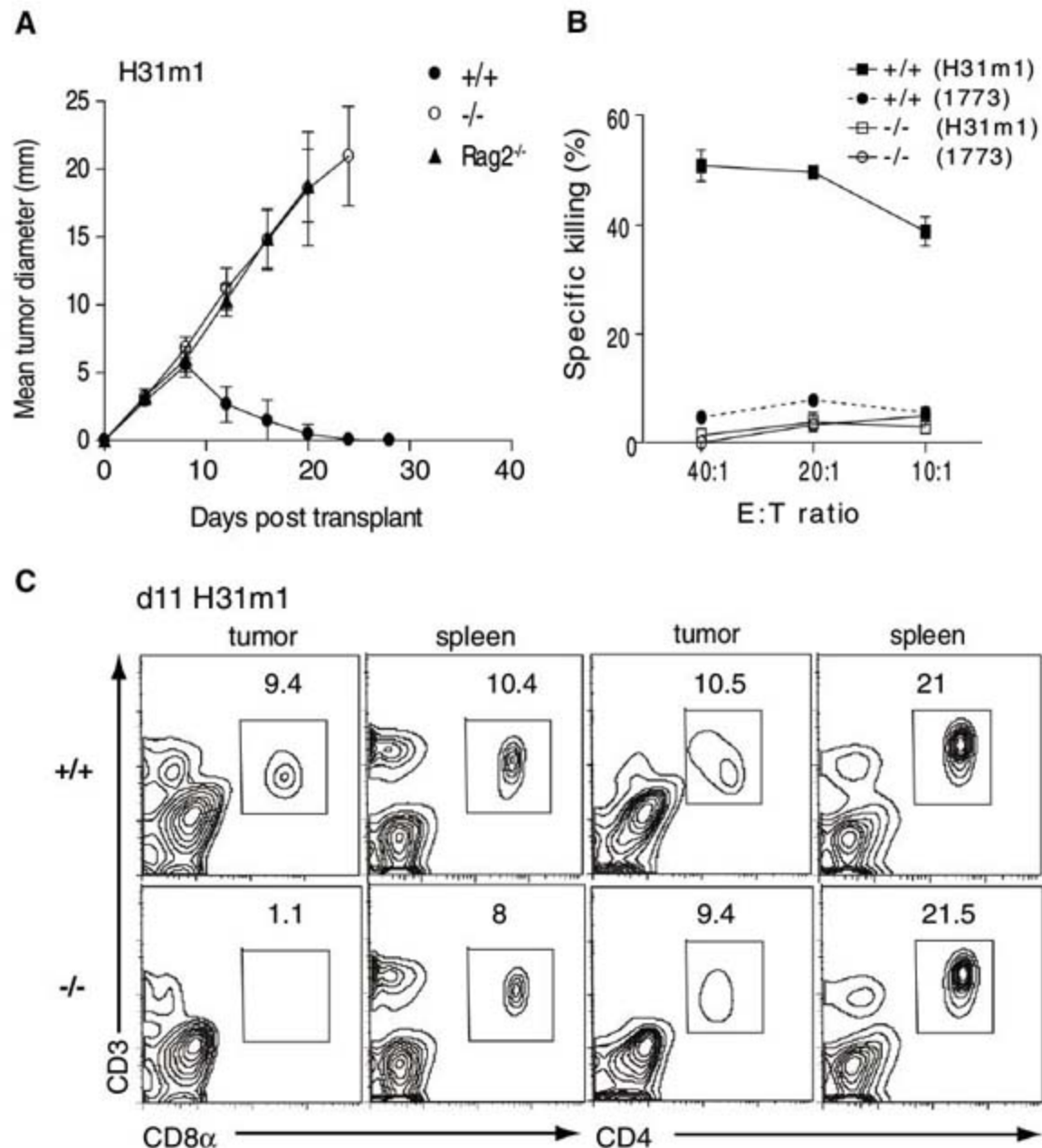


Fig. 3. Lack of cross-presentation and antiviral CTL responses in *Batf3*^{-/-} mice. **(A)** *Batf3*^{+/+} (+/+) or *Batf3*^{-/-} (-/-) splenocytes were depleted of B220⁺ B cells and Thy1.2⁺ T cells, enriched for CD11c by MACS, and cultured with irradiated MHC class I^{-/-} splenocytes as indicated that were either untreated (-ovalbumin), pulsed with 10 mg/ml soluble ovalbumin (+ovalbumin), or cultured with 1 μM Ser-Ile-Ile-Asn-Phe-Glu-Lys-Leu (SIINFEKL) peptide. Carboxyfluorescein succinimidyl ester (CFSE)-labeled CD45.1⁺ OT-I T cells were cultured with these cells, and proliferation was determined by FACS after 60 hours. Single-color histograms of CD8⁺CD45.1⁺ OT-I T cells show the percentage of cells in the indicated gates. **(B)** *Batf3*^{+/+} (+/+) or *Batf3*^{-/-} (-/-) mice were infected with 100 plaque-forming units (PFUs) of WNV. On day 7, isotype-specific anti-WNV E protein titers were

measured. Horizontal lines represent mean titers and dotted line represents limit of detection. **(C)** *Batf3*^{+/+} (+/+) or *Batf3*^{-/-} (-/-) mice were infected with 100 PFUs of WNV or left uninfected. After 7 days, splenocytes were stimulated in vitro with the WNV-specific NS4B peptide (P33), OVA peptide, or phorbol 12-myristate 13-acetate (PMA)/ionomycin as described. CD8⁺ T cells were analyzed for expression of intracellular interferon γ (IFN-γ). Data shown are mean ± SEM (n = 9 to 10). **(D)** *Batf3*^{+/+} (+/+) or *Batf3*^{-/-} (-/-) CD8⁺ T cells were transferred intravenously into *Rag2*^{-/-} recipients. After 24 hours, mice were infected with 100 PFU of WNV (+WNV) or left uninfected (-WNV). After 7 days, splenocytes were harvested and analyzed as described in (C). Data shown are mean ± SEM (n = 6). Three independently performed experiments yielded similar results.

Fig. 4. Lack of tumor rejection in *Batf3*^{-/-} mice. **(A)** 10⁶ H31m1 fibrosarcoma cells were injected subcutaneously into *Batf3*^{+/+} (solid circles), *Batf3*^{-/-} (open circles), or *Rag2*^{-/-} (triangles) mice, and tumor diameter (±SD) (*n* = 10) was measured. **(B)** Mice were treated as in (A). After 9 days, splenocytes were harvested and cocultured with IFN-γ pretreated, irradiated H31m1 or 1773 tumor cells. After 5 days, a CTL killing assay using ⁵¹Cr-labeled H31m1 or 1773 tumor cells as target cells was performed. Shown is specific killing activity as described in (30). **(C)** Tumors and spleens from mice treated as in (A) were removed on day 11, and cells analyzed by FACS. Plots are gated on live CD45.2⁺ cells and show CD3, CD8α, and CD4 expression. Numbers represent the percentage of cells within the indicated gate. Results are representative of at least three mice per group.



and 10⁵ tumor cells grew in all *Rag2*^{-/-} mice, some *Batf3*^{+/+} mice controlled this lower tumor burden (fig. S8, D and E) and developed a tumor-specific CTL response (fig. S8F). Whereas adoptive transfer of wild-type DCs led to partial control of tumor growth in *Batf3*^{+/+} mice, transfer of *Batf3*^{-/-} DCs did not (fig. S12).

Subsets of cDCs have recently been described with functional similarities to CD8α⁺ cDCs. Migratory Langerin⁺ dermal and lung DC subsets express DEC205⁺ and CD103⁺ and, like CD8α⁺ cDCs, are CD11b^{lo/-} (27, 28). CD8α⁺ cDC and migratory CD103⁺ DC populations share the distinctive properties of TLR3 responsiveness (27) and capacity for cross-presentation (26), further supporting the idea that these CD103⁺ subsets may be related. In spleen, CD103 is coexpressed with CD8α on cDCs (fig. S13A) (29) and selectively expressed by the “CD8α equivalent” CD24⁺Sirp-α^{ko-int} cDC subset derived from FL-treated *Batf3*^{+/+} BM (fig. S13C), but is not expressed by *Batf3*^{-/-} splenic cDCs (fig. S13B) or FL-treated *Batf3*^{-/-} BM cells. This suggests that CD103-expressing cDCs may require *Batf3*. In agreement, *Batf3*^{-/-} mice showed a reduced number of CD103-expressing DEC205⁺CD8α⁻CD11b^{lo/-} dermal DCs in skin-draining lymph nodes (fig. S14).

This study describes a transcription factor that controls development of CD8α⁺ cDCs. *Batf3*^{-/-} mice exhibit impaired antigen cross-presentation, impaired CTL responses against viral infection, and impaired responses to tumor challenge. These results suggest an important role for in vivo cross-presentation in CTL responses and provide support for therapeutic approaches that use CD8α⁺ cDCs for the induction of effective immune responses.

References and Notes

1. M. J. Bevan, *J. Exp. Med.* **143**, 1283 (1976).
2. J. M. den Haan, S. M. Lehar, M. J. Bevan, *J. Exp. Med.* **192**, 1685 (2000).
3. K. Shortman, S. H. Naik, *Nat. Rev. Immunol.* **7**, 19 (2007).
4. R. S. Allan et al., *Science* **301**, 1925 (2003).
5. G. T. Belz et al., *J. Immunol.* **172**, 1996 (2004).
6. G. T. Belz, K. Shortman, M. J. Bevan, W. R. Heath, *J. Immunol.* **175**, 196 (2005).
7. O. Schulz et al., *Nature* **433**, 887 (2005).
8. A. Y. Huang et al., *Science* **264**, 961 (1994).
9. A. F. Ochsenbein et al., *Nature* **411**, 1058 (2001).
10. M. C. Wolkers, G. Stoetter, F. A. Vyth-Dreese, T. N. Schumacher, *J. Immunol.* **167**, 3577 (2001).
11. S. Jung et al., *Immunity* **17**, 211 (2002).
12. H. C. Probst et al., *Clin. Exp. Immunol.* **141**, 398 (2005).
13. M. Zenke, T. Hieronymus, *Trends Immunol.* **27**, 140 (2006).
14. M. Iacobelli, W. Wachsman, K. L. McGuire, *J. Immunol.* **165**, 860 (2000).
15. D. Dudziak et al., *Science* **315**, 107 (2007).
16. S. H. Naik et al., *J. Immunol.* **174**, 6592 (2005).

17. M. J. Barnden, J. Allison, W. R. Heath, F. R. Carbone, *Immunol. Cell Biol.* **76**, 34 (1998).
18. N. S. Wilson et al., *Nat. Immunol.* **7**, 165 (2006).
19. M. S. Diamond, B. Shrestha, A. Marri, D. Mahan, M. Engle, *J. Virol.* **77**, 2578 (2003).
20. E. M. Sitati, M. S. Diamond, *J. Virol.* **80**, 12060 (2006).
21. V. Shankaran et al., *Nature* **410**, 1107 (2001).
22. G. P. Dunn et al., *Nat. Immunol.* **6**, 722 (2005).
23. M. L. Lin, Y. Zhan, J. A. Villadangos, A. M. Lew, *Immunol. Cell Biol.* **86**, 353 (2008).
24. G. T. Belz et al., *Proc. Natl. Acad. Sci. U.S.A.* **101**, 8670 (2004).
25. J. Waithman et al., *J. Immunol.* **179**, 4535 (2007).
26. M. L. del Rio, J. I. Rodriguez-Barbosa, E. Kremmer, R. Forster, *J. Immunol.* **178**, 6861 (2007).
27. S. S. Sung et al., *J. Immunol.* **176**, 2161 (2006).
28. L. S. Bursch et al., *J. Exp. Med.* **204**, 3147 (2007).
29. A. D. Edwards et al., *J. Immunol.* **171**, 47 (2003).
30. Materials and methods are available as supporting material on Science Online.
31. This work was supported by the Howard Hughes Medical Institute (K.M.M.), the Emmy Noether Program of the German Research Foundation (K.H.), and a Burroughs Wellcome Fund Career Award for Medical Scientists (B.T.E.).

Supporting Online Material

www.sciencemag.org/cgi/content/full/322/5904/1097/DC1
 Materials and Methods
 Figs. S1 to S14
 References

5 August 2008; accepted 8 October 2008
 10.1126/science.1164206

Del-1, an Endogenous Leukocyte-Endothelial Adhesion Inhibitor, Limits Inflammatory Cell Recruitment

Eun Young Choi,^{1*} Emmanouil Chavakis,^{2*} Marcus A. Czabanka,^{3†} Harald F. Langer,^{1†} Line Fraemohs,⁴ Matina Economopoulou,⁵ Ramendra K. Kundu,⁶ Alessia Orlandi,² Ying Yi Zheng,¹ DaRue A. Prieto,⁷ Christie M. Ballantyne,⁸ Stephanie L. Constant,⁹ William C. Aird,¹⁰ Thalia Papayannopoulou,¹¹ Carl G. Gahmberg,¹² Mark C. Udey,¹³ Peter Vajkoczy,³ Thomas Quertermous,⁶ Stefanie Dimmeler,² Christian Weber,⁴ Triantafyllos Chavakis^{1‡}

Leukocyte recruitment to sites of infection or inflammation requires multiple adhesive events. Although numerous players promoting leukocyte-endothelial interactions have been characterized, functionally important endogenous inhibitors of leukocyte adhesion have not been identified. Here we describe the endothelially derived secreted molecule Del-1 (developmental endothelial locus-1) as an anti-adhesive factor that interferes with the integrin LFA-1–dependent leukocyte-endothelial adhesion. Endothelial Del-1 deficiency increased LFA-1–dependent leukocyte adhesion in vitro and in vivo. Del-1^{-/-} mice displayed significantly higher neutrophil accumulation in lipopolysaccharide-induced lung inflammation in vivo, which was reversed in Del-1/LFA-1 double-deficient mice. Thus, Del-1 is an endogenous inhibitor of inflammatory cell recruitment and could provide a basis for targeting leukocyte-endothelial interactions in disease.

Leukocyte extravasation is integral to the response to infection or injury and to inflammation and autoimmunity. Leukocyte recruitment comprises a well-coordinated cascade of adhesive events, including selectin-mediated rolling, firm adhesion of leukocytes to endothelial cells, and their subsequent transendothelial migration. The interaction between LFA-1 (also known as α L β 2 and CD11a/CD18) and endothelial intercellular adhesion molecule-1 (ICAM-1) is crucial during firm endothelial adhesion of leukocytes

(1–5). Whereas numerous adhesion receptors promoting inflammatory cell recruitment have been identified, very little information exists about endogenous inhibitors of the leukocyte adhesion cascade (1–7).

Developmental endothelial locus-1 (Del-1) is a glycoprotein that is secreted by endothelial cells and can associate with the endothelial cell surface and the extracellular matrix (8–10). Del-1 is regulated upon hypoxia or vascular injury and has been implicated in vascular remodeling during

angiogenesis (10–12). We sought to determine whether endothelially derived Del-1 participates in leukocyte-endothelial interactions.

Del-1 mRNA was observed predominantly in the brain and lung, with no expression in the liver, spleen, or whole blood (Fig. 1A and fig. S1A). Del-1 was expressed in wild-type (WT) but not in Del-1^{-/-} murine lung endothelial cells (Fig. 1B) (9). In lung tissues, Del-1 was present in blood vessels (fig. S1B).

To determine whether Del-1 participates in leukocyte recruitment interactions, we studied the adhesion of primary neutrophils to immobi-

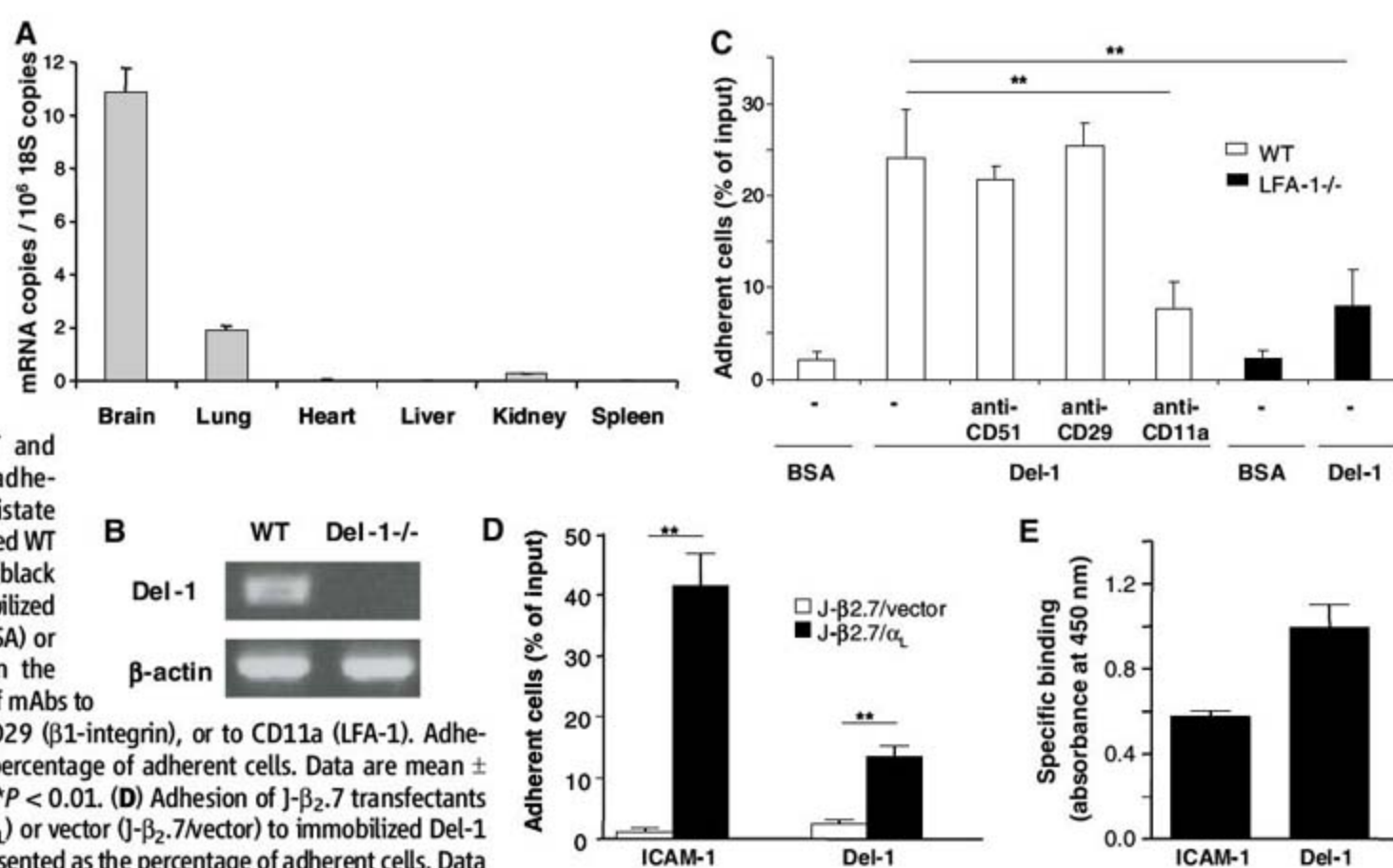
¹Experimental Immunology Branch, Center for Cancer Research, National Cancer Institute (NCI), National Institutes of Health (NIH), Bethesda, MD, USA. ²Molecular Cardiology, Department of Internal Medicine III, J. W. Goethe University, Frankfurt, Germany. ³Department of Neurosurgery, Charité Universitätsmedizin, Berlin, Germany. ⁴Institute for Molecular Cardiovascular Research, RWTH University Hospital, Aachen, Germany. ⁵Laboratory of Cellular Oncology, Center for Cancer Research, NCI, NIH, Bethesda, MD, USA. ⁶Division of Cardiovascular Medicine, Stanford University School of Medicine, Palo Alto, CA, USA. ⁷Laboratory of Proteomics and Analytical Technologies, SAIC-Frederick, NCI, Frederick, MD, USA. ⁸Baylor College of Medicine and Center for Cardiovascular Disease Prevention, Methodist DeBakey Heart and Vascular Center, Houston, TX, USA. ⁹Department of Microbiology, Immunology and Tropical Medicine, George Washington University, Washington, DC, USA. ¹⁰Molecular and Vascular Medicine, Beth Israel Deaconess Medical Center, Harvard Medical School, Boston, MA, USA. ¹¹Department of Medicine/Hematology, University of Washington, Seattle, WA, USA. ¹²Division of Biochemistry, Faculty of Biosciences, University of Helsinki, Finland. ¹³Dermatology Branch, Center for Cancer Research, NCI, NIH, Bethesda, MD, USA.

*These authors contributed equally to this work.

†These authors contributed equally to this work.

‡To whom correspondence should be addressed. E-mail: chavakist@mail.nih.gov

Fig. 1. Del-1 is expressed in endothelial cells and interacts with leukocyte LFA-1. (A) Real-time reverse transcription polymerase chain reaction (RT-PCR) demonstrating the expression of Del-1 mRNA in adult mouse tissues. Del-1 mRNA was normalized against 18S ribosomal RNA. **(B)** RT-PCR in primary lung endothelial cells from WT and Del-1^{-/-} mice. **(C)** Static adhesion of phorbol 12-myristate 13-acetate (PMA)-stimulated WT (white bars) or LFA-1^{-/-} (black bars) neutrophils to immobilized bovine serum albumin (BSA) or mouse Del-1 is shown in the absence (-) or presence of mAbs to CD51 (α v-integrin), to CD29 (β 1-integrin), or to CD11a (LFA-1). Adhesion is presented as the percentage of adherent cells. Data are mean \pm SD ($n = 3$ experiments). ** $P < 0.01$. **(D)** Adhesion of J- β 2.7 transfectants expressing LFA-1 (J- β 2.7/ α _L) or vector (J- β 2.7/vector) to immobilized Del-1 or ICAM-1. Adhesion is presented as the percentage of adherent cells. Data are mean \pm SEM ($n = 3$). ** $P < 0.01$. **(E)** Binding of the LFA-1 I domain to immobilized Del-1 or ICAM-1. Data are mean \pm SEM ($n = 3$).



lized Del-1. Mouse neutrophils specifically bound to Del-1 under static conditions. Adhesion was inhibited by a blocking monoclonal antibody (mAb) to CD11a (the α L-integrin subunit) but not by antibodies to α v-integrin or β 1-integrin (Fig. 1C), suggesting that LFA-1 mediates the interaction of neutrophils with Del-1. Consistently, LFA-1^{-/-} neutrophils displayed reduced adhesion to Del-1 (Fig. 1C). The residual LFA-1-independent binding of neutrophils to Del-1 was blocked by mAb to Mac-1 (fig. S2A), which is consistent with the fact that LFA-1 and Mac-1 are closely related and share several ligands (13). In addition, α L-transfected but not vector-transfected J- β 2.7 cells specifically bound to immobilized Del-1 (Fig. 1D), whereas a direct interaction between Del-1 and the ligand-binding I domain of LFA-1, locked in the open high-affinity conformation, was observed (Fig. 1E and fig. S2B). Thus, Del-1 is a ligand of LFA-1 integrin.

To address whether Del-1 participates in leukocyte-endothelial interactions, we studied neutrophil and monocyte adhesion to WT and Del-1^{-/-} endothelial cells (14, 15). Contrary to our prediction, Del-1^{-/-} endothelial cells promoted significantly higher neutrophil and monocyte adhesion. LFA-1-deficiency on leukocytes and mAb to LFA-1 abolished the enhanced adhesion to Del-1^{-/-} endothelium (Fig. 2A and fig. S3). Thus, enhanced inflammatory cell adhesion to Del-1^{-/-} endothelium is specifically mediated by LFA-1 on leukocytes.

To understand the unexpected inhibitory role of Del-1 in leukocyte-endothelial adhesion, we investigated whether soluble Del-1 interfered with the interaction of LFA-1 with its major ligand, ICAM-1. Mn²⁺-induced binding of ICAM-1-Fc to murine leukocytes in solution was significantly inhibited by soluble Del-1 (Fig. 2B). Moreover, soluble Del-1 inhibited the LFA-1-dependent adhesion of WT neutrophils to immobilized ICAM-1 under physiologic flow conditions, whereas soluble Del-1 did not affect the weaker adhesion of LFA-1^{-/-} neutrophils to ICAM-1 (Fig. 2C).

The finding that endothelial Del-1 antagonizes LFA-1-dependent adhesion (Fig. 2A) appeared to be discordant with the finding that immobilized Del-1 promoted leukocyte adhesion under static conditions (Fig. 1C). We thus assessed the ability of Del-1 and ICAM-1 to promote adhesion when co-immobilized with P-selectin and the chemokine MIP-2 under physiologic flow conditions at low and high shear rates (0.8 and 2 dynes/cm²). In this system, leukocytes first roll on selectin and then arrest on the integrin ligand. Whereas ICAM-1 promoted robust firm adhesion of neutrophils at both shear rates, Del-1 promoted only weak adhesion at the lower shear rate and almost none at the higher shear rate (Fig. 2D). We then analyzed how the presence of plate-bound Del-1 would affect the adhesion of neutrophils to ICAM-1 under flow. Increasing concentrations of Del-1 co-immobilized with ICAM-1, P-selectin, and MIP-2 significantly inhibited neutrophil adhesion to ICAM-1 (Fig. 2E). Thus, although it is

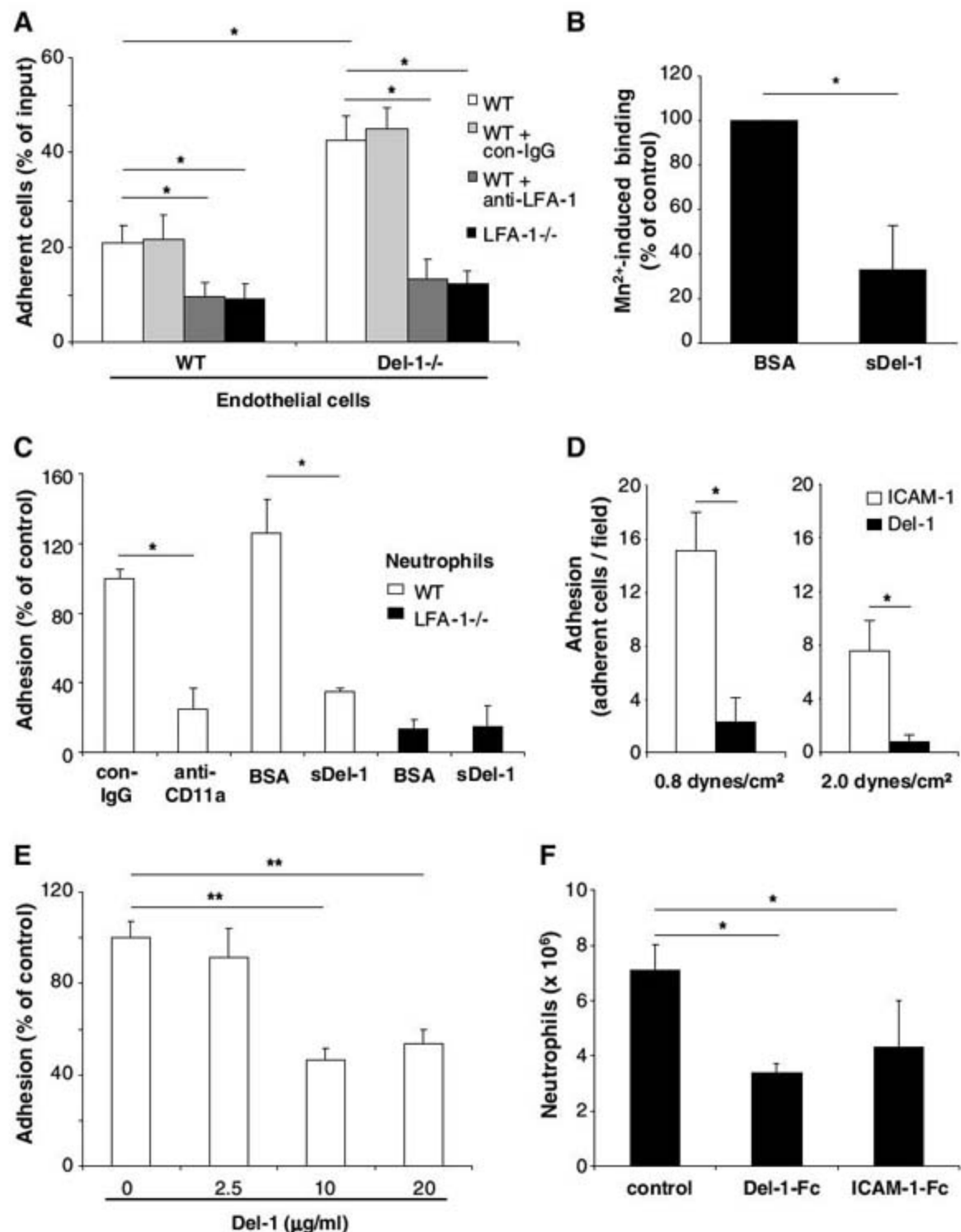


Fig. 2. Del-1 interferes with LFA-1-dependent leukocyte adhesion. (A) PMA-induced adhesion of WT neutrophils in the absence (white bars) or presence of isotype control antibody (light gray bars) or mAb to LFA-1 (dark gray bars), or of LFA-1^{-/-} neutrophils (black bars) to WT or Del-1^{-/-} lung endothelial cells, is shown. IgG, immunoglobulin G. Adhesion is presented as the percentage of adherent cells. Data are mean ± SD (*n* = 4 experiments). **P* < 0.05. (B) Binding of soluble ICAM-1-Fc to mouse bone marrow mononuclear cells in the presence of MnCl₂. Cells were preincubated with BSA or soluble Del-1. Data are mean ± SEM (*n* = 3). **P* < 0.05. (C) Adhesion of WT (white bars) or LFA-1^{-/-} (black bars) neutrophils to immobilized P-selectin, MIP-2, and ICAM-1 under flow (0.8 dynes/cm²) was studied in the presence of mAb to CD11a or isotype control antibody (each mAb at 10 μg/ml) or in the presence of BSA or mouse soluble Del-1 (each at 20 μg/ml). Adhesion is shown as the percentage of control; that is, adhesion of WT neutrophils in the presence of control antibody. Data are mean ± SEM (*n* = 3 perfusion experiments). **P* < 0.05. (D) Adhesion of WT neutrophils to immobilized P-selectin, MIP-2, and ICAM-1 (white bars) or Del-1 (black bars) was studied at indicated shear rates. Adhesion is shown as the number of adherent cells per field. Data are mean ± SEM (*n* = 4 perfusion experiments). **P* < 0.05. (E) Adhesion of WT neutrophils to immobilized P-selectin, MIP-2, and ICAM-1 was studied in the presence of increasing concentrations of Del-1 that was coimmobilized. Adhesion is shown as the percentage of control; that is, adhesion of WT neutrophils in the absence of immobilized Del-1. Data are mean ± SEM (*n* = 6 perfusion experiments). ***P* < 0.01. (F) The numbers of neutrophils at 4 hours after intraperitoneal injection of thioglycollate in WT mice are shown. Mice were treated 30 min before thioglycollate injection with intravenous injection of control Fc protein (control), Del-1-Fc, or ICAM-1-Fc. Data are expressed as absolute numbers of emigrated neutrophils. Data are mean ± SD (*n* = 4 mice per group). **P* < 0.05.

a ligand of LFA-1, Del-1 does not promote firm leukocyte adhesion under flow but interferes with leukocyte adhesion to endothelial ICAM-1.

We then assessed the ability of soluble Del-1 expressed as an Fc fusion protein to inhibit neutrophil recruitment in vivo in acute thioglycollate-

induced peritonitis (14). Intravenous administration of Del-1-Fc 30 min before thioglycollate injection significantly reduced neutrophil accumulation,

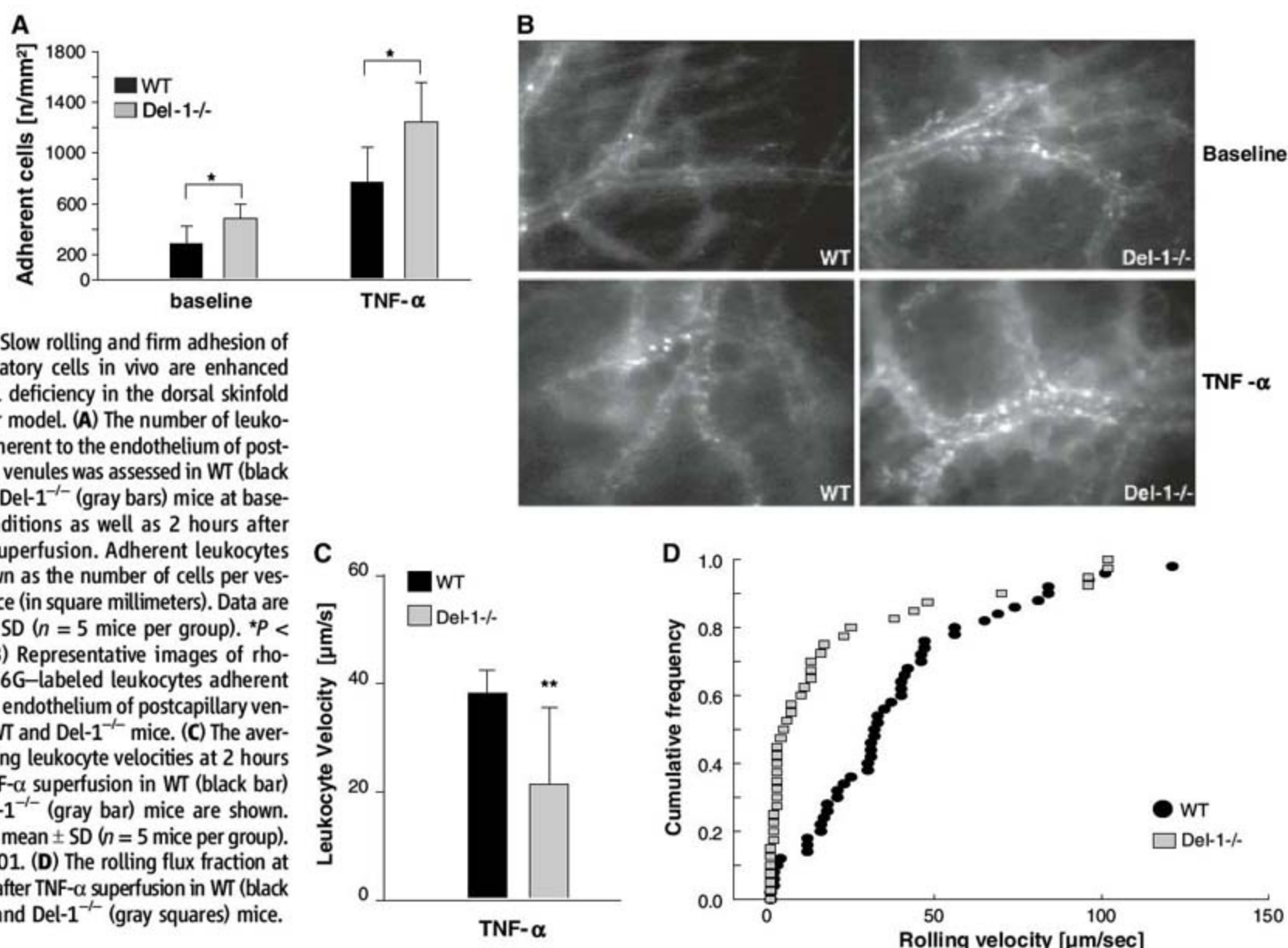
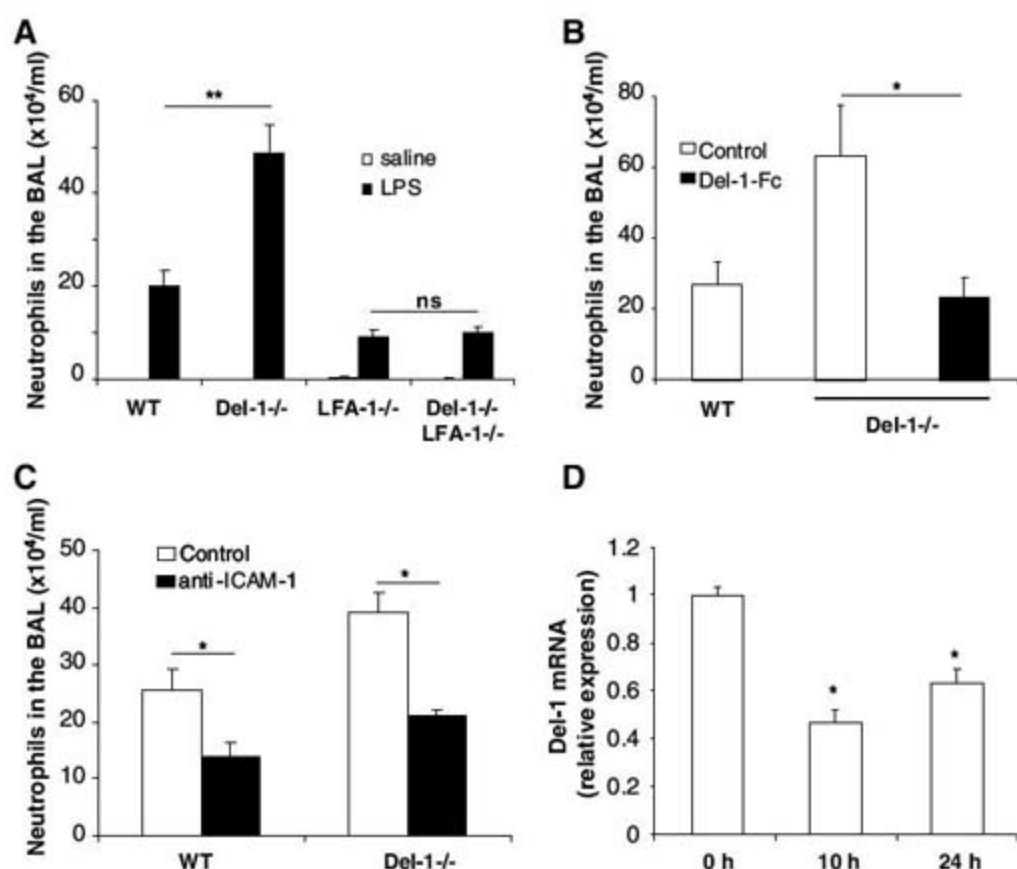


Fig. 3. Slow rolling and firm adhesion of inflammatory cells in vivo are enhanced by Del-1 deficiency in the dorsal skinfold chamber model. (A) The number of leukocytes adherent to the endothelium of postcapillary venules was assessed in WT (black bars) or Del-1^{-/-} (gray bars) mice at baseline conditions as well as 2 hours after TNF- α superfusion. Adherent leukocytes are shown as the number of cells per vessel surface (in square millimeters). Data are mean \pm SD ($n = 5$ mice per group). * $P < 0.05$. (B) Representative images of rhodamine 6G-labeled leukocytes adherent onto the endothelium of postcapillary venules of WT and Del-1^{-/-} mice. (C) The average rolling leukocyte velocities at 2 hours after TNF- α superfusion in WT (black bar) and Del-1^{-/-} (gray bar) mice are shown. Data are mean \pm SD ($n = 5$ mice per group). ** $P < 0.01$. (D) The rolling flux fraction at 2 hours after TNF- α superfusion in WT (black circles) and Del-1^{-/-} (gray squares) mice.

Fig. 4. Increased inflammatory cell recruitment in vivo due to Del-1 deficiency. (A) The numbers of neutrophils in the BAL fluid in WT, Del-1^{-/-}, LFA-1^{-/-}, or Del-1^{-/-}LFA-1^{-/-} mice are shown at 24 hours after nasal administration of saline (white bars) or LPS (black bars). Neutrophil recruitment upon saline inhalation was negligible. Data are expressed as absolute numbers and are mean \pm SEM ($n = 11$ to 16 mice per group). ** $P < 0.01$; ns, not significant. (B) Thirty minutes before LPS administration, WT or Del-1^{-/-} mice received intravenous injections of BSA (control, white bars) or Del-1-Fc (black bar) (each at 90 μg per mouse). Data are expressed as absolute numbers and are mean \pm SEM ($n = 4$ to 11 mice per group). * $P < 0.05$. (C) Thirty minutes before LPS administration, WT or Del-1^{-/-} mice received intravenous injections of isotype control IgG (white bars) or anti-ICAM-1 (black bars) (each at 85 μg per mouse). Data are expressed as absolute numbers and are mean \pm SEM ($n = 8$ or 9 mice per group). * $P < 0.05$. (D) The expression of Del-1 mRNA in mouse lungs at 0 hours, 10 hours, or 24 hours after intranasal LPS administration was analyzed by semiquantitative RT-PCR. The data are shown as relative expression. The ratio of Del-1 mRNA to actin mRNA at 0 hours was set as 1. Data are mean \pm SEM ($n = 4$ mice per group). * $P < 0.05$ as compared to 0 hours.



as compared to Fc control protein (Fig. 2F). Similarly, ICAM-1-Fc reduced neutrophil recruitment into the peritoneum (Fig. 2F).

To provide further evidence for the role of Del-1 in inflammatory cell recruitment in vivo, we performed intravital microscopy using the dorsal skinfold chamber model (16). Del-1^{-/-} mice displayed increased numbers of leukocytes adherent to postcapillary venules both in the baseline condition and upon tumor necrosis factor- α (TNF- α) stimulation (Fig. 3, A and B). Besides firm arrest, the interaction between LFA-1 and ICAM-1 contributes to slow rolling processes (17). A significant decrease in rolling velocity accompanied by an increase in the fraction of slow-rolling leukocytes was observed in Del-1^{-/-} mice (Fig. 3, C and D).

We further studied whether Del-1 could regulate inflammatory cell recruitment in vivo, by performing LPS-induced lung inflammation. Del-1^{-/-} mice displayed significantly higher accumulation of neutrophils in the bronchoalveolar lavage (BAL) fluid than did WT mice (Fig. 4A). LFA-1^{-/-} mice displayed reduced neutrophil accumulation in the BAL upon LPS-induced lung inflammation (Fig. 4A) (18, 19). The increased neutrophil recruitment in vivo due to Del-1 deficiency required the presence of LFA-1, because neutrophil accumulation in the BAL in Del-1^{-/-}LFA-1^{-/-} mice equaled the accumulation of these cells in LFA-1^{-/-} mice (Fig. 4A). The increased leukocyte recruitment due to Del-1 deficiency could not be attributed to an alteration in peripheral blood counts, because constitutive leukocyte numbers were comparable in WT and Del-1^{-/-} mice (fig. S4). In addition, intravenous administration of soluble Del-1 efficiently reversed the increased neutrophil recruitment in Del-1^{-/-} mice (Fig. 4B).

Furthermore, Del-1 deficiency resulted in an up-regulation of baseline ICAM-1 protein expression by lung endothelial cells, which was overridden upon TNF- α stimulation, whereas vascular cell adhesion molecule-1 (VCAM-1) expression was unaffected (fig. S5). No significant increase in ICAM-1 expression, under baseline or inflammatory conditions, was found in Del-1^{-/-} lungs (fig. S6), suggesting that altered ICAM-1 expression is not involved in the increased leukocyte recruitment to Del-1^{-/-} lungs. Moreover, whereas the increased neutrophil recruitment to the lung upon Del-1 deficiency was completely reversed by leukocyte LFA-1 deficiency (Fig. 4A), the inhibition of ICAM-1 by a blocking mAb (18, 20) decreased neutrophil recruitment by the same extent in both WT and Del-1^{-/-} mice (Fig. 4C), suggesting an involvement of other LFA-1 ligands. Thus, Del-1 deficiency enhances LFA-1-dependent leukocyte recruitment in vivo.

We found that Del-1 acted in an anti-inflammatory fashion; however, the expression of Del-1 in inflammation has not been demonstrated. Thus, we analyzed Del-1 mRNA expression in the lung and in endothelial cells upon inflammatory stimulation. Upon LPS administration, lung Del-1

mRNA was significantly reduced (Fig. 4D). Likewise, TNF- α stimulation of endothelial cells induced a significant decrease in Del-1 expression (fig. S7).

Endogenous inhibitors exist in many aspects of inflammation and immunity (21, 22), attenuating exuberant inflammatory and immune activation. The existence of endogenous inhibitors in the leukocyte adhesion cascade, a central paradigm of inflammation and immunity, has been unclear. In this study, endothelially derived Del-1 was shown to intercept LFA-1-dependent leukocyte-endothelial interactions. Given the importance of LFA-1-dependent leukocyte recruitment in several inflammatory and autoimmune disorders (13, 23–25), Del-1 may provide a platform for designing novel attractive therapeutic modalities to target leukocyte-endothelial interactions in disease.

References and Notes

1. T. A. Springer, *Cell* **76**, 301 (1994).
2. N. Hogg, M. Laschinger, K. Giles, A. McDowall, *J. Cell Sci.* **116**, 4695 (2003).
3. D. Vestweber, *Immunol. Rev.* **218**, 178 (2007).
4. B. A. Imhof, M. Aurrand-Lions, *Nat. Rev. Immunol.* **4**, 432 (2004).
5. K. Ley, C. Laudanna, M. I. Cybulsky, S. Nourshargh, *Nat. Rev. Immunol.* **7**, 678 (2007).
6. C. Weber, L. Fraemohs, E. Dejana, *Nat. Rev. Immunol.* **7**, 467 (2007).
7. T. Chavakis, K. T. Preissner, M. Herrmann, *Trends Immunol.* **28**, 408 (2007).
8. C. Hidai, M. Kawana, H. Kitano, S. Kokubun, *Cell Tissue Res.* **330**, 83 (2007).
9. C. Hidai *et al.*, *Genes Dev.* **12**, 21 (1998).
10. H. K. Ho *et al.*, *Circulation* **109**, 1314 (2004).
11. K. Penta *et al.*, *J. Biol. Chem.* **274**, 11101 (1999).
12. J. Zhong *et al.*, *J. Clin. Invest.* **112**, 30 (2003).

13. C. G. Gahmberg *et al.*, *Cell. Mol. Life Sci.* **54**, 549 (1998).
14. Materials and methods are available as supporting material on Science Online.
15. E. Y. Choi *et al.*, *Blood* **111**, 3607 (2008).
16. U. Fiedler *et al.*, *Nat. Med.* **12**, 235 (2006).
17. A. Zarbock, C. A. Lowell, K. Ley, *Immunity* **26**, 773 (2007).
18. A. Basit *et al.*, *Am. J. Physiol. Lung Cell. Mol. Physiol.* **291**, L200 (2006).
19. Z. M. Ding *et al.*, *J. Immunol.* **163**, 5029 (1999).
20. T. Kumasaka *et al.*, *J. Clin. Invest.* **97**, 2362 (1996).
21. R. V. Parry, J. L. Riley, S. G. Ward, *Trends Immunol.* **28**, 161 (2007).
22. R. J. Greenwald, G. J. Freeman, A. H. Sharpe, *Annu. Rev. Immunol.* **23**, 515 (2005).
23. M. Leubwohl *et al.*, *New Engl. J. Med.* **349**, 2004 (2003).
24. A. D. Luster, R. Alon, U. H. von Andrian, *Nat. Immunol.* **6**, 1182 (2005).
25. K. Yonekawa, J. M. Harlan, *J. Leukoc. Biol.* **77**, 129 (2005).
26. We thank X. Feng and M. Sardy for generating the Del-1-Fc protein, N. Hogg for the antibody mAb24, Valantis Inc. for recombinant Del-1 and the antibody to mouse Del-1, T. Veenstra for help with mass spectrometry, D. Winkler for help with genotyping, I. Okumabua for technical assistance, and D. Singer for critically reading the manuscript. This research was supported by the Intramural Research Program of the NIH, NCI (T.C. and M.C.U.); by NIH grants AI067254 (S.L.C.) and RO1 HL082927 (W.C.A.); and by the Deutsche Forschungsgemeinschaft (grants FOR809 and TP6 to C.W.; TR-SFB23 and Exc 147/1 to S.D. and E.C.). A patent application on the anti-inflammatory actions of Del-1 has been filed.

Supporting Online Material

www.sciencemag.org/cgi/content/full/322/5904/1101/DC1
Materials and Methods
Figs. S1 to S8
References

28 August 2008; accepted 9 October 2008
10.1126/science.1165218

Ubiquitin-Like Protein Involved in the Proteasome Pathway of *Mycobacterium tuberculosis*

Michael J. Pearce,¹ Julian Mintseris,² Jessica Ferreyra,¹ Steven P. Gygi,² K. Heran Darwin^{1*}

The protein modifier ubiquitin is a signal for proteasome-mediated degradation in eukaryotes. Proteasome-bearing prokaryotes have been thought to degrade proteins via a ubiquitin-independent pathway. We have identified a prokaryotic ubiquitin-like protein, Pup (Rv2111c), which was specifically conjugated to proteasome substrates in the pathogen *Mycobacterium tuberculosis*. Pupylation occurred on lysines and required proteasome accessory factor A (PafA). In a *pafA* mutant, pupylated proteins were absent and substrates accumulated, thereby connecting pupylation with degradation. Although analogous to ubiquitylation, pupylation appears to proceed by a different chemistry. Thus, like eukaryotes, bacteria may use a small-protein modifier to control protein stability.

Similar to the eukaryotic 20S proteasome, the *Mycobacterium tuberculosis* (Mtb) proteasome is a multisubunit barrel-shaped protease composed of two rings of catalytic β subunits sandwiched by rings of α subunits (1–5). The eukaryotic 26S proteasome is composed of a 20S core particle and one or two 19S regulatory caps, which include adenosine triphosphatases (ATPases)

that recognize, unfold, and translocate substrates into the core for degradation [reviewed in (6)]. In Mtb, Mpa (*Mycobacterium* proteasome ATPase) shares homology with regulatory cap ATPases. Substrates of the Mtb proteasome have been identified (7), but it remains unclear how they were targeted for degradation. Proteins delivered to the eukaryotic proteasome are usually conjugated with

ubiquitin, which covalently attaches to substrate lysines (Lys) as well as onto ubiquitin itself [reviewed in (8)]. Genes encoding ubiquitin-like proteases (Ubls) have not been identified in the *Mtb* genome.

To further define the *Mtb* proteasome system, we looked for proteins that interacted with Mpa using an *Escherichia coli* bacterial two-hybrid system (9, 10). A fusion protein that encoded the last 26 amino acids of Rv211c (here referred to as "Pup") interacted with the Mpa bait fusion [Fig. 1A (10)]. Full-length Pup also specifically interacted with Mpa (Fig. 1A). The *pup* gene has been identified (11, 12), but the function of Pup was unknown. *pup* homologs have so far only been identified in Actinobacteria by BLAST search (13). In *Mtb*, *pup* is part of a putative operon with the proteasome core genes *preB* and *preA* (fig. S2). *pup* is predicted to encode a 64-amino acid protein with a molecular size of 6.9 kD (GenBank accession number EU914921). Recombinant Pup purified from *E. coli* migrated to a position around

15 kD in a denaturing polyacrylamide gel (Fig. 1B); however, certain Ubls, like SUMO-1, migrate more slowly than expected (14, 15).

We then tested the Pup/Mpa interaction in vitro using nickel-nitrilotriacetic acid (Ni-NTA) agarose bound with purified His₆-Pup, and Pup was able to bind Mpa (Fig. 1B) (10). Mpa was not retained by agarose that had first been incubated with *E. coli* lysate or with SigE-His₆, a *Salmonella typhimurium* protein that is similar in size and charge to Pup (16). Thus, Pup specifically and noncovalently interacted with Mpa in an *E. coli* lysate under native conditions.

Additional genetic and biochemical experiments with *E. coli* to test for interactions between Pup and other *Mtb* proteasome components were unsuccessful. Thus, we hypothesized that *E. coli* lacked cofactors that were necessary to promote certain *Mtb* protein-protein interactions. We therefore used a mycobacterial protein fragment complementation assay (17) to test for interactions between various *Mtb* proteasome components and substrates in *Mycobacterium smegmatis* (*Msm*). Surprisingly, we observed a strong positive interaction between Pup and the proteasome substrate FabD [malonyl coenzyme A acyl carrier protein] (Fig. 1C). To confirm the interaction, we expressed constructs encoding FLAG-FabD and His₆-Pup in *Msm*. Antibodies to FLAG (anti-FLAG) de-

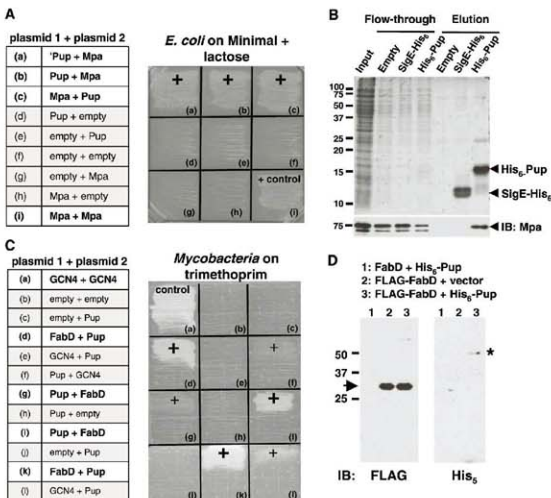
TECTED purified FLAG-FabD at the predicted size of ~30 kD (Fig. 1D). Unexpectedly, His₆-specific antibodies detected a purified ~45-kD species when FLAG-FabD and His₆-Pup were coproduced in mycobacteria (Fig. 1D). We also observed the ~45-kD band upon a longer exposure with anti-FLAG (fig. S3A). This ~45-kD complex, probably representing a Pup-FabD complex, was highly stable because it was maintained under reducing and denaturing conditions. When FLAG-FabD was purified from an *E. coli* strain making His₆-Pup, we were unable to detect the ~45-kD species (fig. S3B). Thus, Pup interacts with an *Mtb* proteasome substrate in a manner that is not supported in *E. coli*, and requires *Mycobacterium*-specific factors.

The formation of a stable complex between our model substrate FabD and Pup was reminiscent of the covalent attachment of ubiquitin to proteasome substrates in eukaryotes. Sequence and structural prediction comparisons between Pup and ubiquitin showed no overall homology. However, we noticed conservation of either of the basic amino acids arginine (Arg) or Lys, followed by two glycines (Gly) at the C terminus (Fig. 2A). This di-Gly motif is conserved in most members of the ubiquitin-like protein family, and is usually followed by one or more amino acids [reviewed in (18)]. The C termini of Ubls are generally processed to expose the di-Gly and

¹Department of Microbiology, New York University School of Medicine, New York, NY 10016, USA. ²Department of Cell Biology, Harvard Medical School, Boston, MA 02115, USA.

*To whom correspondence should be addressed. E-mail: heran.darwin@med.nyu.edu

Fig. 1. Pup interacts with the ATPase Mpa and the proteasome substrate FabD. (A) Mpa interacted with Pup in an *E. coli* two-hybrid system. *E. coli* (*cya*) was transformed with combinations of plasmids encoding either of the two domains of *Bordetella pertussis* Cya, T25 ("plasmid 1") or T18 ("plasmid 2"), fused to test proteins (for plasmid details, see fig. S1A and table S1). 'Pup' represents the 26-amino acid fragment identified from an *Mtb* genomic T25 library with T18C-Mpa as bait (a). Interactions that reconstituted functional Cya permitted growth on minimal lactose agar ("+"). All strains grew on minimal glucose agar (fig. S1A). (B) Mpa interacted with Pup in vitro. His₆-Pup, SigE-His₆, or *E. coli* "vector only" lysate on Ni-NTA agarose was incubated with recombinant Mpa ("input"). Fractions were separated by 15% SDS-polyacrylamide gel electrophoresis (PAGE) and visualized with Coomassie Brilliant Blue (CBB). The same samples were analyzed by anti-Mpa immunoblot (IB, below). (C) Pup interacted with FabD in an *Msm* two-hybrid system. *Msm* was transformed with combinations of plasmids encoding either of the two domains of murine dihydrofolate reductase, F(1,2) ("plasmid 1") or F(3) ("plasmid 2"), fused to Pup, FabD, GCN4 (a *Saccharomyces cerevisiae* leucine zipper domain), or no other protein for plasmid details, see fig. S1B and table S1. Positive interactions permitted growth on trimethoprim (Trim) ("+"). Pup had weak interactions with GCN4 (f, g). All strains grew on media lacking Trim (fig. S1B). (D) Pup formed a stable complex with FabD in *Msm*. FLAG-tagged proteins were enriched from equal amounts of lysates of *Msm* with plasmids encoding FLAG-FabD and either empty vector or His₆-Pup. Untagged FabD was the negative control. Samples were separated by 12% SDS-PAGE, and analyzed by anti-FLAG or anti-His₆ immunoblotting. FLAG-FabD migrated at the predicted size (arrow, left) and at a higher molecular size (fig. S3A); the ~45-kD anti-His₆-reactive protein (asterisk, right) is only seen in mycobacteria producing FLAG-FabD and His₆-Pup.



K173A-His₆ from WT *Msm*. The K173A mutant was markedly more stable than WT FabD (Fig. 4, A and B), providing further evidence that pupylation is a signal for degradation. We then purified radiolabeled His₆-pupylated proteins from WT and *mpa*-deficient *Msm* and observed the disappearance of these proteins over time in WT but not *mpa*-deficient bacteria

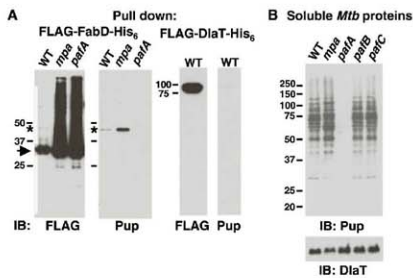
(Fig. 4C and fig. S7). Thus, Pup covalently conjugates to a specific Lys of an *Mtb* proteasome substrate, and pupylated proteins are degraded in an *Mpa*/proteasome-dependent manner (fig. S8).

There are similarities between the ubiquitin and Pup systems, but there are also notable differences. Unique aspects of pupylation may include the mechanism of Pup activation and

conjugation to substrates, the chemistry involved in the linkage of Pup to Lys, and the involvement of PafA. We speculate that PafA plays a part in conjugating Pup to substrates, but this idea requires further investigation. Additionally, it remains to be determined if proteins can be poly-pupylated in *Mtb*.

Aside from a role in protein degradation, Pup and other small protein modifiers may have important implications for other cellular processes in bacteria. Considering the multitude of activities coordinated by ubiquitylation or SUMOylation in eukaryotes (19, 21), prokaryotes may also use posttranslational protein modifiers for functions ranging from subcellular sorting to secretion.

Fig. 3. Pupylation is associated with *Mtb* proteasome substrates. (A) Aberrant amounts of pupylation correlated with proteasome-defective states. Equal amounts of soluble *Mtb* lysates from WT, *mpa* and *paqA* strains were incubated with Ni-NTA agarose for enrichment of FLAG-FabD-His₆. Samples were deliberately overloaded to detect pupylated protein and observe the relative amounts of unpupylated versus pupylated FabD. Anti-FLAG immunoblots of Ni-NTA eluates detected both unpupylated (arrow) and pupylated (asterisk) FLAG-FabD-His₆. Anti-Pup immunoblots of the same samples detected Pup-FLAG-FabD-His₆ (asterisk) in WT and *mpa* *Mtb* but not in the *paqA* strain. As a control, FLAG-DiaT-His₆ was purified from WT *Mtb*. Anti-FLAG immunoblots detected a protein at the predicted size of FLAG-DiaT-His₆, but no pupylated species was detected. Ponceau S staining shows that protein is present on this membrane (fig. S6B). (B) Multiple pupylated proteins were present in *Mtb*, but not in a *paqA* mutant. Anti-Pup immunoblots of *Mtb* lysates from WT, *mpa*, *paqA*, *paqB*, and *paqC* strains. Equivalent cell numbers were analyzed and the same blot was used for detection of endogenous DiaT. All samples were separated by 10% SDS-PAGE.



References and Notes

1. N. Benaroudj, P. Zwick, E. Seemüller, W. Baumeister, A. L. Goldberg, *Mol. Cell* **11**, 69 (2003).
2. M. Gröll et al., *Nature* **386**, 463 (1997).
3. G. Hu et al., *Mol. Microbiol.* **59**, 1417 (2006).
4. G. Lin et al., *Mol. Microbiol.* **59**, 1405 (2006).
5. M. Unno et al., *Structure* **10**, 609 (2002).
6. W. Baumeister, J. Walz, F. Zühl, E. Seemüller, *Cell* **92**, 367 (1998).
7. M. J. Pearce et al., *EMBO J.* **25**, 5423 (2006).
8. A. Herlihy, A. Chechiner, *Annu. Rev. Biochem.* **67**, 425 (1998).
9. G. Karimova, J. Pidoux, A. Ullmann, D. Ladant, *Proc. Natl. Acad. Sci. U.S.A.* **95**, 5752 (1998).
10. Materials and methods are available as supporting material on Science Online.
11. N. Knäuper, T. E. Shaver, *Mol. Microbiol.* **25**, 375 (1997).
12. T. Tamura et al., *Curr. Biol.* **5**, 766 (1995).
13. S. F. Abtschul et al., *Nucleic Acids Res.* **25**, 3389 (1997).
14. R. Mahajan, C. Delphin, T. Guan, L. Gerace, F. Melchior, *Cell* **88**, 97 (1997).
15. M. J. Matunis, E. Coutavas, G. Blobel, *J. Cell Biol.* **135**, 1457 (1996).
16. K. H. Darwin, L. S. Robinson, V. L. Miller, *J. Bacteriol.* **183**, 1452 (2001).
17. A. Singh, D. Mai, A. Kumar, A. J. Steyn, *Proc. Natl. Acad. Sci. U.S.A.* **103**, 11346 (2006).
18. M. Hochstrasser, *Nat. Cell Biol.* **2**, E153 (2000).
19. O. Kerscher, R. Felberbaum, M. Hochstrasser, *Annu. Rev. Cell Dev. Biol.* **22**, 159 (2006).
20. D. S. Kikpatrick, C. Denison, S. P. Gygi, *Nat. Cell Biol.* **7**, 750 (2005).
21. R. Geiss-Friedlander, F. Melchior, *Nat. Rev. Mol. Cell Biol.* **8**, 947 (2007).
22. R. A. Festa, M. J. Pearce, K. H. Darwin, *J. Bacteriol.* **189**, 3044 (2007).
23. R. Chenna et al., *Nucleic Acids Res.* **31**, 3497 (2003).
24. We thank S. Eht, D. Ladant, V. Miller, and A. Steyn for plasmids used in this study. We are grateful to C. Arias and C. Perez for advice on pulse-labeling experiments and to T. Huang, I. Mohr, and M. Pagano for helpful discussions. We thank A. Darwin and M. Pagano for critical review of this manuscript. This work was supported by NIH grants AI065437 and HL092774 (to K.H.D.) and GM67945, HG3456, and HG3616 (to S.P.G.). M.J.P. was supported by grant 5732A07189-25.

Supporting Online Material

www.sciencemag.org/cgi/content/full/271.6388B/DC1

Materials and Methods

Figs. S1 to S8

Table S1

28 July 2008; accepted 16 September 2008

Published online 2 October 2008;

10.1126/science.1163885

Include this information when citing this paper.

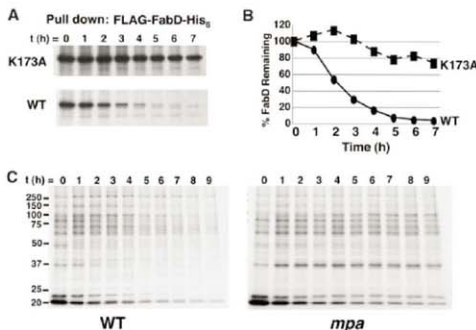


Fig. 4. Pupylation is required for *Mpa*-dependent protein degradation. (A) K173A mutation stabilized FabD. WT *Msm* expressing *YfabD* or *YfabD* with the K173 codon mutated to alanine was pulse labeled with ³⁵S-methionine and cysteine. Samples were collected over time and FLAG-FabD-His₆ (WT or K173A mutant) was purified and analyzed by 10% SDS-PAGE (10). This image represents a 12-hour exposure. A 6-hour exposure of the same gel is shown in fig. S7A. Immunoblot analysis showed that the K173A mutant was also not efficiently pupylated (fig. S7B). (B) Quantification of labeled protein in (A). (C) Pupylated proteins were degraded in an *Mpa*-dependent manner. WT and *mpa* mutant *Msm* were treated as in (A) and His₆-pupylated proteins were purified and analyzed. Total ³⁵S protein labeling is shown in fig. S7C. All data are representative of at least two independent experiments.

Genome of an Endosymbiont Coupling N₂ Fixation to Cellulolysis Within Protist Cells in Termite Gut

Yuichi Hongoh,^{1*†} Vineet K. Sharma,^{2,3*} Tulika Prakash,^{2,3} Satoko Noda,¹
Hidehiro Toh,^{2,3} Todd D. Taylor,^{2,3} Toshiaki Kudo,^{1‡} Yoshiyuki Sakaki,^{2,§}
Atsushi Toyoda,^{2,4†} Masahira Hattori,^{2,5} Moriya Ohkuma¹

Termites harbor diverse symbiotic gut microorganisms, the majority of which are as yet uncultivable and their interrelationships unclear. Here, we present the complete genome sequence of the uncultured Bacteroidales endosymbiont of the cellulolytic protist *Pseudotriconympha grassii*, which accounts for 70% of the bacterial cells in the gut of the termite *Coptotermes formosanus*. Functional annotation of the chromosome (1,114,206 base pairs) unveiled its ability to fix dinitrogen and recycle putative host nitrogen wastes for biosynthesis of diverse amino acids and cofactors, and import glucose and xylose as energy and carbon sources. Thus, nitrogen fixation and cellulolysis are coupled within the protist's cells. This highly evolved symbiotic system probably underlies the ability of the worldwide pest termites *Coptotermes* to use wood as their sole food.

The Formosan subterranean termite *Coptotermes formosanus* is one of the most destructive species, causing severe economic damage in temperate and subtropical regions worldwide (1). *C. formosanus* annually costs residents about 1 billion dollars in the United States (2) and several hundred million dollars in Japan (3). Termites are keystone animals in the global carbon cycle (4), and their ability to digest lignocellulose is being explored to promote the development of novel biofuels from woody biomass (5). The mechanism underlying the ability of the termites to thrive solely on such a recalcitrant and nitrogen-poor food source as wood remains unclear. Although this capacity has long been attributed to the termite's symbionts, the interrelationships are complex and the organisms resistant to available culture techniques (6, 7).

Hence, we attempted to acquire the complete genome sequence of a prokaryote belonging to the order Bacteroidales, and called phylogroup CfPt1-2, which lives specifically within the cells of the uncultivable, cellulolytic protist *Pseudotriconympha grassii* found in the gut of *C. formosanus* (8) (fig. S1). About 1×10^5 CfPt1-2 cells are housed within a single *P. grassii* cell, contributing, in total, 70% of the bacterial

cells in the gut of *C. formosanus* (8). The parabasalid host *P. grassii* is the most important and indispensable protist species and is essential for the degradation of wood particles in the gut of *C. formosanus* (9). *Pseudotriconympha* species harboring the Bacteroidales endosymbionts are widely distributed among diverse subterranean termites (family Rhinotermitidae) (10) (fig. S2). Thus, elucidation of the metabolic functions of CfPt1-2 is crucial for understanding the symbiotic mechanism in *C. formosanus* and other subterranean termites.

A single cell of *P. grassii* was physically isolated from the gut microbiota, and 10^3 to 10^4 cells of its endosymbionts were collected by rupturing the host membrane in buffer (11). The collected cells were subjected to isothermal whole-genome amplification for sequence analysis. From the amplified sample, a single circular 1,114,206-base pair (bp) chromosome was unambiguously reconstructed (fig. S3). The chromosome contains 758 putative protein-coding sequences (CDSs), 38 transfer RNA genes, and 4 ribosomal RNA genes (table S1 and S2). The rRNA genes do not constitute an operon, and a region containing the 16S rRNA gene and tRNA^{Ile} gene has been duplicated (12). Phylogenetic analysis based on concatenated sequences of ribosomal proteins confirmed that this bacterium belongs to the order Bacteroidales (fig. S4).

Additionally, four circular plasmids were reconstructed (table S1 and fig. S5). Three of the four showed synteny with each other (fig. S6), as well as with the chromosome region 974,000 to 1,042,400 (fig. S7) (12). This 68.4-kb-long chromosome region contains three to four duplications of the plasmid-derived sequences. These insertions and duplications imply active rearrangements in this genome. Genes involved in DNA repair and recombination are relatively abundant compared with other known intracellular symbionts (table S3).

The predicted metabolic pathways of CfPt1-2 are shown in Fig. 1. The most striking feature of this bacterium that we uncovered in this study was its ability to fix dinitrogen. The genes encoding nitrogenase (NifHDK), Mo-Fe cofactor biosynthesis proteins, *nif*-operon regulator NifA, and Mo²⁺-transporter, all of which are essential for N₂ fixation, were identified on the chromosome (table S4 and fig. S8). Although N₂-fixing activity has been demonstrated in diverse termites, including *C. formosanus* (13, 14), the discovery of the requisite genes in a member of the Bacteroidetes was unexpected, because there have been no previous reports of nitrogenase genes in this phylum.

The *nifH* gene of CfPt1-2 was phylogenetically affiliated with a cluster of clones previously obtained from termite guts (14, 15) (fig. S9). It showed only low sequence similarity to the *nifH* genes of any known bacterial species, including the N₂-fixing spirochetes isolated from termite guts (16). The expression of the *nifH* gene of CfPt1-2 in the gut was confirmed by reverse-transcription polymerase chain reaction using universal primers for *nifH*. Ninety of 91 sequenced clones were identical or nearly identical to CfPt1-2 *nifH*, which suggests that this bacterium is the principal N₂-fixer in *C. formosanus* gut (12). A genus and species, "*Candidatus* Azobacteroides pseudotriconymphae," is proposed here for the CfPt1-2 bacterium (12).

In CfPt1-2, the predicted pathways suggest that the fixed nitrogen, in the form of NH₃, is assimilated initially by the activity of glutamine synthetase and then used for biosynthesis of diverse amino acids and cofactors (Fig. 1). This bacterium also possesses a gene encoding an ammonium transporter and a gene cluster encoding urease and a urea transporter. The orthologs of the latter genes have never previously been found in the Bacteroidales order. The ability to import and assimilate ammonium and urea implies that CfPt1-2 not only fixes atmospheric nitrogen but also recycles the putative nitrogen waste products of parabasalid protists (17). The amount of nitrogen in the diet alters the N₂-fixation activity of *C. formosanus* (13), possibly because CfPt1-2 can repress N₂ fixation and recycle urea and ammonia when these are abundant in the host cytoplasm. N₂ fixation requires a large amount of energy and thus its regulation is important.

CfPt1-2 possesses genes for using monosaccharides derived from lignocellulose, that is, glucose, xylose, and hexuronates, which are likely to be abundant in the cytoplasm of the cellulolytic host protist. In addition, the genome encodes enzymes involved in a glycogen cycle for storing carbohydrates. Thus, CfPt1-2 is unlikely to experience energy and carbon starvation unless the termite host itself is starved. CfPt1-2 retains a glycolytic pathway, and energy production is achieved through fermentation of sugars to acetate and by fumarate respiration (Fig. 1). Because the genome lacks genes for

¹Ecomolecular Biorecycling Science Research Team, RIKEN Advanced Science Institute, Saitama 351-0198, Japan.
²RIKEN Genomic Sciences Center, Kanagawa 230-0045, Japan.
³MetaSystems Research Team, RIKEN Advanced Science Institute, Kanagawa 230-0045, Japan.
⁴Comparative Genomics Laboratory, National Institute of Genetics, Shizuoka 411-8540, Japan.
⁵Department of Computational Biology, Graduate School of Frontier Sciences, University of Tokyo, Chiba 277-8561, Japan.

*These authors contributed equally to this work.

†To whom correspondence should be addressed. E-mail: yhongoh@riken.jp; atoyoda@lab.nig.ac.jp

‡Present address: Faculty of Fisheries, Nagasaki University, Nagasaki 852-8521, Japan.

§Present address: Toyohashi University of Technology, Aichi 441-8580, Japan.

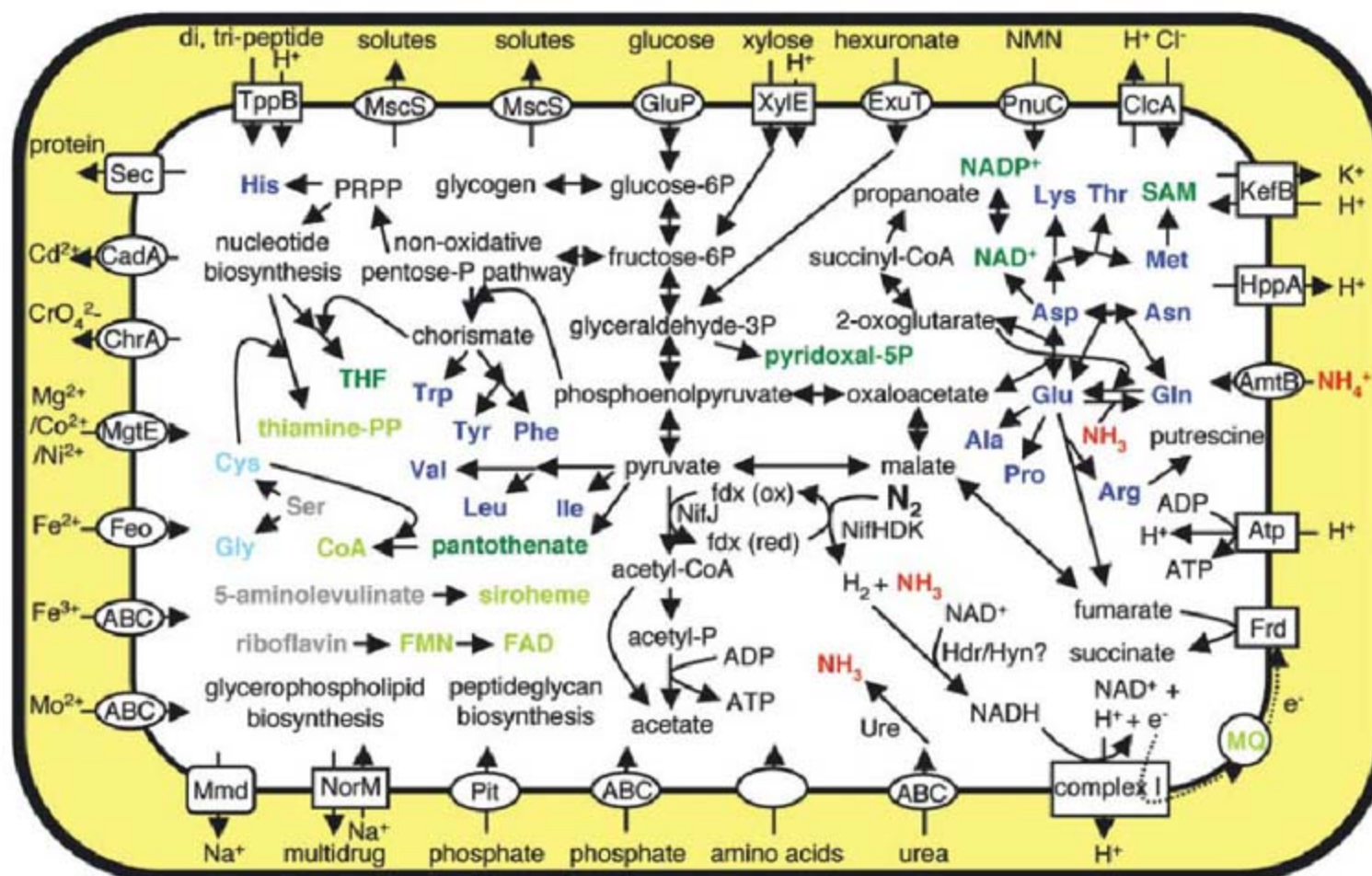


Fig. 1. Predicted metabolic pathways of phylotype CfPt1-2. Blue, synthesized amino acids; green, cofactors. Amino acids and cofactors that can be synthesized from imported precursors are shown in pale colors. The genome

encodes pathways for biosynthesis of 19 amino acids. Compounds that should be imported are shown in gray. Provision of menaquinone (MQ) or its precursor 1,4-dihydroxy-2-naphthoate is probably required for fumarate respiration.

catalase, superoxide dismutase, and cytochrome oxidase, CfPt1-2 is strictly anaerobic and cannot use O_2 as an electron acceptor.

Interestingly, this bacterium is known to take up hydrogen (18), although no typical hydrogenase gene exists in its genome. The candidates for this function form a cluster of seven genes, including homologs of heterodisulfide reductase and hydrogenase-like components (fig. S10). Molecular H_2 is abundantly produced during both lignocellulose fermentation and N_2 fixation, and is an ideal alternative energy source. Moreover, the removal of excess H_2 theoretically promotes both lignocellulose fermentation and N_2 fixation (fig. S11).

Comparison of the CfPt1-2 genome with those of other known Bacteroidales show that its guanine/cytosine content and CDS density are lower, the number of pseudogenes is larger, and its genome size is smaller (table S5). Although genes involved in nitrogen metabolism have been abundantly retained, CfPt1-2 has no genes encoding extracellular glycosylhydrolases, has few genes for biosynthesis of lipopolysaccharide for a cell wall, and possesses only a few regulatory genes. All of these genes are numerous in Bacteroidales human gut symbionts such as *Bacteroides thetaiotaomicron* (19). Although the profile of orthologous groups of CfPt1-2 proteins greatly differs from those of other Bacteroidales, it is strikingly similar to that of phylotype Rs-D17 in the candidate phylum Termite Group 1 (TG1), a bacterial endosymbiont of the cellulolytic protist

Trichonympha agilis found in the gut of the termite *Reticulitermes speratus* (20) (fig. S12). The TG1 endosymbiont also has a reduced and streamlined genome specialized for biosynthesis of amino acids and cofactors (20), but unlike CfPt1-2, TG1 cannot fix N_2 .

Endosymbionts of cellulolytic protists are probably required by their protist hosts for the biosynthesis of nitrogen compounds that are deficient in woody materials. The cellulolytic protist with its N_2 -fixing endosymbionts, in turn, enables highly efficient growth of the host termite and its colony without being limited by nitrogen deficiency. The combined metabolic capacity of these organisms has allowed termites to take advantage of a nutrient-limited resource to humankind's detriment.

References and Notes

- N. Y. Su, *Sociobiology* **41**, 7 (2003).
- A. R. Lax, W. L. A. Osbrink, *Pest Manag. Sci.* **59**, 788 (2003).
- K. Tsunoda, *Sociobiology* **41**, 27 (2003).
- A. Sugimoto, D. E. Bignell, J. Macdonald, in *Termites: Evolution, Sociality, Symbioses, Ecology*, T. Abe, D. E. Bignell, M. Higashi, Eds. (Kluwer Academic Publishers, Netherlands, 2000), pp. 409–436.
- F. Warnecke *et al.*, *Nature* **450**, 560 (2007).
- M. Ohkuma, *Trends Microbiol.* **16**, 345 (2008).
- N. Shinzato, M. Muramatsu, T. Matsui, Y. Watanabe, *Biosci. Biotechnol. Biochem.* **69**, 1145 (2005).
- S. Noda *et al.*, *Appl. Environ. Microbiol.* **71**, 8811 (2005).
- T. Yoshimura, *Wood Res.* **82**, 68 (1995).
- S. Noda *et al.*, *Mol. Ecol.* **16**, 1257 (2007).
- Materials and methods are available as supporting material on Science Online.
- See SOM Text.

- J. A. Breznak, W. J. Brill, J. W. Mertins, H. C. Coppel, *Nature* **244**, 577 (1973).
- M. Ohkuma, S. Noda, T. Kudo, *Appl. Environ. Microbiol.* **65**, 4926 (1999).
- S. Noda, M. Ohkuma, T. Kudo, *Microbes Environ.* **17**, 139 (2002).
- T. G. Lilburn *et al.*, *Science* **292**, 2495 (2001).
- J. M. Carlton *et al.*, *Science* **315**, 207 (2007).
- J. Inoue, K. Saita, T. Kudo, S. Ui, M. Ohkuma, *Eukaryot. Cell* **6**, 1925 (2007).
- J. Xu *et al.*, *PLoS Biol.* **5**, e156 (2007).
- Y. Hongoh *et al.*, *Proc. Natl. Acad. Sci. U.S.A.* **105**, 5555 (2008).
- We are grateful to all the technical staff of the Sequence Technology Team at RIKEN Genomic Sciences Center (GSC) and the Ecomolecular Biorecycling Science Research Team for their assistance. This work was supported in part by a grant for the President's Discretionary Fund of RIKEN; a Special Fund for RIKEN GSC; grants for the Bioarchitect Research Program and the Eco Molecular Science Research Program from RIKEN; a Discovery Research Institute Research Grant to Y.H. from RIKEN; a Grant-in-Aid for Scientific Research on Priority Areas "Comprehensive Genomics" from the Ministry of Education, Culture, Sports, Science, and Technology of Japan to M.H.; and a Grant-in-Aid for Scientific Research from Japan Society for the Promotion of Science to Y.H. and M.O. The authors declare no competing financial interests. The sequence data have been deposited in GenBank/DBJ/EMBL under accession numbers AP010656–60.

Supporting Online Material

www.sciencemag.org/cgi/content/full/322/5904/1108/DC1
Materials and Methods
SOM Text
Figs. S1 to S12
Tables S1 to S7
References

5 September 2008; accepted 8 October 2008
10.1126/science.1165578

Globally Distributed Uncultivated Oceanic N₂-Fixing Cyanobacteria Lack Oxygenic Photosystem II

Jonathan P. Zehr,^{1*} Shellie R. Bench,¹ Brandon J. Carter,¹ Ian Hewson,¹ Faheem Niazi,² Tuo Shi,¹ H. James Tripp,¹ Jason P. Affourtit²

Biological nitrogen (N₂) fixation is important in controlling biological productivity and carbon flux in the oceans. Unicellular N₂-fixing cyanobacteria have only recently been discovered and are widely distributed in tropical and subtropical seas. Metagenomic analysis of flow cytometry–sorted cells shows that unicellular N₂-fixing cyanobacteria in “group A” (UCYN-A) lack genes for the oxygen-evolving photosystem II and for carbon fixation, which has implications for oceanic carbon and nitrogen cycling and raises questions regarding the evolution of photosynthesis and N₂ fixation on Earth.

Biological N₂ fixation (BNF) is catalyzed by the enzyme nitrogenase, which is present in diverse Bacteria and Archaea (1). Marine BNF is particularly important in the oligotrophic open-ocean gyres, where nitrogen (N) inputs to stratified surface waters are stoichiometrically related to photosynthetic carbon (C) fixation and the vertical export of C to the deep ocean (2). Biogeochemically based estimates of oceanic N₂ fixation rates are much higher than previously believed (2–5). Oceanic BNF was assumed to be primarily due to the filamentous cyanobacteria *Trichodesmium* (6, 7) and the symbiotic filamentous cyanobacteria *Richelia* (8, 9), until the recent discovery that oceanic unicellular cyanobacteria are impor-

tant in oceanic N₂ fixation (10, 11). The unicellular N₂-fixing cyanobacteria were initially discovered only by amplification of nitrogenase genes and gene transcripts (mRNA) from oceanic water samples (12, 13), because they cannot be detected with traditional net collection methods and microscopy as can *Trichodesmium* and *Richelia*.

One phylogenetic group of unicellular N₂-fixing cyanobacterial nitrogenase gene sequences (“group A” or UCYN-A *nifH*) (13) is most closely related to sequences from the marine unicellular cyanobacterium *Cyanothece* sp. strain ATCC 51142, a marine strain isolated from an intertidal habitat, and to those of the unicellular cyanobacterial symbiont of the diatom *Rhopalodia gibba* (14). UCYN-A *nifH* gene sequences have been reported from the Atlantic and Pacific Oceans (15), but UCYN-A cyanobacteria have not been successfully cultivated despite repeated attempts. These microorganisms express nitrogenase genes with maximum transcript abundances

during the light period (11, 16). The daytime expression of nitrogenase presents an enigma, because the enzyme is inactivated by oxygen evolved during photosynthesis. Most cyanobacteria use temporal or spatial separation of photosynthesis and N₂ fixation to prevent nitrogenase inactivation (17). However, we found that UCYN-A cyanobacteria have a genotype not previously known in free-living cyanobacteria and are genetically incapable of oxygenic photosynthesis, which also explains why they can fix N₂ during daylight.

We initially assumed that the UCYN-A cyanobacteria would have cell diameters of 2 to 8 μm, similar to those of typical coastal (*Cyanothece*) and oceanic (*Crocospaera watsonii*, UCYN-B) cyanobacteria (18), but discovered that the UCYN-A cells were less than 1 μm in diameter (19). Natural populations of UCYN-A cells could not be completely separated from other small phototrophic and heterotrophic populations by flow cytometry (FCM), but highly enriched cell sorts were obtained by screening cells sorted by fluorescence-activated cell sorting (FACS) for UCYN-A *nifH* genes with a quantitative real-time fluorescence polymerase chain reaction (QPCR) assay, Real-Time TaqMan (16, 20). We refined sort parameters (fig. S1) from those we previously used (19) to sort natural populations of UCYN-A cells from numerous North and South Pacific Ocean water samples (Fig. 1). We found that the populations are widely distributed, which indicated that our sorting strategy for UCYN-A cells was robust (table S2).

Amplification of 16S ribosomal RNA (rRNA) genes from the sorted cells, using PCR with universal 16S rRNA primers, showed that the sorted population contained some noncyanobacterial Bacteria (such as *Pelagibacter ubique*) and non-N₂-fixing cyanobacteria (*Prochlorococcus* and *Synechococcus*) in addition to the UCYN-A cyanobacteria (table S1). The per-

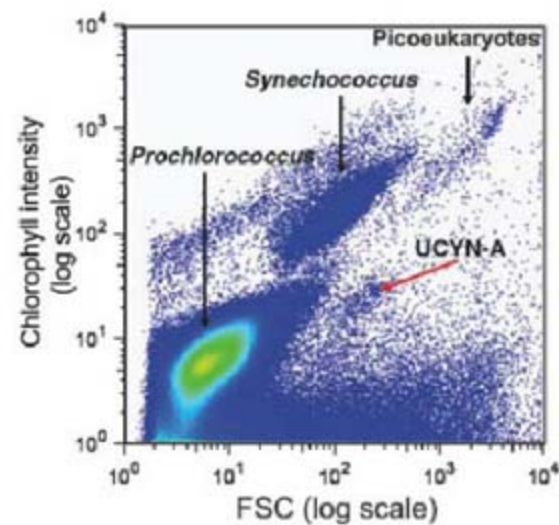


Fig. 1. Cytogram of the forward scatter (x axis) and chlorophyll fluorescence (y axis) profile from concentrated water samples collected from a depth of 15 m at Station ALOHA (North Pacific) in late January 2008. The UCYN-A population sorted for MDA genome amplification and subsequent sequencing indicated by the red arrow.

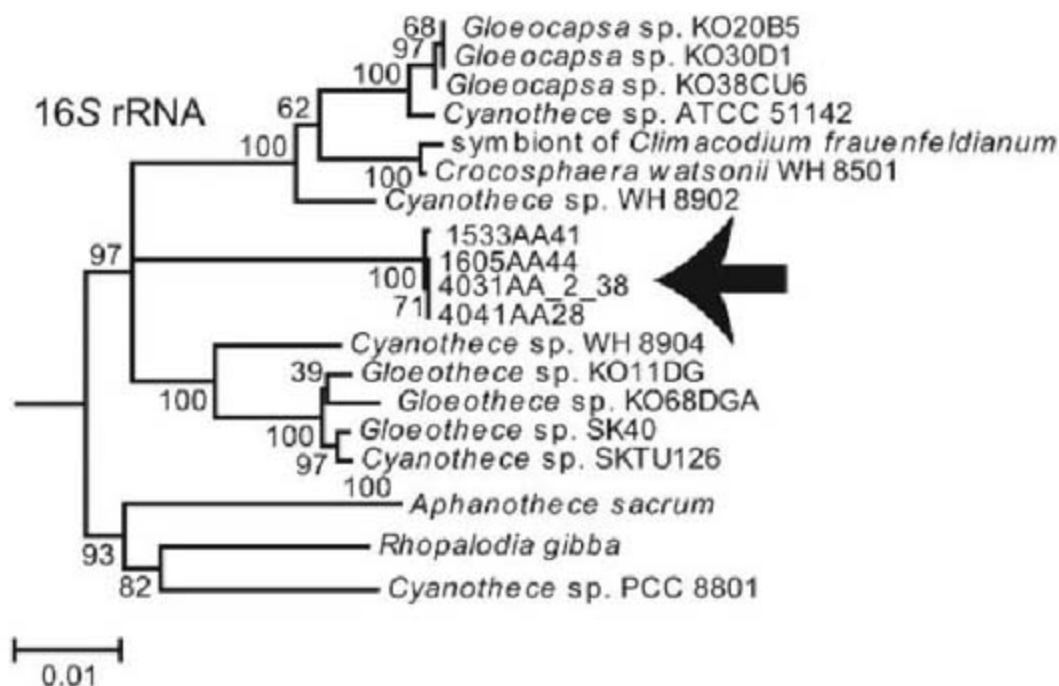


Fig. 2. Phylogenetic tree of North and South Pacific Ocean UCYN-A full-length 16S rRNA nucleotide gene sequences showing the relationship of UCYN-A to *Cyanothece* sp. ATCC 51142 and other unicellular cyanobacteria. The arrow indicates the UCYN-A group.

¹Ocean Sciences Department, University of California, Santa Cruz, 1156 High Street, Santa Cruz, CA 95064, USA.

²454 Life Sciences, 20 Commercial Street, Branford, CT 06405, USA.

*To whom correspondence should be addressed. E-mail: zehrj@ucsc.edu

centage of UCYN-A cells in the defined sort region varied depending on the source of the (tables S1 and S2).

All 16S rRNA, *nifH*, and *nifD* sequences amplified from sorted cells were consistent with the UCYN-A cells being *Cyanothece*-like unicellular N₂-fixing cyanobacteria (13) (Fig. 2 and figs. S2 and S3) even though they were much smaller. The 16S rRNA *Cyanothece*-like sequence was linked to the UCYN-A *nifH* gene by FACS-sorting single cells and multiplex gene amplification (fig. S2) of *nifH* and 16S rRNA genes from individual cells in which the positive single-cell QPCR reaction mixtures for *nifH* were used as a template for the second 16S rRNA amplification (21). Reactions that were negative for UCYN-A *nifH* were also negative for unicellular N₂-fixing cyanobacterial 16S rRNA (fig. S2).

A water sample collected from a depth of 15 m at the North Pacific Ocean long-term monitoring site Station ALOHA in late January 2008 (during Hawaii Ocean Time-series cruise HOT 199) indicated the presence of a high proportion (51%) of UCYN-A cells (Fig. 1). We used this population for metagenomic analysis, using Titanium sequencing technology from 454 Life Sciences (21). Multiple displacement amplification (MDA) (21) of DNA from approximately 5000 sorted cells was used to generate a genomic shotgun library that we estimate gave at least 10-fold genomic coverage of the 2- to 3-Mb UCYN-A genome in approximately 400,000 sequence reads (assuming that roughly one-third of the reads in the run were not UCYN-A). 177,834 sequence reads were most similar to the N₂-fixing unicellular cyanobacteria *Cyanothece* sp. ATCC 51142, *Cyanothece* sp. CCY 0110, or *C. watsonii* WH 8501, on the basis of a BLAST analysis (21), whereas only 40,593 sequences had best BLAST hits to *Prochlorococcus* proteins, and 96,341 sequences were most similar

to proteins from other microorganisms, including noncyanobacterial Bacteria. The 16S rRNA sequences also showed that the library was dominated by UCYN-A DNA sequences (Fig. 3), and they agreed with the QPCR data for UCYN-A cyanobacteria. The sequence read library represented good coverage of the UCYN-A genome because it contained the entire nitrogenase gene cluster on one assembled contig (Fig. 4) (21). The nitrogenase gene arrangement and composition were very similar to those of *Cyanothece* sp. ATCC 51142 and of the *R. gibba* symbiont (Fig. 4). Most of the proteins in the common cyanobacterial genome core (22) were identified by BLAST. Comparison of sequences to the cyanobacterial genome core (21) indicated that at least 79% of the core cyanobacterial genome had been sampled (fig. S4).

Although the core genes and all the *nif* genes were present, no candidate UCYN-A sequences were found that corresponded to C fixation, C concentration, or photosystem II (PSII) and associated pigments (such as phycoerythrin or phycobiliprotein linker). However, good coverage of candidate UCYN-A PSI genes was obtained (Fig. 5). In comparison, we had equal coverage of *Prochlorococcus* PSI and PSII genes, although they were a much smaller component of the sequence library (Fig. 5). However, we did detect a complete PSI *psaA* gene, found on one single assembled contig [5788 base pairs (bp) assembled from 948 sequence reads], followed immediately by 1857 bp of the *psaB* gene, which clustered with sequences from other unicellular N₂-fixing cyanobacteria (fig. S3). No unicellular N₂-fixing cyanobacteria phycoerythrin or phycocyanin genes (or associated linkers) were found in the metagenome, which is consistent with the observation that UCYN-A cyanobacteria were not detected by phycoerythrin fluorescence in FCM (19). Additional PCR experiments readily amplified the UCYN-A PSI

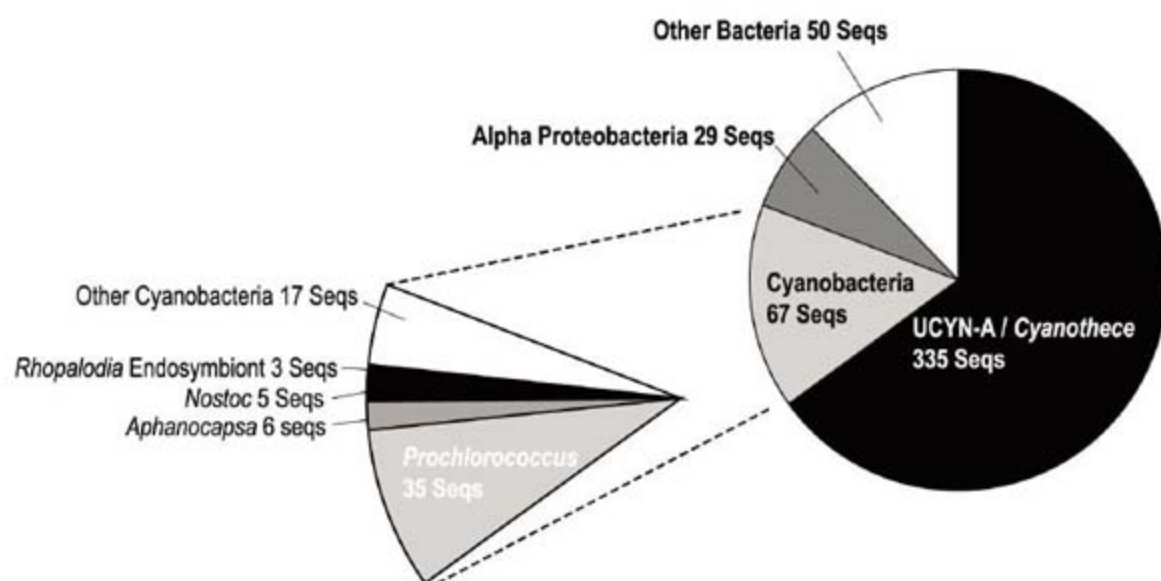


Fig. 3. Phylogenetic affiliation of 16S rRNA sequences from metagenome sequences obtained from the station ALOHA 15-m sample. Sequences matching 16S rRNA were first retrieved by comparing the metagenome reads against those of the Ribosomal Database Project. Matching sequences were then assigned phylogenetically by BLASTn comparison to the nonredundant database at the National Center for Biotechnology Information (NCBI).

genes found on the genomic contig, but no C fixation or PSII genes were obtained. We obtained further evidence that UCYN-A lack PSII genes by amplifying photosynthetically critical genes using degenerate PCR primers (21). From

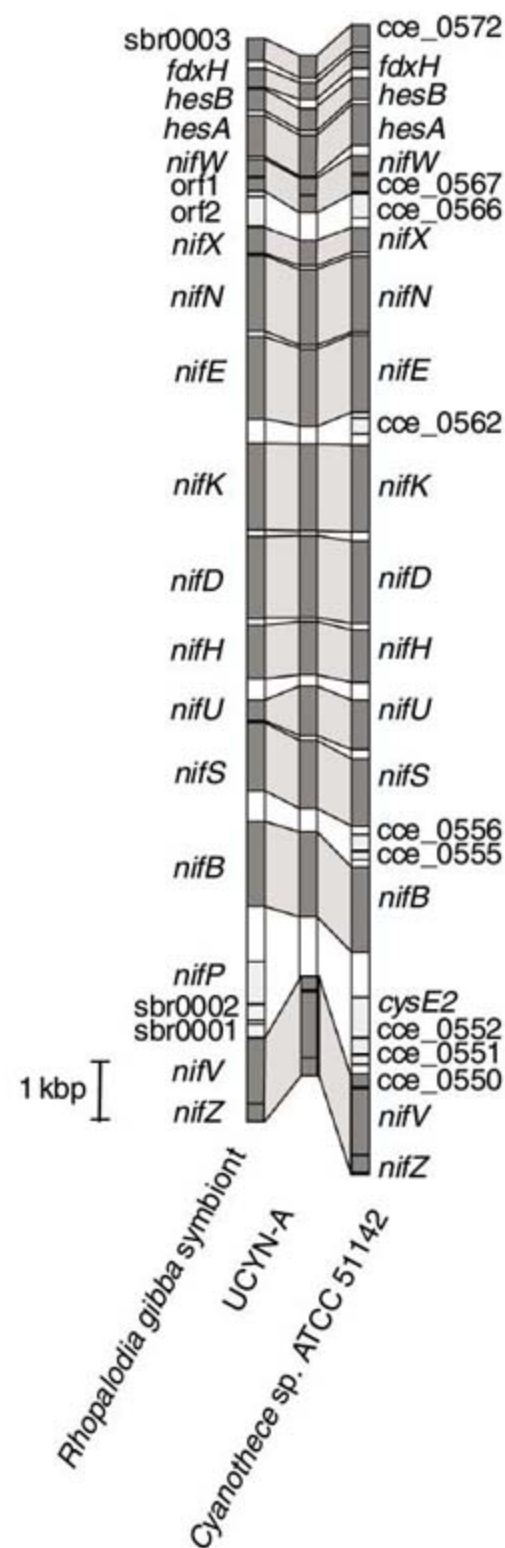


Fig. 4. Comparison of the UCYN-A *nif* gene cluster to those of *Cyanothece* sp. ATCC 51142 and the *R. gibba* symbiont. The *nif* cluster was located on a large (135,849 bp) contig assembled from 5161 sequence reads. The figure shows the synteny of approximately 23 kbp of coding sequences for the *nif* gene clusters of UCYN-A (contig 02671, NCBI accession no. FJ170277), a N₂-fixing endosymbiont of *R. gibba* (NCBI accession no. AY728387), and the circular chromosome of *Cyanothece* sp. ATCC 51142 (EMBL accession no. CP000806). Genes with full-length matches of amino acid sequence are shown in dark gray, genes with no matches are shown in light gray, and noncoding DNA is shown in white.

multiple samples of sorted cells, we successfully amplified UCYN-A *psaA* fragments with DNA sequences >98% identical to those genes found on the genomic contigs. However, attempts to amplify genes for the PSII D1 protein (*psbA*) as well as the RuBisCO large subunit yielded only sequences that were >98% identical to those of *Prochlorococcus* or >94% identical to those of *Synechococcus* species, and none that were similar to those of unicellular diazotrophs, as expected for UCYN-A sequences. The absence of any candidate UCYN-A PSII genes is clear, given the random and complete coverage of the sequencing effort, the high percentage of genome core coverage, the lack of amplification when degenerate primers were used, and the random location of photosynthesis genes in cyanobacterial genomes (23). Although it has been shown that some cyanobacteria can uncouple PSI from PSII using either organic (24) or inorganic (25) substrates as electron donors, this is the first observation of a cyanobacterium that completely lacks the PSII apparatus. This conclusion is striking because there are no reports to our knowledge of free-living cyanobacteria that are not oxygenic phototrophs.

The UCYN-A phylogeny and poor pigmentation (dim chlorophyll fluorescence) resemble those seen in observations of the *R. gibba* symbiont (14). Although the *R. gibba* symbiont sequences are no closer to UCYN-A sequences phylogenetically than to those of other cyanobacteria in the unicellular N₂-fixing cyanobacterial lineage (Fig. 2 and fig. S3), the symbiont of *R. gibba* also appears to have lost photosynthetic capabilities and pigmentation (14, 26). In the *R. gibba* symbiont, some of the PSII proteins

(*psbC* and *psbD*) have become pseudogenes (14, 26). We did not detect UCYN-A cells in association with large cells, neither in size-fractionation filtration nor by FCM, and it appears to be a free-living organism.

Our work shows that oceanic UCYN-A cyanobacteria are missing the entire PSII apparatus, although the PSI apparatus appears to be intact (Fig. 5). It is possible that UCYN-A cyanobacteria are photoheterotrophic cells that generate adenosine triphosphate with PSI and are not able to fix C by the Calvin-Benson-Basham cycle as oxygenic photoautotrophs do. It is unclear how PSI functions in the absence of PSII. The UCYN-A strain, like the *R. gibba* symbiont, fixes N₂ during the daytime, judging by its nitrogenase gene expression pattern (11). The lack of a functional PSII in the UCYN-A cells means that nitrogenase will not be poisoned by oxygen evolved from photosynthesis. The lack of oxygenic photosynthesis in UCYN-A cells has implications for C and N cycling in the oceans, as well as for the evolution of photosynthesis and N₂ fixation. UCYN-A cyanobacteria overlap in size and fluorescence characteristics with non-N₂-fixing microbial populations in the open ocean, including *Prochlorococcus*, *Synechococcus*, and other Bacteria, making them difficult to detect and quantify in the oceanic picoplankton. However, unicellular cyanobacteria may have a substantial impact on the N budget (10, 11), particularly in this case, because N₂ fixation is not linked to C fixation. It is critical to determine the global importance of N₂ fixation by this unusual photoheterotrophic cyanobacterial group in order to better constrain the global ocean N budget.

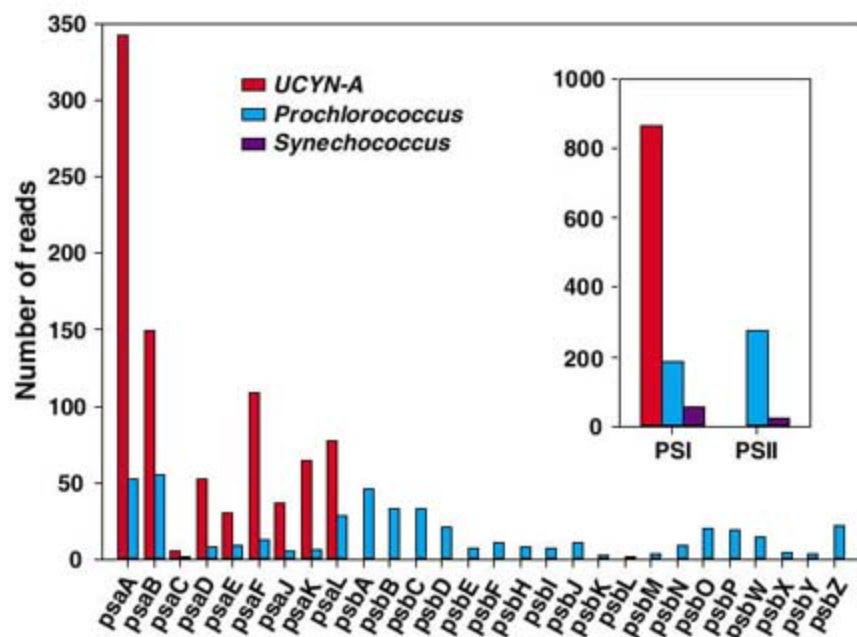


Fig. 5. Photosystem genes identified from sequencing of FACS-sorted environmental samples. The distribution of the number of sequence reads having top BLAST matches to individual photosystem genes in metagenomes of UCYN-A and *Prochlorococcus* is shown. Candidate UCYN-A photosystem sequences were identified by screening for reads having top BLAST matches to photosystem genes in *Cyanothece*, *Crocospaera watsonii* WH8501, and *Synechocystis*, which are phylogenetically related to UCYN-A and hence collectively represent a proxy of the UCYN-A metagenome. The inset shows the distribution of the total number of PSI and PSII genes identified in metagenomes of UCYN-A, *Prochlorococcus*, and marine *Synechococcus*.

References and Notes

1. J. P. W. Young, in *Genomes and Genomics of Nitrogen-Fixing Organisms*, R. Palacios, W. E. Newton, Eds. (Springer Netherlands, Dordrecht, Netherlands, 2005), vol. 3, pp. 221–241.
2. C. Mahaffey, A. F. Michaels, D. G. Capone, *Am. J. Sci.* **305**, 546 (2005).
3. D. A. Hansell, N. R. Bates, D. B. Olson, *Mar. Chem.* **84**, 243 (2004).
4. A. F. Michaels et al., *Biogeochemistry* **35**, 181 (1996).
5. N. Gruber, J. L. Sarmiento, *Global Biogeochem. Cycles* **11**, 235 (1997).
6. D. G. Capone et al., *Global Biogeochem. Cycles* **19**, GB2024 (2005).
7. J. LaRoche, E. Breitbart, *J. Sea Res.* **53**, 67 (2005).
8. E. J. Carpenter et al., *Mar. Ecol. Prog. Ser.* **185**, 273 (1999).
9. E. L. Venrick, *Limnol. Oceanogr.* **19**, 437 (1974).
10. J. P. Montoya et al., *Nature* **430**, 1027 (2004).
11. J. P. Zehr et al., *Limnol. Oceanogr.* **52**, 169 (2007).
12. J. P. Zehr et al., *Nature* **412**, 635 (2001).
13. J. P. Zehr, M. T. Mellon, S. Zani, *Appl. Environ. Microbiol.* **64**, 3444 (1998).
14. J. Precht, C. Kneip, P. Lockhart, K. Wenderoth, U. G. Maier, *Mol. Biol. Evol.* **21**, 1477 (2004).
15. L. I. Falcón, F. Cipriano, A. Y. Chistoserdov, E. J. Carpenter, *Appl. Environ. Microbiol.* **68**, 5760 (2002).
16. M. J. Church, C. M. Short, B. D. Jenkins, D. M. Karl, J. P. Zehr, *Appl. Environ. Microbiol.* **71**, 5362 (2005).
17. P. Fay, *Microbiol. Rev.* **56**, 340 (1992).
18. J. B. Waterbury, R. Rippka, in *Bergey's Manual of Systematic Bacteriology*, J. T. Staley, M. P. Bryant, N. Pfennig, J. G. Holt, Eds. (Williams & Wilkins, Baltimore, MD, 1989), vol. 3, pp. 1728–1729.
19. N. L. Goebel et al., *J. Phycol.* **44**, 1212 (2008).
20. M. J. Church, B. D. Jenkins, D. M. Karl, J. P. Zehr, *Aquat. Microb. Ecol.* **38**, 3 (2005).
21. Materials and methods are available as supporting material on Science Online.
22. T. Shi, P. Falkowski, *Proc. Natl. Acad. Sci. U.S.A.* **105**, 2510 (2008).
23. T. Shi, T. S. Bibby, L. Jiang, A. J. Irwin, P. Falkowski, *Mol. Biol. Evol.* **22**, 2179 (2005).
24. H. S. Misra, N. P. Khairnar, S. K. Mahajan, *J. Plant Physiol.* **160**, 33 (2003).
25. Y. Cohen, B. B. Jorgensen, N. P. Revsbech, R. Poplawski, *Appl. Environ. Microbiol.* **51**, 398 (1986).
26. C. Kneip, C. Vobeta, P. Lockhart, U. Maier, *BMC Evol. Biol.* **8**, 30 (2008).
27. We thank J. Montoya, D. Karl, M. J. Church, J. K. Doggett, the Hawaii Ocean Time-series crew, and the captain and crew of the R/V *Kilo Moana* for facilitating sample collection and analysis. We also thank E. Mondragon, P. Moisaner, M. Hogan, K. Pennebaker, R. Beinart, and the Zehr laboratory for technical support. This work was partially supported by the Gordon and Betty Moore Foundation [J.P.Z. and the Microbial Environmental Genomics: Modeling, Experimentation and Remote Sensing (MEGAMER) facility], NSF (OCE0425363) (J.P.Z.), and the NSF Center for Microbial Oceanography Research and Education (CCF424599) (J.P.Z.). Support for sequencing was provided by 454 Life Sciences, a Roche Company. The GenBank accession numbers of the sequences generated from PCR in this study are EU187504 to EU187629 and FJ189800 to FJ190047. For a complete list of GenBank accessions, please see the supporting online material (21).

Supporting Online Material

www.sciencemag.org/cgi/content/full/322/5904/1110/DC1

Materials and Methods

References

Figs. S1 to S4

Tables S1 and S2

2 September 2008; accepted 2 October 2008
10.1126/science.1165340

Arabidopsis Stomatal Initiation Is Controlled by MAPK-Mediated Regulation of the bHLH SPEECHLESS

Gregory R. Lampard,* Cora A. MacAlister,* Dominique C. Bergmann†

Stomata, epidermal structures that modulate gas exchange between plants and the atmosphere, play critical roles in primary productivity and the global climate. Positively acting transcription factors and negatively acting mitogen-activated protein kinase (MAPK) signaling control stomatal development in *Arabidopsis*; however, it is not known how the opposing activities of these regulators are integrated. We found that a unique domain in a basic helix-loop-helix (bHLH) stomatal initiating factor, SPEECHLESS, renders it a MAPK phosphorylation target *in vitro* and modulates its function *in vivo*. MAPK cascades modulate a diverse set of activities including development, cell proliferation, and response to external stresses. The coupling of MAPK signaling to SPEECHLESS activity provides cell type specificity for MAPK output while allowing the integration of multiple developmental and environmental signals into the production and spacing of stomata.

In *Arabidopsis*, stomatal fate and pattern are regulated by three closely related basic helix-loop-helix (bHLH) transcription factors—SPEECHLESS (SPCH), MUTE, and FAMA—that, in partnership with the more distantly related bHLHs ICE1/SCREAM and SCREAM2, control initiation of asymmetric divisions, proliferation of transient precursor cells, and differentiation of stomatal guard cells, respectively (Fig. S1) (1–4). Acting in opposition to these stomatal promoting factors are signaling systems that limit stomatal density and establish pattern. These negative regulators include the ERECTA (ER) family of leucine-rich repeat (LRR) receptor-like kinases (5, 6) and the LRR receptor-like protein TOO MANY MOUTHS (TMM) (7) that both may work in concert with the putative ligand EPFL1 (8). A subtilisin protease, SDD1, also negatively regulates stomatal production but may act independently of this receptor-ligand module (8, 9).

Genetic evidence places a mitogen-activated protein kinase (MAPK) signaling cascade downstream of the receptors in stomatal development (10, 11). In all eukaryotes, MAPK cascades control a diverse array of activities, including the regulation of cell division and differentiation and the coordination of responses to environmental inputs (12, 13). The MAPK components implicated in stomatal development (YODA, MKK4/5, and MPK3/6) are broadly expressed (11, 14) and are involved in multiple activities. For example, YODA is required for asymmetric cell divisions in the embryo (15), and MKK4/5 and MPK3/6 were initially characterized by their roles in stress and pathogen responses (16, 17). Because of these multiple roles, a major challenge in MAPK signaling is to understand how common signaling elements evoke specific responses. Spatially or

temporally restricted expression of MAPK substrates could provide this specificity. Developmental MAPK substrates have not been previously described in plants; however, the cell type-specific expression and activities of SPCH, MUTE, and FAMA make these proteins attractive candidates for such specificity factors. Here we show that SPCH is a substrate of MPK3 and MPK6 *in vitro*, that specific phosphorylation sites on SPCH regulate its activity *in vivo*, and that known components of the stomatal development signaling network modulate SPCH behavior.

The *SPCH* loss-of-function phenotype is strikingly similar to that caused by constitutive activa-

tion of the MAPK pathway components YODA and MKK4/5 (10, 11), and *spch* is epistatic to *yoda* (2); these results are consistent with SPCH being a downstream target of MAPKs in the epidermis. To test whether SPCH is regulated by MAPK activity, we examined the expression of transcriptional (*SPCHpro::GFP*) and translational (*SPCHpro::SPCH-GFP*) reporters (GFP, green fluorescent protein) in plants expressing constitutively active (CA) YODA (*YODApro::CA-YODA*) (11). At 5 days post-germination (dpg), both wild-type plants (20 of 20) and *YODApro::CA-YODA* plants (19 of 20) expressed *SPCHpro::GFP* (Fig. S2, A and B). Wild-type plants also expressed *SPCHpro::SPCH-GFP* (20 of 20), but *YODApro::CA-YODA* plants did not (0 of 20; Fig. S2, C and D); this result suggests that YODA does not prevent transcription of *SPCH*, but rather limits the production or abundance of SPCH protein.

Phosphorylation of transcription factors can modulate their levels and activities (18, 19). We tested whether SPCH was an *in vitro* substrate for phosphorylation by the MAPKs previously implicated in stomatal development (MPK3 and MPK6) (10). SPCH, but not its paralogs FAMA and MUTE, could be phosphorylated by both MPK3 and MPK6 (Fig. 1B and Fig. S3A). Alignment of SPCH, MUTE, and FAMA proteins reveals high sequence conservation in their bHLH domains and C termini (Fig. 1A) (2). However, SPCH also has a unique 93-amino acid domain [herein referred to as the MAPK target domain (MPKTD)] that contains 10 consensus MAPK phosphorylation target sites. Five of these sites

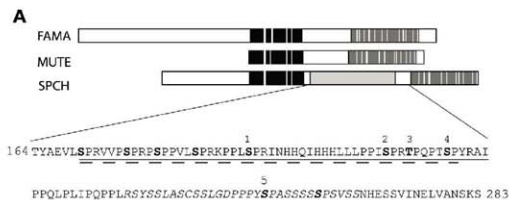


Fig. 1. SPCH is a stomatal regulator

that contains a unique MAPK phosphorylation target domain. (A) Protein alignment of SPCH, MUTE, and FAMA. Highest conservation is in the bHLH domain (black) and C terminus (dark gray). White lines within these domains indicate nonidentical residues. The sequence of the MPKTD is shown with beginning and ending amino acid residue positions. Deletions are denoted as a solid underline for Δ93, a long-dashed underline for Δ49, and a short-dashed underline for Δ31. Italics denote the predicted PEST sequence. MAPK target sites are in bold. High-stringency sites are denoted 1 (Ser¹⁰³), 2 (Ser²¹³), 3 (Thr¹¹⁵), 4 (Ser¹¹⁹), and 5 (Ser²⁵⁵). Abbreviations for amino acid residues: A, Ala; C, Cys; D, Asp; E, Glu; G, Gly; H, His; I, Ile; K, Lys; L, Leu; N, Asn; P, Pro; Q, Gln; R, Arg; S, Ser; T, Thr; V, Val; Y, Tyr. (B) *In vitro* activity of recombinant MPK3 (top) and MPK6 (bottom) on bacterially expressed SPCH variants. Lane labels indicate specific SPCH variant tested. Arrows correspond to phosphorylated SPCH and autophosphorylation of MPKs.

Department of Biology, Stanford University, Stanford, CA 94305, USA.

*These authors contributed equally to this work.

†To whom correspondence should be addressed. E-mail: ebergmann@stanford.edu

contain a Pro-X-Ser/Thr-Pro (P-X-S/T-P) motif, marking them as high-stringency sites (20) (Fig. 1A). Because SPCH differs from the nonsubstrate MUTE and FAMA proteins primarily in the MPKTD, we performed phosphorylation assays with a version of SPCH lacking the MPKTD and with the MPKTD alone. All MPK3 and MPK6 in vitro phosphorylation target sites appear to be contained within the SPCH MPKTD (Fig. 1B and fig. S3).

We then tested the functional importance of the SPCH MPKTD by using both the strong, broadly expressed 35S promoter and the endogenous SPCH promoter to express full-length SPCH and SPCHΔMPKTD variants in plants. Expression of 35S::SPCH was previously reported to induce divisions in pavement cells (2) and to produce extra stomatal lineage cells (3). 35S::SPCH expression in wild-type plants resulted in additional

divisions in pavement cells and a modest increase in total epidermal cell number (Fig. 2B), whereas expression of SPCHpro::SPCH in the wild type resulted in no significant phenotypic effects (Fig. 3). In contrast to these results with full-length SPCH, SPCHΔMPKTD variants markedly affected epidermal development. When the entire domain was deleted (35S::SPCHΔ93 or SPCHpro::SPCHΔ93), the epidermis of transformed plants exhibited large clusters of stomata (Fig. 2C and fig. S4), a phenotype similar to that produced by 35S::MUTE (2, 3). The SPCHΔ93 results are unsurprising given the strong similarity of SPCH and MUTE—particularly when the MPKTD is removed (Fig. 1A)—and in light of previous reports that overexpression of FAMA deletion variants mimics 35S::MUTE (1).

More informative were the phenotypes induced by expressing a smaller deletion that eliminates

eight target sites (four of five high-stringency sites) but leaves the fifth high-stringency site (Ser²⁵⁵) intact (SPCHΔ49, Fig. 1A) or the complementary deletion that removes the remaining target sites (SPCHΔ31, Fig. 1A). Expression of each deletion variant produced excessive numbers of asymmetric cell divisions in the epidermis, with SPCHΔ49 producing a stronger but qualitatively similar phenotype to that of SPCHΔ31 when expressed with the same promoter (Fig. 2D and fig. S4, B to D). The divisions induced by SPCHΔ49 and SPCHΔ31 were physically asymmetric and created cells with meristemoid morphology, much like the stomatal lineage-establishing divisions that SPCH promotes during normal development. To better characterize the cells produced by ectopic divisions, we monitored the expression of cell fate markers. Nearly all small, ectopic cells expressed TMMpro::TMM-GFP, a general marker of cells in the stomatal lineage (Fig. 2, E and F) (7). A smaller fraction expressed MUTEpro::GFP, a marker that is normally expressed in meristemoids just before their transition to guard mother cells (GMCs) (2). Thus, the population evidently consists of both meristemoids and other stomatal lineage cells (fig. S4H).

The division-promoting behavior of both SPCHΔ49 and SPCHΔ31 suggests that multiple residues within the MPKTD are functionally important. To define the specific residues, we repeated the in vitro and in vivo assays with SPCH variants in which the phosphorylatable S/Ts of the five high-stringency phosphorylation sites were substituted with nonphosphorylatable alanines. Each of these S/T → A variants was made as a fusion protein with yellow fluorescent protein (YFP) at the C terminus and was expressed with the SPCH promoter (21). Converting all five high-stringency MAPK target residues to alanines (SPCHpro::SPCH1-5 S/T>A) resulted in a protein that created ectopic stomata like those created by SPCHpro::SPCHΔ93 (Fig. 2G). Converting the first four sites to alanines (SPCHpro::SPCH1-4 S/T>A) resulted in ectopic division phenotypes similar to those seen with SPCHpro::SPCHΔ49 (Fig. 2H). The effect of SPCHpro::SPCH5 S/T>A, however, was much weaker than that of SPCHpro::SPCHΔ31 (Fig. 3 and fig. S4, D and E).

To test whether specific S/T residues or the overall number of S/T sites were important for SPCH regulation, we made additional combinations of S/T → A changes and assayed their ability to induce additional cell divisions. In representative lines from each variant (21), the ability to promote excess asymmetric cell division increased as more sites were eliminated (Fig. 3 and fig. S4). These results strongly suggest that multiple P-X-S/T-P sites are biologically important sites for SPCH regulation. Using mass spectrometry, we found evidence of phosphorylation at several of these functionally critical sites (fig. S5).

Elimination of MAPK target sites generated SPCH variants with greater activity, consistent with phosphorylation of the MPKTD having a repressive role. If the MPKTD is solely a negative regulatory domain, then each of the variants

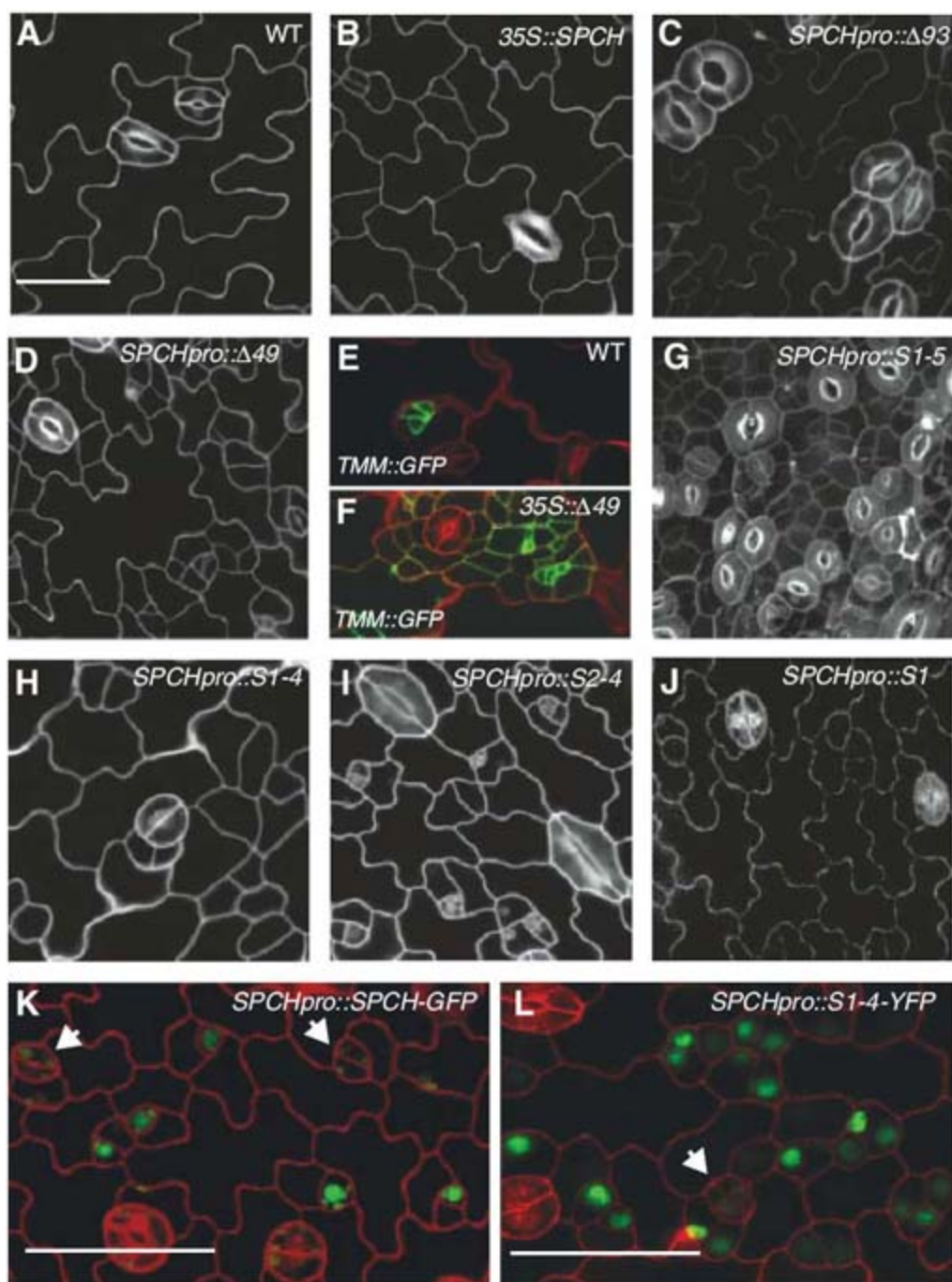


Fig. 2. Confocal images of phenotypes of SPCH variants expressed in plants. (A to D and G to J) Confocal images of 7-dpg abaxial cotyledons. Specific genotypes are noted in upper right corner of images. (E and F) Expression of TMMpro::TMM-GFP (green) in 35S::SPCHΔ49 (F) compared to wild-type (WT) control (E). (K and L) Comparison of expression pattern for full-length SPCH (K) and SPCH variant with four S/T → A substitutions (L) in abaxial leaves 1 and 2 at 11 dpg. SPCH expression in nuclei is shown in green. Note additional SPCH-expressing cells and persistence of SPCH in young guard cells (white arrow) in (L). Images in (A) to (J) are at the same magnification. Scale bars, 50 μm.

should still rescue *spch* mutant phenotypes. We assayed rescue of *spch-3* by MPKTD deletion and S/T → A variants (fig. S6); in the course of this experiment, we found it necessary to refine our criteria for rescue to include not only the production of stomata (the ultimate result of *SPCH* activity) but also the generation of physically asymmetric cell divisions (the immediate consequence of *SPCH* activity), because multiple *SPCH* variants appeared

to separate these two processes. For example, *SPCHpro::SPCH1-4 S/T>A*, *SPCHpro::SPCHΔ49*, and *35S::SPCHΔ49* did not produce stomata but did induce additional asymmetric divisions (figs. S4I and S6). It was possible to trace the failure to rescue *spch* to a single mutation (Ser¹⁹³ → Ala in *SPCHpro::SPCH1 S>A*) (fig. S6), indicating a positive role for phosphorylation in the MPKTD in addition to negative regulatory elements.

Fig. 3. Production of divisions and stomata by *SPCH* variants in the wild type. Shown are average numbers of stomata and nonstomatal cells (pavement, meristemoid, and small dividing cells) in 0.25-mm² sections of 7-dpg abaxial Col cotyledons expressing the indicated *SPCH* variant with the *SPCH* promoter. Asterisk indicates significant difference from *SPCHpro::SPCH* phenotype [joint confidence coefficient $P = 99\%$ (21)]. Error bars are \pm SE.

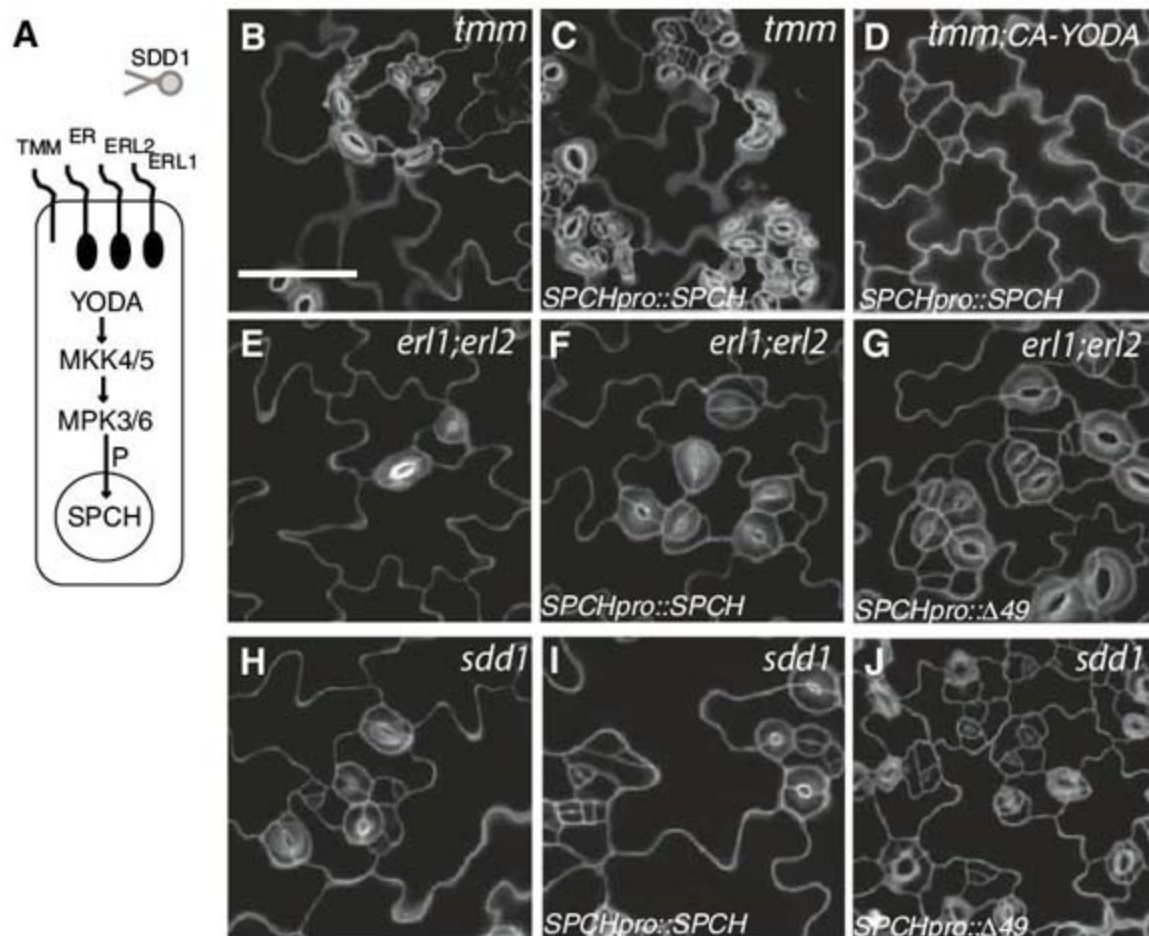
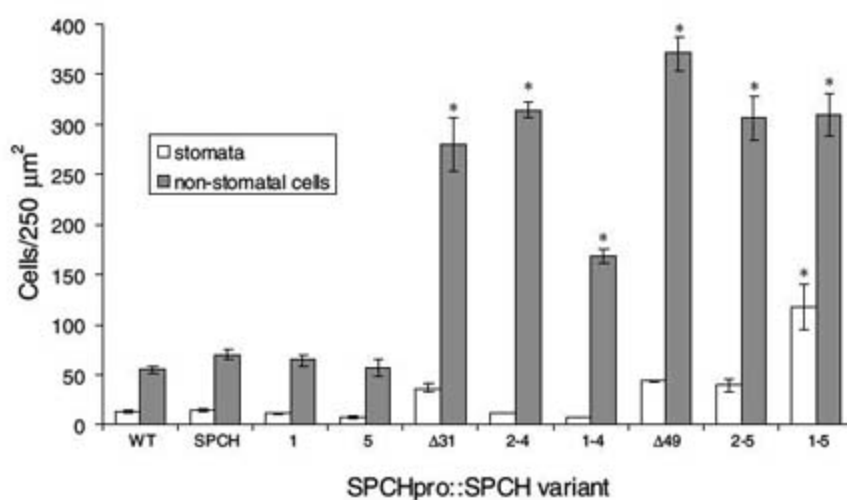


Fig. 4. Effects of endogenous stomatal regulators on *SPCH* function. (A) Scheme of known stomatal regulatory pathway (P, phosphorylation). (B to D) Suppression of *tmm-1*-mediated enhancement of *SPCHpro::SPCH* phenotypes by *CA-YODA*. (B) Baseline of *tmm-1* clustered stomata. (C) Enhanced clusters in *SPCHpro::SPCH; tmm-1*. (D) Block in excess stomatal production by *CA-YODA* in *SPCHpro::SPCH; tmm-1*. (E to G) Enhancement of *SPCH* activity in *erl1;erl2* mutant background. (E) *erl1;erl2* with no stomatal clusters, (F) *SPCHpro::SPCH; erl1;erl2*, and (G) *SPCHpro::SPCHΔ49; erl1;erl2* all result in a statistically significant increase in the stomatal density and fraction of stomata in clusters. (H to J) Lack of enhancement of *SPCH* by *sdd1*. (H) *sdd1* mutants exhibit pairing of stomata and increased density. Expression of *SPCHpro::SPCH* (I) or *SPCHpro::SPCHΔ49* (J) in *sdd1* does not enhance the *sdd1* stomatal overproduction phenotype.

Results with the S/T → A *SPCH* variants suggested that negative regulation by phosphorylation can be a mode of *SPCH* regulation. If the known stomatal regulators and MAPK components are endogenous regulators, then *SPCH* activity should be enhanced when these regulators are eliminated by mutation. Our results support this hypothesis; *SPCHpro::SPCH-GFP* expression in a *tmm-1* background yielded a massive overproduction of stomata instead of a subtle increase in epidermal cell divisions (2) (Fig. 4, B and C). This stomatal overproliferation phenotype could be suppressed by expressing *CA-YODA* in *SPCHpro::SPCH-GFP; tmm-1* plants (Fig. 4D). We further tested the effects of known stomatal regulators on *SPCH* behavior by expressing *SPCHpro::SPCH* and *SPCHpro::SPCHΔ49* in backgrounds with mutations in either *MPK3* or *MPK6* and in a double mutant of the putative upstream receptor-like kinases *ERL1* and *ERL2*. These backgrounds were specifically chosen because none has a stomatal patterning defect on its own (10, 22). In each MAPK and receptor mutant background, the phenotypic effect of *SPCH* expression was significantly enhanced relative to the wild type, consistent with these proteins being endogenous upstream regulators (Fig. 4, E to G, and fig. S7). As a control for whether the effect on *SPCH* activity was specific to MAPK-related stomatal regulators, we also expressed the variants in *sdd1*. *SDD1* is also a negative regulator of stomatal development but was recently shown to act independently of *YODA*, *TMM*, and *ER* in perception of *EPF1* (8). There was no statistically significant increase in stomatal production or clustering when *SPCHpro::SPCH* or *SPCHpro::SPCHΔ49* were expressed in *sdd1* (Fig. 4, H to J, and fig. S7, A and B). Taken together, the behavior of *SPCH* in these mutant backgrounds suggests that members of the established stomatal receptor/MAPK signaling system modulate *SPCH* activity in vivo. These results do not rule out additional regulators or MAPK pathway members being involved in *SPCH* regulation. Furthermore, although these results are consistent with *TMM*, *ER*-family receptors, and the MAPKs controlling *SPCH* activity itself, it is also possible that these proteins regulate the behavior of cells produced by *SPCH* activity.

Eliminating MAPK target sites affects *SPCH* function and subsequent stomatal development; however, these experiments do not address the mechanism by which phosphorylation affects *SPCH*. Substrates of MAPK phosphorylation are often associated with changes in localization, stability, or interaction partners (23, 24). All *SPCH* variants are constitutively nuclear (2) (Fig. 2, K and L), which suggests that *SPCH* phosphorylation does not alter its subcellular localization; however, it is possible that *SPCH* phosphorylation alters *SPCH* persistence. A structural hint of this mechanism is the presence of a predicted PEST domain [PESTfind score +7.63 (21)] in the *SPCH* MPKTD (fig. S5). Functionally, elimination of MPKTD phosphorylation sites results in excess *SPCH* protein as visualized by YFP expression.

Typically, early in leaf development, *SPCHpro::SPCH-YFP* is expressed in many small cells, but fluorescence diminishes as cells become morphologically distinct meristemoids (2) (Fig. 2K). Relative to equivalently staged *SPCHpro::SPCH-YFP* plants, *SPCH* variants with strong overproliferation phenotypes displayed increased numbers of YFP-positive cells early (Fig. 2L) and a trend toward increased protein persistence into meristemoid, GMC, and guard cell stages later (Fig. 2L and fig. S8). When expressed in a *CA-YODA* background (in which *SPCH* was predicted to be phosphorylated), full-length *SPCH-GFP* was not visible, nor could it promote stomatal development (figs. S2 and S9C). However, GFP-*SPCHΔ49*, which is missing phosphorylatable residues, was detectable and was able to drive asymmetric divisions (fig. S9D).

SPCH is closely related to two other bHLH transcription factors that control stomatal development. We have shown, however, that a novel domain of *SPCH* renders it uniquely subject to phospho-regulation by a group of kinases that have been demonstrated to transduce signals downstream of both cell-cell and plant-environment interactions (fig. S10). In general, the domain mediates repression of *SPCH* and does so in a quantitative manner; the more potential MAPK sites eliminated, the stronger the effect of the *SPCH* variant on stomatal development. However, one specific residue phosphorylated by MPK6, Ser¹⁹³, is required positively for activity, which suggests that the MPKTD is the integration site for complex regulatory inputs. The MPKTD is of unknown origin; it is not present in *Arabidopsis* proteins other than *SPCH* but is found in *SPCH*

homologs from a variety of plant species (fig. S11) (25), hence MAPK regulation of a stomatal bHLH is likely to be a widespread regulatory strategy.

SPCH solves a problem intrinsic to MAPK signaling—how is a set of generally used MAPKs recruited to a specific biological event?—by providing the important effector in a spatially and temporally restricted domain. From the perspective of stomatal control, *SPCH* guards the entry into the stomatal lineage, including the production of self-renewing cells that contribute to later flexibility in epidermal development. This important decision point is likely the target of developmental, physiological, and environmental regulation (26, 27). Coupling the MPK3/6 signaling module to the activity of *SPCH* provides a unified, yet tunable, output for the complex set of inputs from these sources. Understanding the elements of the MAPK/*SPCH* regulatory system that coordinate stomatal production with the prevailing climate may allow the production of food or bioenergy crops with the ability to respond and adapt to changes in that climate.

References and Notes

1. K. Ohashi-Ito, D. Bergmann, *Plant Cell* **18**, 2493 (2006).
2. C. A. MacAlister, K. Ohashi-Ito, D. Bergmann, *Nature* **445**, 537 (2007).
3. L. J. Pillitteri, D. Sloan, N. Bogenschutz, K. Torii, *Nature* **445**, 501 (2007).
4. M. M. Kanaoka *et al.*, *Plant Cell* **20**, 1775 (2008).
5. E. D. Shpak, J. M. McAbee, L. J. Pillitteri, K. U. Torii, *Science* **309**, 290 (2005).
6. J. Masle, S. Gilmore, G. Farquhar, *Nature* **436**, 866 (2005).
7. J. A. Nadeau, F. D. Sack, *Science* **296**, 1697 (2002).
8. K. Hara, R. Kajita, K. Torii, D. Bergmann, T. Kakimoto, *Genes Dev.* **21**, 1720 (2007).
9. D. Berger, T. Altmann, *Genes Dev.* **14**, 1119 (2000).

10. H. Wang, N. Ngwenyama, Y. Liu, J. Walker, S. Zhang, *Plant Cell* **19**, 63 (2007).
11. D. C. Bergmann, W. Lukowitz, C. R. Somerville, *Science* **304**, 1494 (2004).
12. C. Jonak, L. Okresz, L. Bogre, H. Hirt, *Curr. Opin. Plant Biol.* **5**, 415 (2002).
13. M. Karin, *Ann. N.Y. Acad. Sci.* **851**, 139 (1998).
14. H. Wang *et al.*, *Plant Cell* **20**, 602 (2008).
15. W. Lukowitz, A. Roeder, D. Parmenter, C. Somerville, *Cell* **116**, 109 (2004).
16. T. Asai *et al.*, *Nature* **415**, 977 (2002).
17. Y. Kovtun, W. Chiu, G. Tena, J. Sheen, *Proc. Natl. Acad. Sci. U.S.A.* **97**, 2940 (2000).
18. J.-X. He, J. Gendron, Y. Yang, J. Li, Z. Wang, *Proc. Natl. Acad. Sci. U.S.A.* **99**, 10185 (2002).
19. T. L. Tootle, I. Rebay, *Bioessays* **27**, 285 (2005).
20. C. Widmann, S. Gibson, M. Jarpe, G. Johnson, *Physiol. Rev.* **79**, 143 (1999).
21. See supporting material on Science Online.
22. E. D. Shpak, M. Lakeman, K. Torii, *Plant Cell* **15**, 1095 (2003).
23. S. Joo, Y. Liu, A. Lueth, S. Zhang, *Plant J.* **54**, 129 (2008).
24. M. Ebisuya, K. Kondoh, E. Nishida, *J. Cell Sci.* **118**, 2997 (2005).
25. X. Li *et al.*, *Plant Physiol.* **141**, 1167 (2006).
26. D. Bergmann, F. Sack, *Annu. Rev. Plant Biol.* **58**, 63 (2007).
27. A. M. Hetherington, F. Woodward, *Nature* **424**, 901 (2003).
28. We thank lab members for discussion and comments on the manuscript, The Carnegie Department of Plant Biology for use of microscopes, and L. Smith for identification of maize homologs. Supported by NSF grant IOS-0544895, U.S. Department of Energy grant DE-FG02-06ER15810, a Terman award, and the Stanford Genome Training Program (National Human Genome Research Institute).

Supporting Online Material

www.sciencemag.org/cgi/content/full/322/5904/1113/DC1
Materials and Methods

SOM Text

Figs. S1 to S11

References

24 June 2008; accepted 14 October 2008

10.1126/science.1162263

Regulatory Genes Control a Key Morphological and Ecological Trait Transferred Between Species

Minsung Kim,^{1,3*} Min-Long Cui,^{1*} Pilar Cubas,^{1,4*} Amanda Gillies,² Karen Lee,¹ Mark A. Chapman,^{2,5} Richard J. Abbott,² Enrico Coen^{1†}

Hybridization between species can lead to introgression of genes from one species to another, providing a potential mechanism for preserving and recombining key traits during evolution. To determine the molecular basis of such transfers, we analyzed a natural polymorphism for flower-head development in *Senecio*. We show that the polymorphism arose by introgression of a cluster of regulatory genes, the *RAY* locus, from the diploid species *S. squalidus* into the tetraploid *S. vulgaris*. The *RAY* genes are expressed in the peripheral regions of the inflorescence meristem, where they promote flower asymmetry and lead to an increase in the rate of outcrossing. Our results highlight how key morphological and ecological traits controlled by regulatory genes may be gained, lost, and regained during evolution.

Changes in regulatory genes have been implicated in a range of evolutionary transitions, operating from the micro- to macro-evolutionary scales (1–3). These changes have largely been considered as occurring independently within different species. However, it is

also possible that interspecific hybridization plays an important role in evolution (4). One consequence of such exchanges is that they may allow traits that are lost because of short-term selective pressures to be regained at a later stage. For example, members of the sunflower family (Asteraceae)

share a composite flower head, with each head comprising numerous small flowers (florets). In radiate species, the outer florets (ray florets) have large attractive petals, whereas the inner florets (disc florets) tend to be less conspicuous. Loss of the radiate condition has occurred multiple times within the Asteraceae, yielding nonradiate species with only disc florets (5). These events often correlate with shifts to higher levels of self-pollination (6), which should be favored when mates and/or pollinators occur at low densities (7). Partial or complete reversals from the nonradiate back to the radiate condition have been described (8), some of which appear to involve interspecific hybridization events (9). One explanation for such evolutionary gains and losses is that key regulatory genes control-

¹Department of Cell and Developmental Biology, John Innes Centre, Colney Lane, Norwich NR4 7UH, UK. ²School of Biology, University of St. Andrews, St. Andrews KY16 9TH, UK.

³Faculty of Life Sciences, University of Manchester, Manchester M13 9PT, UK. ⁴Centro Nacional de Biotecnología/CSIC, Darwin 3, Campus UAM, 28049 Madrid, Spain. ⁵Department of Plant Biology, University of Georgia, Athens, GA 30602, USA.

*These authors contributed equally to this work.

†To whom correspondence should be addressed. E-mail: enrico.coen@bbsrc.ac.uk.

ling the trait can be modified and exchanged between species. To test this idea, we analyzed a well-documented case of interspecific exchange in *Senecio*.

Senecio vulgaris (Groundsel) (Fig. 1A) is an allotetraploid nonradiate species, native to Europe and occurring throughout temperate zones. Radiate forms of *S. vulgaris* (Fig. 1B) arose in the United Kingdom after the introduction of *S. squalidus* (Fig. 1C), a diploid radiate species originating from Sicily. *S. squalidus* was brought to the Oxford Botanic Garden about 300 years ago (10), from where it spread. As *S. squalidus* became dispersed throughout the United Kingdom, it crossed with *S. vulgaris*, yielding triploid hybrids (11). Although such triploids have low fer-

tility [seed set <0.02% (9)], some viable progeny occur as a result of backcrosses with *S. vulgaris*. Further rounds of backcrossing are thought to have led to introgression of the radiate trait into some populations of *S. vulgaris* (12, 13). The resulting polymorphism for the radiate condition in *S. vulgaris* is controlled by a single chromosome region or genetic locus, here termed *RAY* (14). Thus, the hypothesized introgression would have involved transfer of the *RAY* locus from *S. squalidus* into *S. vulgaris*.

The *RAY* locus affects floral symmetry. Disc florets have fivefold radial symmetry, whereas ray florets are bilaterally symmetrical (zygomorphic), having enlarged ventral (abaxial) and reduced dorsal (adaxial) petal lobes (Fig. 1D). *CYCLOIDEA*

(*CYC*) is a primary gene controlling floral symmetry in *Antirrhinum majus*, a species with entirely zygomorphic flowers (15). *CYC* encodes a DNA-binding protein belonging to the TCP family (16). Proteins from this family contain a conserved basic helix-loop-helix region that binds DNA (the TCP domain) and have a range of regulatory roles in plant development (16, 17). On the basis of *Antirrhinum* mutant phenotypes, it has been proposed that *CYC*-like genes might also control the development of ray florets in the Asteraceae (18). Supporting this theory, ectopic expression of a *CYC*-like gene from *Gerbera hybrida*, *GhCYC2*, has differential effects on ray and disc floret development in this horticultural species (19).

To determine whether *CYC*-like genes are involved in the *RAY* locus, homologs were isolated from *S. vulgaris*. RNA in situ hybridizations on radiate plants revealed that two of these genes, termed *RAY1* and *RAY2*, were specifically expressed in ray floret primordia (Fig. 2, A and B). *RAY1* and *RAY2* were expressed in a similar pattern in radiate (*R/R*) and nonradiate (*N/N*) genotypes (Fig. 2, A to D). However, the signal appeared to be stronger in *N/N* compared with *R/R*. This difference was confirmed by the expression levels in RNA from young flower heads (Fig. 2E). Stronger expression of the *N* alleles was also seen in RNA from *N/R* heterozygotes, suggesting that it reflects cis-regulatory changes (Fig. 2E). Phylogenetic analysis showed that *RAY1* and *RAY2* belong to a subfamily of TCP genes that include genes known to control flower asymmetry (clade in orange, Fig. 2F). *RAY1* and *RAY2* arose by a duplication event ~30 million years ago (20) that occurred early in the evolution of the Asteraceae, before divergence of *Helianthus*, *Gerbera*, and *Senecio* but after divergence of the Asteraceae from the Lamiales (Fig. 2F). *RAY2* appears to be orthologous to *GhCYC2* from *Gerbera*, which is also expressed preferentially in ray florets (19).

Fig. 1. Flower head of non-radiate *S. vulgaris* (A), radiate *S. vulgaris* (B), and *S. squalidus* (C). Scale bars, 3 mm. (D) Section through a flower head and two individual florets taken by optical projection tomography. Disc floret petals are outlined in orange, whereas ray floret petals are outlined in red (dorsal) or yellow (ventral).

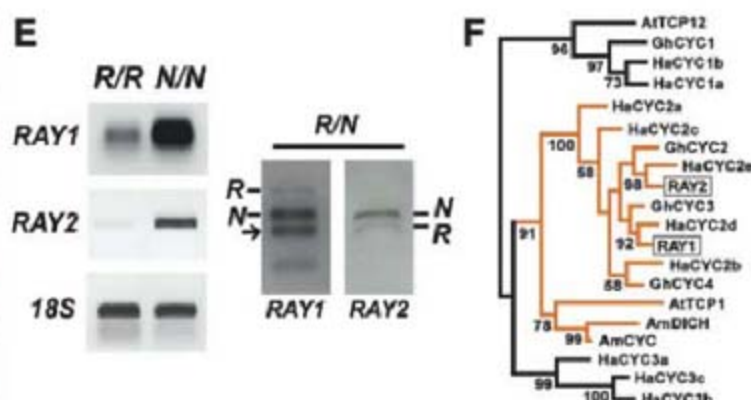
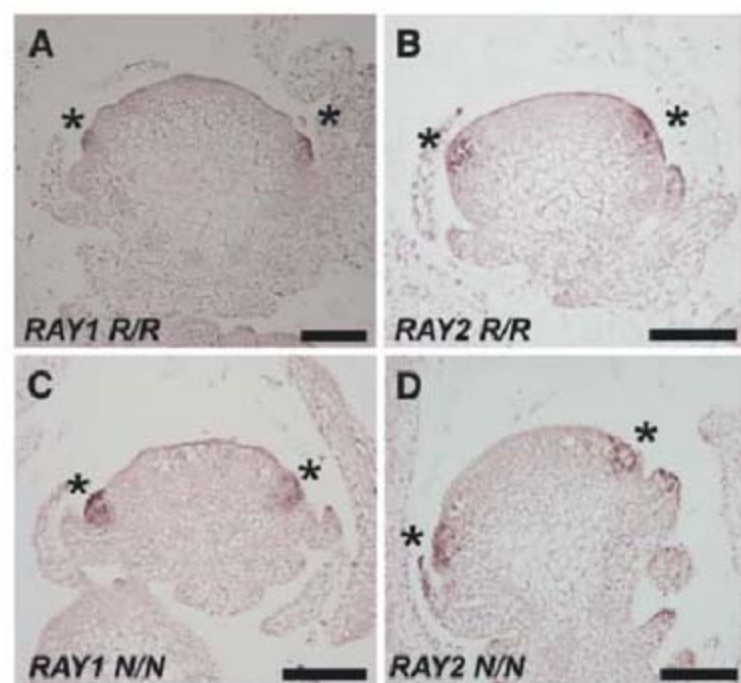
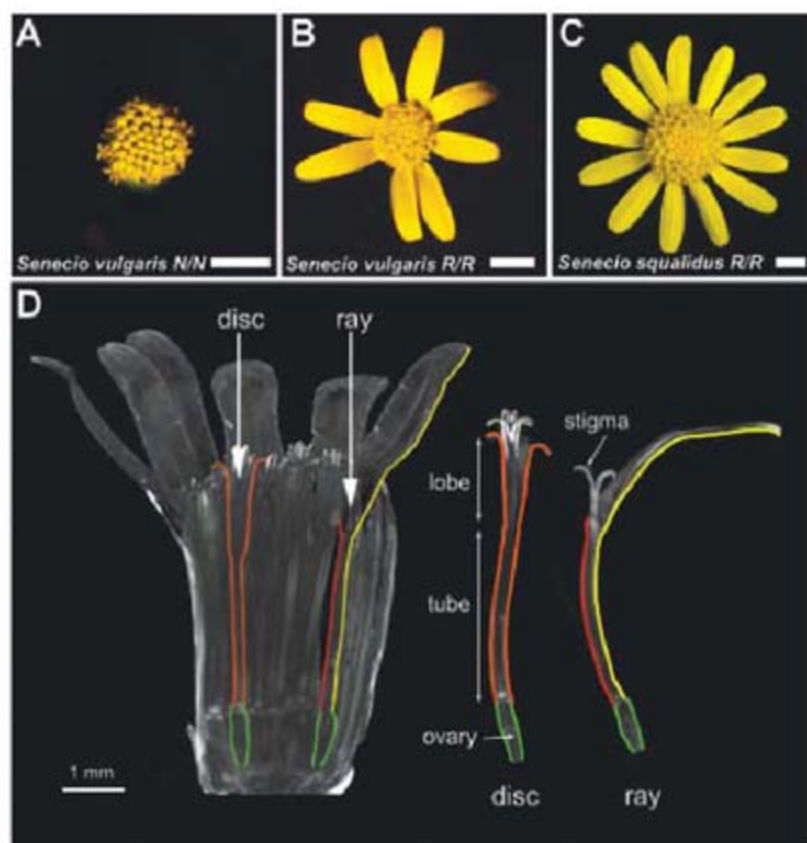


Fig. 2. (A) Expression pattern of *RAY1* in a longitudinal section of a developing radiate (*R/R*) flower head. (B) Expression of *RAY2* in radiate form. (C) Expression of *RAY1* in nonradiate (*N/N*) form. (D) Expression of *RAY2* in nonradiate form. In all cases, *RAY1* and *RAY2* are expressed in the outer floret primordia (marked by *). Scale bars, 100 μ m. (E) Semiquantitative reverse transcription polymerase chain reaction (RT-PCR) showing *RAY1* and *RAY2* expression in young flower heads of *R/R*, *R/N* and *N/N* genotypes. A common band for *R* and *N* is indicated with an arrow in the *R/N* genotype. 18S RNA control is also shown. (F) Phylogenetic relationships between *RAY1*, *RAY2*, and a sample of other genes from the TCP family on the basis of a maximum likelihood analysis of amino acid sequences. *RAY1* and *RAY2* belong to a clade with *CYC* and *DICH*, which control floral symmetry in *Antirrhinum* (15). Bootstraps of 500 replicates (where greater than 50%) are shown. Species abbreviations and GenBank accession numbers are given in (30).

Fig. 3. (A) RAY1: a 412-bp band that cosegregates with *R* and a 238-bp and a 174-bp band with *N* in an F2 population. **(B) RAY2:** a 540-bp and a 156-bp band that cosegregate with *R* and a 696-bp band with *N*. PCR products of *RAY1* and *RAY2* coding regions were digested with *TaqI* and *EcoRI*, respectively. **(C)** Variable sites at *RAY1* and *RAY2* in and around the coding regions for the four haplotypes *N*, *NI*, *R*, and *R1*. Polymorphisms that are diagnostic for *N/NI* versus *R/R1* haplotypes are shown surrounded by black and white, respectively. All other polymorphisms are highlighted in gray. Nucleotide polymorphisms that cause amino acid changes are indicated with asterisks. Positions of deletions of TAAGGAAATCCAAACCCCA and ATAGAAA in the *RAY2-R1* haplotype are marked with arrows.

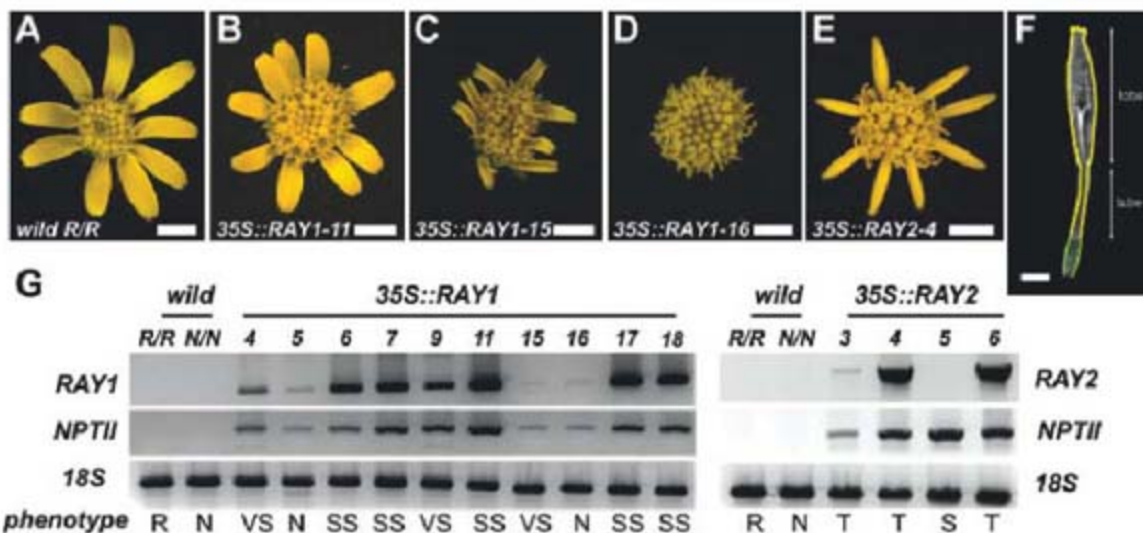
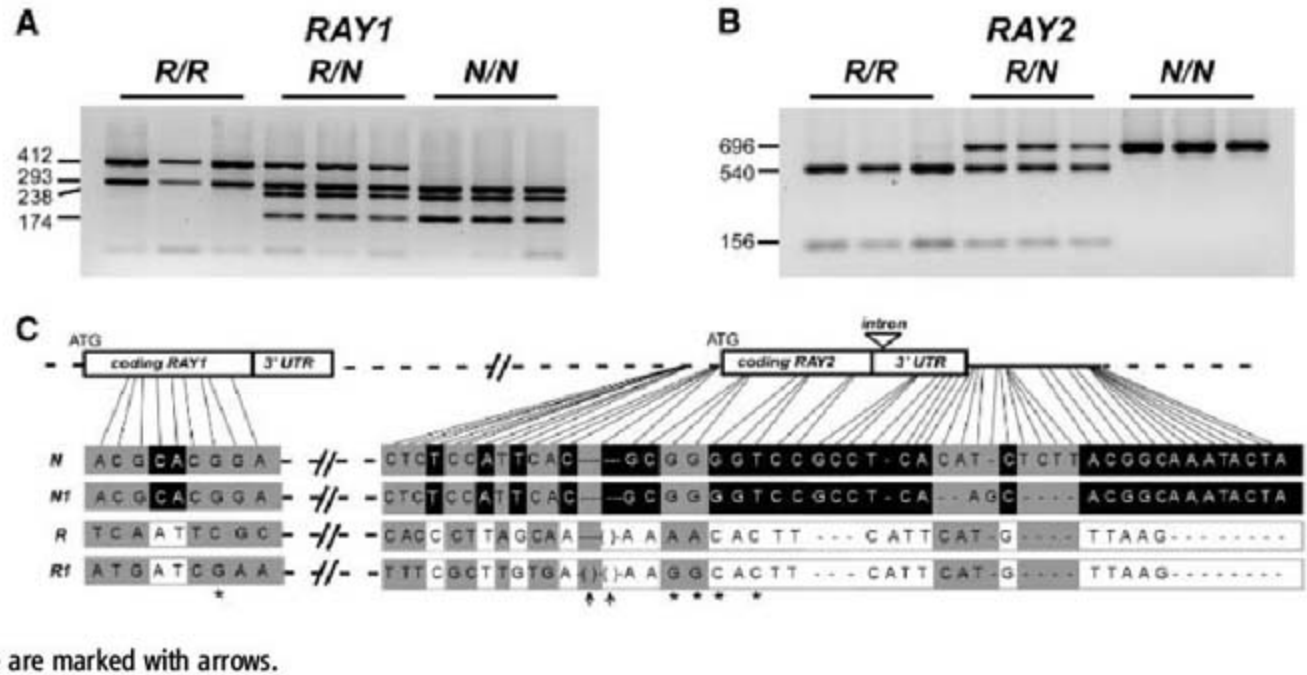


Fig. 4. (A) Flower-head phenotypes of *RR* nontransgenic control plant. **(B)** Flower head with slightly short rays from a transgenic plant overexpressing an internal fragment of *RAY1 N* allele coding sequences in a radiate (*R/R*) *S. vulgaris* background. **(C)** Flower head from a *RAY1* transgenic, as in (B), with very short ray florets. **(D)** Flower head from a *RAY1* transgenic, as in (B), giving no ray florets. **(E)** Flower head from a transgenic overexpressing the *RAY2 N* allele coding sequences in a radiate (*R/R*) *S. vulgaris* background, giving tubular ray florets. **(F)** Section through a ventralized ray floret, color-coded as in Fig. 1D. All transgenics are T1 generation, obtained by self-pollinating the primary transformants. **(G)** Semiquantitative RT-PCR showing expression levels of *RAY1* and *RAY2* in the transgenics, together with controls for 18S RNA and the kanamycin resistance gene (*NPTII*). R, normal radiate head; N, nonradiate or discoid head; SS, slightly short rays; S, short rays; VS, very short rays; T, tubular rays with ventralized petals. Scale bars, 2 mm [(A) to (E)] and 1 mm (F).

To determine whether *RAY1* or *RAY2* map to the *RAY* locus, their sequence was determined for parental radiate (*R/R*) and nonradiate (*N/N*) plants, allowing genotype-specific CAPS (cleaved amplified polymorphic sequences) to be designed (Fig. 3, A and B). Genotyping an F2 population derived from these parents revealed that both *RAY1* and *RAY2* segregated with flower-head phenotype, and we observed no recombinants in more than 700 plants. Linkage between *RAY1* and the *RAY* locus was further confirmed by bulk segregant analysis on *R/R* and *N/N* genotypes, and no recombinants were observed out of 2800 chromosomes. CAPS were also used to genotype accessions of radiate and nonradiate forms from various locations in the United Kingdom (table S1). In all cases, the *RAY1* and *RAY2* geno-

types matched the phenotype, confirming a tight association with each other and with the *RAY* locus. This was further confirmed by sequencing the *RAY* genes from several U.K. *S. vulgaris* accessions: All sequences from *R/R* genotypes were identical, while two minor variants were found among *N/N* genotypes, termed *N* and *NI* (Fig. 3C). Thus, both *RAY1* and *RAY2* are tightly linked and associated with *RAY*, and we were able to define three haplotypes: *N*, *NI*, and *R*. Because the radiate condition in *S. vulgaris* is thought to have originated from *S. squalidus*, *RAY1* and *RAY2* were also sequenced from various U.K. accessions of *S. squalidus*. This revealed two haplotypes, one identical to the *R*-haplotype of *S. vulgaris* and another that was a variant of *R* and was termed *R1* (Fig. 3C and table S1). These results provide

molecular proof that the radiate form of *S. vulgaris* arose through hybridization with *S. squalidus* plants and show that the *R*-haplotype was introgressed through this process.

Comparing the sequences of the haplotypes revealed several differences between *N/NI* and *R/R1* (Fig. 3C and fig. S1A). No diagnostic amino acid substitutions were found for *RAY1*, whereas two amino acid substitutions (S to F, D to E) were associated with the *N/NI* alleles of *RAY2*. The substitutions found in the *N* and *NI* alleles of *RAY2* were also found in the radiate species *S. vernalis* and *S. glaucus* (fig. S1B), making it unlikely that they are responsible for the nonradiate condition. Several diagnostic differences were also found in the 5' and 3' noncoding regions. As these represent only a limited sample of flanking sequence, it is likely that further differences would also be found in regions extending further out from the genes. Thus, the *N/NI* and *R/R1* haplotypes have accumulated multiple nucleotide differences since they diverged from their common ancestor and it is likely that the functionally important changes lie outside the *RAY1* and *RAY2* coding regions.

The rapid spread of the radiate trait in *S. vulgaris*, despite the strong reproductive barrier between *S. vulgaris* and *S. squalidus*, suggests that the introgression of the *R* haplotype may have been driven by selection, presumably acting on differences outside the *RAY1* and *RAY2* coding regions. However, testing for selection by analyzing sequence variation at the *RAY* locus is not straightforward because most selection tests assume a single interbreeding population (21), whereas introgression of *R* involved exchange between two divergent species separated by a major reproductive barrier.

As a further test of whether *RAY1* and *RAY2* play a role in ray floret development, we transformed radiate *S. vulgaris* with two constructs, both of which are driven by the constitutive 35S promoter (the radiate background was chosen because *N* is semidominant and is thought to

represent the derived condition). Expression of an internal fragment of the *RAY1* coding region (*N* allele) that includes the conserved TCP and R domains, yielded 10 independent transformants. Five of these plants produced slightly shorter ray florets (Fig. 4, A and B), three produced very short ray florets (Fig. 4C), and two had only disc florets (Fig. 4D), resembling nonradiate plants. These results suggest that overexpression of *RAY1* is repressing ray floret development, consistent with the higher levels of *RAY1* expression observed in *N/N* genotypes. However, the level of transgene expression did not correlate in a simple manner with the severity of the phenotype; transgenics with slightly short ray florets had higher levels of expression than the discoid transgenics (Fig. 4G). There was also no correlation with the endogenous levels of *RAY1* gene expression, because these levels were similar in transgenics with different phenotypes (fig. S1D). The variation in transgenic phenotype may reflect differences in the pattern of transgene expression, posttranscriptional interactions with the internal *RAY1* fragment used in the transformations, or perhaps promotive as well as inhibitory effects of *RAY1* on ray floret development. Whatever the explanation, the results indicate that *RAY1* plays a critical part in controlling ray versus disc floret identity.

Expression of the entire *RAY2* coding region (*N* allele) in the radiate background produced tubular ray florets in three independent transgenics (Fig. 4E). All petal lobes in these florets resembled the long ventral (abaxial) petal lobes of normal ray florets (Fig. 4, E and F), which suggests that *RAY2* is involved in promoting ventral identity in ray florets. Unlike ectopic expression of *GhCYC2* in *Gerbera hybrida* (19), disc floret development was not modified by expression of *RAY2*. This difference may reflect the fact that the innermost florets in *Gerbera hybrida* are not fully radially symmetrical (19) and may have some raylike character even in untransformed horticultural varieties.

We conclude that the *RAY* locus comprises a cluster of *CYC*-like genes that have played a key role in the evolution of the radiate condition.

Radiate development in the Asteraceae can be compared to the functionally analogous process controlling the development of individual flowers. For both systems, peripheral expression of regulatory genes is involved in establishing the identity of the attractive organs—*CYC* genes for radiate heads and MADS box genes for the flower (22–24). The main difference is that for radiate heads, peripheral expression is organized with respect to the inflorescence apex, whereas for floral organ identity it is organized in relation to the floral apex. Dorsoventral asymmetry within individual flowers is also established in relation to the inflorescence apex (18, 25). Thus, the ability of *CYC* genes to respond to a basic prepattern, centered on the inflorescence apex, could have led to their co-option and involvement in a key evolutionary innovation in the Asteraceae: radiate development.

The subsequent loss of the radiate condition in lineages of the Asteraceae most likely reflects tradeoffs involved in the evolution of breeding systems. Self-fertilization allows reproductive assurance under conditions where mates and/or pollinators are absent or occur at low densities (7) and may be favored, therefore, in colonizing and weedy species, such as *S. vulgaris* (26, 27), despite barriers imposed by inbreeding depression (28) and pollen discounting (29). However, a self-fertilization strategy may impose long-term limitations on responding to changing environmental conditions. Reintroduction of genes that promote outcrossing may therefore allow a self-pollinating species to revert and prevent extinction in the longer term. Our results therefore highlight the interplay between regulatory genes, development, and life history, and show how gene transfers between species may play an important part in the evolution of key ecological and morphological traits.

References and Notes

1. S. B. Carroll, J. K. Grenier, S. D. Weatherbee, *From DNA to Diversity: Molecular Genetics and the Evolution of Animal Design* (Blackwell Scientific, Malden, MA, 2001).
2. J. Doebley, A. Stec, L. Hubbard, *Nature* **386**, 485 (1997).

3. D. L. Stern, *Nature* **396**, 463 (1998).
4. M. L. Arnold, *Evolution Through Genetic Exchange* (Oxford Univ. Press, Oxford, 2006).
5. J. Q. Liu, Y. J. Wang, A. L. Wang, O. Hideaki, R. J. Abbott, *Mol. Phylogenet. Evol.* **38**, 31 (2006).
6. D. F. Marshall, R. J. Abbott, *Heredity* **52**, 331 (1984).
7. C. Goodwillie, S. Kalisz, C. G. Eckert, *Annu. Rev. Ecol. Syst.* **36**, 47 (2005).
8. C. A. Stace, *Heredity* **39**, 383 (1977).
9. A. J. Lowe, R. J. Abbott, *Am. J. Bot.* **87**, 1159 (2000).
10. S. A. Harris, *Watsonia* **24**, 31 (2002).
11. D. F. Marshall, R. J. Abbott, *Heredity* **45**, 133 (1980).
12. R. J. Abbott, P. A. Ashton, D. G. Forbes, *Heredity* **68**, 425 (1992).
13. R. Ingram, J. Weir, R. J. Abbott, *New Phytol.* **84**, 543 (1980).
14. A. H. Trow, *J. Genet.* **2**, 239 (1912).
15. D. Luo, R. Carpenter, C. Vincent, L. Copey, E. Coen, *Nature* **383**, 794 (1996).
16. P. Cubas, N. Lauter, J. Doebley, E. Coen, *Plant J.* **18**, 215 (1999).
17. D. G. Howarth, M. J. Donoghue, *Proc. Natl. Acad. Sci. U.S.A.* **103**, 9101 (2006).
18. E. S. Coen *et al.*, *Philos. Trans. R. Soc. London Biol. Sci.* **350**, 35 (1995).
19. S. K. Broholm *et al.*, *Proc. Natl. Acad. Sci. U.S.A.* **105**, 9117 (2008).
20. M. A. Chapman, J. H. Leebens-Mack, J. M. Burke, *Mol. Biol. Evol.* **25**, 1260 (2008).
21. F. Tajima, *Genetics* **123**, 585 (1989).
22. M. Egea-Cortines, H. Saedler, H. Sommer, *EMBO J.* **18**, 5370 (1999).
23. T. Jack, L. L. Brockman, E. M. Meyerowitz, *Cell* **68**, 683 (1992).
24. E. M. Kramer, V. F. Irish, *Nature* **399**, 144 (1999).
25. J. I. Clark, E. S. Coen, *Plant J.* **30**, 639 (2002).
26. H. G. Baker, *Evolution* **9**, 347 (1955).
27. G. L. Stebbins, *Am. Nat.* **91**, 337 (1957).
28. D. Charlesworth, B. Charlesworth, *Annu. Rev. Ecol. Syst.* **18**, 237 (1987).
29. K. E. Holsinger, *Am. Nat.* **138**, 606 (1991).
30. Materials and methods are available as supporting material on Science Online.
31. We thank C. Walton for critical discussion. Supported by EMBO and HFSP long-term fellowship (M.K.), BBSRC grant BB-D017742 (M.C.), BBSRC grant G10929 (R.J.A.) and NERC/S/A/2000/03636 studentship (M.A.C.). GenBank accession numbers for *RAY1* and *RAY2* are FJ356698 to FJ356704.

Supporting Online Material

www.sciencemag.org/cgi/content/full/322/5904/1116/DC1

Materials and Methods

Fig. S1

Table S1

References

7 August 2008; accepted 7 October 2008

10.1126/science.1164371

New Products Focus: Automation



Culture Sample Barcode Labeler

The Labelmaster II is an automated system for labeling and organizing culture media samples in clinical, food, and pharmaceutical testing laboratories. Designed to print and affix labels to petri dishes, the pneumatic system allows up to a thousand plates per hour to be processed and sorted accurately. An optional storage unit increases this capacity to 1,900. Labels are printed and applied directly to the underside edge of the sample plates, which are then stacked and sorted one by one. Applying the label in this way allows automatic plate readers to be used, protects the barcode from scratches and spills, and ensures the label remains attached to the base containing the sample, should the lid become dislodged.

Don Whitley Scientific

For information +44-(0)-1274-595-728

www.dwscientific.co.uk

Personal Automation System

The Maxwell 16 Flexi Method Firmware features a new software system that provides users with flexibility and control of automated instrument operation. The new functionality helps research labs develop and optimize instrument methods to maximize performance for unique sample types and address specific application requirements. The Maxwell 16 System with the Flexi Method Firmware delivers flexible results from diverse sample types; controls key aspects of instrument operation; simplifies workflow with fully integrated prefilled cartridges and preprogrammed protocols; and requires only as much space as a laptop computer. The system can simultaneously purify up to 16 samples without user intervention.

Promega

For information 608-274-4330

www.promega.com

Baculovirus Titer System

A novel titration system, deltaTITER enables researchers to accurately quantify the amount of baculovirus in a sample in just one hour. The kit offers a significant five-day time saving and accuracy benefits compared with the traditional method of plaque assay, which requires skilled personnel and often gives variable results. Measurement of baculovirus titer is an important workflow component for protein expression, in both research and production laboratories. The automated kit is based on a proprietary buffer system, and is designed to be used with deltaDOT's high-performance capillary electrophoresis tool, the Peregrine.

deltaDOT

For information +44-(0)-207-594-1001

www.deltadot.com

Liquid Handling Module

A new Liquid Handling Module extends the functionality of the ArrayScan VTI HCS Reader. The combination of synchronous dispensing-while-imaging capability, kinetic image capture, a range of image analysis algorithms, and "on-the-fly" processing allows

the real-time capture of cellular phenotypes and rapid biological responses. Multiple aspirate/dispense options enable dye loading, media replacement, incubation, and stimulus addition to be fully automated. The Cellomics ArrayScan VTI with Liquid Handling Module provides an automated solution for pharmacological studies, including G protein-coupled receptor biology, cell pathway analysis, compound pharmacology, and in vitro toxicology. Compatible with 96-well and 384-well plates, the module makes use of disposable tips with a dispensing volume range of 3 μ l to 200 μ l.

Thermo Fisher Scientific

For information 905-332-2000

www.thermofisher.com

Magnetic Particle Processors

The MagMAX Express platform is an automated system for nucleic acid isolation that incorporates the rapid, reliable, and cost-effective magnetic bead-based extraction of nucleic acids. MagMAX Isolation Kits extract both genomic and viral nucleic acid from diverse sample matrices, with products available for gene expression analysis, small RNA research, and microarray profiling.

Applied Biosystems

For information 800-327-3002

www.appliedbiosystems.com

Vial Barcode Labeler

The Label X 2D barcode labeler is a stand-alone unit designed to accommodate a wide range of glass vials. This semiautomated labeler applies barcode labels to the bottom of vials and features a compact footprint. The labeler is equipped with interchangeable manifolds so it is simple to change between sample vials without the use of tools. Manifold options include eight, 24, and 96 vials, ranging in diameter from 6.5 mm to 28 mm. It is pneumatically operated and requires no electrical connection, applying up to 96 labels in less than 20 seconds.

MatriCal

For information 509-343-6225

www.matricall.com

Electronically submit your new product description or product literature information! Go to www.sciencemag.org/products/newproducts.dtl for more information.

Newly offered instrumentation, apparatus, and laboratory materials of interest to researchers in all disciplines in academic, industrial, and governmental organizations are featured in this space. Emphasis is given to purpose, chief characteristics, and availability of products and materials. Endorsement by *Science* or AAAS of any products or materials mentioned is not implied. Additional information may be obtained from the manufacturer or supplier.